# FAST high-temperature consolidation of Oxide-Dispersion Strengthened (ODS) steels : Process, microstructure, precipitation, properties

Xavier Boulnat

# THÈSE

## FAST high-temperature consolidation of Oxide-Dispersion Strengthened (ODS) steels : process, microstructure, precipitation, properties.

Présentée devant
### l'Institut National des Sciences Appliquées de Lyon

pour obtenir
### le GRADE DE DOCTEUR

École doctorale :
### Matériaux de Lyon

Spécialité :
### Matériaux

par
# Xavier BOULNAT

Ingénieur de l'Institut National Polytechnique de Grenoble

Thèse soutenue le 18 décembre 2014 devant la Commission d'examen

### Jury

| | | |
|---|---|---|
| ROLAND LOGÉ | Professeur, EPF Lausanne | Président |
| ALEXIS DESCHAMPS | Professeur, SIMaP | Rapporteur |
| ERNST KOZESCHNIK | Professeur, TU Wien | Rapporteur |
| MARTA SERRANO | Ingénieur de Recherche, CIEMAT Madrid | Examinateur |
| MARTINE BLAT | Ingénieur de Recherche, EDF R&D | Examinateur |
| YANN DE CARLAN | Ingénieur de Recherche, CEA | Encadrant CEA |
| DAMIEN FABRÈGUE | Maître de Conférences HDR, INSA Lyon | Directeur de thèse |
| MICHEL PEREZ | Professeur, INSA Lyon | Directeur de thèse |

MATEIS - UMR CNRS 5510 - INSA de Lyon
25, avenue Jean Capelle, 69621 Villeurbanne Cedex (FRANCE)

## INSA Direction de la Recherche - Ecoles Doctorales – Quinquennal 2011-2015

| SIGLE | ECOLE DOCTORALE | NOM ET COORDONNEES DU RESPONSABLE |
|---|---|---|
| **CHIMIE** | **CHIMIE DE LYON**<br>**http://www.edchimie-lyon.fr**<br><br>Sec :Renée EL MELHEM<br>Bat Blaise Pascal<br>3e etage<br>Insa : R. GOURDON | M. Jean Marc LANCELIN<br>Université de Lyon – Collège Doctoral<br>Bât ESCPE<br>43 bd du 11 novembre 1918<br>69622 VILLEURBANNE Cedex<br>Tél : 04.72.43 13 95<br>directeur@edchimie-lyon.fr |
| **E.E.A.** | **ELECTRONIQUE,<br>ELECTROTECHNIQUE, AUTOMATIQUE**<br>**http://edeea.ec-lyon.fr**<br><br>Secrétariat : M.C. HAVGOUDOUKIAN<br>eea@ec-lyon.fr | M. Gérard SCORLETTI<br>Ecole Centrale de Lyon<br>36 avenue Guy de Collongue<br>69134 ECULLY<br>Tél : 04.72.18 60.97 Fax : 04 78 43 37 17<br>Gerard.scorletti@ec-lyon.fr |
| **E2M2** | **EVOLUTION, ECOSYSTEME,<br>MICROBIOLOGIE, MODELISATION**<br>**http://e2m2.universite-lyon.fr**<br><br>Insa : H. CHARLES | Mme Gudrun BORNETTE<br>CNRS UMR 5023 LEHNA<br>Université Claude Bernard Lyon 1<br>Bât Forel<br>43 bd du 11 novembre 1918<br>69622 VILLEURBANNE Cédex<br>Tél : 06.07.53.89.13<br>e2m2@ univ-lyon1.fr |
| **EDISS** | **INTERDISCIPLINAIRE SCIENCES-<br>SANTE**<br>**http://www.ediss-lyon.fr**<br><br>Sec :<br>Insa : M. LAGARDE | Mme Emmanuelle CANET-SOULAS<br>INSERM U1060, CarMeN lab, Univ. Lyon 1<br>Bâtiment IMBL<br>11 avenue Jean Capelle INSA de Lyon<br>696621 Villeurbanne<br>Tél : 04.72.68.49.09 Fax :04 72 68 49 16<br>Emmanuelle.canet@univ-lyon1.fr |
| **INFOMATHS** | **INFORMATIQUE ET<br>MATHEMATIQUES**<br>**http://infomaths.univ-lyon1.fr**<br><br>Sec :Renée EL MELHEM<br>Bat Blaise Pascal<br>3e etage<br>infomaths@univ-lyon1.fr | Mme Sylvie CALABRETTO<br>LIRIS – INSA de Lyon<br>Bat Blaise Pascal<br>7 avenue Jean Capelle<br>69622 VILLEURBANNE Cedex<br>Tél : 04.72. 43. 80. 46 Fax 04 72 43 16 87<br>Sylvie.calabretto@insa-lyon.fr |
| **Matériaux** | **MATERIAUX DE LYON**<br>**http://ed34.universite-lyon.fr**<br><br>Secrétariat : M. LABOUNE<br>PM : 71.70 –Fax : 87.12<br>Bat. Saint Exupéry<br>Ed.materiaux@insa-lyon.fr | M. Jean-Yves BUFFIERE<br>INSA de Lyon<br>MATEIS<br>Bâtiment Saint Exupéry<br>7 avenue Jean Capelle<br>69621 VILLEURBANNE Cedex<br>Tél : 04.72.43 83 18 Fax 04 72 43 85 28<br>Jean-yves.buffiere@insa-lyon.fr |
| **MEGA** | **MECANIQUE, ENERGETIQUE, GENIE<br>CIVIL, ACOUSTIQUE**<br>**http://mega.universite-lyon.fr**<br><br>Secrétariat : M. LABOUNE<br>PM : 71.70 –Fax : 87.12<br>Bat. Saint Exupéry<br>mega@insa-lyon.fr | M. Philippe BOISSE<br>INSA de Lyon<br>Laboratoire LAMCOS<br>Bâtiment Jacquard<br>25 bis avenue Jean Capelle<br>69621 VILLEURBANNE Cedex<br>Tél :04.72 .43.71.70 Fax : 04 72 43 72 37<br>Philippe.boisse@insa-lyon.fr |
| **ScSo** | **ScSo***<br>**http://recherche.univ-lyon2.fr/scso/**<br><br>Sec : Viviane POLSINELLI<br>    Brigitte DUBOIS<br>Insa : J.Y. TOUSSAINT | M. OBADIA Lionel<br>Université Lyon 2<br>86 rue Pasteur<br>69365 LYON Cedex 07<br>Tél : 04.78.77.23.86 Fax : 04.37.28.04.48<br>Lionel.Obadia@univ-lyon2.fr |

*ScSo : Histoire, Géographie, Aménagement, Urbanisme, Archéologie, Science politique, Sociologie, Anthropologie

# Acknowledgements

Warm thanks are due to Professor R. Logé, who made me a great honor by presiding the jury of my dissertation. I sincerely acknowledge Professor E. Kozeschnik for his help on the oxide precipitation modeling. I really appreciated the time spent on discussing physical metallurgy in Vienna. I thank him for being reviewer of this manuscript, as well as Professor A. Deschamps and Professor G. Robert Odette for accepting to review this manuscript so carefully. I sincerely thank my two additional committee members, M. Blat and M. Serrano for their valuable input.

Je remercie Yann de Carlan pour la confiance qu'il m'a accordée dès le début et dont le soutien a été un réel moteur durant ces trois années. Je voudrais remercier mes directeurs de thèse Michel Perez et Damien Fabrègue. Michel, je pense que ta grande force est la remise en cause systématique des acquis [1], ce qui m'a permis de me poser les bonnes questions. Damien, ta curiosité scientifique et ton enthousiasme contagieux sont un cadeau pour un thésard. Je te dis ici toute ma gratitude.

Je remercie l'ensemble du Service de Recherches Métallurgiques Appliquées du CEA de Saclay. Particulièrement, je remercie Jean-Luc Béchade, chef du Laboratoire d'Analyse Microstructurale des Matériaux, pour sa disponibilité et sa collaboration sur la ligne DIFFABS. Je remercie toutes les personnes que j'ai cotoyées au SRMA : Stéphane, Elodie, Didier, Annick, Jérome, Sébastien, France, Benoît, Joël et Joël, Jean-Christophe, Nicolas, Denis, Thomas, Mickaël, Louise, Emma, Julie. J'aimerais dire à Marie-Hélène Mathon toute ma sympathie et voudrais saluer son énergie. Je remercie tous ceux qui m'ont accueilli à Paris et ses environs : Alain et Yveline, Fredo, Dine, Ivan, Lolie et Christian, François et Caro.

Je voudrais aussi remercier les membres du laboratoire MATEIS de l'INSA de Lyon. Je suis extrêmement reconnaissant envers tous ceux qui ont fait que j'étais heureux de venir au travail tous les jours, cela a compté bien plus que les résultats de ce manuscrit. Dans ce monde relativement solitaire de la thèse, je remercie mon binôme de fortune Nicolas Sallez. On aura derrière nous de belles anecdotes, entre le synchrotron, Séville et San Diego. Un grand merci à Didier Bardel, qui est aussi brillant que modeste ; je te remercie pour tes échanges entre deux Roudor. Un grand merci à Bassem. Je remercie Edouard et Adama que j'ai eu le plaisir d'encadrer et qui ont donc contribué à cette thèse. Je remercie Florian Mercier pour ses compétences au SPS. Je remercie Thierry Douillard pour les discussions microscopie et

---

1. *ou le paradoxe du syndicaliste*

bien sûr Sophie Cazottes que mes échantillons magnétiques n'ont jamais effrayée. Un énorme merci à Corinne, Laurence et Frida côté MATEIS et Liliane côté CEA pour leur disponibilité et leur gentillesse. Merci à Carole pour nos discussions variées toujours agréables. Un gros merci aux thésards qui m'ont supporté trois ans : Anto, Paul, Aude, Vincent, Itziar, Joël. Bon courage aux jeunes lascars du deuxième, c'est bientôt la fin !

Je voudrais enfin rappeler toute mon admiration pour ces gens qui font avancer la recherche et l'innovation en France. Je tire mon chapeau à ces ingénieurs, chercheurs, enseignants, techniciens et personnels, qui au quotidien partagent leurs connaissances et sont heureux de le faire. Cette thèse n'est rien d'autre qu'un petit morceau de ce qu'ai appris à leur côté.

Je dédie cette thèse à P.F. Gobin.

Merci à mes parents.

Merci à la femme que j'aime. Quelle chance de t'avoir à mes côtés !

*'Nel mezzo del cammin di nostra vita
mi ritrovai per una selva oscura
ché la diritta via era smarrita.'*

*Dante Alighieri, Primo Canto dell'Inferno, La Divina Commedia.*

# Résumé

Ce travail vise à améliorer la compréhension de la microstructure d'aciers ferritiques inoxydables à durcissement structural appelés **aciers ODS**[2]. Ces aciers sont d'excellents candidats pour les matériaux de gainage des réacteurs nucléaires à neutrons rapides. Ils sont fabriqués par métallurgie des poudres, ce qui inclut le cobroyage d'une poudre ferritique avec une fine poudre d'oxydes, suivi de la consolidation à haute température de la poudre ainsi élaborée. La consolidation permet de former un matériau dense renforcé par des particules nanométriques qui sont responsables des bonnes propriétés mécaniques à haute température. Cependant, les procédés conventionnels, notamment la Compaction Isostatique à Chaud, provoquent des microstructures hétérogènes qui étaient jusqu'à ce jour mal comprises.

Ainsi, la technique rapide de consolidation assistée par courant électrique appelée **"Spark Plasma Sintering" (SPS)**, a été testée afin d'étudier la microstructure. Pour la première fois, on montre que d'excellentes **propriétés mécaniques** peuvent être obtenues par SPS, comparables à celles des matériaux ODS obtenus classiquement par Compaction Isostatique à Chaud, mais avec un temps de procédé largement réduit.

Cependant, la consolidation par SPS échoue quand il s'agit d'obtenir une **microstructure ferritique homogène**. En effet, malgré la cinétique rapide de consolidation, on obtient des grains dits ultrafins (D<500 nm) entourée de grains plus grossiers (D>10 $\mu$m). Une caractérisation microstructurale poussée a permis de comprendre l'évolution du matériau durant la consolidation. Une expérience montée sur le synchrotron SOLEIL a permis un suivi *in situ* de la croissance hétérogène dans les ODS. Un modèle d'évolution microstructurale a été proposé. Le calcul des pressions gouvernant la mobilité des interfaces souligne l'importance de la déformation plastique hétérogène issue du cobroyage des poudres. Par ailleurs, il est montré que la précipitation des particules d'oxydes ancre les joints de grains et stabilise la microstructure hétérogène, même à très haute température. On montre aussi qu'augmenter la teneur en yttrium, titane et oxygène n'empêche pas la **croissance anormale** mais permet cependant de contrôler la fraction et la taille de grains ultrafins, et donc les propriétés mécaniques des aciers ODS. Ce travail permet de proposer des solutions technologiques à tester pour mieux contrôler la taille de grains dans les ODS ferritiques.

Parce que les particules à travers l'**ancrage des joints de grains** jouent un rôle primordial dans la croissance des grains, une caractérisation fine de l'état de **précipitation** a été réalisée sur les matériaux consolidés par SPS. L'étude par Microscopie Electronique en Transmission, Diffusion des Neutrons aux Petits Angles et

---

2. Oxide-Dispersion Strengthened

Sonde Atomique Tomographique révèle une grande densité d'oxydes qui varient en taille et en composition chimique. Cela démontre l'extrême propension des oxydes à former dès les premières minutes de consolidation. Un **modèle thermodynamique** de type germination/croissance/coalescence a été développé pour simuler les cinétiques de précipitation des phases $Y_2O_3$ et $Y_2Ti_2O_7$ durant les étapes de consolidation non isothermes. Tant les résultats expérimentaux que numériques démontrent la précipitation rapide des nano-particules qui sont ensuite extrêmement stables durant les recuits. Ce modèle permet de mieux comprendre la spécificité des microstructures et de la précipitation dans les ODS, de la formation rapide de particules nanométriques à la précipitation grossière d'oxydes de titane aux interfaces.

Pour conclure, ce travail de thèse illustre donc la difficulté d'éviter la croissance anormale dans les aciers ODS ferritiques, même avec des temps de consolidation très courts. Différents chemins de fabrication sont toutefois envisageables. Par exemple, on démontre l'avantage de la **transformation allotropique ferrite/austenite** uniquement permise dans les aciers Fe-9/12Cr, avec une microstructure ferrito-martensitique fine et homogène obtenue par SPS. On recommande de réduire la teneur actuelle en titane afin de prévenir la formation de gros oxydes de titane, principalement aux joints de grains, qui est néfaste à la ductilité des aciers ODS en traction et probablement en fluage.

**MOTS-CLÉS:** Aciers ODS, Métallurgie des Poudres, Spark Plasma Sintering, Croissance de Grains, Ferrite, Recristallisation, Transformation de Phase, Précipitation, Modélisation, Caractérisation Microstructurale, Microscopie, Synchrotron, Propriétés Mécaniques

# Abstract

This work aims to lighten the understanding of the behavior of a class of metallic materials called **Oxide-Dispersion Strengthened (ODS) ferritic steels**. They are excellent candidates for tube cladding materials of Sodium-cooled Fast neutron Reactors (SFR). ODS steels are produced by powder metallurgy with various steps including atomization, mechanical alloying and high-temperature consolidation. The consolidation involves the formation of **nanoparticles** in the steel and various evolutions of the microstructure of the material that are not fully understood.

In this thesis, a novel consolidation technique assisted by electric field called **"Spark Plasma Sintering" (SPS)** or "Field-Assisted Sintering Technique" (FAST) was assessed. Excellent **mechanical properties** were obtained by SPS, comparable to those of conventional hot isostatic pressed (HIP) materials but with much shorter processing time. Also, a broad range of microstructures and thus of tensile strength and ductility were obtained by performing SPS on either milled or atomized powder at different temperatures.

However, SPS consolidation failed to avoid **heterogeneous microstructure** composed of ultrafine-grained regions surrounded by micronic grains despite of the rapid consolidation kinetics. A multiscale **characterization** allowed to understand and model the evolution of this complex microstructure. An analytical evaluation of the contributing mechanisms can explain the appearance of the complex grain structure and its thermal stability during further heat treatments. Inhomogeneous distribution of plastic deformation in the powder is argued to be the major cause of heterogeneous **recrystallization** and further grain growth during hot consolidation. Even if increasing the solute content of yttrium, titanium and oxygen does not impede **abnormal growth**, it permits to control the fraction and the size of the retained ultrafine grains, which is a key-factor to tailor the mechanical properties.

Since **precipitation** through **grain boundary pinning** plays a significant role on grain growth, a careful characterization of the precipitation state was performed on consolidated ODS steels. The experimental data obtained by transmission electron microscopy, small angle neutron scattering and atom-probe tomography evidenced the presence of dense and nanosized particles in SPS ODS steels, similarly to what is observed in conventional ODS steels. This is of great importance since it proves that the precipitation is very rapid and mainly occurs during the heating stage of the consolidation process. Using a **thermodynamic model**, the precipitation kinetics of $Y_2O_3$ and $Y_2Ti_2O_7$ were successfully reproduced at various consolidation temperatures. Both experimental and numerical findings agree with the rapid precipitation of nanoparticles that are then extremely stable, even at high temperature. Consequently, this model can be an efficient tool to design ODS steels

by the optimization of the precipitation state.

To conclude, this thesis emphasizes the difficulty to avoid abnormal growth in ODS ferritic steels, even with short consolidation process by Spark Plasma Sintering. Several paths are though opened for the design of optimized ODS steels. The $\alpha$-ferrite to $\gamma$-austenite phase transformation exclusively permitted in the 9-12 chromium ferritic steels was confirmed to be the best solution, for both conventional or SPS techniques. Last but not least, one suggests to minimize the amount of titanium in ODS steels, since it is responsible for the formation of coarse oxides ($TiO_2$ or equivalent) that are detrimental for the damage behavior. Given that this study moderates the difference in the thermal stability of $Y_2Ti_2O_7$ compared to that of $Y_2O_3$, titanium-free ODS ferritic steels would still exhibit excellent behavior at high temperature.

KEY-WORDS: ODS steels, Powder metallurgy, Spark Plasma Sintering, Tensile properties, Strengthening model, Grain growth, Recrystallization, Phase transformation, Precipitation modeling, EBSD, SANS, TEM, Synchrotron X-ray diffraction, Multiscale characterization

# List of scientific communications

**Publications in peer-reviewed journals**

[A] X. Boulnat, D. Fabrègue, M. Perez, M-H. Mathon, Y. de Carlan, High-temperature tensile properties of Nano-Oxide Dispersion Strengthened ferritic steels produced by Mechanical Alloying and Spark Plasma Sintering, Metallurgical and Materials Transactions A, 2013, Vol. 44, Issue 6, pp. 2461-2465

[B] X. Boulnat, D. Fabrègue, M. Perez, S. Urvoy, D. Hamon, Y. de Carlan, Assessment of the consolidation of ODS ferritic Steels by Spark Plasma Sintering : from laboratory scale to industrial products, Powder Metallurgy, 2014, Vol. 57, pp. 204-211.

[C] B. Mouawad, X. Boulnat, D. Fabrègue, M. Perez, Y. de Carlan, Tailoring the microstructure and the mechanical properties of ultrafine grained ferritic steels by powder metallurgy, Journal of Nuclear Materials, in press.

[D] X. Boulnat, M. Perez, D. Fabrègue, T. Douillard, M-H. Mathon, Y. de Carlan, Microstructure evolution in nano-reinforced ferritic steels processed by Mechanical Alloying and Spark Plasma sintering, Metallurgical and Materials Transactions A, 2014, Vol. 45A, pp. 1485-1497.

[E] N. Sallez, X. Boulnat, A. Borbély, J.L. Béchade, Y. de Carlan, C. Mocuta, P. Donnadieu, D. Fabrègue, M. Perez, Y. Bréchet, *In situ* characterization of microstructural instabilities in nanocrystalline powder : recovery, recrystallization and abnormal growth in nano-reinforced steels, Acta Materialia, Vol. 87, 2015, pp. 377–389.

[F] X. Boulnat, N. Sallez, M. Dadé, A. Borbély, J.L. Béchade, Y. de Carlan, J. Malaplate, P. Donnadieu, F. de Geuser, A. Deschamps, Y. Bréchet, D. Fabrègue, M. Perez, Influence of oxide volume fraction on abnormal growth of nanostructured ferritic steels during anisothermal treatments : an *in situ* study, to be submitted.

[G] X. Boulnat, M. Perez, D. Fabrègue, S. Cazottes, Y. de Carlan, Characterization and modeling of precipitation kinetics of nanosized oxides in ferritic steels during rapid non-isothermal treatments, to be submitted.

## Presentations in conferences

1. X. Boulnat, D. Fabrègue, M. Perez, S. Cazottes, Y. de Carlan, *Assessment of the Sintering of ODS Materials by SPS*, 2012 International Conference on Powder Metallurgy & Particulate Materials, Nashville, Tennessee, USA.

2. X. Boulnat, R. Forté, A. Lamontagne, D. Fabrègue, M. Perez, S. Cazottes, Y. de Carlan, *Elaboration par frittage flash (SPS) d'aciers nano-renforcés (ODS)*, 7ème Colloque Science et Technologie des Poudres, 2012, Toulouse, France.

3. X. Boulnat, D. Fabrègue, M. Perez, Y. de Carlan, *Processing and mechanical properties of ODS ferritic Steels by Spark Plasma Sintering*, EUROMAT 2013, in High strength ODS steels, Sevilla, Spain.

4. X. Boulnat, N. Sallez, A. Borbely, J-L. Béchade, Y. de Carlan, P. Donnadieu, C. Mocuta, L. Hennet, D. Fabrègue, D. Thiaudière, J. Malaplate, P. Moeyaert, M. Perez, Y. Bréchet, *Effect of Milling and Precipitation Reinforcement on Grain Growth in Oxide-Dispersion Strengthened Steels*, in Materials and Fuels for the Current and Advanced Nuclear Reactors III, 2014 TMS Annual Meeting, San Diego, USA.

5. X. Boulnat, M. Perez, S. Cazottes, M.H. Mathon, D. Fabrègue, Y. de Carlan, *Multiscale Characterization and Modeling of Precipitation in Ferritic Nanoreinforced Steels*, in Phase Transformation and Microstructural Evolution, 2014 TMS Annual Meeting, San Diego, USA.

6. X. Boulnat, D. Fabrègue, J-L Flament, P. Wident, Y. de Carlan, M. Perez, *Microstructure and Mechanical Properties of Ultrafine Grained Ferritic Steels Processed by Spark Plasma Sintering and Hot Isostatic Pressing : A Comparative Study*, in Powder Processing of Nanomaterials, 2014 TMS Annual Meeting, San Diego, USA.

7. X. Boulnat, Y. de Carlan, M-H. Mathon, T. Douillard, D. Fabrègue, M. Perez, *Microstructure Evolution in Nano-reinforced Ferritic Steel Processed by Mechanical Alloying and Spark Plasma Sintering*, in Materials Processing Fundamentals, 2014 TMS Annual Meeting, San Diego, USA.

# Contents

# Contents

# Introduction

## Industrial context

In the last decades, the energy policy led to the emergence of 435 nuclear reactors worldwide [1, 2], currently producing 370 GW$_e$ [3]. In France, 80% of the electricity comes from Pressurized Water Reactors (PWR) of second and third generations. These last years, a co-operative international endeavor called Generation IV International Forum was organized to develop new concepts of competitive nuclear reactors that aim at optimizing the resources and minimizing the resulting wastes. Among the possible options for the construction of a fourth generation fast neutron reactor, the concept of Sodium-cooled Fast Reactor (SFR) is the most advanced system in France thanks to a large feedback. Making reactors competitive requires demanding specifications in terms of irradiation dose and temperature. Indeed, the targeted (20 at%) burn-ups [4] for the new cores lead to doses up to 150 displacements per atom (dpa [5]) in the cladding material. This irradiation damage can create numerous defects in metallic materials that will result in significant swelling of the tubes. Since the design targets a minimum liquid sodium fraction and thus a configuration where fuel pins are close to each other, the dimensional variation of the in-service cladding tubes must be limited. Face-centered cubic (fcc) austenitic steels, well-known to exhibit excellent creep behavior, were however observed to drastically swell under irradiation dose higher than 100 to 130 dpa. To face this potential issue, the austenitic steels formerly used in SFRs may be replaced by base-centered cubic (bcc) ferritic/martensitic steels, which demonstrate much higher resistance to swelling.

Since ferritic steels exhibit moderate resistance to thermal creep compared to austenitic steels, new ferritic steels reinforced by oxides particles were designed to improve these properties. In that case, dense nanometer-sized particles act as obstacles to dislocations and impede their motion at high temperature, which drastically reduces the creep strain. Due to their high creep strength and excellent swelling resistance, ferritic/martensitic oxide-dispersion strengthened (ODS)

---

3. The production of 1 electrical Gigawatt requires approximately 3 thermal Gigawatts due to the limitation of the steam-turbine efficiency (Rankine cycle).

4. Roughly the amount of energy released per fuel unit mass

5. 1 dpa corresponds to one displacement of an atom from its lattice site to another [3].

1

steels are thus serious candidates for tube cladding materials and are widely studied [4, 5]. Their processing route involves powder metallurgy with powder milling and further high-temperature consolidation and extrusion. The whole fabrication is therefore heavy and makes the microstructure evolution study not straightforward. Recent development led to two main options for ODS steel design: (i) 9-12Cr ODS ferritic/martensitic steels are easily workable. Thanks to the allotropic $\alpha$-to-$\gamma$ phase transformation, the anisotropic cold-worked microstructure can be conveniently transformed into a novel isotropic recrystallized microstructure. (ii) 14Cr ODS fully ferritic steels consist of an excellent alternative because their high chromium content enhances the corrosion resistance. Yet, their microstructure is much tougher to tailor since no allotropic transformation can be used. Specially, ODS ferritic steels exhibit abnormal grain growth leading to a microstructure with both very fine (submicronic) and very large (D > 10 $\mu m$) grains. This is also accompanied with an extraordinary resistance to recrystallization up to very high temperature. The choice between transformable 9Cr or fully ferritic 14Cr ODS steels will be governed by the best compromise between fabrication and in-service performance, which has not been determined yet. In this context, every technological means must be investigated to assess the production of ODS steels. In order to study technological and metallurgical issues as well, a simpler method to produce model alloys to characterize would be interesting. In this context, Spark Plasma Sintering (SPS) was considered. SPS is a pressure and electric field-assisted consolidation technique that allows the powder to be directly heated up by a high current intensity. Combined with sufficient hydrostatic pressure, this would allow to drastically reduce the overall consolidation time and thus obtain dense materials.

# Adopted approach

This thesis was carried out with the following purposes (Fig. 1):

- Assess the consolidation of ODS ferritic steels by an alternative field-assisted sintering technique called Spark Plasma Sintering, with a validation criterion based on the mechanical properties of the consolidated materials.

  *Is it possible to produce ODS steels by SPS with high-temperature properties comparable to conventional ODS steels?*

- Use the Spark Plasma Sintering as a tool to generate various ferritic microstructures in order to characterize and understand the evolution of (abnormal) grain growth of ODS ferritic steels.

  *Is rapid SPS consolidation able to avoid abnormal growth? What does make the bimodal microstructure so stable?*

**ODS STEELS BY SPARK PLASMA SINTERING:**

**(i) Consolidation**

**(ii) Characterization**

**(iii) Modeling**
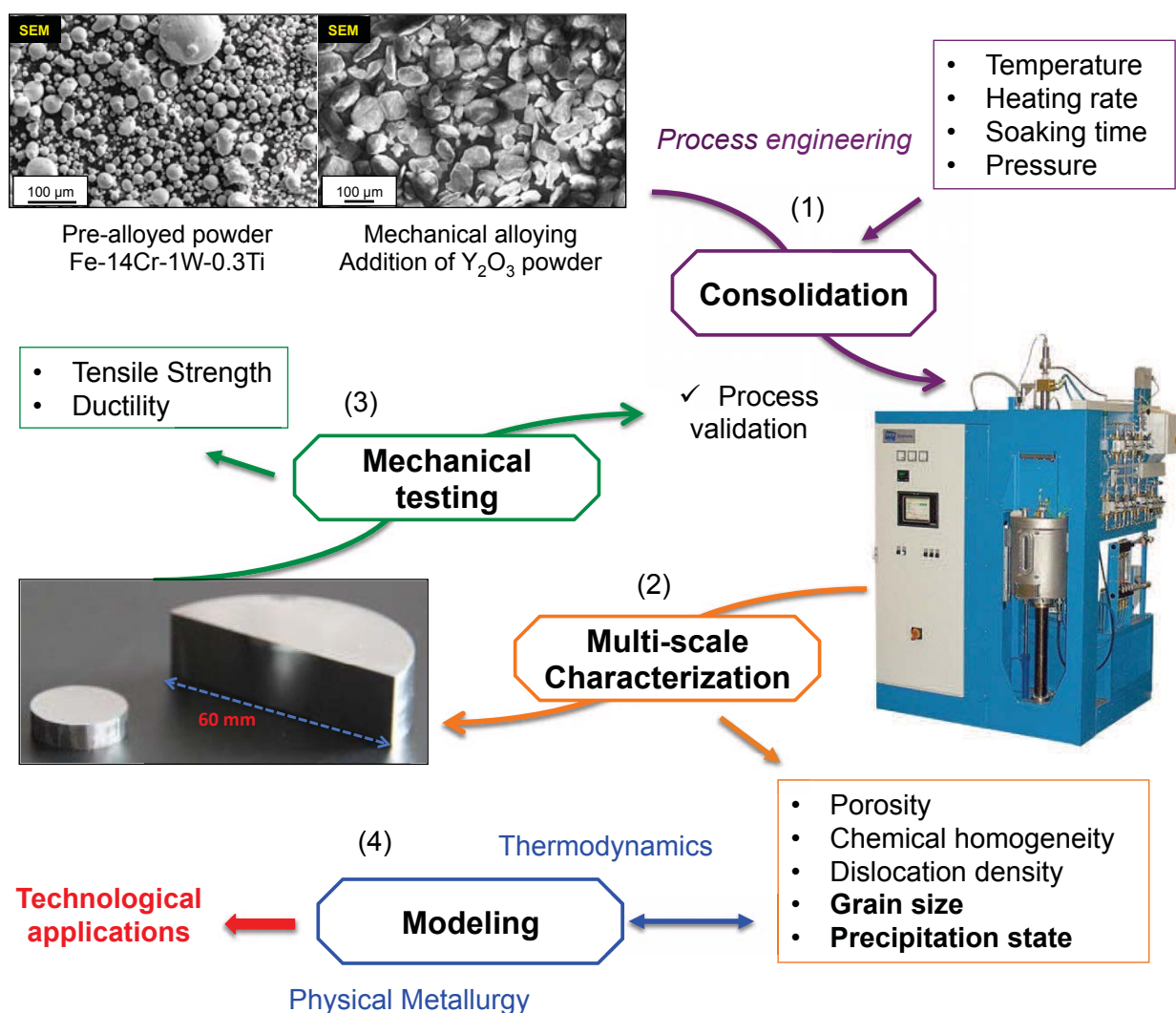


**Figure 1:** PhD thesis general approach. SPS is not only a process that may be included in the ODS fabrication route but also an efficient and helpful laboratory tool to produce various microstructures. In this project, different metallurgical states were characterized so that experimental inputs were available for microstructure and precipitation modeling and understanding.

- Develop modeling tools for precipitation of nanometer-sized oxides during high-temperature consolidation and heat-treating. The model could be compared to experimental observations of the precipitation state at nanoscale.

  *Are nanoparticles able to form in a short SPS consolidation (few min)? Does thermo-mechanical kinetics have any effect on precipitates nucleation, growth and coarsening?*

This manuscript is divided into 5 chapters.

First of all, the conventional processing routes and their effects on the microstructure and the resulting mechanical properties are presented. Then, Spark Plasma Sintering (SPS) is described as one of the available tools for nanostructured powder processing, with specific emphases on the production of ODS materials. This concise review only gives primary tools to understand the thesis motivation and more consistent literature is gradually compared to our present results all along the manuscript.

Secondly, the attempt of SPS consolidation is presented. Influence of processing parameters on the compacts properties is described, with a particular focus on the compromise between full density and small grain size. The technological issues linked to carbon diffusion and coarse precipitation are discussed.

In the third chapter, the tensile properties of the SPSed ODS ferritic steels are compared to those of conventional ODS steels. In order to understand the role of the microstructure on the mechanical properties, various microstructures with and without oxides were created by SPS and the resulting mechanical properties were measured. In particular, the role of the obtained bimodal microstructure with both ultrafine and coarse grains is discussed.

The fourth chapter is then focused on the reason why this bimodal microstructure appears and is stable, with a strong resistance to recrystallization. Especially, abnormal growth was understood using a multi-scale microstructure characterization. We suggest a model that takes into account the plastic deformation heterogeneities within the milled powder. The competition between driving and pinning pressures[6] is quantitatively described. Also, the kinetics of abnormal growth was characterized by synchrotron X-Ray diffraction during *in situ* non-isothermal treatments, similar to the consolidation processes. Specially, the role of yttrium and titanium contents and thus precipitation on abnormal growth was studied.

Since the particles govern the pinned grain size and enhance the creep properties, their precipitation behavior was studied. Lots of experimental investigations have been done on the nanoparticles in ODS steels. In the last chapter, a model is

---

6. Even if driving "force" is admitted and widely used, these are actually "pressures" (in MPa) and should be stated as such.

---

4

proposed to describe the precipitation kinetics using the nucleation, growth and coarsening theory. The simulated mean radius and number density of yttrium and titanium oxides were compared with experimental data from the present work and the literature.

Finally, conclusions about the assessment of the consolidation of ODS ferritic steels are given. The conclusion is supported by the comparison of the SPS consolidation of 9Cr ODS ferritic/martensitic steels versus 14Cr ODS fully ferritic steels.

# Chapter 1

# State-of-the-art and motivation

*This chapter summarizes how these specific materials shall respond to drastic requirements for nuclear application and what this involves for their microstructure and mechanical properties. Then, the interest of Spark Plasma Sintering to produce ODS ferritic steels but also to understand their microstructure evolution is discussed.*

## Contents

## 1.1   ODS steels for nuclear applications

Advanced nuclear energy systems require improved cladding and core structural materials. The specifications for fusion reactors, sodium fast reactors (SFR), very-high temperature reactors (VHTR), super critical water reactors (SCWR) or other GEN IV nuclear energy systems are different but all necessitate the development of high-performance materials (Fig. 1.1).
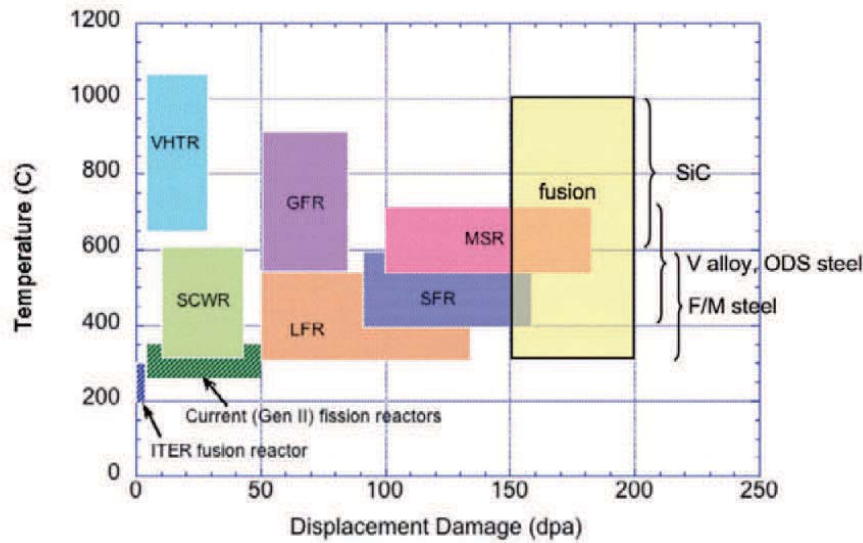


**Figure 1.1:** Overview of operating temperatures and displacement damage dose regimes for structural materials in current (generation II) and proposed future (Generation IV) fission and fusion energy systems. The six Gen IV fission systems are Very High Temperature Reactor (VHTR), Super Critical Water Reactor (SCWR), Lead Fast Reactor (LFR), Gas Fast Reactor (GFR), Sodium Fast Reactor (SFR), and Molten Salt Reactor (MSR) [6]

In particular, the considered sodium inlet and outlet temperatures in SFR are 400°C and 550°C, respectively, with a Nominal Cladding Temperature (NCT) of around 620°C. The mechanical dimensioning of the fuel rods must induce a final internal pressure due to the fission gas that is estimated around 100 MPa for an in-service time between 50,000 and 80,000 hours. This temperature range combined to mechanical stresses and irradiation damage may give rise to (i) thermal and irradiation creep deformation ; (ii) irradiation-induced swelling ; (iii) degradation of the Ductile-to-Brittle temperature (DBTT). Little *et al* [7] measured the deformation after irradiation of a series of pure ferritic Fe-Cr alloys and concluded that ferritic steels possessed a strong resistance to swelling. The two main reasons of this good resistance are the following:

- According to Odette [8], a bias exists for self-interstitial atoms to preferentially annihilate at dislocations owing to long-range strain field interactions. Swelling decreases with decreasing dislocation bias. Ferritic and tempered martensitic bcc (body-centered-cubic) steels have lower bias compared with fcc austenitic

stainless steels [9] due to both differences in the defect relaxation volumes [10] and the dominance of screw dislocations in bcc alloys.

- High self-diffusion (and solute diffusion) coefficients $D_{sd}$ reduce swelling and radiation-enhanced diffusion. Ferritic-martensitic bcc alloys have higher $D_{sd}$ than do fcc austenitic stainless steels [8]. High $D_{sd}$ increases the flux of vacancies that drive processes toward equilibrium. Moreover, solute atoms in ferritic steels are efficient recombination sites and create atmospheres around dislocations, limiting the trapping effect of interstitial.

Moreover, the greatest advantage of the nanometer-sized oxides are their good stability under high-temperature and irradiation, which provides significant strength advantages over ferritic–martensitic alloys up to extreme conditions [1] [2, 13, 14]. An added benefit of these fine particles is their role in healing radiation damage. The high particle density presents a very large surface area for point defect trapping, promoting self-healing via recombination and thus keeping the net accumulated radiation damage at a low value [15].

Regardless the creep and radiation issues, materials workability is of prime importance. Also, various environment-related phenomena must be considered: external corrosion induced by the liquid sodium and internal corrosion caused by the pellet-clad interaction can occur. The release of corrosion products from the tube cladding during the fuel reprocessing (fuel dissolution in nitric acid) has to be limited as well. Therefore, the selected material must exhibit an excellent resistance to high-temperature creep deformation, to irradiation-induced swelling and to severe corrosion. This will govern the design of the steel chemical composition.

## 1.2    Recent development of ODS steels

There are two primary types of the ODS class of steels: (i) high-chromium entirely ferritic steels that (theoretically) fall outside the austenite $\gamma$-loop (Fig. 1.2) (ii) ferritic-martensitic tempered ODS steels that may contain martensite, depending upon the quenchability (ability to form martensite during rapid cooling). The boundary between ferrite and austenite is of course not so obvious in multi-components system like ODS steels since each solute element (tungsten, oxygen, carbon, titanium, silicon, etc) may influence the stability of either ferrite or austenite.

Since the hoop rupture strength would limit the primary stress mode in fission gas-pressurized fuel pins, the **fabrication of equiaxed grains** [2] along with the increase of the biaxial creep strength and ductility of mechanically alloyed ODS steels for cladding have been critical development issues [16]. The strength anisotropy of rolled ODS alloys has been attributed to sliding at the grain boundary of extremely

---

1. Though partial amorphization of particles was observed under ion irradiation, depending on the temperature range [11, 12].
2. Or elongated under the hoop direction, which is perpendicular to the rolling direction!
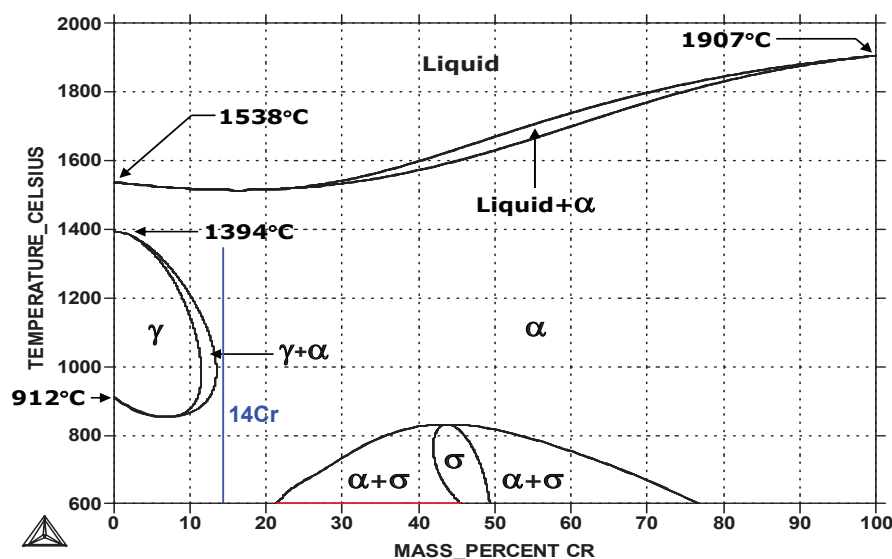
**Figure 1.2:** Binary iron-chromium phase diagram [*www.calphad.com*].

elongated, bamboo-like grains in the longitudinal direction. Extruded and rolled ODS steels generally have a very fine grain size ($<1~\mu m$). A large columnar structure is usually obtained by zone annealing, which also produces a strong texture due to secondary recrystallization (also referred to as abnormal grain growth). In order to soften the materials hardened by extrusion and rolling and suppress strength degradation, the grain morphology must be controlled. Two different methods for manufacturing ODS steel tubes with equiaxed and homogeneous grains have been investigated:

(i) **Recrystallization of mechanically alloyed ODS ferritic steels** with at least 12 wt%Cr (corrosion resistant alloys) by adequate heat treatments following the cold rolling manufacturing of the cladding tubes [17, 18, 19].

(ii) **Transformation of the ferritic/martensitic $\alpha$-phase steel** with 0.1–2wt%C and 9–11 wt%Cr into austenitic $\gamma$-phase.

## 1.2.1 Ferritic/martensitic ODS steels (Cr<12 wt%)

One of the specificities of this type of material is the occurrence of the $\alpha-\gamma$ phase transformation beyond 800°C. This is a major advantage for the shaping of tubes but could be a drawback in accidental situations when the cladding temperature might reach higher values. Thanks to this phase transformation, which can be triggered at different tube shaping steps, one can obtain an equiaxed microstructure with isotropic textures. This phase transformation also reduces considerably the material hardness after a few cold rolling passes. According to the Japanese teams, the creep properties of these materials are sufficient for cladding application.

Because of their lower chromium content, one can question their resistance to

internal corrosion and their behavior during fuel reprocessing. For instance, corrosion behavior of the ODS ferritic steels was investigated in supercritical water (SCW) to clarify the effects of alloying elements, such as Cr, Al, W, Ce, Hf, and Zr [20]. They concluded that the alloy compositions of Cr and Al adequate for corrosion resistance in SCW was ranging from 14 to 16 wt% for Cr and 3.5 to 4.0 wt% for Al. So high-chromium steel are much more favorable regarding corrosion issues. Worth noticing is the benefit of adding yttrium. Indeed, yttrium may act as cation barrier and enhances the formation of chromium oxide layer when it diffuses at grain boundaries. However, whether the yttrium nanoclusters themselves may play a positive role on corrosion resistance is still on discussion [21].

### 1.2.2 High-chromium ODS ferritic steels (Cr>12 wt%)

High-chromium steels have been widely developed because they are more resistant to corrosion. These materials have no phase transformation between room and melting temperature (see Fig. 1.2), which is a crucial asset for the behavior in incidental or accidental conditions. But due to the lack of "renewing" phase transformation, they exhibit an anisotropic and deformed microstructure that makes their cold-working behavior far more detrimental than isotropic softened materials.

The impact properties of this type of grades are very sensitive in relation to their microstructure and as soon as the recrystallization of the matrix occurs, a significant increase of the Ductile-to-Brittle Transition Temperature (DBTT) is observed [22]. The chromium content upper limit must be below 15% in order to avoid thermal ageing embrittlement. Indeed, Cr-rich $\alpha$' due to the miscibility gap between iron and chromium and $\sigma$ phases were observed to form during ageing at 500°C and 600°C, respectively. Both induced embrittlement, specially the $\sigma$ phase responsible for cleavage fracture [23]. Nowadays, the best compromise between workability and corrosion resistance is still to be found.

## 1.3 Metallurgy of ODS steels

ODS ferritic steels are fabricated by powder metallurgy. Hot isostatic pressing and hot extrusion are conventionally used to obtain fully dense materials, the latter being further cold worked into thin tubes with the desired dimensions (Fig. 1.3).

### 1.3.1 Powder production

The precipitation of the nanoparticles requires the use of specific powder metallurgy processes. In conventional metal industry, the alloys are produced by continuous casting. The raw material is smelted and cast into molds to form the primary ingots that can be either hot worked or cold worked into appropriate shapes. During the smelting step, various alloying elements can be added to the material to enhance particular properties: carbon and tungsten for strengthening, manganese
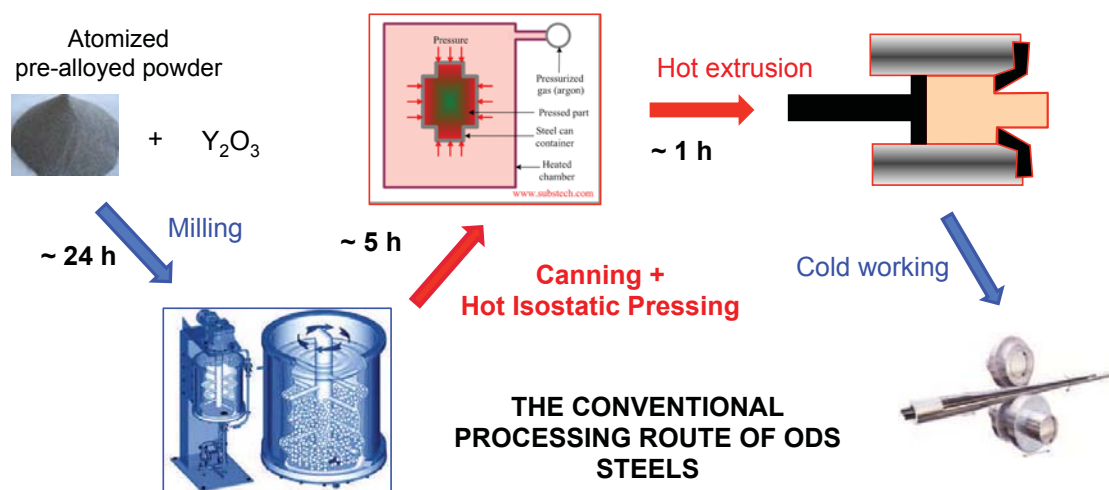
**Figure 1.3:** Conventional processing route of ODS steels: from raw powders to thin-walled tubes.

and silicon for formability. Yet, some chemical elements are not easy to put into the smelting ingot in a proper way. Among these elements, oxygen and yttrium are specifically hard to tailor because of their extremely poor solubility and wettability in liquid steel. Consequently, the production of high-performance steels with a proper amount of oxygen and yttrium needs another process. In 1970, Benjamin published a new finding: "a new process called "mechanical alloying" has been developed which produces homogeneous composite particles with an intimately dispersed, uniform internal structure" [24]. Meanwhile, the R&D on fuel cladding conducted at SCK·CEN (Belgium) focused on ferritic ODS alloys for $3^{rd}$ generation claddings [25]. The milling process can be done by either ball milling or attrition. The device called attritor is composed of a tank in which the powder is submitted to successive impacts with horizontal arms (Fig. 1.3). This is generally admitted that attrition process involves higher energy and thus boosts the alloying process compared to ball milling. Upon mechanical alloying, the powder particles are successively deformed, broken and cold welded [26]. The balance between fracture and welding is generally favored by adding a lubricant when the particles, if ductile, are too many incline to weld. The blend of ductile steel powder with yttria particles permits the fine dispersion of the brittle phase in the ductile matrix. The solid solutioning of yttrium and oxygen atoms is probably partial, the remaining atoms may be homogeneously distributed with subnanometric fragments within the powder [27, 28, 29, 30]. Generally, ODS steel powders are nanostructured, with crystallite size down to 20 nm. Recently, an interesting research area came out: cryomilling. The idea is to mill the powder under cooled gas atmosphere, so that powder particles are embrittled and more inclined to fracture instead of weld. This may result in microstructure refinement [31]. Also, local heating during classic milling would be impeded, which may retard the eventual formation of clusters during milling. This has been done on 14Cr ODS ferritic steels with an increase of strength but a loss of ductility [32, 33]. Low tem-

12

perature milling seems to be effective in terms of grain size refinement and with respect to oxide particle size reduction. One could question whether this reduction is a matter of decreased diffusion process or more about oxygen/vacancy binding energy variation with temperature.

## 1.3.2 Microstructure after high-temperature consolidation

From the mechanically alloyed powder, several processing strategies may be used. The most common one consists in canning the powder into a steel container, degas the powder to minimize oxidation and then perform hot isostatic pressing (HIP) and/or hot extrusion. Some recent projects also involved direct hot rolling just after HIPing [34]. HIP represents a huge part of powder metallurgy market. This technique is well established with some enormous industrial units. HIP consists of the consolidation of a powder by combining the effect of temperature (sintering) and pressure, the latter being set by a pressurized gas or lubricant within a closed chamber. Hot extrusion consists in heating of a precompact subsequently drawn through a reduced section in order to obtain a fixed cross-sectional rod. The most important difference between the two processes is that HIP involves hydrostatic pressure whereas hot extrusion induces large anisotropic deformation and resulting microstructure. This induces the formation of highly deformed grains with an aspect ratio close to 10 for industrial MA 957 or 14YWT [22, 35].
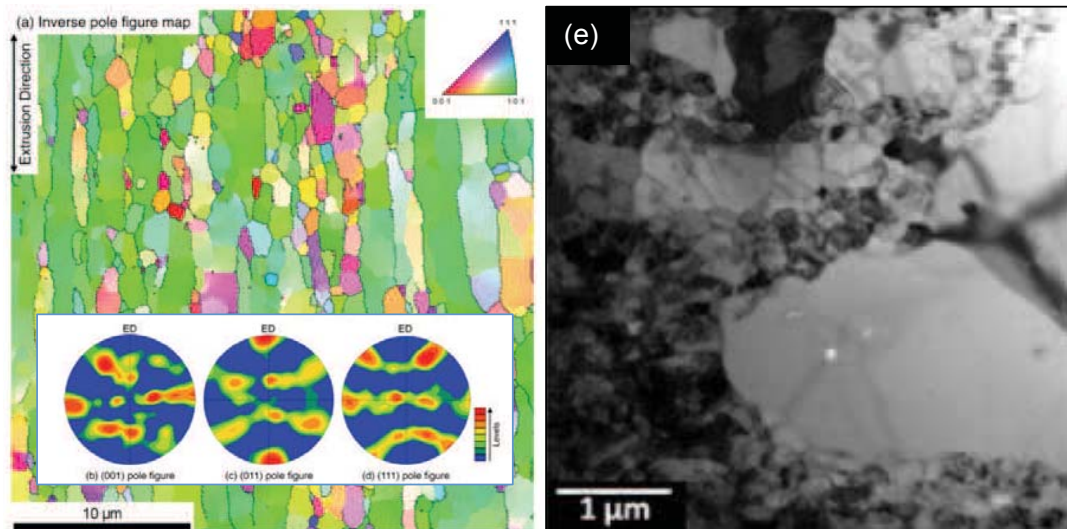


**Figure 1.4:** (a) Orientation map obtained by EBSD of extruded 14Cr ODS ferritic steel. Corresponding pole figures are also given in (b) (110), (c) (200) and (d) (111), after [36]. (e) TEM image of HIPed 14Cr ODS ferritic steel highlighting bimodal microstructure, after [37].

Hot extrusion also induces (continuous) dynamic recrystallization where new nuclei form due to high shear stresses involved in the process. This particular microstructure evolution is of great interest and has been studied by A. Karch during

his PhD thesis [38]. The grains are elongated along the extrusion direction, with a size of few microns in the longest dimension and a few hundreds nanometers in the transverse direction (Fig. 1.4(a)). The crystallographic texture of extruded ODS ferritic steels is pronounced with an $\alpha$-fiber type (Fig. 1.4(a)), parallel to the extrusion direction [36, 39]. Also, dislocation densities in extruded ODS steels are quite high and can reach $10^{16}$ m$^{-2}$ in MA 957 [22]. Martensitic 9Cr ODS steels have equiaxed and homogeneous grain structure with a mean diameter of few $\mu m$ [40, 41]. The anisotropy is somehow annihilated by the high temperature phase transformation. In rare cases, abnormal structures were observed though in 9Cr ODS steel. In the case of 9Cr Eurofer with 1% $Y_2O_3$ reinforcement, abnormal grains could originate from ferrite to austenite transformation during HIP, whereas other ultrafined grains were not transformed to austenite due to particles pinning [42].

The microstructural heterogeneity is even more evident in ODS steels consolidated by HIP. In this case, neither crystallographic nor morphological textures are observed, even for ferritic steels [37]. The latter have a bimodal microstructure with both ultrafine and coarse grains (Fig. 1.4(e)). Since the ferritic microstructure depends on many parameters (composition, milling, consolidation temperature, etc), the cause of the bimodal microstructure is not easy to understand. One clear trend is the extraordinary resistance of HIPed ODS ferritic steels to primary recrystallization. Compared to extruded materials, HIPed steels undergo less work-hardening and thus have lower dislocation density. Dislocations have a tendency to localize at ultrafine grains boundaries [43]. Knowing that the driving pressure for recrystallization is directly proportional to the dislocation density, one could expect a further cold-working step to make the recrystallization process easier. However, Olier *et al* [44] found that cold-working strain due to rolling had no significant effect on the recrystallization temperature of ODS ferritic steel, the later being above 1400°C even after 60% cold roll thickness reduction. Isselin *et al* [45] also reported that the recrystallized grain size of ODS ferritic steels was not observed to change with cold rolling rate. It seems so that texture may have more important effect than stored energy. Réglé [46] demonstrated that texture had a strong influence on the recrystallization behavior, since far different microstructures were obtained depending on the cold-working process. Inhibition of grain growth in highly textured materials is mainly due to low mobility of grain boundaries due to texture whereas dispersoids have weak influence on recrystallization. Thus, the decrease in the recrystallization temperature shall be obtained through the decrease in the crystallographic texture. This point is actually questionable and will be discussed in Chapter 4. Indeed, crystallographic texture is no longer at stake in HIPed ferritic steels but abnormal grains are almost systematically present. Consequently, abnormal growth during high-temperature isostatic consolidation seems to be not directly related to the crystal orientation. Toualbi *et al* showed that strain-induced boundary migration may occur in extruded material [47]. This involves the preferential migration of a grain boundary from a relatively 'dislocation-free' grain toward a more deformed grain. This process was also observed in nickel base alloys [48]. Also, Réglé [46]

14

stated that at very high temperature, the variation in migration rate between grains is lowered and thus each grain fairly grows at the same rate. In this case, normal growth of pinned grains occurs.

An efficient way to facilitate the primary recrystallization would be to drastically increase the stored energy. Grosdidier *et al* succeeded on extruded FeAl ODS alloy with a compressive strain threshold of 8%, above which primary recrystallization is completed during further heat treatment [49] (Fig. 1.5).
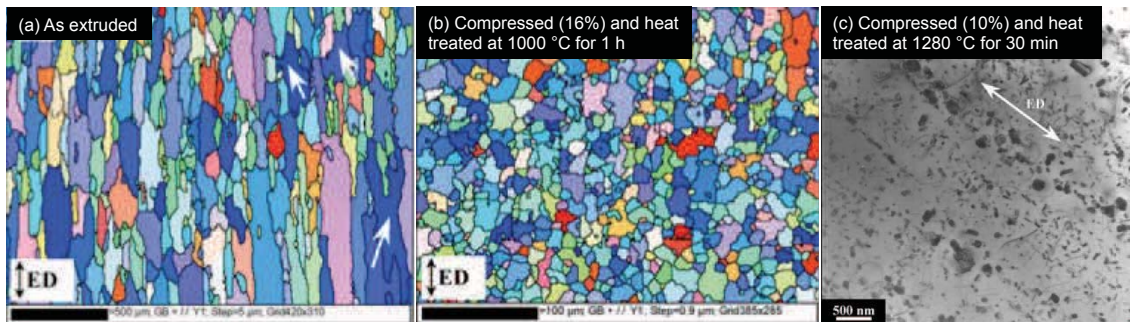


**Figure 1.5:** EBSD maps obtained from longitudinal sections of samples as extruded (a) and heat treated for 1 h at 1000 °C after compression by 16% (b). ED is the extrusion direction. (c) TEM image showing the preferential alignment of the particles along the extrusion direction (ED) after heat treatment at 1280 °C.

Similarly to what Réglé observed [46], secondary recrystallization occurred in some cases, which gave rise to large elongated grains. This most likely expresses the influence of oxides particles that are aligned along the extrusion direction and preferentially decrease the grain boundary mobility along the transverse direction (Fig. 1.5(c)). At larger strains, higher density of nuclei leads to rapid mutual impingement of the growing grains that are thus fairly equiaxed after primary recrystallization. This microstructure is far more stable and remains equiaxed even after long-term annealing during which competitive grain growth takes place without abnormal grain growth. This demonstrates the complex competition between stored energy that enhances grain boundary mobility through either strain-induced boundary migration or primary recrystallization and second-phase particles through homogeneous or heterogeneous pinning effect. The appearance of abnormal grains cannot thus systematically be linked to precipitation only. For instance, it has been observed that drastic grain growth occurred at temperature 100°C higher than that of $\gamma'$ particles dissolution [50].

Hard to avoid, the abnormal microstructure could be though refined *a posteriori*. Indeed, as observed during high-temperature extrusion, continuous dynamic recrystallization (CDRX) induces nucleation of new fine grains that reduces the overall aspect ratio. One way to create grain refinement through CDRX is severe plastic deformation. Recently, a HIPed ODS ferritic steel with bimodal microstructure was processed by severe plastic deformation thanks to equal channel angular extrusion (ECAE) at 300 and 700°C [51]. Coarse grains up to several microns in diameter

were successively refined down to a diameter of 500 nm by ECAE, suggesting effective dynamic recrystallization (Fig. 1.6). ECAD at lower temperature is more efficient in grain refinement, probably because the process involves higher pressure and therefore boosts the plastic deformation needed to form new grains. This is consistent with the contrast observed in (Fig. 1.6(c)).
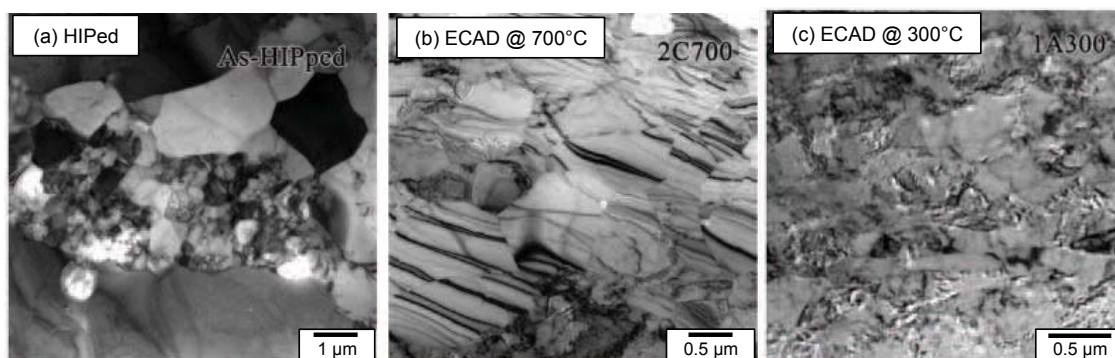


**Figure 1.6:** Bright field TEM micrograph of (a) as-HIPed ODS steel having a bimodal structure and (b-c) ODS steel following ECAD at 700 and 300°C, respectively (after [51]).

## 1.3.3 Precipitation

Precipitation-hardening is widely used in metallurgy. This consists in forming thermodynamically stable phases to strengthen the base alloys. $\gamma'$ $Ni_3Al$ are used in nickel-based alloys [52, 53], silicates in aluminum alloys [54, 55], nitrides and carbides in microalloyed steels [56]. The strengthening effect is directly related to the precipitates/dislocations interactions [52]. Thus, the higher is the particle density, the more efficient is the hardening effect. Consequently, both chemical composition and processing parameters must be optimized to obtain the highest number density of the smallest particles. In ODS materials, yttria ($Y_2O_3$) was introduced because of its high melting point and its low solubility in steels and nickel superalloys, replacing radioactive thoria ($ThO_2$) [24]. Yet, since oxygen solubility in ferrite is very low, various types of oxides can form in the presence of other solute elements. In steels, the oxides can be composed of aluminum, yttrium, titanium, lanthanum, cerium, chromium, and so on. In this way, the microstructure can become rather complex with the presence of various populations of oxides of different composition and size. Historically, aluminum was added for corrosion issues and therefore (Al-Y) oxides were largely reported in ODS steels. However, these oxides are quite large (D>100 $\mu m$) and mainly located at grain boundaries, which can be detrimental to ductility. So aluminum has been suppressed in modern grades for RNR-Na materials. Lately, titanium was found to refine the precipitation state [40, 57] and typical oxides in currently developed ODS steels are $Y_2O_3$, $Y_2Ti_2O_7$ and $Y_2TiO_5$ [58]. What gives singularity in ODS steels development is the extreme stability of the hardening particles, not only thermodynamically - they do not dissolve - but also kinetically,

16

with a resistance to coarsening up to very high temperatures [59] (almost 0.9 times the solidus temperature of steel). The consequence is that precipitates dissolution is not a way to allow recrystallization and other "microstructure renewal" during or after processing. We will discuss in more details the precipitation behavior of oxides in ODS ferritic steels in the Chapter 5 dedicated to precipitation characterization and modeling.

## 1.4 Mechanical properties of ODS ferritic steels

### 1.4.1 Tensile properties

Given that various grades of ODS steels produced by different processes are widely studied, mechanical data available in literature are a bit scattered. One general trend is that tensile strength of ODS steels is higher than that of the same steels without oxide-hardening. The best properties are obtained with the highest and finest dispersion of particles, since the precipitation hardening is related to the mean distance between particles that interact with dislocations [60]. This is why grades containing titanium, known to refine the precipitates distribution, have higher strength that grades reinforced with coarser oxides such as yttrium or aluminum oxides.

Once again, a distinction between extruded anisotropic and HIPed isotropic steels is necessary. Extruded ODS steels show much less ductility when tested in the transverse direction (TD) than in the extrusion direction (ED) [61, 62]. This different behavior that gives rise to a decrease of the elongation in the TD may be due to two combined effects: a more favorable grain boundary sliding between the elongated grains located along the ED during the deformation process and the existence of some particles located at the grain boundaries of the elongated grains which are acting as nucleation points of defects and promoting the grain boundary sliding [63]. Indeed, Kasada *et al* [36] highlighted the importance of reducing coarse oxides or carbides along elongated grain boundaries to enhance ductility.

Extruded steels exhibit higher tensile strength at low to moderate temperatures than the HIPed steel since hot extrusion yields important work hardening effects and thus higher dislocation density [64]. Also, dislocations annihilation can be impeded by solute drag and precipitation, leading to limited recovery and further significant hardening. It has been observed that dislocation forest hardening and precipitation hardening were in the same range, around 400 MPa [65]. At higher temperatures, extruded and HIPed steels can have a similar tensile strength, which could indicate the influence of microstructure recovery during the tests.

Also, solid solution strengthening is not negligible: chromium contributes due to its high content and tungsten, which has lower content (between 1 to 2 wt%) but strong hardening effect [66]. Worth noticing is that an excess of 2 wt% of tungsten would lead to lave phases $FeW_2$ responsible for a loss of ductility [67].

A common property of ODS steels is a peak of ductility around 600°C, depending on the material [62]. A competition between distinct deformation mechanisms could explain this behavior: (i) viscoplasticity that enhances ductility and (ii) vacancy diffusion along grain boundaries that can propagate damage, both increasing with temperature [68].

Even if the creep properties are the critical targets, tensile tests (specially at high temperature) are suitable characterization means to assess more rapidly the mechanical behavior of ODS steels.

## 1.4.2 Creep behavior

Austenitic stainless steels and Ni base alloys are usually preferred for applications involving elevated temperatures due to their good creep strength and corrosion resistance. However, for application in nuclear reactors, void swelling resistance is also an important parameter and both alloys have poor void swelling resistance. Susila *et al* demonstrated that ODS ferritic steels with finer dispersoids showed higher creep resistance [60]. However, the stress exponents indicated that dislocation creep was the dominant deformation mechanism, whatever the dispersoids size. Diffusional or Nabarro–Herring (N–H) creep models predict overestimated creep strain rates compared to experimental rates observed in ODS steels. An interesting point is the surprising weak influence of grain size on the creep behavior of ODS steels [69]. Indeed, ODS ferritic steels usually contain a high fraction of ultrafine grains due to impeded growth by nanoparticles whereas large grains are known to reduce the creep deformation. Hayashi *et al* evidenced that a drastic change in grain size from submicronic to anomalously grown grains did not lead to any drastic variation in creep rate [35]. Thus, the creep strength is attributed to highly stable nanoclusters that appear to pin the grain structure and present strong obstacles to dislocation motion in the large grains. This relatively limited influence of grain size contradicts the study from Alamo *et al* who observed a better creep behavior for coarse grained recrystallized MA857 compared to the identical fine grained alloy [22].

## 1.5 Spark Plasma Sintering (SPS)

In the field of materials science, nanostructured and ultrafine grained components are booming in recent decades. Besides the growing severe plastic deformation methods, powder metallurgy is a more established way to produce nanocrystalline metallic or ceramic components. Since the use of nanopowders implies specific handling and safety issues, nanostructures can be obtained by milling micron-size powders. Liquid phase sintering, high-pressure or multi-step consolidation techniques have yielded dense materials. However, the relatively slow kinetics of the most sintering processes requires the development of new rapid consolidation processes. It

is to meet this need that the Spark Plasma Sintering (SPS) has experienced strong growth since the 1960s. The initial idea was to create a plasma by electric spark to enhance the sintering mechanisms. Even though this was patented in 1960 by Inoue, SPS technique had been widely launched only when the third generation of devices had been developed in Japan, reaching a market of more than 200 devices in 2004[3]. SPS is a process similar to hot isostatic pressing: the powder is introduced into a chamber where it is heated and mechanically loaded. The singularity of the method is the internal heating system that is induced by a strong continuous electric current[4] under a low difference of electric potential (few V). The electric current thus goes through the material and/or the containing matrix and creates a rapid heating effect. Increasing the possible heating rates is undoubtedly the main asset of SPS. Depending upon the chemical and physical parameters of the powder and the dimensions of the compacts, heating rates up to 1000 °C.min$^{-1}$ can be reached. Therefore SPS could allow the overall consolidation processing time to be shortened, which is of great importance for nanostructured materials processing. This technique has been widely used to consolidate ceramics but much less applied to metallic materials [70, 71]. A comparative study between SPS and HIP on ceramics demonstrated that SPS could produce finer microstructure [72].

## 1.5.1 Consolidation mechanisms

Sintering may be defined as a consolidation, under heating, of a powder with no complete fusion of it. This consolidation is accompanied by an increase in relative density that induces a global shrinkage (decrease of the apparent volume). Whether the material reaches its solidus temperature or not, the sintering is called liquid or solid. These two kinds of sintering methods involve completely different physical features of the system. Wettability and viscosity are key factors for liquid sintering whereas point defects are actually of great importance for solid sintering. The consolidation temperatures applied during SPS are lower than the solidus temperature of high-chromium steel, so only the mechanisms that occur during solid sintering are described. Solid sintering consists of mass transport allowing the system to minimize its total surface energy.

Due to the presence of pulsed electric currents in the SPS process, hypothetical sintering mechanisms were investigated. Based on a *"in chamber"* direct visualization combined with microstructure investigation, Zhang *et al* tended to prove that spark discharge was effective on metallic and ceramic system [73]. The high temperature spark plasma could momentarily be generated in the gaps due to the electrical discharge effect between powder particles at the beginning of ON–OFF DC pulse energizing. Then the fast and efficient sintering can be achieved under the combined action of spark discharge (result in spark plasma and local spark impact pressure), Joule heating, electrical diffusion and plastic deformation effect in the SPS process.

---

3. With no single device in France!
4. It can reach 10,000 Amperes!
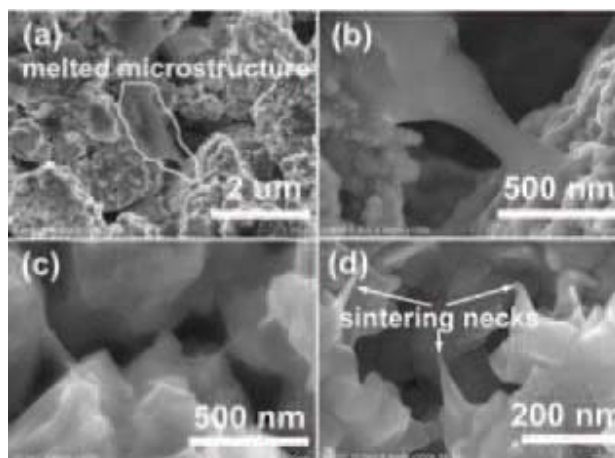
**Figure 1.7:** Characteristic microstructures of the fracture surfaces of the ultrafine copper synthe-
sized by SPS technique at 600 °C: (a) partially melted microstructure between two copper particles,
(b) the magnified melted and sputtered microstructure of copper, (c) sintering necks formed on
the surface of the copper particles, and (d) the magnified sintering necks [73].

Few years ago, a careful investigation led to contradictory conclusions [74, 75].
The existence of plasma was investigated using *in situ* atomic emission spectroscopy,
direct visual observations and ultrafast *in situ* voltage measurements. Using a vari-
ety of powders and SPS conditions, all the employed experimental methods indicated
that there was no plasma, sparking or arcing present during the SPS process, ei-
ther during the initial or in the final stages of sintering. Experimental attempts to
determine whether the electric current plays a role or not are dependent on the in-
vestigation methods and the studied material. Regardless this controversy, a proper
analysis and modeling of the involved phenomena would be useful. Electric current
can indeed contribute to the mass transport by electromigration. It has been showed
that the application of an external electric field influences the crystal defects mo-
bility, nucleation and grain growth, or oxidation mechanisms [76, 77]. In particular,
the presence of an electric field can result in the increase of grain growth kinetics
and point defects mobility in intermetallic composites [78]. Also, it has been showed
that recrystallization of copper was facilitated by the application of an electric field,
even if the physical cause is unclear [79].

By now, there is probably a lack of realistic constitutive model of consolida-
tion mechanisms during SPS. In this sense, Olevsky and Froyen [80] quantified the
contribution of electric current to the diffusion mass transport leading to densifi-
cation. Two major components of densification-contributing mass transfer during
SPS were considered: (i) grain-boundary diffusion and (ii) power-law creep. The
driving sources for these material transport mechanisms are: (i) externally applied
load, (ii) sintering stress (surface tension), and (iii) steady-state electromigration
(electric field contribution to diffusion). They showed in the case of aluminum that
electromigration was only relevant for large grain size and small porosity (Fig. 1.8).

20
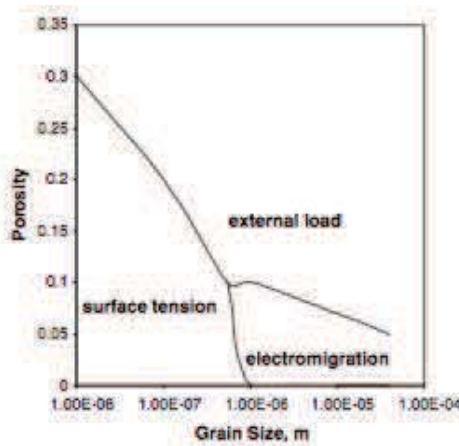
**Figure 1.8:** Porosity-grain size densification map for aluminum powder [80].

Chen *et al* studied the role of electric pulses on the reactivity of Mo-Si-Mo composite material. Specially, the ON/OFF pulses ratio was changed from 2/8 to 8/2 at constant electric power. It was shown that the heating power was governed by the effective tension, and so was the targeting temperature. Besides, the upper layer thickness was not dependent on the pulse nature. Electic field can also be visualized by field lines through the sample and the matrix and punches. Anselmi-Tamburini *et al* determined that the current density distribution was somehow heterogeneous within both conductive (copper) and insulating (alumina) materials [77]. In a copper 3 mm thickness specimen submitted to an intensity of 5 kA, a radial temperature gradient of 15°C was found between the center and the edge of the specimen. The temperature is the key parameter in the powder densification that is thermally activated. Its effective control is thus a *sine qua none* condition for the reproducibility of the thermo-mechanical treatments by SPS. The possible bias between measured and actual temperatures were on the focus of recent studies. One way is to use a well-known polymorph material with a well-known transformation temperature so that one can accurately measure the consolidation temperature by observing the resulting microstructure. A study on conductive Ti-Al and insulating materials SiC and $Al_2O_3$ showed a temperature gradient between the core and the edge of the sample. A FEM method was accurately applied and gave rise to a gradient of 100 °C between the die external layer and the specimen [81].

## 1.5.2 Application to ODS materials

Non ferrous and intermetallic ODS alloys have been widely processed by SPS. Co-based alloys were successfully produced with heterogeneous microstructure. Indeed, both $\gamma$-fcc fine grains and coarse $\epsilon$-hcp and $\gamma$-fcc grains composed the as-sintered microstructure. The bimodal microstructure exhibit extreme thermal stability after annealing at 1000 °C for 240 hours. The authors explain this stability by the

presence of multiple fine particles, mainly $Al_2O_3$, $Y_2Hf_2O_7$, and the $Y_3Al_5O_{12}$. Torralba *et al* consolidated various aluminum milled powders reinforced with titanium and yttria ($Y_2O_3$) by SPS [82]. The major fraction of the initial nanostructure was retained after consolidation. A constitutive study of the consolidation of aluminum intermetallic alloys was performed by Sasaki *et al* [83]. They pointed out heterogeneous recrystallization that, from their point of view, came from temperature gradient between powder particles. Ji *et al* made very careful and systematic analysis of SPSed FeAl ODS alloys [84]. A clear onset of the recrystallization start was observed due to the oxides [71]. They also evidenced the presence of a thin oxide layer at the powder particles interfaces due to internal oxidation. In this particular system, is seems that the layer is broken over 900°C [85].

Consolidation of oxide-dispersion strengthened steels by SPS is very recent [5]. In 2011, two austenitic and martensitic fine grained ODS steels were produced, each based on one commercial powder milled with yttria particles [**?**]. Heintze *et al* characterized SPSed 9Cr ferritic/martensitic steels at the nanometric scale using transmission electron microscopy (TEM), small-angle neutron scattering (SANS) and atom-probe tomography (APT) [86, 87]. For Fe9Cr–0.6 wt.%$Y_2O_3$, TEM results indicated a peak radius of the size distribution of $Y_2O_3$ particles of 4.2 nm with radii ranging up to 15 nm, and a volume fraction of 0.7%, whereas SANS indicated 3.8 nm and 0.6%, respectively. They found two kinds of nanoparticles, namely Y-free clusters containing Fe, Cr and impurity elements, and Y-O-rich clusters. They also performed HIP after SPS, which resulted in a slight increase of the mean radius of the Y-free particles. This was a first evidence of nanosized precipitation after very short thermo-mechanical treatment.

Attempt to quantify the mechanical properties of SPSed ODS steels were scarcely made. The main reason is that SPS is a laboratory tool designed to produce small specimen and answers particularly well the need of microstructure characterization but starts being limited to produce large scale compacts. Auger *et al* consolidated 14 Cr ODS ferritic steels with both SPS and HIP and obtained quite similar microstructure [88]. However, poor tensile properties with very limited ductility were observed for the SPSed ODS compared to the HIPed ODS. According to the authors, this was due to important remaining porosity within the SPSed material. Study of hot hardness behaviour of ultrafine grained ferritic ODS alloys in the temperature of 20 °C to 700 °C revealed a transition temperature of ≈ 400°C above which hardness decreased rapidly. This is possibly due to the enhanced GB mediated plasticity at these temperatures and pronounced reduction in Hall–Petch coefficient with increase in temperature [89].

A completely different route to produce ODS steel by SPS was proposed by Sun *et al* [90]. They consolidated ODS steels produced by a sol-gel method, which is a chemical synthesis of powder. This technique is not widely used in ODS steels community. The main reason is that sol-gel method does not lead to nanostructures,

---

5. 85% of the references used in this section were published from 2011, which means that these studies were concomitant to this PhD...!

thus the mechanical strength is largely degraded. A similar study on aluminum containing ODS steels by the same authors gave rise to equivalent results. In these alloys, aluminum oxides were also observed [91].

In 2013, Allahar *et al* achieved to consolidate fully dense materials with a fine submicronic microstructure [92]. They measured the difference in densification behavior between Y-O, Y-Ti-O and Y-Ti-O free powders. What was emphasized is the considerable refinement of the microstructure when titanium was added, resulting in no significant difference in grain size and hardness with sintering time of the Y-Ti-O containing ODS steel. Thus, similar alloying effect seems to be relevant in SPSed ODS steels, even if the consolidation kinetics drastically differs from conventional process. Also, the grain size was heterogeneous - bimodal - regardless the milling process. Finally, a slight increase in grain size was showed in the titanium free alloy, demonstrating that $Y_2O_3$ particles have less effective effect on pinning the microstructure than do complex Y-Ti-O particles. Regarding the consolidation parameters, pressures greater than 80 MPa were recommended for improved densification as higher sintering temperatures and longer sintering times at 80 MPa did not improve the relative density beyond 97.5%.

Another study focused on the consolidation mechanisms involved in the spark plasma sintering of ODS steels. The compaction was performed under 10 MPa up to 400 °C then under 30 MPa up to 850 °C, the holding temperature. The densification behavior was found to be better with than without $Y_2O_3$ dispersoids addition [93], since it reached higher relative density at equivalent temperature. ODS steels exhibited much higher hardness than that of ODS-free steel consolidated at the same temperature range between 950 and 1050°C. In this case, the presence of nanosized nonconducting $Y_2O_3$ particles was assumed to cause charge build up at the metal–dispersoid interfaces resulting localized heat generation and further faster mass transfer. Due to the very low yttria particles size ($\approx$ 20 nm) compared to the powder particles ($\approx$ 60 $\mu$m) and the low second-phase fraction, whether nanoparticles play a role on the diffusion and thermal mechanisms is debatable. For instance, contradictory behavior was observed on 14Cr ODS alloy reinforced by lanthanum, titanium and/or yttrium [94]. This can be explained by the influence of hard and dense nanoparticles that can impede powder particles arrangement at the early stages of densification and slow down the compaction kinetics. However, at higher temperature, they may have minor role on the compaction because grain boundary diffusion is the main mechanism for reducing the porosity.

## 1.6   Concluding remarks

ODS ferritic steels are excellent candidates for advanced fission applications. They are very resistant to irradiation damage and can operate at high temperatures. Yet, the practical development of 14Cr fully ferritic ODS steels faces some significant challenges.

Especially, the microstructure evolution with changeable recrystallization behavior upon processing is a key issue for efficient tube manufacturing. A softened recrystallized isotropic microstructure is indeed highly desirable when dealing with low temperature processes such as cold rolling. Consequently, the microstructure of ODS ferritic steels still needs to be optimized. The influence of the high-temperature consolidation kinetics on grain growth and oxides precipitation must be better understood. As highlighted in this chapter, most of studies are based on the characterization of conventional ODS ferritic steels consolidated either by HIPing or extrusion in a tight temperature range around 1100°C and for few hours.

In the present study, thanks to the SPS technique, the fast consolidation of ODS ferritic steels is assessed in order to obtain a homogeneous microstructure. The strong reduction in processing time compared to conventional techniques is expected to limit grain growth. Also, the precipitation of nanosized oxides during SPS consolidation shall be different and may influence the overall microstructural behavior of the materials. So, the purpose of this thesis is not only to test a rapid process but also to utilize this technique for a better understanding of the microstructural evolution of ODS steels during high-temperature consolidation.

Also, it was shown throughout this chapter that the precipitation of oxides in steels is rather complex. The nanoscale experimental characterization is costly, time consuming and generate results that depend on various parameters, including the techniques themselves. Hence, modeling tools for oxides precipitation would be helpful to better understand the behavior of these particles, from their nucleation to their coarsening. Thus, almost independently, a precipitation model was developed in order to try to understand the stability of the oxides in steels, how they form and which key factors govern their stability. This kind of model could of course be used to reproduce a given precipitation state after SPS or HIP at a given composition. But more importantly, this could constitute an efficient tool to design the composition of ODS steels, specially the amount of yttrium, titanium and oxygen.

# Chapter 2

# Consolidation of ODS steels by Spark Plasma Sintering

*The attempt to consolidate ODS ferritic steels by Spark plasma sintering and the relative key processing parameters are presented. A basic characterization at the macro and microscale of the compacts illustrates the consolidation behavior of the powder. This enables the optimization of the SPS consolidation in order to achieve good tensile properties.*

*Related published articles: [A] and [B].*

## Contents

## 2.1 The base powder

The composition and the morphology of the base powder was not changed during this PhD thesis. The conditions of the atomization and the milling process were kept constant in order to study the influence of the consolidation process only.

### 2.1.1 Atomization

The base powder was a high-chromium ferritic steel (Fe-14wt%) produced by gas atomization by Auvert & Duval. This method allows large industrial production of metallic powder. This consists in smelting an ingot or some good quality scraps of metal in a furnace by induction or arc melting. The molten alloy with a given composition is then put through a flow of an inert gas or water and solidified into fine droplets. Various types of gas atomization systems have been patented [95]. The main advantage of the method is that the composition design is flexible and only limited by the miscibility of solutes in liquid steel. The overall batch was then sieved to select powder particles with a diameter smaller below 100 $\mu$m. The particles are spherical and have regular shape (Fig. 2.1). After this step, the powder
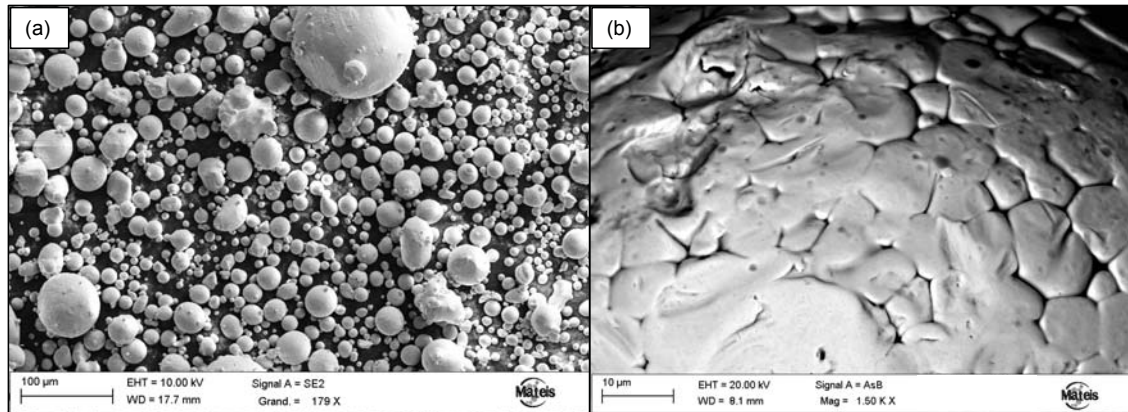


**Figure 2.1:** (a) SEM images (Secondary Electrons) of atomized powder particles (b) Zoom on the surface of one powder particle using the in lens SE detector.

particles have fully ferritic structure with a mean diameter of 40 $\mu$m, as described in Fig. 2.2. Some pores are located at 'triple' grain junctions and in grains. One can also notice some microstructure heterogeneities with disturbed and finer grains at some powder particles edges. (Fig. 2.12(a, inset)). The overall composition is 14 wt% of chromium, 1 wt% of tungsten, 0.3 wt% of titanium, 0.3 wt% of silicon and other minor elements such as manganese, carbon and vanadium. The latter were quantified on the milled powder by electron probe microanalysis.

26
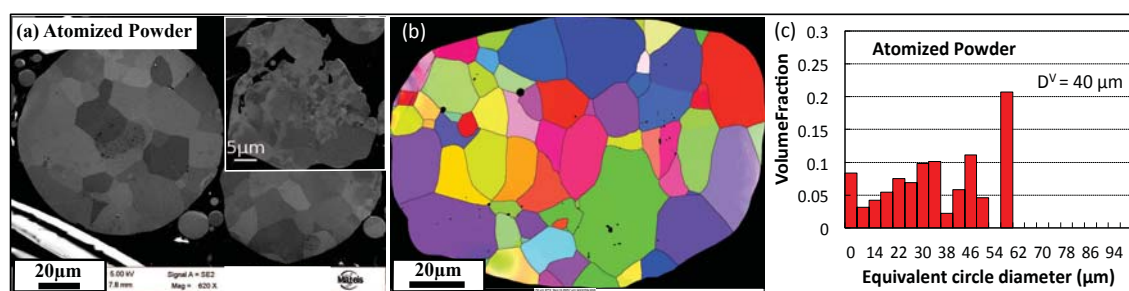
**Figure 2.2:** (a) SEM images (Secondary Electrons) of solidified microstructure (b) EBSD map in one powder particles and (c) corresponding grain size distribution.

## 2.1.2 Mechanical alloying

The ferritic powder was then mechanically alloyed with submicronic yttria particles (with a diameter of around 20 nm) using an industrial high-energy attritor at Plansee SE. The two powders were directly fed into the vertical attritor with no premixing. The milled powder was produced by batches of 10 to 13 kg in order to assess the feasibility to produce homogeneous powder at large scale. The size and morphology of the powder were investigated by scanning electron microscopy (Fig. 2.3). The particles have a diameter centered around 70 $\mu$m and have irregular shape due to the enormous amount of deformation applied during high-energy attrition. Typical cold-welded nuggets-like particle possesses rough surface (Fig. 2.3(b)).
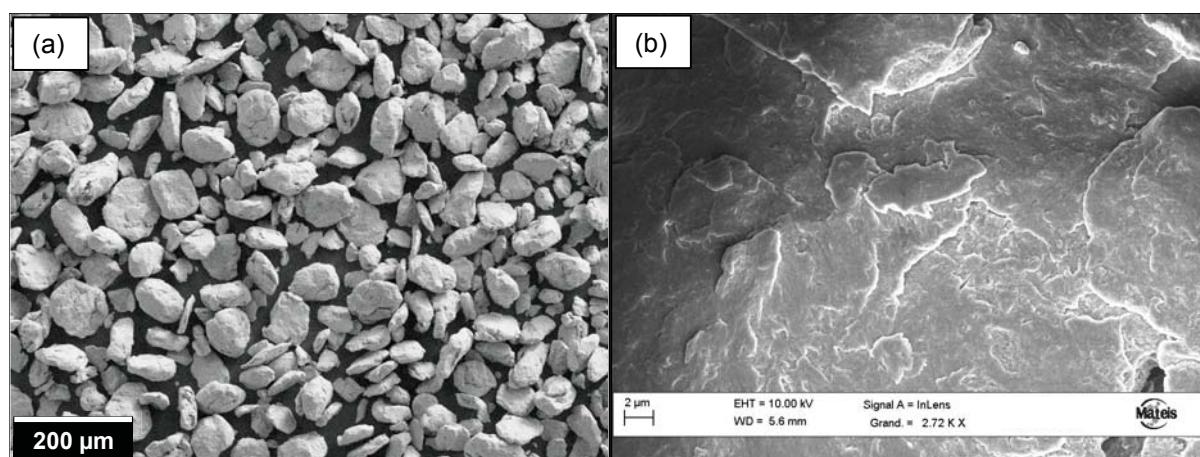


**Figure 2.3:** SEM image of powder particles after mechanical alloying. Particles have irregular geometry due to successive fracture and cold welding during attrition.

The global chemical composition of the milled powder is reported in Table 2.1. At microscale, chemical homogeneity of the milled powder was characterized by electron probe microanalysis (EPMA) using a device SX 100 CAMECA. Samples were mechanically polished with a finishing using Silica suspension solution. The column conditions were a voltage of 15 kV and a current of 100 nA. To ensure

27

**Table 2.1:** Composition of the as-milled powder measured by electron probe microanalysis

| Chemical element | Fe | Cr | W | Ti | + $Y_2O_3$ |
|---|---|---|---|---|---|
| Composition (wt%) | Bal. | 14 | 1 | 0.16 | 0.3 |

that the initial dispersion of yttrium, titanium and oxygen was homogeneous, metallographic cuts were done on 5 powder particles randomly chosen from the same batch, with diameter ranging from 50 to 80 $\mu m$. A qualitative cartography shows an homogeneous repartition of the investigated elements, such as titanium, yttrium, oxygen and silicon (Fig. 2.4). One slight local enrichment in oxygen seems to be
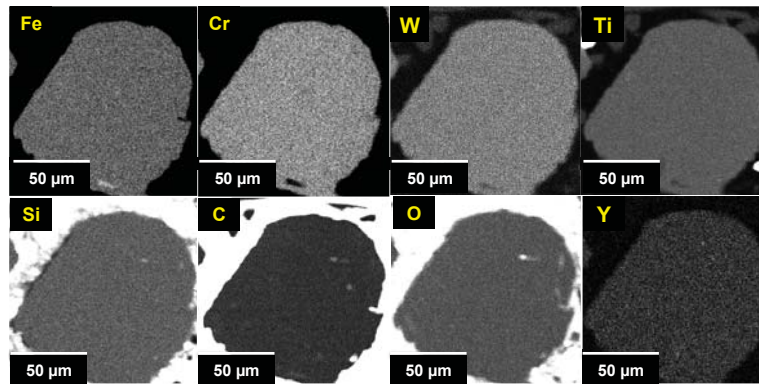


**Figure 2.4:** Chemical qualitative cartography (EMPA) of Chromium, Carbon, Yttrium, Titanium and Oxygen in as-milled powder particles. *Higher the brightness, higher the solute concentration.*

present in the powder particle, but was not systematically observed in others. The content of the main solute elements was quantified along each investigated powder particle to detect eventual inhomogeneities. As shown in Fig. 2.5, the solute are homogeneously distributed within the milled powder. Yet, sparse local enrichment
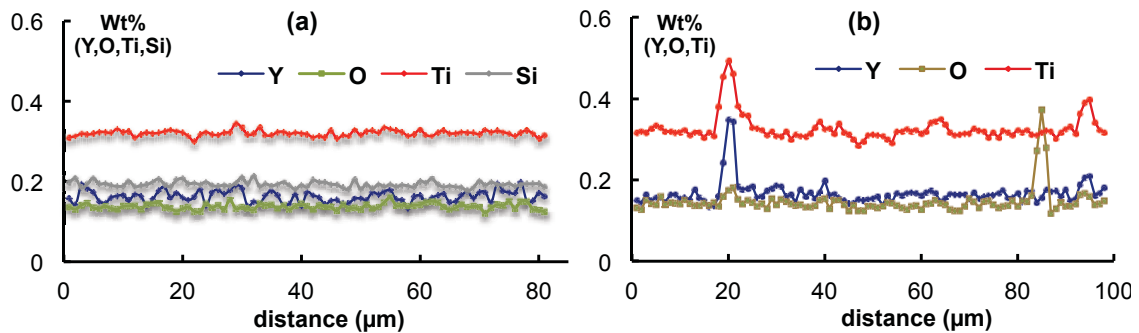


**Figure 2.5:** Quantification of the main solute contents within the as-milled powder. Among the 5 investigated powder particles, only one presented some variations in the content of yttrium, titanium and oxygen at the micronic scale.

in titanium, oxygen and yttrium were detected in two powder particles (Fig. 2.5(b)). This means that even if the powder seems to be chemically homogeneous, there are

still some local variation in the solute contents, probably due to some remaining fragments of yttria ($Y_2O_3$) particles. To observe the distribution of yttrium and oxygen atoms within the milled powder, a nanoscale characterization would be necessary. However, it is quite well established that sufficient milling energy and time imply a homogeneous distribution of either solute atoms or subnanometric Y-O groups of few atoms [96, 30].

## 2.2 Consolidation by Hot Isostatic Pressing

### 2.2.1 Consolidation cycle
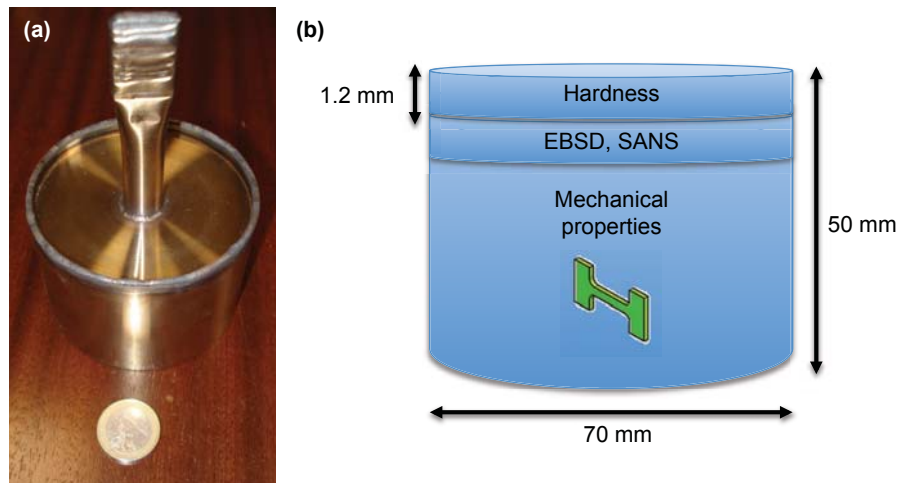


**Figure 2.6:** (a) ODS steel after Hot Isostatic Pressing encapsulated in a can (before machining) (b) Final dimension after machining

Before going into SPS, hot isostatic pressing (HIP) was performed on the as-milled powder in order to produce more conventional ODS steels. The main drawback of this process lies in the particularly long heating cycle, due to a general soaking step of few hours combined with slow heating and cooling rates ($\approx 5 \, deg/min$ for industrial units). Also, shrinkage anisotropy within the container is often observed, mainly due to non-uniformity in the temperature field and the macrostructure parameters such as porosity field [97]. The choice of container geometry and constitutive material is not straightforward. The latter should be deformable enough to enable densification whereas it has to withstand long high-temperature treatments. This is material and temperature dependent because the extent of the container impact on the shape distortion is considerably sensitive to the magnitude of the power law creep exponent and, consequently, to the type and physical mechanism of the creep [98]. Here, the milled powder was encapsulated in a can in 316 stainless steel subsided by SOMEC (Fig. 2.6). The powder was then degassed under secondary vacuum at 400°C for 2 hours. Then HIP was performed at Bodycote Nevers Magny-

Cours, with a thermo-mechanical cycle at 1160°C for 3 hours under a pressure of 1000 bars (100 MPa). The specifications indicate a heating rate below 10 K.min$^{-1}$. The whole cycle was thus representative of typical industrial HIP with a duration of approximately 8 hours. The HIPed ODS steel was machined in order to perform microstructure and mechanical characterization (Fig 2.6(b)).

## 2.2.2 Basic characterization

Since HIP allows the powder to be fully densified, the HIP compact density was measured and further taken as reference for SPS compact relative density calculation. To do so, the modified Archimedes' principle was used [99], which permits to calculate the volume of water displaced by an immersed object. The final density of this ODS ferritic steel is 7.782 ± 0.005 g.cm$^{-3}$.

The Vickers hardness HV$_1$ (load of 1 kg) was measured on the HIPed material after machining and mechanical polishing. The mean value is HV = 334 ± 12. This is lower than the ODS steel HIPed (reference $J$56) at CEA, which had a hardness of 380 [37].

## 2.2.3 Electron probe microanalysis (EPMA)

Electron probe microanalysis was performed on the HIP compact. Titanium-rich lines lie on former powder particles boundaries, sometimes associated with a decrease in yttrium content (Fig. 2.7). This was also observed in other HIPed ODS ferritic steels [37]. These results emphasize the formation of coarse titanium oxides, sometimes associated with aluminum [100]. Aluminum can originate from either atomized powder or contamination during mechanical alloying. This coarse precipitation was further quantified thanks to a filiation of 200 $\mu$m by EPMA. Also, a finer quantification (step size < 1 $\mu$m) through a powder particle boundary was performed (Fig. 2.8).

There are significant simultaneous increase in titanium and oxygen contents (up to 3 wt% and 0.4 wt%, respectively) at grain boundaries. This is associated with a decrease in the chromium content. Since the chemical heterogeneities in the as-milled powder were more scarcely found in the powder with an increase in solute content much lower than these current findings, one can conclude that coarse precipitation is due to titanium diffusion during high-temperature consolidation. The latter will be discussed in the next section. Yttrium seems at the opposite not associated with neither titanium or oxygen, at least at microscale.
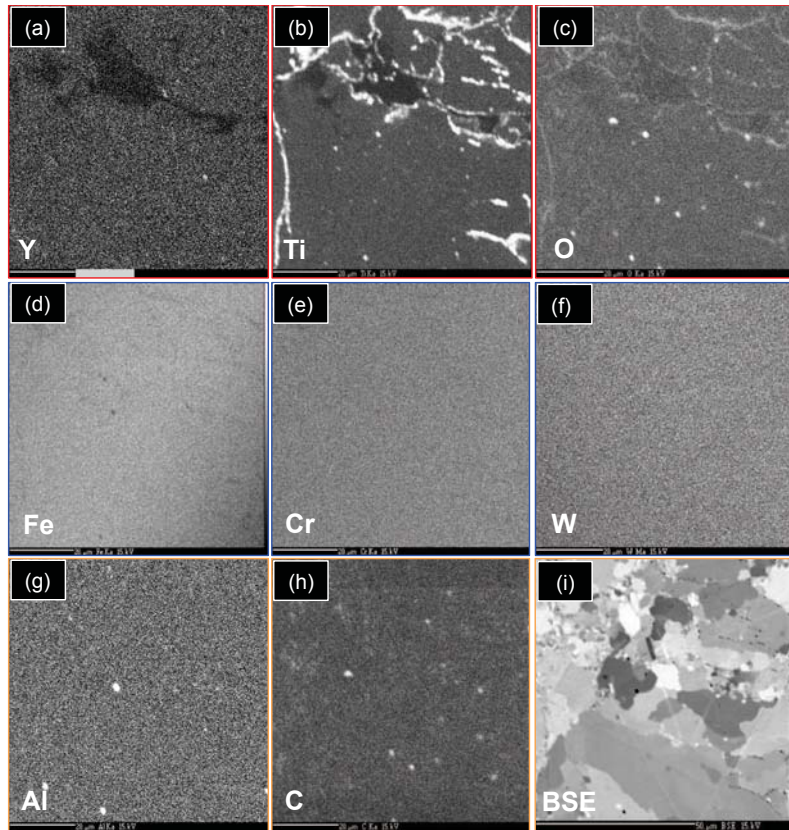
**Figure 2.7:** Qualitative analysis by EPMA of the HIP compact: (a) yttrium, (b) titanium, (c) oxygen, (d) iron, (e) chromium, (f) tungsten, (g) aluminum, (h) carbon and (i) backscattered electron mode image of the probed zone
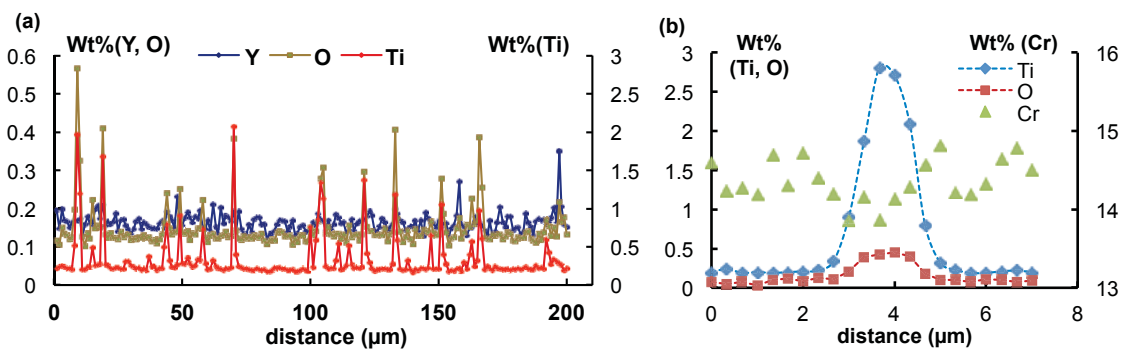


**Figure 2.8:** Quantitative analysis by EPMA of yttrium, titanium, and oxygen within the HIP compact.

## 2.3 Consolidation by Spark Plasma Sintering

### 2.3.1 Consolidation cycles
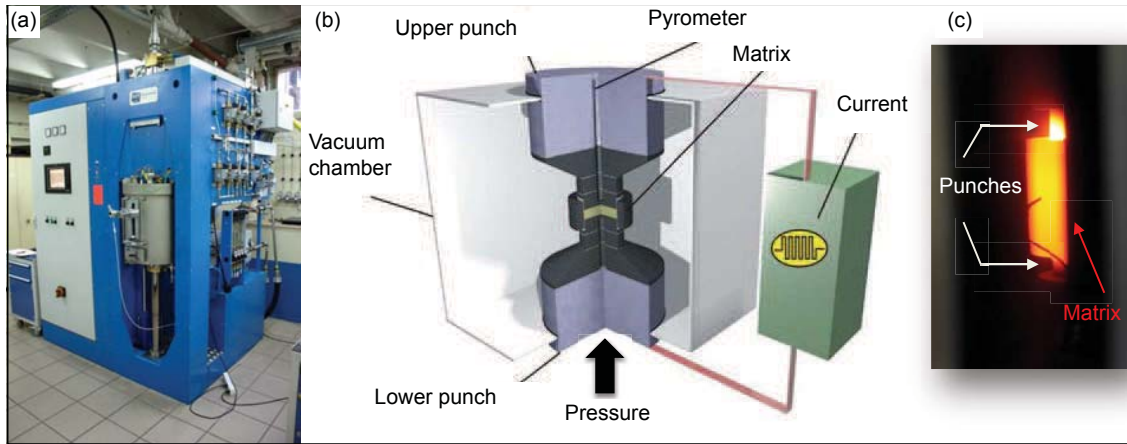


**Figure 2.9:** (a) SPS unit in INSA of Lyon (b) Diagram of the device (c) Picture of reddened matrix and punches during high temperature consolidation.

The same powder was then compacted at MATEIS laboratory (INSA Lyon) by various thermo-mechanical treatments in the SPS apparatus HP D 25 of FCT Systeme GmbH equipped with graphite die and punches (Fig. 2.9).

The vacuum chamber is composed of stainless steel blanket to protect from any injury. In between, a transparent window allows the user to look into the chamber. The temperature given in this work was measured by a vertical pyrometer and tailored by an optimized PID controller. In order to compare the densification kinetics in the same temperature range of hot isostatic pressing, SPS was performed between 850°C (1123 K) and 1150°C (1423 K). To minimize the total processing time, high heating rates were chosen. Some comparison between HIPing and SPS for equivalent heating ramps (5 to 50 K.min$^{-1}$) can be found in the literature [101]. However, the interest of this work deals with rapid consolidation. This is why a heating rate of 500 K.min$^{-1}$ was chosen and the soaking time was set between 2 to 20 min. The consolidation treatment was pressure-assisted by a compressive load of 60 to 76 MPa, the latter being the highest pressure applicable to graphite matrix. Finally, cooling was induced by direct contact with water-cooled punches.

The system allows us to follow the punch displacement upon consolidation / sintering. Yet, these data should be corrected in order to take into account the thermal dilatation of the materials and the graphite tools. This is why the Figure 2.10 only aims to qualitatively describe the densification kinetics. The punch displacement related to the powder compaction describes three main stages (Fig. 2.10):

(i) At low temperature, the pressure applied by the punches induces the rearrangement of the powder particles, mostly by interfaces sliding. The low plasticity (deformability) of the powder at room temperature limits this compaction, which
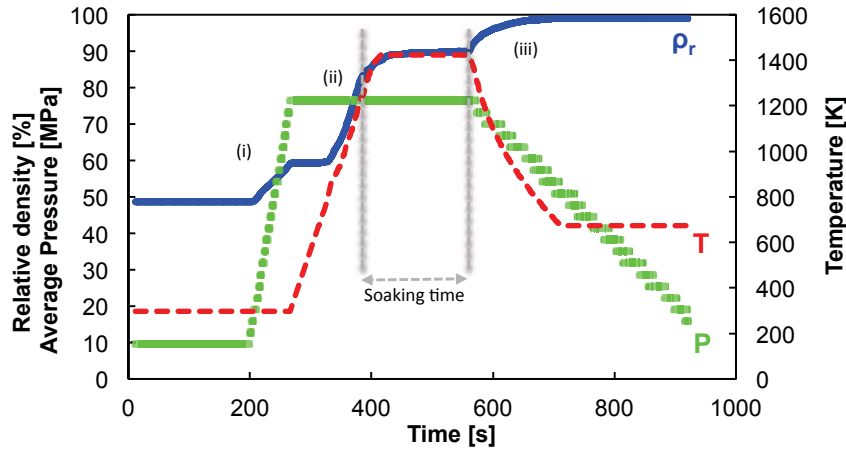
**Figure 2.10:** Thermo-mechanical treatment performed using the SPS apparatus. Pressure and heating can be applied independently. The evolution of the relative density $\rho_r$ is biased by the thermal dilatation, this is why it increases during the shrinkage induced by cooling.

gives rise to a plateau of relative density. The latter is slightly dependent upon the applied average pressure, typically 0.56 under 60 MPa and 0.6 under 76 MPa. This value is very moderate, which is justified by the irregular geometry of the powder particles (Fig. 2.3) that are sharp and elongated, significantly reducing their mobility. The consolidation behavior is enhanced by the powder particles size distribution (from 10 to 80 $\mu$m) that allows the smaller particles to glide in empty spaces between larger particles [26]. During the heating step, the diffusion mechanisms induce the formation and the growth of diffusion necks between particles and the annihilation of porosity by matter transfer into the pores. This stage promotes a rapid densification of the material that strongly depends on the maximum soaking temperature.

(ii) During consolidation at 1423 K (1150°C), the material relative density increases from 0.6 to 0.95 in less than 5 min.

(iii) Finally, the cooling phase is promoted by the direct contact between water-cooled punches and the compact. The cooling rate of 200 K.min$^{-1}$ can be reached, however it can be slower for larger parts. This phase is accompanied by a volume shrinkage of the heated compact.

SPS compacts were cylindrical with a diameter of 20 mm diameter and a heigth of 6 mm at a laboratory scale and with a diameter of 60 mm and a heigth of 20 mm for the semi-industrial compacts (Fig. 2.11). The sets of parameters for processing the small parts are given in Table 2.2.
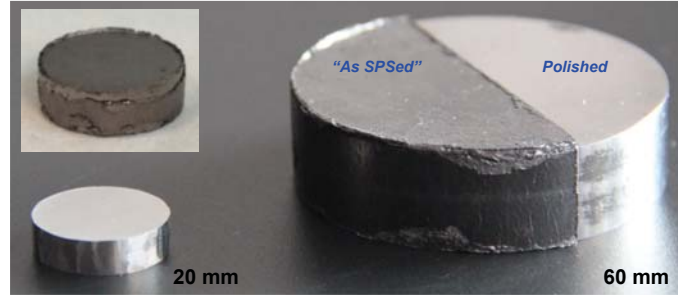
**Figure 2.11:** Small and large compacts of ODS steels consolidated by SPS, before and after removing the welded graphite foils

**Table 2.2:** Processing parameters used to consolidate small compacts and the resulting porosity

| Sample ID | SPS5 | SPS1 | SPS7 | SPS14 | SPS10 |
|---|---|---|---|---|---|
| Heating rate (K.min$^{-1}$) | 500 | 500 | 500 | 500 | 500 |
| Soaking temperature (°C) | 850 | 1150 | 1150 | 1150 | 1150 |
| Soaking time (min) | 5 | 2 | 20 | 200 | 2 |
| Cooling rate (K.min$^{-1}$) | 200 | 200 | 200 | 200 | 200 |
| Average pressure (MPa) | 60 | 60 | 60 | 60 | **76** |
| Relative density (%) | 84 ±1 | 95 ±1 | 97 ±1 | 98 ±1 | 99 ±1 |

## 2.3.2 Characterization of SPS compacts

Influence of pressure, soaking time and maximum temperature on the consolidation behavior was investigated.

**At low pressure (60 MPa)**, temperature plays a significant role on consolidation. At 850 °C, large pores subsist between sintered powder particles, with a relative density of 84 % after 5 min sintering. At 1150 °C for 2 min, porosity is much reduced but there are still few pores located at the interfaces (Fig. 2.12). At this pressure, soaking time has to be increased.
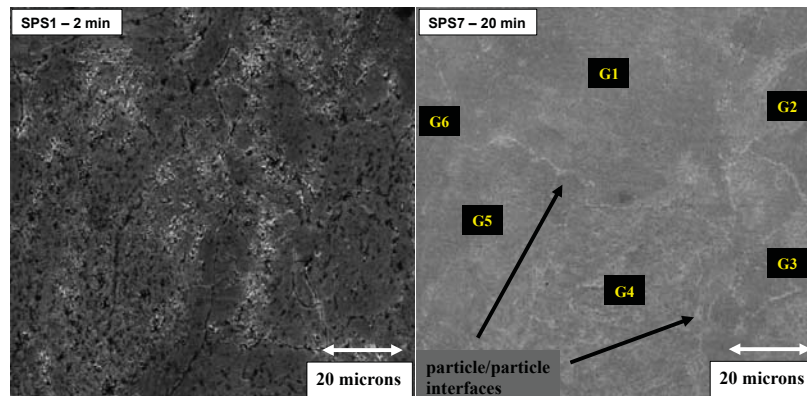


**Figure 2.12:** SEM images of compacts SPSed at 1150 °C under 60 MPa for 2 min (SPS1) and 20 min (SPS7). Under 60 MPa, increasing the soaking time has influence on relative density.

For instance, most of interfaces after 20 min sintering are correctly consolidated and form distinguishable grain boundaries with chemical contrast with respect to the bulk.

To test the homogeneity of the sample (porosity, microstructure), a series of hardness testing was made on samples consolidated at 1150 °C for various soaking times (Fig. 2.13). Vickers hardness measurements were performed on the devices Wolpert 2RC and LECO M-400 H2 under loads of 10 and 1 kg respectively with a displacement step of 1 mm and 200 $\mu$m. The 10 kg indentation impacts more than one powder particle (the diagonals of the indentation is above 100 $\mu$m, see Fig. 2.13). Hardness $HV_{10}$ does not vary with the diameter. This means that the
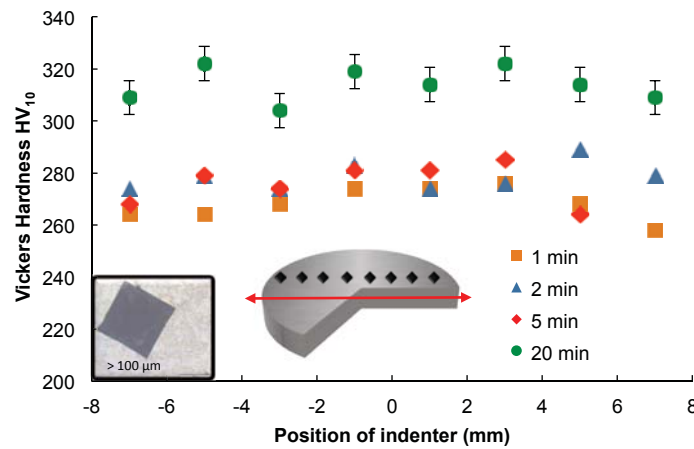


**Figure 2.13:** Hardness profile along the diameter for SPSed compact at 1423 K (1150°C) under 60 MPa for various soaking times.

consolidated structure is homogeneous at the scale of several powder particles, that is there is no gradient of porosity or grain size within the consolidated samples. A noticeable increase of hardness between samples SPSed for $t \leq 5\ min$ to $t = 20\ min$ is likely due to a decrease in porosity during the consolidation stage.
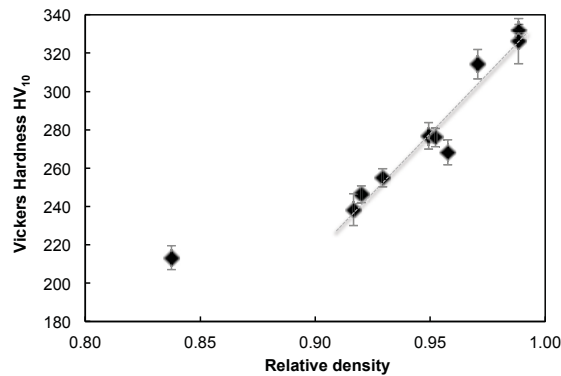


**Figure 2.14:** Evolution of hardness as a function of relative density measured on SPSed compacts. One can notice the linear dependence of hardness with remaining porosity.

If we consider the evolution of hardness with relative density for various ODS steels consolidated by SPS (Fig. 2.14), it is worth noticing that there is a direct linear correlation between macrohardness and relative density for a relative density above 0.9. It is though very difficult to apply any physical model capable to describe the evolution of the hardness with porosity. Cho *et al* showed that no less than seven models could fit such hardness data [102].

Highest relative density was obtained after consolidation under **76 MPa**. At this pressure, soaking time has moderate influence on the relative density. Under this pressure, increasing the temperature was also necessary to reduce porosity. Indeed, the maximum relative density of 99% was achieved on compacts processed at 1150 °C for either 2 or 5 min. The resulting hardness was equal to $HV_{10} = 332 \pm 6$, equivalent to what was obtained by HIP.

To quantify the homogeneity of the microstructure at a finer scale, a microhardness linescan was performed from the center part to the edge part of compacts processed at 1150 °C for various dwelling times. They were conducted on micro-instrumented indenter MHT (Micro Hardness Testor) CSM Intruments under loads of 500 mN (50 g) with a displacement step of 30 $\mu$m. Drops in hardness correspond to indentation on or at the vicinity of the remaining pores (Fig. 2.15).
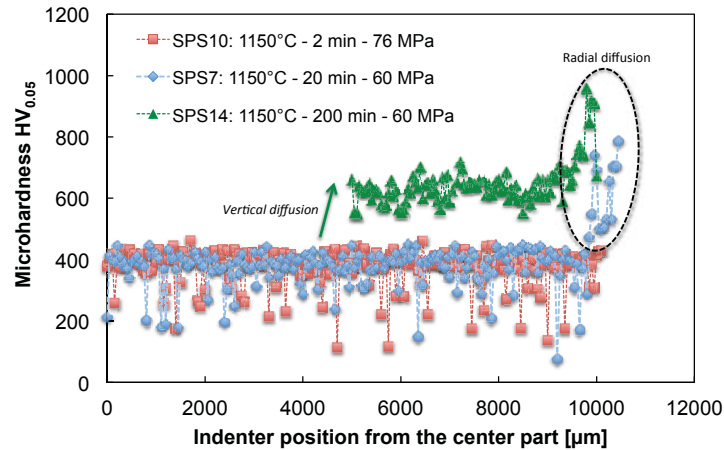


**Figure 2.15:** Microhardness profile ($HV_{0.05}$) along the diameter from the center to the edge part of compacts SPSed at 1150 °C (1423 K) for 2, 20 and 200 min.

The mean microhardness of the sample SPS10 consolidated under 76 MPa is $HV_{0.05} = 377 \pm 67$, which is in correct agreement with the macrohardness measurements done on the same material ($HV_{10} = 332 \pm 9$). There is then an abrupt increase of the microhardness from the edge to the center part of the compact for long soaking time (Fig. 2.15). This sudden change may be due to the diffusion of the carbon contained in the graphite foil and die into the ferritic matrix. This was quantified by electron microprobe analysis, as described in the next section.

Unfortunately, increasing the temperature above 900 °C gives rise to the appearance of abnormal grain structure (Fig. 2.16). The microstructure is composed of
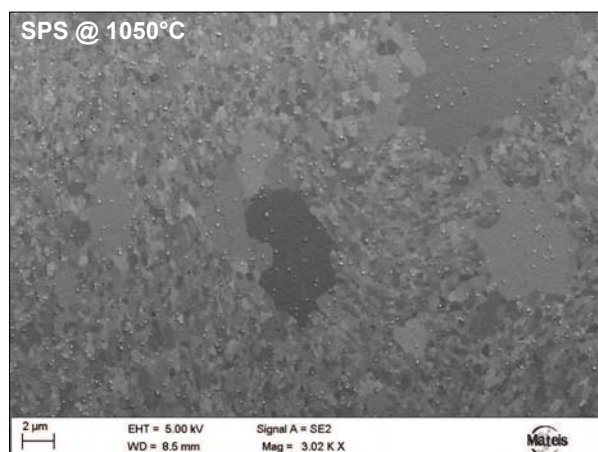
**Figure 2.16:** Bimodal microstructure of one compact consolidated at 1050 °C for 5 min. *Small white spots are polishing colloidal particles.*

ultra-fine grains with a diameter down to 50 nm and of coarser grains with a diameter up to 20 $\mu$m. The occurrence of such abnormal growth can be explained by (i) heterogeneous recrystallization due to unequal repartition of plastic deformation during milling (ii) the nanosized precipitation that exerts a strong pinning effect on grain boundaries. These recrystallization/growth mechanisms will be discussed in Chapter 4.

### 2.3.3   Diffusion and coarse precipitation

The eventual carbon diffusion was quantified by electron microprobe analysis on sample SPS7 (Fig. 2.17). At the vicinity of the edge part of the SPS compact, the carbon content increased from 0.4 to 1 wt%. If we consider the Fe-C and the Fe-Cr phase diagrams, it turns out that either cementite $Fe_3C$ or carbides (e.g. $Cr_{23}C_6$) can form during consolidation. Carbon in solid solution or tungsten/chromium carbides $M_{23}C_6$ are well-known for hardening steels. This hardening effect takes place at the edge part of the sample and expands up to 400 to 800 $\mu$m within the consolidated material. Such hardening can be detrimental for the ductility of the materials and should be avoided for high-temperature applications. As the diffusion is limited thanks to short processing time, a simple machining can solve the problem.

In order to quantify solute diffusion kinetics within the bulk of the consolidated materials, EPMA analysis was made on samples SPS7 and SPS14 (Fig. 2.18). The probed zone was roughly 150 $\mu$m $\times$ 150 $\mu$m. This zone contained numerous ferritic grains (see Fig. 2.16). A map of the solute repartition was done with a particular focus on titanium, oxygen, yttrium, tungsten and carbon. Titanium, oxygen and yttrium were quantified because these solute are candidates to form nanoparticles responsible for the good mechanical properties at high temperature. Tungsten was homogeneously distributed within the matrix in the two investigated samples (not
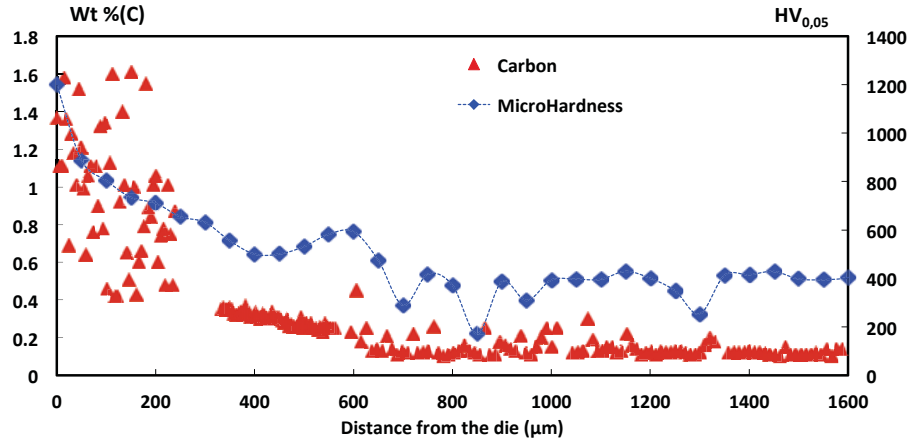
**Figure 2.17:** Microhardness and carbon radial profile from the edge of the compact SPS7 processed at 1150°C for 20 min. Carbon content and hardness are clearly correlated.

represented here). After 20 min of sintering, yttrium content seems to be spatially constant, though there are few depleted zones in yttrium at some interfaces. Titanium and oxygen are concentrated on particle/particle boundaries, that is interfaces between consolidated powder particles. After 200 min of consolidation, there is the same local enrichment in titanium and oxygen at the interfaces. These coarse titanium oxides are thus thermally stable at high temperature. Considering that these
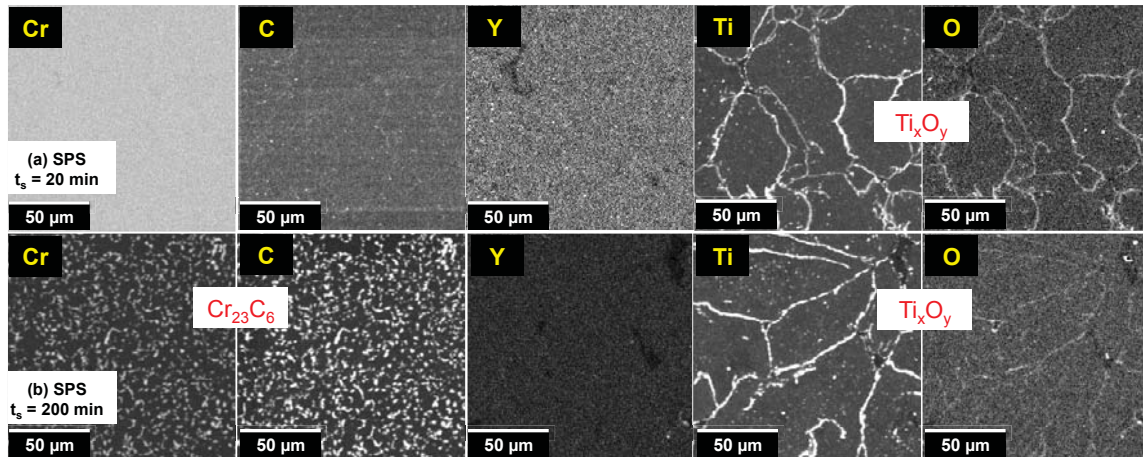


**Figure 2.18:** Chemical cartography of Chromium, Carbon, Yttrium, Titanium and Oxygen in compacts SPSed at 1150°C (1423 K) for (a) 20 min and (b) 200 min.

coarse particles are brittle and located at the interfaces, they may degrade the mechanical behavior of the consolidated ODS steels. It is thus necessary to reduce as much as possible their amount by minimizing the contamination during milling. These titanium-rich oxides can form due to:

- (i) An initial chemical inhomogeneity within as-milled powder particles. However, this has been demonstrated that the solute elements including titanium

and oxygen were well distributed within the milled powder.

- (ii) The rapid diffusion of titanium and oxygen with respect to that of other solutes, such as Yttrium and Tungsten. The characteristic diffusion lengths of Y, Ti and O in $\alpha$-Fe, calculated using equation (2.1), are reported in Fig. 2.19.

$$\lambda_{1150°C} \approx 2\sqrt{D_{diff}.t} \tag{2.1}$$
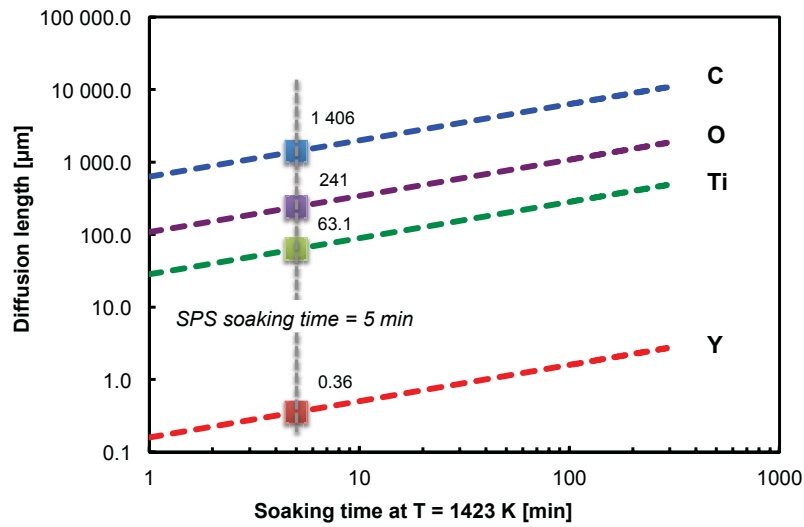


**Figure 2.19:** Diffusion lengths at 1150°C (1423 K). They illustrate the high mobility of titanium and oxygen in $\alpha$-iron.

Also, carbon atoms can diffuse into the $\alpha$-ferrite over few mm if we consider a soaking time of 20 min 1150°C, which is consistent with hardening at the sample's edge. Worth mentioning is that these values are calculated for bulk materials. In reality, early diffusion occurred in particulate materials where diffusion is mainly along interfaces and is even faster before full density is achieved. At temperatures used for ODS consolidation, titanium and oxygen diffusion lengths are equivalent or even larger than the diameter of the milled powder particles, that is 10 to 70 $\mu$m. This means that these two solutes can migrate onto the free surface when porosity is not entirely suppressed yet. Regardless the compaction method, coarse oxides Ti-(Al,Cr)O are able to form at powder particles interfaces. Due to their size and low volume fraction, they most likely do not have a strong pinning effect. However, they may be detrimental to the mechanical properties if they are located at metallurgical grain boundaries since they can act as nucleation sites for damage voids.

### 2.3.4 Process scale-up, toward mechanical properties

The tensile properties of materials processed by spark plasma sintering are not so often reported in the literature because the technique has been assessed to produce only small parts on which mechanical testing is difficult. Most of studies use the very simplified relationship between hardness and the tensile strength [103]:

$$\sigma_{UTS} = (3.0 \pm 0.3) \times HV \qquad (2.2)$$

where $\sigma_{UTS}$ is the ultimate tensile strength and $HV$ the Vickers hardness. This relation was established for the ultimate tensile strength and is much more debatable when dealing with the yield strength $\sigma_{YS}$ [103]. To quantify the global tensile behavior of the ODS steel consolidated by SPS, a scale-up from a 20 mm-diameter small compact to a 60 mm-diameter large compact was assessed. The processing parameters to consolidate the large compact are given in Table 2.3.

| Product | Small parts | Semi-industrial parts |
|---|---|---|
| Dimensions (mm×mm) | d × h = 20 × 6 | d × h = 60 × 25 |
| Weight | 15 g | 450 g |
| Heating rate | 500 K.min$^{-1}$ | 300 K.min$^{-1}$ |
| Soaking temperature | 1150°C | 1150°C |
| Soaking time | 2-5 min | 5 min |
| Cooling rate | 200 K.min$^{-1}$ | 200 K.min$^{-1}$ |
| Average pressure | 76 MPa | 76 MPa |
| Relative density | ≥ 99 % | 98 ±1 % |
| Vickers Hardness | 326 ± 12 | 344 ± 18 |

**Table 2.3:** Processing parameters used to consolidate small and semi-industrial compacts

They are the same as those used for the small parts except that the heating rate was decreased from 500 K.min$^{-1}$ to 300 K.min$^{-1}$. This change was necessary to ensure that the powder was heated up as homogeneously as possible. Specially, the targeting temperature was in excellent agreement with the measured temperature all along the heating and the soaking steps.

As quantified in the previous section, carburization occurred from the graphite/powder interface into the ODS compact. This can make difficult to tailor the exact composition of carbon within the final material, which is primordial though. However, it is much easier to remove few 100s $\mu m$ at the compact edges rather than machining the steel can if one compares to hot isostatic pressing. The relative density was comparable but 1% smaller than that of the small part, indicating that the pressure to get a fully dense material should be higher than 76 MPa. However, this would require to replace the graphite die and punches by very hard and much more expensive material, such as tungsten carbide. This could be more deeply discussed if the

industrialization of ODS consolidation by Spark Plasma Sintering was considered, which was not the case in this project.

Hardness measured in the large SPS compact is 344 kg.mm$^{-2}$, which is slightly higher to that of 14Cr HIPed ODS steel [37]. Thus acceptable mechanical properties can be expected.

Similarly to what was obtained on small compact, the large compact has far heterogeneous and complex microstructure. A detailed study of this specific microstructure was performed by 3D focused ion beam (FIB) combined with ion and electron imaging (Fig. 2.20). One can observe both ultrafine grains with a diameter below 1 $\mu$m and much coarser grains. Also, various kinds of precipitates can be found in the ODS steel. Even if the composition was not determined, there is a large size range that most likely originates from particles of various compositions.

## 2.4    Conclusion on ODS consolidation

From the same Fe-14Cr powder milled with yttria (Y$_2$O$_3$) particles, HIP and SPS can be used to fabricate dense ODS ferritic steels.

Both acceptable relative density and hardness were achieved by SPS with a consolidation of 5 min at 1150 °C under 76 MPa. This was performed on a pellet large enough to be further extruded in order to demonstrate that SPS can be inserted in the production of quite large units. However, many technological aspect of the SPS consolidation have to be improved. The main drawback is that SPS is a unit-by-unit process whereas HIP permits to produce many units in the same time.

However, even if SPS is much faster than HIP, a heterogeneous microstructure was obtained, composed of utrafine grains and coarse grains. Since this abnormal microstructure was obtained by HIP as well, the consolidation technique is not responsible for abnormal growth. This specific microstructure evolution will be carefully discussed in Chapter 4.
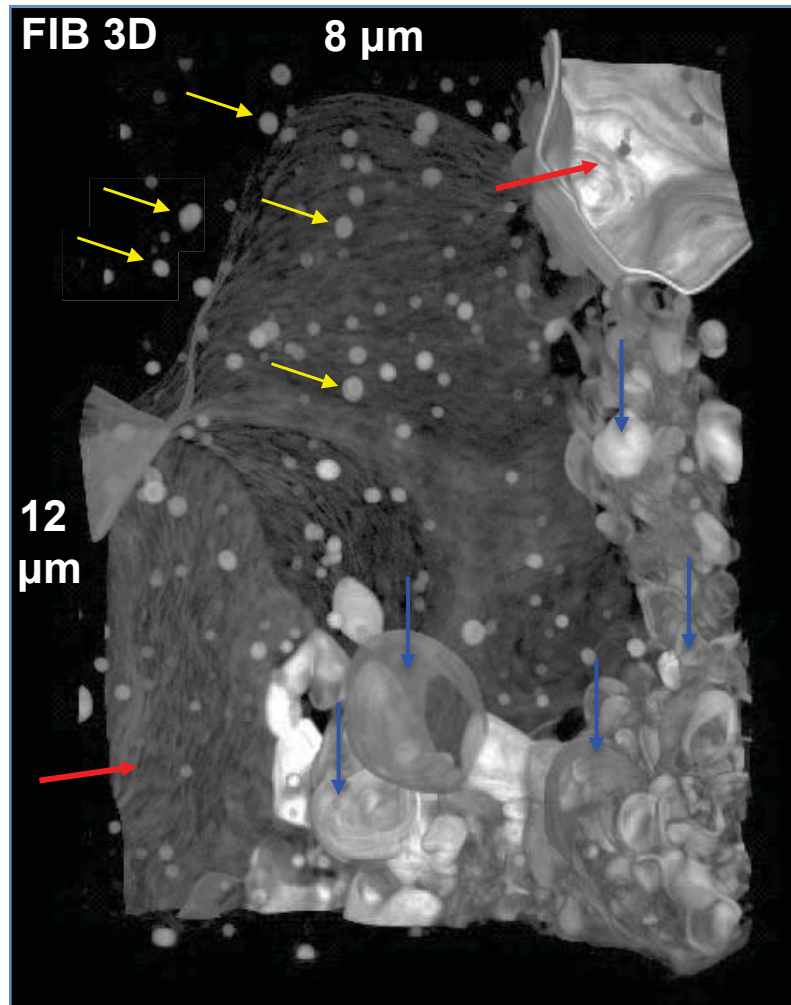
**Figure 2.20:** Sample volume of ODS ferritic steel consolidated by SPS. Rebuilt from 515 slices with elementary thickness of 10 nm. Images were acquired in EsB and in lens imaging mode (EHT 1kV, EsB Grid 800V) with a voxel size of $10\times10\times10$ nm$^3$, resulting in a total volume of $8.29 \times 11.62 \times 5.15$ $\mu m^3$. Yellow arrows: 'coarse' precipitates (D$\approx$ 100 nm) ; Blue arrows: ultrafine grains (D$\leq$1 $\mu m$ ; Red arrows: coarse grains)

# Chapter 3

# Mechanical properties of consolidated materials

*In this chapter, the tensile properties of SPSed and HIPed ODS ferritic steels are presented. The role of heterogeneous microstructure on tensile strength and ductility was investigated by producing various microstructures with SPS. Also, complementary in situ tensile test in a scanning electron microscopy was performed.*

*Related published article(s): [A] and [C].*

## Contents

## 3.1 Mechanical properties of consolidated ODS steels

### 3.1.1 Tensile behavior of SPSed ODS steels

In order to observe the influence of the heterogeneous microstructure described previously on strength and ductility, tensile properties of the compacted sample were determined at various temperatures. Tensile specimen were machined in the semi-industrial compact in both axial and radial directions. The samples were flat with a gage length of 6 mm and a cross section of 0.75 mm × 1.5 mm (drawing in Annexes of Chap. 3). Mechanical tests were carried out at room temperature and at 600, 650 and 700 °C with a strain rate of $7 \times 10^{-4}$ s$^{-1}$. The measured room temperature yield strength and ultimate tensile strength are 975 and 1054 MPa, respectively (Fig. 3.1).
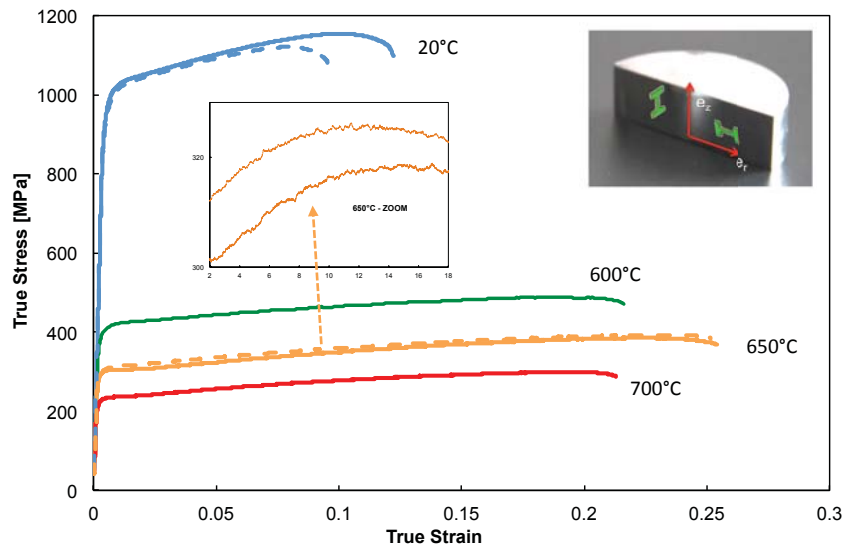


**Figure 3.1:** Tensile properties under axial (plain lines) and radial (dash lines) directions at room and high temperature [104].

The tensile strength calculated from the Vickers hardness of the small part processed with the same parameters would be $\sigma_{UTS} \approx 3 \times 326 = 978$ MPa [103] (see Table 2.3). This shows that reproducibility of properties from small parts to semi-industrial compacts can be achieved. These results also demonstrate that an important improvement of the tensile strength at room temperature has been achieved when comparing with two previous studies of SPS compaction. Indeed, with a 2-step compaction followed by heat treatment, Sun *et al* consolidated by SPS an ODS steel powder elaborated via sol–gel process [90]. Yield strength at room temperature was 585 MPa (Fig. 3.2). One can expect that the sol–gel method does not produce nanocrystalline powder, contrary to high-energy milling. Thus, hardening due to

44
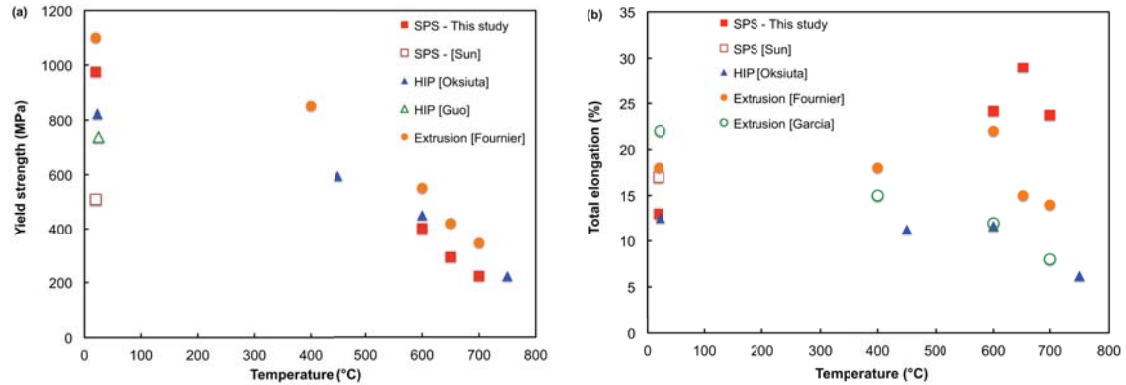
**Figure 3.2:** Yield strength (a) and total elongation (b) of SPSed ODS steels, compared with other Fe-14Cr ODS consolidated by SPS, hot isostatic pressing (HIP) and hot extrusion [104].

grain size and defects density was very limited. Another study reported a lack of ductility of an ODS ferritic steel consolidated by spark plasma sintering [88]. The SPSed ODS Fe–14Cr alloy exhibited quite brittle behavior with a uniform elongation limited to few %. As stated by the authors, this was probably due to an "extensive intergranular decoration of large Chromium-rich particles and the residual porosity". The yield strength was also moderate for an ODS ferritic steel (around 620 MPa). In our study, it seems that porosity was low enough (less than 2%) to avoid a brittle behavior. Indeed, a uniform elongation of 10% is obtained. At high temperatures, the total elongation is increased to reach 30% at 650°C. At this temperature, a peak of ductility is observed, as reported in classic ODS steels [68, 62]. Interestingly, the elongation is also higher than in some HIPed ODS steels found in the literature [106]. Then, as observed in [107], a high dislocation density combined with a very dense dispersion of nanoparticles confer to the materials an excellent tensile strength. The ductility observed at room temperature is also encouraging. As highlighted in Fig. 2.16, the presence of both large grains and nanosized to ultra-fine grains likely gives rise to a good compromise between strength and ductility. Indeed, a non negligible amount of coarse grains in nanostructured materials may enhance the work-hardening through dislocation motion, boosting the tensile ductility [108]. Yield strength at room temperature is higher for SPSed materials when comparing to a 4-hour hot isostatic pressured steel (YS of 823 MPa), whereas the two processes tend to induce the same results at high temperature [63, 106]. Higher tensile strength of extruded steel is likely related to the powder compaction mechanisms that induce strong work hardening through high density of dislocations and point defects [64, 62, 109]. Thus, hardening caused by dislocation forest is expected to be lower after SPS, which applied much less pressure than extrusion. Yet, as the process induces a very dense and fine nano-oxides dispersion within the ferritic matrix, Orowan strengthening through by-passing of nanoparticles is highly probable at room temperature, as demonstrated by Takahashi *et al* [109] and Steckmeyer *et al*

[68]. It is worth noticing that the mechanical behavior of SPSed materials is isotropic regarding both tensile strength and total elongation, not only at room temperature but also at 650°C. This contrasts with what is usually observed on extruded ferritic steels [36]. For example, Fe-13.5Cr ODS steels produced by mechanically alloying and hot extrusion at 1100 °C led to an anisotropy ratio between total elongations in transverse and axial directions of 0.3 and 0.4, at room temperature and at 600°C, respectively [68]. Based on the same criteria, SPSed ODS steel anisotropy ratios are 0.8 at room temperature and 1 at 650°C. As tensile specimen geometry/thickness may have a role on strain-softening behavior [110], it is worth noticing that isotropy is observed on both uniform and total elongation.

### 3.1.2 Comparison between HIPed and SPSed ODS steels properties
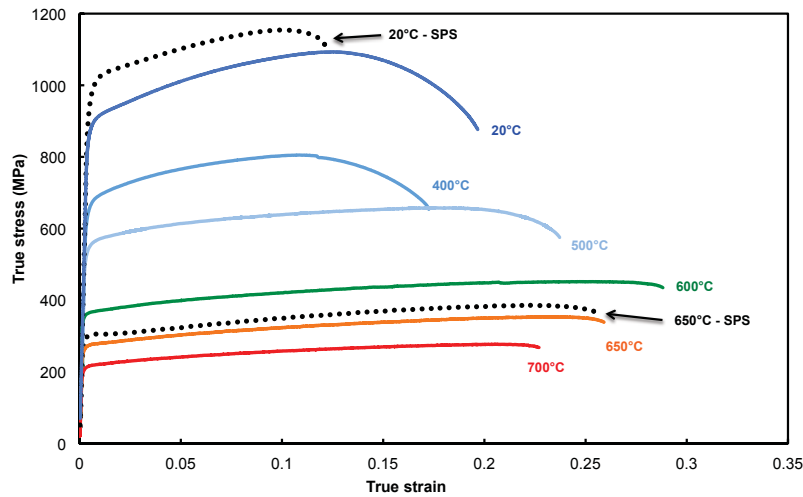


**Figure 3.3:** Tensile properties of HIPed ODS steels compared to those obtained on SPSed ODS steels at various temperatures.

One demonstrated that SPSed ODS steels had good tensile properties compared to those from literature. However, the mechanical properties highly depend on the initial milled powder whose 'quality' in terms of nanostructure and homogeneity can vary a lot between batches. Thus, it was more appropriate to compare SPSed ODS steels to HIPed ODS steels processed from the same powder. This was done using the HIPed ODS steels consolidated under the conditions recalled in Chapter 2. Tensile specimen had the same dimensions and were tested under the same conditions with a strain rate of $7 \times 10^{-4}$ s$^{-1}$. The tensile behavior is presented in Fig. 3.3. Yield strength of HIPed material is 875 MPa at 20°C and 272 MPa at 650°C against 950 MPa and 300 MPa for the SPSed ODS steel. Higher tensile strength on one hand and ductility loss on the other hand are compatible with slight microstructural variations observed between the two materials:

(i) the consolidation kinetics is much faster with SPS. The grain size is thus smaller. However, it is not straightforward to quantify Hall-Petch effect in bimodal microstructure. One can here question whether ultrafine grains play an important role on hardening or not since a high (volume) fraction of coarse grains is observed in both SPSed and HIPed materials.

(ii) Higher dislocation density since recovery and recrystallization may be limited during short SPS consolidation.

(iii) From small-angle neutron scattering (SANS) experiments, there is no significant difference in precipitates distribution between the two materials. Therefore, precipitation strengthening must be of the same order.

(iv) Finally, one can mention the contribution of remaining porosity, estimated at 2% after SPS against 0% after HIP. This could explain the sooner break of SPS specimen compared to HIP material, the latter having a long post-necking range where stress decreases.

Fractographic examinations of SPS and HIP tensile specimen are reported in Fig. 3.4. The fracture surface is essentially covered by dimpled features (Fig. 3.4(a3,b3,c2)), characteristic of ductile behavior. It shows various degrees of ductility, noted by the dispersion in the size of the microvoids formed during necking. This was observed in a scattered way across the surface of the fractured specimen and can be a manifestation of the abnormal grain growth. This connection between heterogeneous grain structure and dimpled surface has already been reported on nanocrystalline Cu-Nb prepared by mechanical alloying and equal angle channel extrusion [111]. However, double population of precipitates acting as brittle phases should play a significant role on fracture [112, 113]. Spare cleavage zones are found at room temperature in both SPS (Fig. 3.4(a2)) and HIP (Fig. 3.4(c4)) samples. Several crack paths were identified on brittle zones. The latter were running through interface between powder granules, whose size varied from 1 to 50 $\mu$m. This type of intergranular and transgranular cleavages was also reported on sintered Fe-Al powder [85]. This highlights the interest of reducing the processing artefacts responsible for ductility loss, as showed on bulk nanostructured Nickel [114]. In this sense, one-step compaction by SPS can be an answer. Also, coarse titanium and silicon-rich oxides were observed in cleavage zones, which tend to prove the detrimental role of coarse particles on the damage behavior (Fig. 3.4(c6)).

Most importantly, heterogeneous grain distribution with ultrafine (d < 1 $\mu$m) and larger grains seems to be a good compromise for strength and ductility [115]. Small grains, as in pure nanocrystalline metals, induce outstanding strength when grains large enough to favor dislocation activity can provide substantial strain-hardening, therefore boosted ductility [116]. This statement is of prime interest as abnormal grain growth systematically occurs during SPS consolidations above 1050°C (1323 K). Thus, the ratio of ultrafine grained region to coarse-grained region is almost constant within a temperature range 1050°C-1150°C and permits sufficient reproducibility of the tensile properties.

47
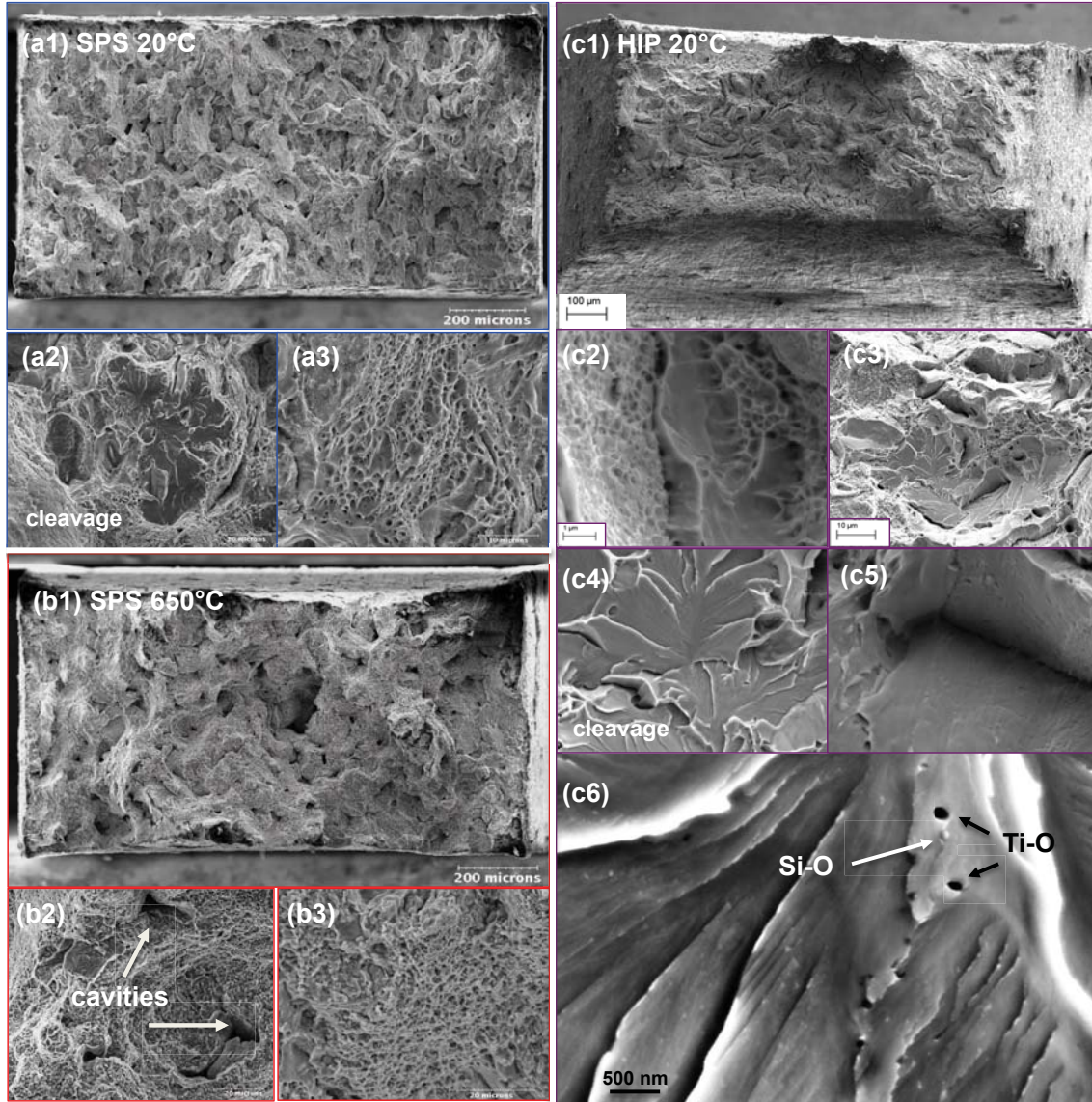
**Figure 3.4:** Fracture surface of SPSed ODS ferritic steels tested at (a) 20 °C and (b) 650 °C (c) HIPed ODS ferritic steel tested at 20 °C and zoom of its microstructure features.

This can be validated by the work of Grosdidier *et al* [71] which states that getting hetero-nanostructured ODS FeAl results from the combination of local heating during SPS processing and the use of heavily cold-worked milled powders.

In order to determine a bit more about the role of heterogeneous microstructure on the mechanical properties, a fine characterization by EBSD was performed on the broken specimen of SPSed ODS steel (K29-M2). Specially, two specimen tested at 20°C and 650°C (tensile curve in Fig. 3.1) were investigated. In Fig 3.5, the intragranular orientation gradient in coarse grains underlines the formation of subgrains. Kernel average misorientation calculations show few degrees of misorientation after plastic accumulation. No drastic morphological evolution characterizes the coarse

48

grains that keep their isotropy even after 13% of deformation at 20°C or 30% of deformation at 650°C. These results tend to prove that coarse grains effectively accumulate plastic strain through organized subgrains or rotation. These observations are more difficult to emphasize in the UFGs. Superplasticity and grain boundary sliding between UFGs are most likely the predominant mechanisms in the UFGed region.
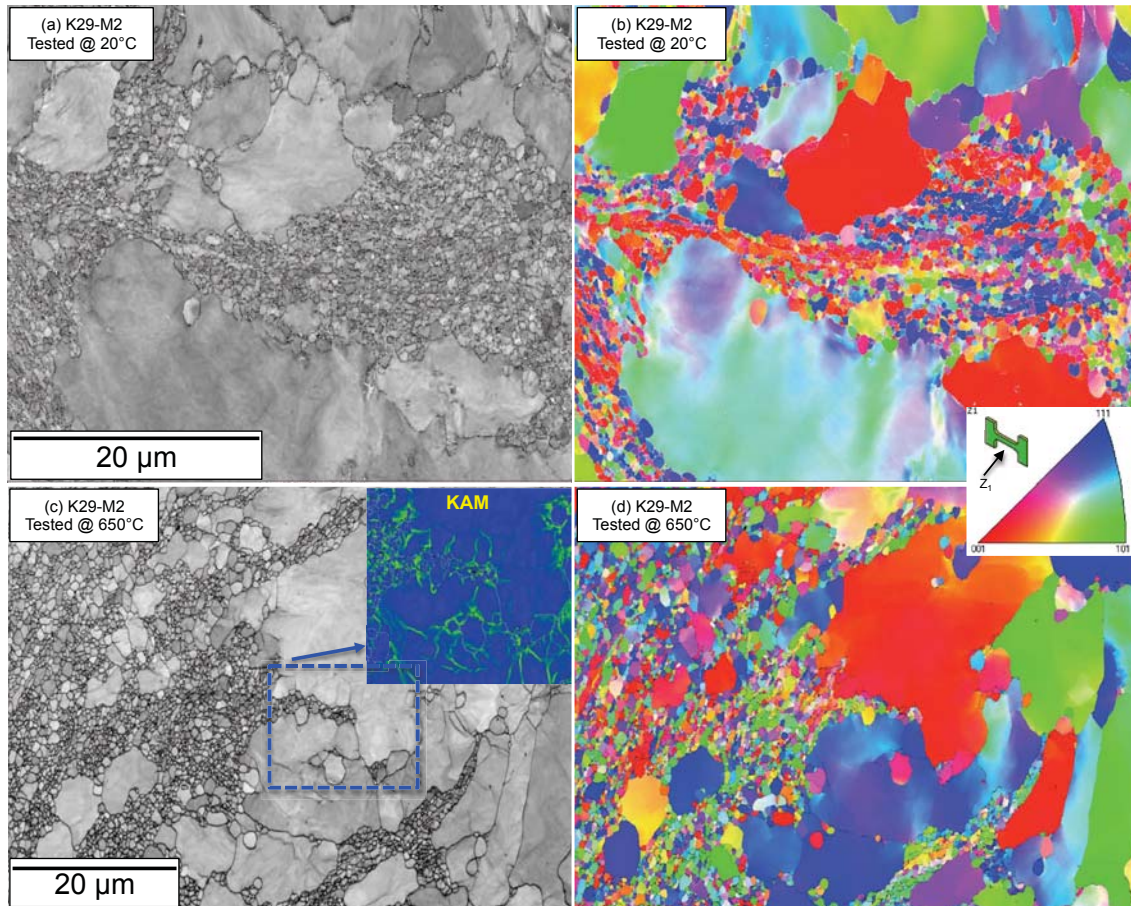


**Figure 3.5:** (a) Band contrast and (b) Orientation map of a zone close to the rupture surface of a broken specimen tested at 20°C (c) Band contrast with inset where subgrains are highlighted by Kernel Average Misorientation (KAM) in a coarse grain (d) Orientation map of a zone close to the rupture surface of a broken specimen tested at 650°C

In conclusion, dense ODS steels produced by SPS at 1100°C in less than 20 min have bimodal microstructure with submicronic grains surrounded by larger grains. This specific microstructure is most likely responsible for: (i) High tensile strength induced by small grains – some are still substructured and deformed – and high density of fine complex nano-oxides. (ii) Good ductility, especially because larger grains can accept decent work-hardening. However, other plasticity mechanisms at high temperature, such as superplasticity, may occur. Indeed, grain boundary sliding (GBS) involving ultrafine grains was observed to play a significant role on

strain-hardening [116]. Moreover, tensile properties are isotropic along the whole temperature range, suggesting no influence of texture in the materials.

## 3.2 Influence of milling and oxide dispersion on the tensile properties

*Related published article: [C]*. This work was performed with B. Mouawad.

Three model materials (i) atomized (ii) milled nanostructured and (iii) nanostructured alloyed with yttria ($Y_2O_3$) and titanium - were consolidated at 850, 950 and 1050 °C. Depending on the materials, nanostructured, bimodally ultrafine-grained materials and finally coarse-grained materials were obtained. Influence of grain size is dominant for bimodal UFG materials and deviates from Hall-Petch law, though well captured by the coarse-grained ferritic steel. At constant chemical composition, the tensile strength can be tailored from 500 to 1200 MPa with total elongation from 8 to 35%.

### 3.2.1 Base Materials

The atomized powder $PA$ was produced by gas atomization under argon atmosphere of a prealloyed smelted steel Fe-14Cr-1W. This powder was then milled in order to obtain a nanostructured ferritic powder $PM$. Also, the atomized powder was milled with yttria ($Y_2O_3$) and $TiH_2$ powders in order to produce ODS ferritic steel by mechanical alloying (MA). The chemical composition of the three powders is given in Table 3.1.

| Element (wt%) | Fe | Cr | W | Y | O | Ti |
|---|---|---|---|---|---|---|
| Power (atomized) - PA | Bal. | 14.6 | 0.99 | / | 0.1 | 0.1 |
| Power (milled) - PM | Bal. | 14.5 | 1.01 | / | 0.1 | 0.1 |
| Power (Mechanically alloyed) - ODS | Bal. | 14.5 | 1.01 | 0.16 | 0.15 | 0.32 |

**Table 3.1:** Chemical composition (wt%) and samples ID of the three powders

The powders were then consolidated by SPS to form a dense cylindrical pellet of 20 mm diameter and 6 mm height. SPS device was a HP D 25 (FCT System, Germany). Sintering cycles were performed under 90 MPa average pressure, with a heating rate of 300 K.min$^{-1}$ up to the holding temperature for a soaking time of 5 min. The maximum temperature was chosen at 850, 950 and 1050 °C.

The powder particles were machined by focused ion beam (FIB) and observed by SEM and EBSD. After atomization, the powder particles have fully ferritic structure with a mean diameter of 40 $\mu$m, as described in Fig. 3.6(a). Some pores are located both at 'triple' grain junctions and in the grains. One can also notice some

microstructure heterogeneities with disturbed and finer grains at some powder particles edges. (Fig. 3.6(a, inset)). The two milled powders with and without yttria are nanostructured. However, the ODS powder particle investigated here contains larger grains up to 1 $\mu$m. More systematic investigation using classic imaging mode showed also homogeneous and ultrafine grained zone (not shown here). Consequently, one will consider in the discussion that the two milled powders are both ultrafine-grained structure with no relevant difference in size. Influence of grain size is more relevant when comparing atomized and milled powders
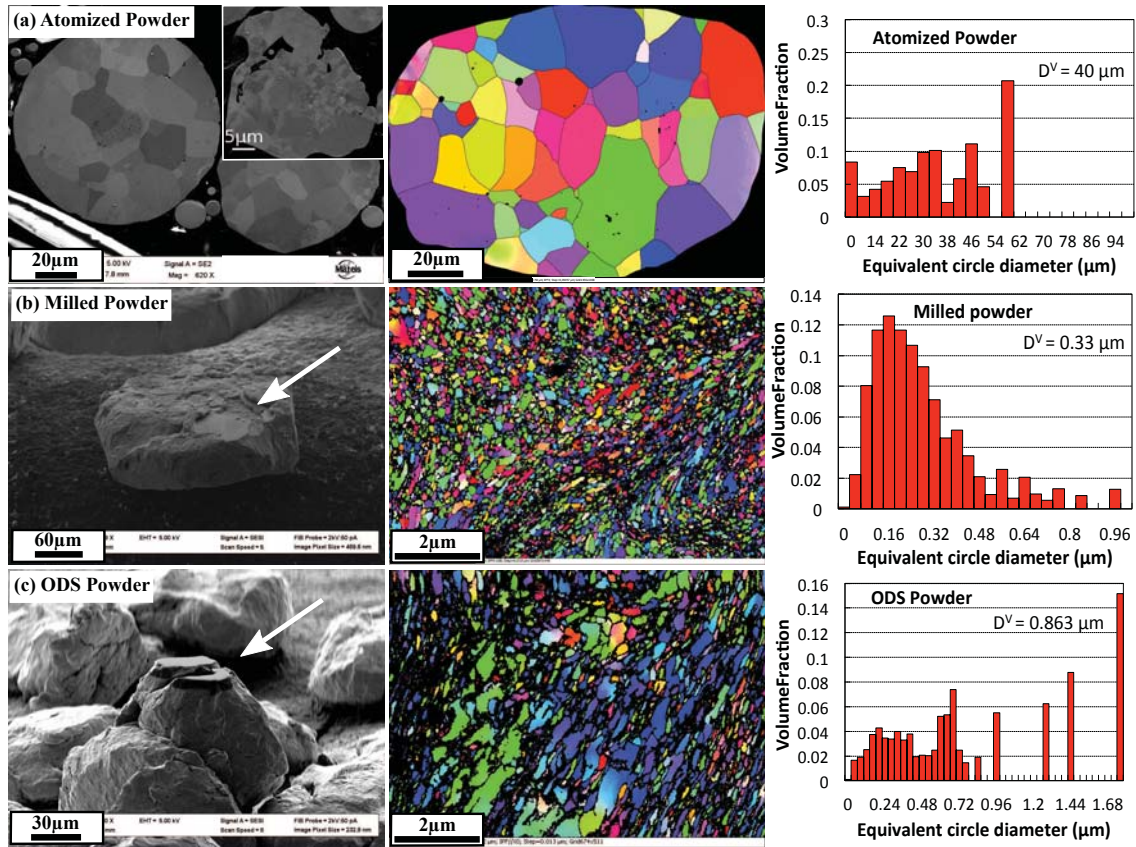


**Figure 3.6:** Initial state of powders with for each specimen: Secondary Electron SEM image, EBSD orientation map and corresponding grain size distribution in volume fraction

## 3.2.2 Consolidation behavior

The 3 powders were then consolidated by SPS, as detailed in the previous section. Figure 3.7 describes the hardness and relative density of consolidated samples. PA clearly has better densification behavior since is has higher relative density at the three temperatures compared to the two others. The hardness plateau with temperature expresses the relatively limited grain growth between 850 °C and 950 °C. Then, a more complex mechanisms involving the formation of martensite occurs at
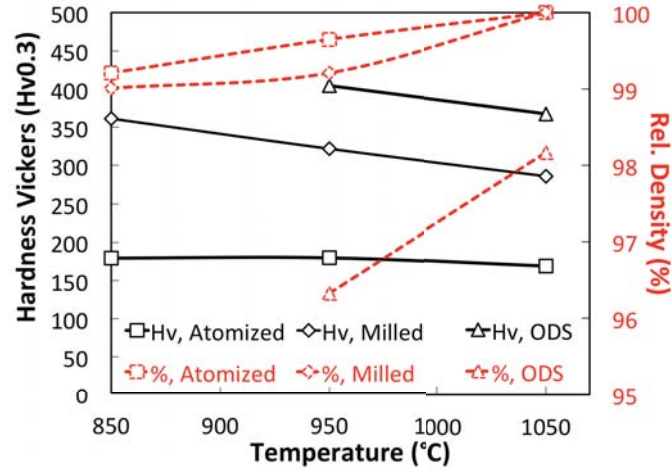
**Figure 3.7:** Hardness and relative density of consolidated samples

1050 °C, as quantified latter. The good densification behavior of PA compared to PM and ODS is related to both regular and spherical shape and lower particles hardness that facilitates plastic-induced rearrangement and densification. Indeed, the limit density up to the material can plastically densify is related to the yield strength of the bulk materials. The latter is much lower in atomized than in nanostructured milled powders. Interestingly, the milled powder PM observes the equivalent densification behavior with a shift toward lower relative density at lower temperatures (850 and 950 °C) and tends to be fully dense at 1050 °C as well. PM samples clearly follow a continuous decrease of hardening with temperature, which tends to prove that the gain in relative density is not sufficient to compensate the decrease of Hall-Petch strengthening. One can conclude that at 1050 °C, PM and PA are totally consolidated and PM has probably much finer microstructure that gives rise to an increase in hardness of more than 100 kg.mm$^{-2}$.

| Initial Powder | Ref. | T [°C] | $\rho_r$ [%] | HV | D$^N$ [$\mu$m] | D$^V$ [$\mu$m] | Rp$_{0.2}$ [MPa] | UTS [MPa] | $n$ | k [MPa] |
|---|---|---|---|---|---|---|---|---|---|---|
| PA | PA850 | 850 | 99.2 | 179.3 | 20.03 | 34.88 | 302 | 653 | 0.197 | 906 |
| | PA950 | 950 | 99.6 | 179.5 | 20.04 | 38.85 | 292 | 643 | 0.192 | 871 |
| | PA1050 | 1050 | 100 | 168.1 | 21.71 | 283.82 | 262 | 563 | 0.196 | 742 |
| PM | PM850 | 850 | 99 | 361.1 | 1.6 | 1.62 | 862 | 1215 | 0.101 | 1571 |
| | PM950 | 950 | 99.2 | 321.6 | 1.78 | 8.95 | 791 | 1065 | 0.092 | 1312 |
| | PM1050 | 1050 | 100 | 285.7 | 1.96 | 12.29 | 610 | 972 | 0.126 | 1261 |
| ODS | ODS950 | 950 | 96.3 | 404.4 | 1.54 | 9.82 | 1064 | 1135 | 0.069 | 1510 |
| | ODS1050 | 1050 | 98.1 | 367.4 | 1.67 | 16.67 | 950 | 1106 | 0.054 | 1248 |

**Table 3.2:** Relative density, Hardness Vickers, Mean grain size from Number and Volume fraction, and mechanical properties for all consolidated samples

52

Regarding ODS steels, ODS950 has much lower relative density than that of PA950 and PM950 consolidated at the same temperature. At 1050 °C, the difference diminishes but not enough to get fully densification (around 98 %). Since the hardness is higher than both PA and PM, higher yield strength of powder particles is expected to reduce the ability to densify at moderate temperature. Then, diffusion mechanisms such as grain boundary sliding or volume diffusion are probably not enough completed to achieve full consolidation at short times. This is even more emphasized at 850 °C where ODS powder had lots of remaining pores (not shown here). The evolution of hardness with temperature seems to vary with the nature of the powder. One will discuss this in the next section, based on the microstructure characterization.

### 3.2.3   Microstructure of consolidated materials
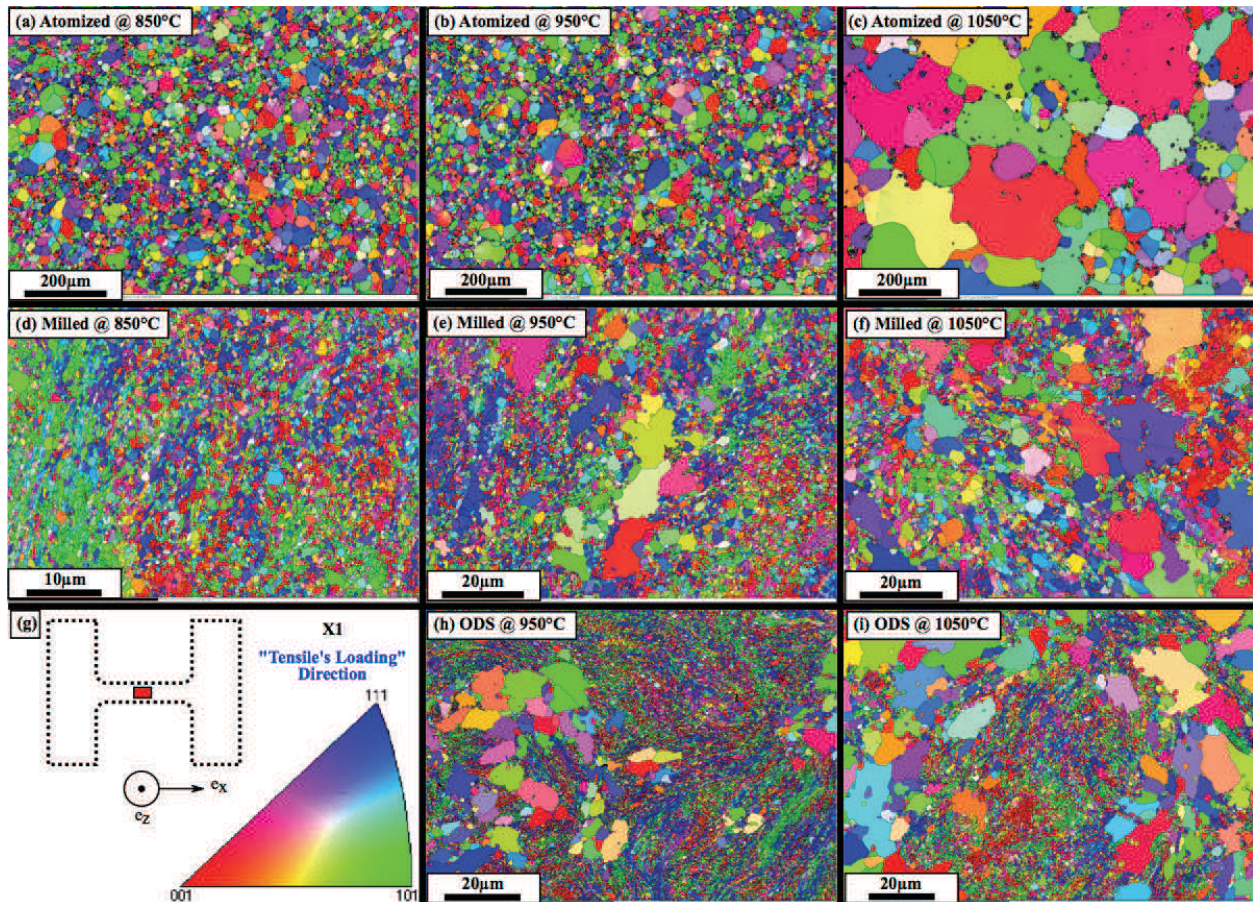


**Figure 3.8:** EBSD map orientation of the 8 SPS compacts showing various metallurgical states. The microstructure was characterized on the gage length of the tensile specimen.

In order to understand the role of microstructure on the mechanical properties, a systematic investigation by SEM-FEG and EBSD was carried out on the 8 SPS

53

compacts (porous ODS850 was excluded). Based on the EBSD maps presented in Fig 3.8, one can discuss the grain growth behavior of each sample. The grain size was determined based on either the arithmetical mean $D_n$ or the volume-weighted mean size $D_v$:

$$D_n = \frac{1}{N} \sum_{i=1}^{n} D_i \tag{3.1}$$

$$D_v = \sum_{i=1}^{n} f_i^v \cdot D_i \tag{3.2}$$

with $N$ the number of grains on the EBSD map and $D_i$ the diameter of each grain $i$, $f_i^v$ the volume fraction of each class in the grain size distribution (GSD) determined by EBSD. One key result is the quite constant GSD between the as-atomized powder and PA850 (Fig. 3.9). Even if the GSD measured on the PA is not enough representative and most likely overestimated, the mean diameter was around 40 $\mu$m, which is equivalent to that of the PA850 sample. This demonstrates the limited grain growth at this temperature. Grain growth is also very slow at 950 °C but completely
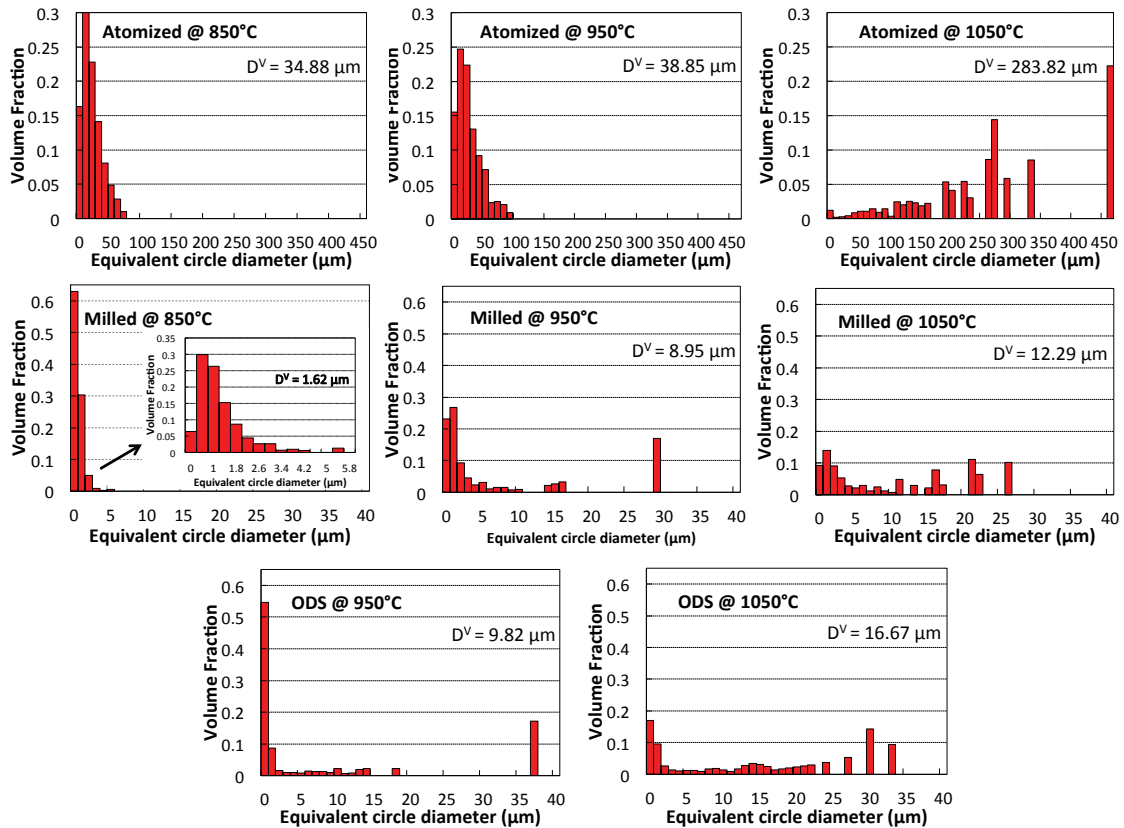


**Figure 3.9:** Grain size distribution of the 8 metallurgical states with mean grain size $D_v$.

increases at 1050 °C where the mean grain size reaches 284 $\mu$m. When focusing on interparticles boundaries, one can notice blocks of finer grains with a diameter below

54

1 $\mu$m. This can be interpreted by the formation of martensite blocks between ferrite grains (Fig. 3.8(c)). This martensite may nucleate from either local carbon-rich zones or scarcely dispersed inclusion, such as sulfites [117]. These blocks were also observed in the SPSed milled powder but not in the SPS ODS powder. This can be explained by the austenite-stabilizing effect of both titanium and oxygen added in the ODS powder compared to the two others. Formation of low fraction of austenite was observed by neutron in situ study by Zhang *et al* [73]. Back to the hardness plateau observed in the atomized powder, one can conclude that the formation of austenite and further martensite during cooling can harden the material sufficiently to compensate the strength loss due to significant grain growth.

Milled powder PM undergoes abnormal growth between 950 and 1050°C. PM do not contain high density of particles but can contain carbides that may pin grain boundaries. Even this could lead to abnormal growth, the main cause of this bimodal microstructure is most likely heterogeneous stored energy after milling. The driving force for strain-induced boundary migration (SIBM) is high enough to induce abnormal growth of selected grains at the expense of more deformed ones. This was demonstrated on milled ferritic powders consolidated by either spark plasma sintering or hot isostatic pressing [107]. Abnormal growth mechanisms can be multiple and the microscopic description of it would fall out of the scope of this present article. This bimodal microstructure consists of both ultrafined grains with a mean diameter of 750 nm and coarse grains with a diameter up to 30 $\mu$m. Increasing the temperature gives similar microstructure, even if the UFG to coarse grains ratio decreases. Although it is not shown here, martensite blocks were also scarcely observed within the PM950 and PM1050.

ODS950 and ODS1050 microstructures are also heterogeneous, with similar grain size than that of oxide-free consolidated powders. This shows very limited effect of oxide dispersion on the appearance of abnormal grains. This demonstrates that regardless the precipitation state, strain-induced boundary migration plays a significant role on the onset of abnormal grain growth. Also, within the studied temperature range, the bimodal microstructure seems to be stable.

### 3.2.4   Tensile properties

The tensile properties exhibit a large range of strength (with ultimate tensile strength of 1215 MPa for the PM850 and of 563 MPa for the PA1050) and of ductility (from 2% to 33%) for the same chemical composition (Fig. 3.10). PA samples show limited variation in both strength and elongation. As shown before, small martensite blocks may compensate the decrease of tensile strength due to grain growth. However, the Hall-Petch hardening seems to be very moderate in coarse grained ferrite. PA samples have quite constant total elongation, showing a moderate effect of grain size on ductility for coarse grained ferrite.

Fractographic examinations were performed on the broken specimen (Fig. 3.11). The necking-induced area reduction (NAR) was measured on each sample (Fig. 3.12).
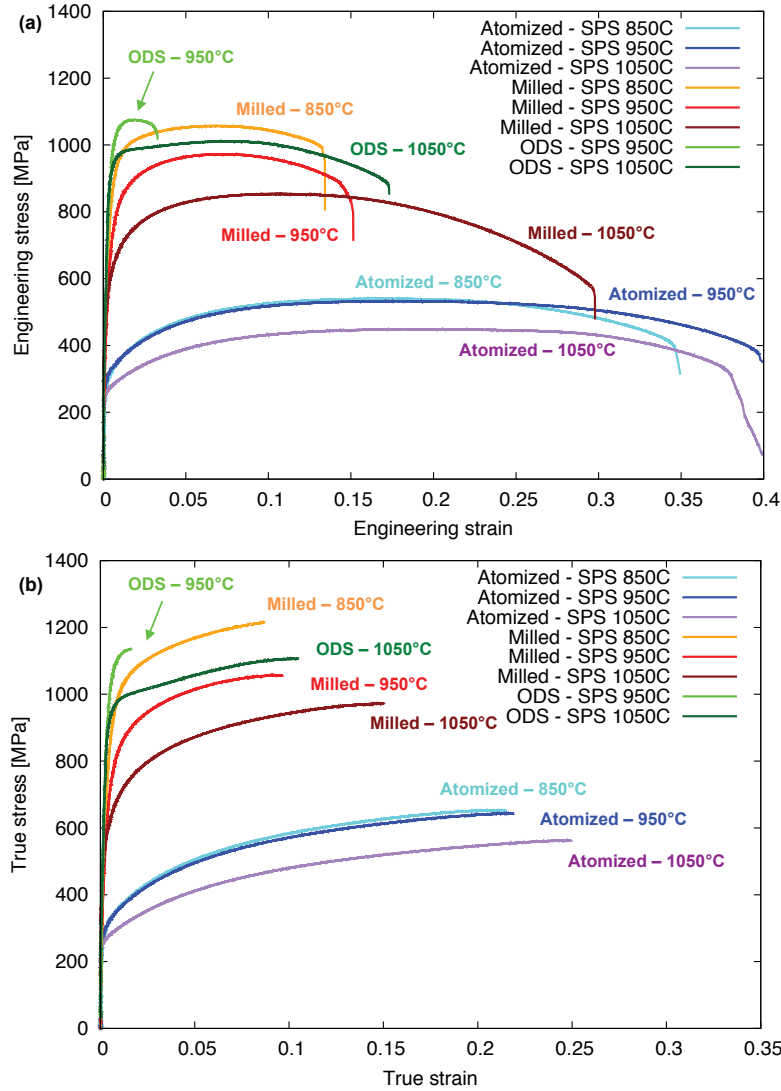
**Figure 3.10:** Room temperature tensile behavior of the consolidated samples.

The NAR of the three PA samples slightly increases from 60 to 68.3% for PA850 and PA1050, respectively. They all exhibit ductile damage mode with numerous dimpled features. MP850 and MP950 show mixed ductile and intergranular damage mode whereas MP1050 sample has full ductile behaviour. In this sample, the size and the geometry of the dimpled features are bimodal, which seems to be related to the grain structure observed by EBSD. ODS950 has remaining porosity that is detrimental to damage resistance. However, dimpled features are also observed, which demonstrates that porosity is not fully detrimental to plastic deformation. ODS1050 shows similar behaviour to MP1050 with bimodal dimpled features most likely related to the bimodal grain structure. MP1050 has the same NAR as that of coarse-grained AP1050, which demonstrates that large grains significantly boost the ability to accumulate plasticity.
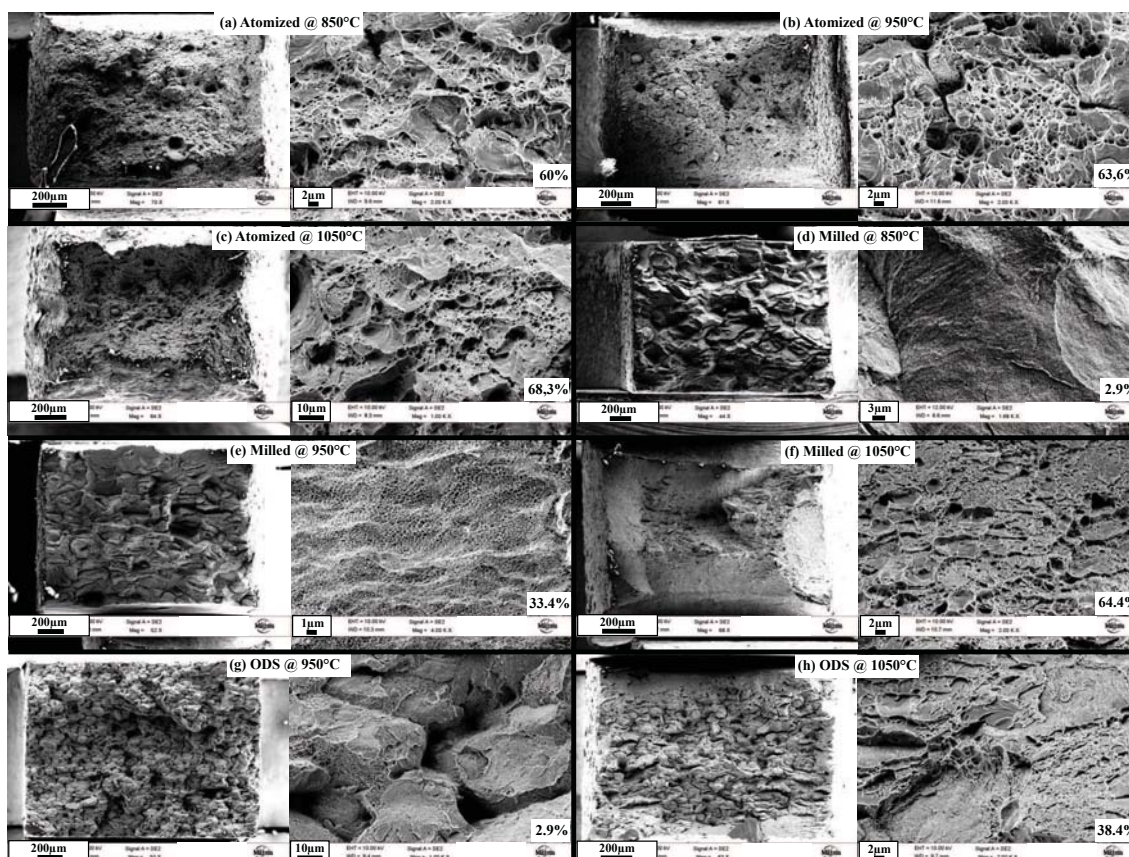
**Figure 3.11:** SEM characterization of the broken specimen. The area reduction coefficient is given for each sample.

It can be concluded that the bimodal grain structure participates to the accumulation of plastic deformation, which results in bimodal dimpled features observed at the surface of the broken specimen. Also, remaining pores seen at the surface of the sample ODS950 explains the limited plastic deformation of the sample. This confirms that for ODS powder, a higher consolidation temperature is needed to achieve sufficient ductility.
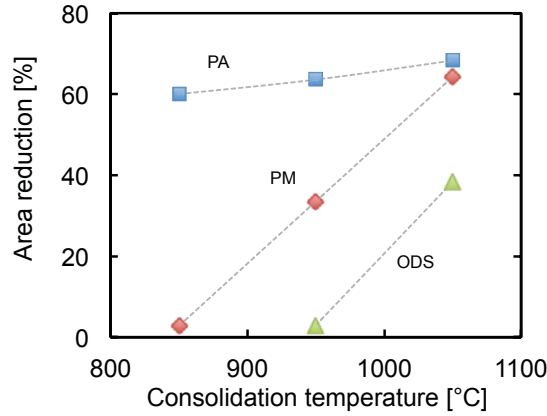
**Figure 3.12:** Area reduction as a function of the temperature consolidation.

### 3.2.5 Tensile strength modeling

The yield strength of a metallic material comes from many microstructure contributions. One can summarize the strengthening mechanisms as follows [118, 119]:

$$\sigma_{YS} = \sigma_0 + \sigma_{ss} + \sigma_{HP} + \sqrt{\sigma_{dis}^2 + \sigma_{ppt}^2} \qquad (3.3)$$

where $\sigma_0$ is the Peierls-Nabarro friction stress in pure iron, which is needed for a dislocation to move into an atomic plane [120]. Based on Alinger's thesis [121], Hin *et al* chose a value of 125 MPA in a simple strengthening model [122].

The strengthening contribution due to solid solution $\sigma_{ss}$ is classically used for fcc materials with the following form:

$$\sigma_{ss} = \sum_i k_i.X_i^z \qquad (3.4)$$

with $X_i$ the mass or atomic fraction and $k_i$[1] a hardening constant of the element $i$. Actually, the original model by Mott and Nabarro dealt with the solute concentration rather than the mass fraction since there is no reason that the atomic weight plays on role on the hardening efficiency [123]. However, in the recent literature, the hardening constants $k_i$ are calculated using this model. Whereas $z = {}^2\!/\!{}_3$ is suitable for fcc materials like aluminum alloys [124, 125], $z = {}^3\!/\!{}_4$ for substitutional solid solution (Cr,W) [126, 37, 127] and $z = {}^1\!/\!{}_2$ for interstitial elements (N,C) [128, 129, 130] are more suitable in bcc alloys[2].

The grain size contribution $\sigma_{HP}$ is referred to the Hall-Petch effect. This expresses the influence of grain boundaries on dislocations behavior. Indeed, disloca-

---

1. One should keep in mind that $k_i$ and other constants used for the model incorporates the Taylor factor $M$, since equation (3.3) was originally designed for a slip plane only.

2. $z$ tends to ${}^1\!/\!{}_3$ in martensite [129]

tions are gradually stacked at grain boundaries and form pile-ups until they reach the threshold-stress to pass into the next grain. This is given by:

$$\sigma_{HP} = \frac{k_{hp}}{\sqrt{D}} \tag{3.5}$$

where $k_{hp} = 0.2\mu\sqrt{b}$ [27] and $D$ is the mean grain size. In the case of heterogeneously grained material, such as bimodally structured steel, one can question whether the (arithmetic) mean grain size is reliable enough. Indeed, if the largest grains have much higher size than the smallest grains, the latter will most likely have a weak influence on dislocations pile-up at grain boundaries. Thus, the area-weighted grain size or even the whole grain size distribution would become more relevant [131]. For homogeneous ultrafine grained ferritic steels, Takaki *et al* determined $k_{hp} = 0.6$ MPa.$\sqrt{m}$ [132].

In addition to the two aforementioned contributions, two major mechanisms take part to the strengthening of ODS steels. Dislocation forest hardening $\sigma_{dis}$ takes into account the interaction between existing dislocations (before mechanical testing, inherited from thermo-mechanical processing in non-fully recrystallized steels) and dislocations propagating during mechanical testing. This contribution is given by:

$$\sigma_{dis} = M\alpha\mu b\sqrt{\rho} \tag{3.6}$$

where $M$ is the Taylor factor that depends on the crystallographic structure and the texture of the material, $\alpha$ a numerical constant which equals to 0.38 in ferrite [133], $\mu$ the shear modulus, $b$ the Burgers vector, $\rho$ the dislocation density.

Finally, the precipitation hardening can be quantified thanks to the Ashby-Orowan equation [134]:

$$\sigma_{ppt} = 0.84 \cdot \frac{1.2M\mu b}{2\pi\lambda_p}\ln(\frac{2r_p}{2b}) \tag{3.7}$$

where $\lambda_p = \sqrt{2\pi/3f_p} \cdot r_p$ the mean distance between particles, $r_p$ and $f_p$ the precipitates mean radius and fraction. This kind of model was previously applied on either HIPed or extruded steels [27, 135, 136] but never on ODS ferritic steels produced by Spark Plasma Sintering. Also, various microstructural features were obtained by SPS, allowing to study the influence of each microstructural parameter at one time. This model was applied on the various samples consolidated by SPS and compared to experimental yield strengths (Fig. 3.13). Consolidated PA samples allowed the solid solution, Hall-Petch and dislocation forest strengthening to be validated thanks to the experimental values (Table 3.3).

A dislocation density of fully recrystallized ferrite was chosen for the PA samples, that is $1 \times 10^{13}$ m−2. Dislocation densities of M850, M950 and M1050 and O950
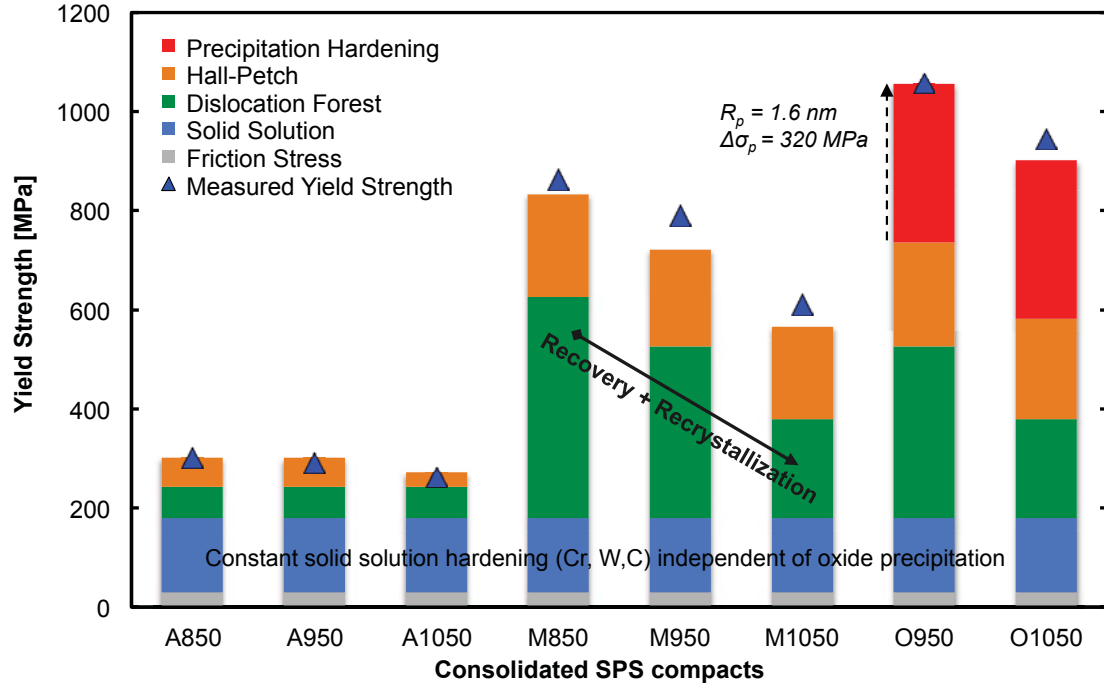
**Figure 3.13:** Calculated yield strength using strengthening model from equation (3.3). The Hall-Petch contribution was calculated using the arithmetical mean grain size.

| Parameters | Values |
|---|---|
| $\sigma_0$ [MPa] | 30 [128] |
| $k_{Cr}$ [MPa/at%$^{3/4}$] | 9.65 [126, 128, 135] |
| $k_W$ [MPa/at%$^{3/4}$] | 75.79 [126, 128, 135] |
| $k_C$ [MPa/at%$^{1/2}$] | 1122.5 [129] |
| $b$ [nm] | 0.248 |
| M | 2.77 [133] |
| $\alpha$ | 0.38 [133] |
| $\mu$ [GPa] | 83 |
| $r^c$ [nm] | 2.5 [136] |
| $r_p$ [nm] | 1.6 [58, 96, 107, 137] |
| $f_p$ [%] | 1 [107] |
| $\lambda_p$ [nm] | 49.5 [107] |

**Table 3.3:** Parameters used for the strengthening model

60

and O1050 samples were set at 5, 3 and 1 $\times 10^{14}$ m$^{-2}$ and 3 and 1 $\times 10^{14}$ m$^{-2}$, according to Synchrotron X-Ray diffraction study [138, 139]. Precipitation hardening can be overestimated since the fraction of by-passed particles was not accurately determined. However, this value (423 MPa) is consistent with ODS steels properties at room temperature [68]. The model using the arithmetical mean grain size is in better agreement than that with the volume-weighted grain size (Fig. 3.13). The strength difference between atomized and milled consolidated powders is due to both dislocation density and grain refinement. Hall-Petch effect is the most effective on M850 where most of nanosized to ultrafine grains was retained in the consolidated sample. M950 and M1050 have higher tensile strength than the predicted values. Since no precipitation hardening was taken into account in these samples, one can estimate that coarse precipitates such as carbides may participate to strengthening. This simple model also reproduces the higher tensile strength of ODS steels compared to oxide-free milled steels. However, one should keep in mind that ODS950 has poor ductility due to remaining porosity (Fig. 3.10). ODS1050 has both good tensile strength and ductility, which can be interpreted by the combination of:

(i) bimodal microstructure that brings grain boundary hardening thanks to ultrafine grains and work-hardening potential thanks to coarse grains

(ii) additional strengthening thanks to the fine and dense oxides precipitation, which brings to ODS1050 higher strength than that of the M1050 for instance.

In order to better understand the role of grain size and precipitation on ductility, the effect of microstructure on the work-hardening behavior must be quantified.

### 3.2.6 Work-hardening behavior

Work-hardening quantifies the ability of a metallic material to get hardened under mechanical loading. The work-hardening rate is governed by the competition between dislocations formation due to plastic deformation and dynamic recovery occurring during mechanical testing. This balance between these two antagonists mechanisms is expressed in the Kocks-Mecking equation [124, 140]:

$$\frac{\partial \rho}{\partial \gamma_p} = \left( \frac{\partial \rho}{\partial \gamma_p} \right)^+ - \left( \frac{\partial \rho}{\partial \gamma_p} \right)^- = k_1 \sqrt{\rho} - k_2 \rho \tag{3.8}$$

where $\gamma_p$ is the plastic shearing, $\rho$ the dislocation density and $k_1$ and $k_2$ constant values. More generally, any additional obstacle other than dislocations themselves, such as precipitates or grain boundaries, must have a role on the dislocations behavior during mechanical loading. In that case, Estrin proposes that the obstacle densities are additive, so that the dislocation density evolution is finally given by [140, 125]:

$$\frac{\partial \rho}{\partial \epsilon_p} = M[k_1 \sqrt{\rho} + \overbrace{\frac{1}{b.D}}^{\text{at grain boundaries}} + \underbrace{\frac{1}{b.L_{bp}}}_{\text{on second-phase particles}} - k_2 \rho] \tag{3.9}$$

where $D$ and $\bar{L}_{bp}$ are the grain size and the mean distance between second-phase particles that are **by-passed**, respectively. Indeed, for by-passed precipitates, a Frank-Read-like mechanism is activated on particles: dislocations can be pinned by particles and multiply, which contributes to the forest hardening. Fribourg [141] proposed to modify the dislocation forest hardening with the following equation:

$$\sigma_{dis} = M\alpha\mu b\sqrt{\rho + \rho_{ppt}} \tag{3.10}$$

where the dislocation density generated by particles $\rho_{ppt}$ depends on the precipitate density and radius. The WH rate was calculated from the flow stress / strain curve by:

$$\theta = \frac{\partial \sigma_p}{\partial \epsilon_p} \tag{3.11}$$

where $\sigma_p$ and $\epsilon_p$ are the plastic flow stress and the plastic strain, respectively. The work-hardening behavior of each consolidated sample is reported in Fig. 3.14. For quantitative comparison, the strain-hardening coefficient $n$ was derived assuming a Hollomon description of the flow stress (Fig. 3.14(b)):

$$\sigma = \sigma_0 + k \cdot \epsilon^n \tag{3.12}$$
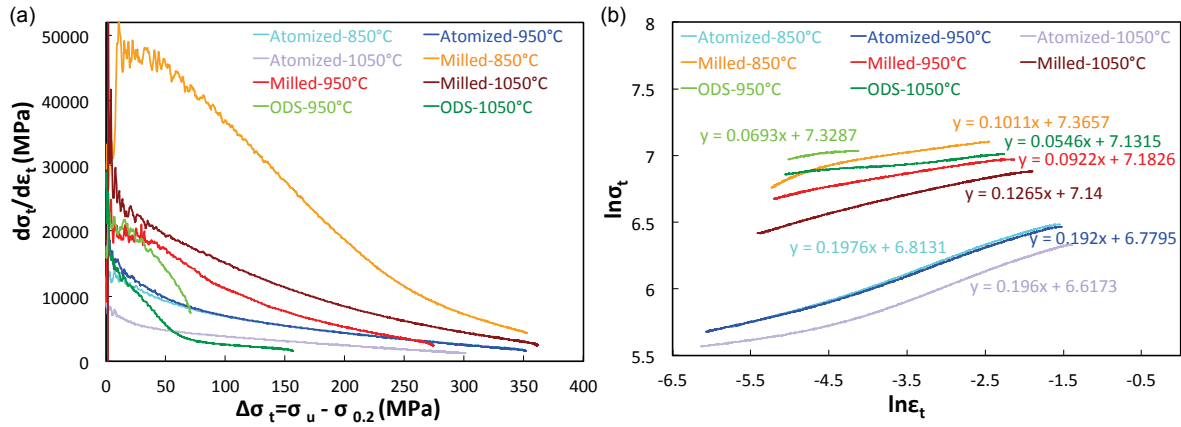


**Figure 3.14:** Experimentally derived work-hardening rate from equation (3.11).

The two-stage work-hardening behavior of the PA samples is most likely the expression of the successive role of coarse ferrite and martensite upon plastic deformation [142], even if the martensite fraction is very low. More importantly, the PA samples have much higher strain-hardening coefficients compared to ultrafine grained PM and ODS samples. There is also a gain in SH coefficient in bimodal microstructures (PM1050) compared to uniformly ultrafine grained materials (PM850). The benefit of bimodal grain size was also reported to increase ductility due to boosted work-hardening in coarse grains [108, 104].

For comparison, SH coefficients for both fine grained and coarse grained ferrites are reported in Fig. 3.15. The consolidated milled powder PM has consistent SH

coefficient compared to fine grained ferrite [142]. What is interesting is the effect of oxide precipitation that is translated in the decrease of the SH coefficient from 0.12 to 0.07 at constant grain size. This is a antagonist effect compared to the addition of finely dispersed cementites in ultrafine grained steels [143]. This effect most likely depends on the mean distance between obstacles. The latter for the mentioned cementites was around 900 nm, which is much larger than in the present study ($\lambda_p \approx 50\ nm$).
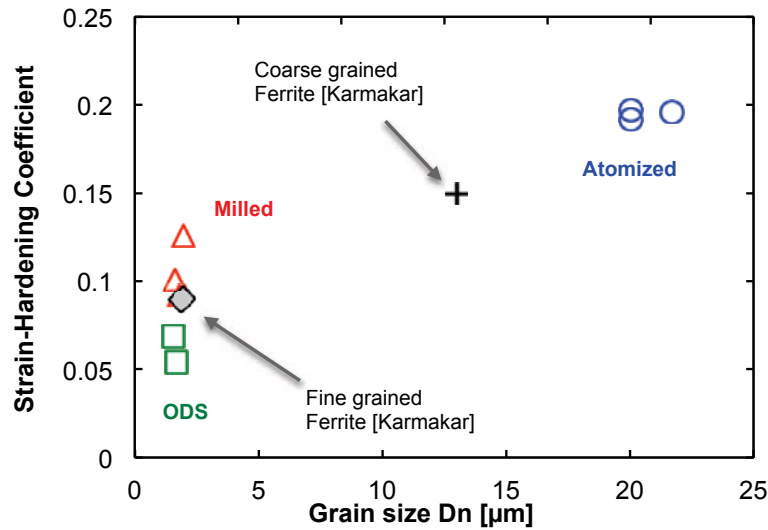


**Figure 3.15:** Strain-Hardening coefficients derived from Hollomon equation for each sample.

### 3.2.6.1 Conclusion

Various microstructures were obtained by high-temperature consolidation of three different powders. The bimodally structured materials achieve both ductility and tensile strength. The strain-hardening coefficient is increased by the presence of coarse grains. ODS steels have lower SH coefficient. The effect of precipitates seems to be detrimental to the work-hardening behavior. This is in contradiction to what was recently found in precipitation hardened aluminum alloys [141] or in cementites dispersed ultrafine grained steels [143].

However, a complete physical variables-based model is needed to understand the role of second-phase particles and grain boundaries on the work-hardening behavior [140, 125]. To do so, cyclic tests on ODS ferritic steels would permit to determine work-hardening fitting parameters and further quantify the effect of microstructure and precipitation on ductility [144, 145].

## 3.3 Complementary result: *In situ* SEM tensile test

The previous discussion emphasized the potential role of coarse grains in boosting the materials ductility thanks to the increase in dislocations mobility. In order to understand the role of those coarse grains, one tried to visualize the evolution of a coarse grained region during plasticity accumulation. To do so, an *in situ* tensile testing was performed in a Scanning Electron Microscope (SEM) chamber on a HIPed ODS ferritic steel with a bimodal microstructure. First, a tensile test was performed on the micro tensile machine (Gatan Debeen Mtest 2000E) outside the SEM chamber in order to quantify the tensile behavior of the specimen. This permitted to confirm whether the specimen geometry and the tensile machine response were accurate or not. Since the tensile strength was equivalent to that formerly measured on the classic tensile machine, the *in situ* test was performed.
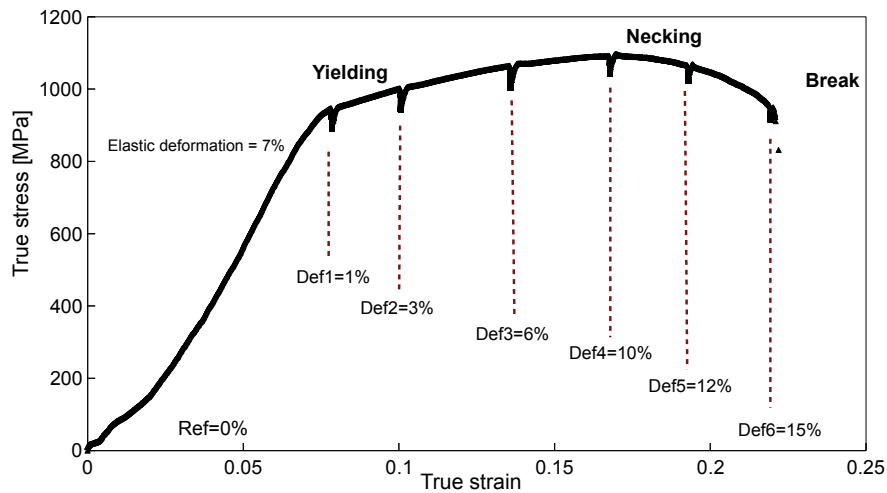


**Figure 3.16:** *In situ* tensile curve describing the strain levels at which the microstructure was investigated. Annotations correspond to plastic strains only (elastic strain of 7% subtracted).

The specimen is pre-tilted at 70 degrees relative to normal incidence of the electron beam, which allows to observe the same zone during the whole mechanical test. The working distance was 22 mm, which does not correspond to fully optimized imaging conditions, though the microstructure is clearly visible. At a certain amount of plastic strain, one can interrupt the test. This corresponds to a relaxation test: the stress value rapidly decreases down to a plateau. Microstructure observations were done at several strain levels, as highlighted in Fig. 3.16. Specially, orientation maps were acquired on the same zone, which contained both ultrafine and coarse grains.

(i) At 1% strain (Fig. 3.17(b)), the grains keep the same orientation. Slip bands show up in the coarse grain G3 but nothing appears in G2.
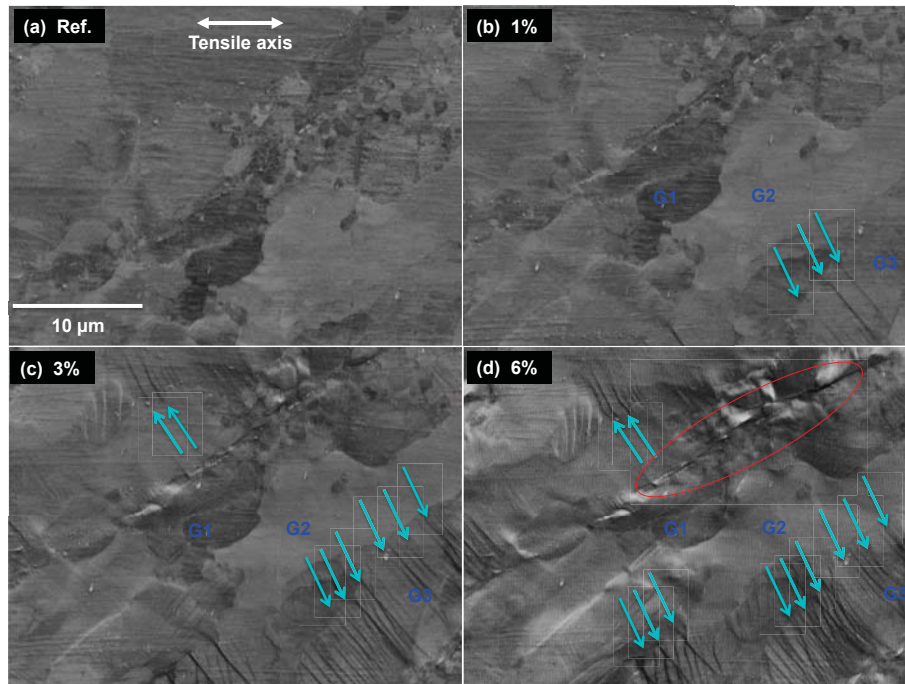
**Figure 3.17:** Microstructure evolution (SEM images in BSE mode) with the increase of plastic strain during tensile testing. Slip bands are highlighted by turquoise arrows.

(ii) At 3% strain (Fig. 3.17(c)), slip bands density increases in G3. Other coarse grains accumulate plasticity with a high number of slip bands. G2 is slip band free but changes its orientation around the boundary G2/G3.

(iii) At 6% strain (Fig. 3.17(d)), G2 keeps rotating whereas no slip band appears. A strain concentration zone clearly comes out (see red line in Fig. 3.17(d). This region contains "coarse" precipitates (D < 300 nm) that constitute evidences of former grain powder particles interfaces. This zone may be a preferential zone of plastic accommodation insomuch that de-cohesion emerges. Regarding the role of ultrafined grains (UFGs), a quantitative study would require a better spatial imaging resolution (in both EBSD step size and SEM magnification). However, the rotation of some UFGs is illustrated in Fig. 3.18. The post-necking damage evolution was followed up by classic SEM imaging. Multiple cavities form in the considered region. Once again, "coarse" particles are located in de-cohesive interfaces (Fig. 3.19)

This *in situ* tensile test validates the setup, in particular the specimen geometry and the micro-machine. The mechanical properties are equivalent to what was previously observed, even if the strain rate was slightly smaller than that at CEA ($2.8 \times 10^{-4}$ s$^{-1}$ against $7 \times 10^{-4}$ s$^{-1}$). One could observe significant microstructure evolution at the metallurgical grain scale during tensile testing:

(i) formation of slip bands in the coarse grains

(ii) Rotation of coarse grains in which subgrains form as we go along the plastic strain.
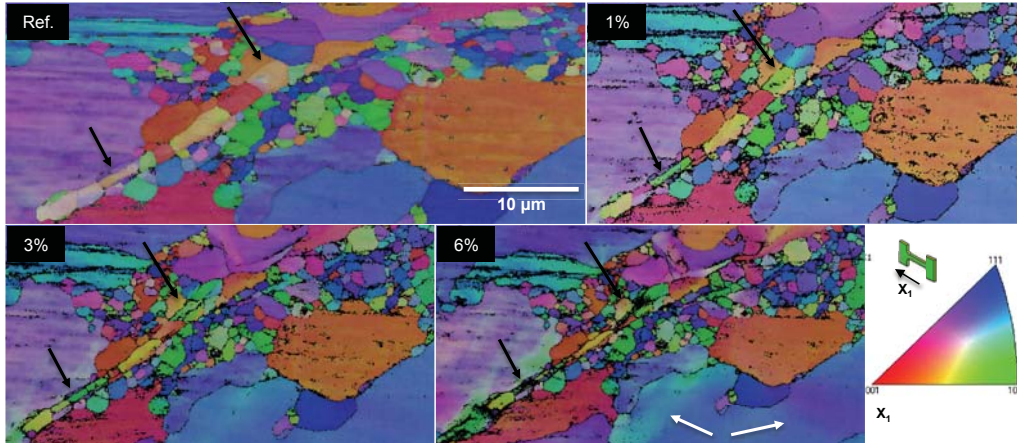
**Figure 3.18:** Orientation maps with increasing plastic strain. Only 3 UFGs seem to rotate (relative to the considered direction, that is parallel to the tensile direction).

(iii) Ultrafined grains seem to rotate along grain boundaries. This could be a mechanism similar to grain boundary sliding or superplasticity, even if the latter is mainly occuring at high temperature. From surface observations, grain boundary sliding was confirmed in ODS steel by a tensile test in the loading direction perpendicular to the elongated cold-rolled grains [146]. However, considering the literature, the presence of UFG cannot produce consistent ductility. One therefore concludes that the formation of subgrains in coarse grains is most likely the major mechanism of plastic deformation accumulation in the bimodally structured alloy.
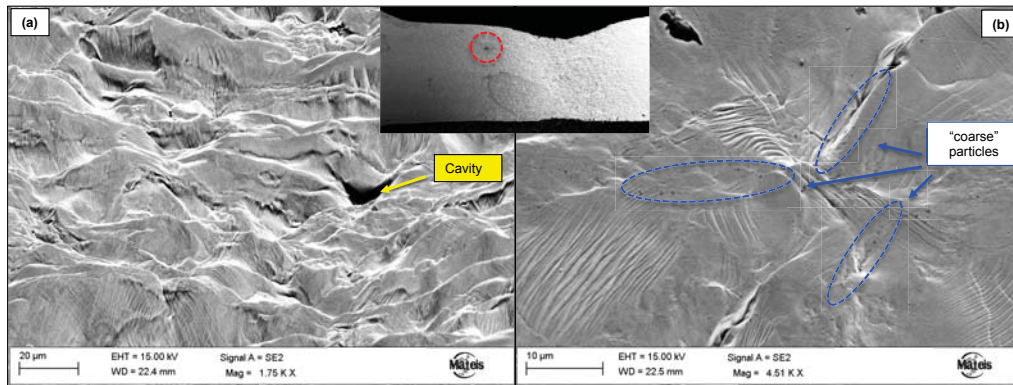


**Figure 3.19:** De-cohesive zones juste before breaking. The electron beam contaminated zone is annotated by the dashed red line, close to the necking point.

(iv) Regarding the damage mechanisms, it seems that the interfaces between former powder particles play an important role on the fracture. In these particular locations, "coarse" titanium oxides formed during high-temperature consolidation. The latter can act as crack initiating sites for many reasons: lack of cohesion with the matrix, particles more brittle that the ferritic matrix, coincident sites with remaining pores. Due to the fact that titanium has high affinity with oxygen and diffuses very

66

rapidly in steel, one can question the benefit of adding titanium in ODS steel. Does titanium-induced creep strain rate decrease worth more than the degradation of the ductility? This kind of effect is being investigated by M. Dadé in his PhD thesis.

## 3.4 Conclusion on the mechanical properties

SPSed ODS ferritic steels have similar tensile properties to conventional ODS steels like HIPed materials.

Tensile strength is mainly due to the rapid precipitation of very fine particles during consolidation but also due to high dislocation density and ultrafine grains. Ductility is most likely achieved due to coarse grains since they accumulate plastic deformation. However, the goal of using SPS was to achieve homogeneous and ultrafine microstructure. Systematically, abnormal grains appeared at high temperature despite of the rapid consolidation cycle.

One choose here to study the potential causes of this unexpectedly fast-acting abnormal growth. In the next chapter, a focus will be made on the physical metallurgy occurring during high-temperature consolidation in order to understand why the bimodal microstructure appears and is stable.

# Chapter 4

# Microstructure evolution during high-temperature consolidation

*In this chapter, one describes how the initial nanostructure evolves during non-isothermal high-temperature consolidation and subsequent heat-treating.*

*Related published article(s): [D], [E], [F].*

## Contents

# 4.1 Microstructure of consolidated ODS steels

*Related published article: [107].*

Despite of rapid consolidation of nanostructured powders, a bimodal microstructure is obtained. A special focus is made on the possible mechanisms governing the grain growth of the nanostructured powder.

## 4.1.1 Grain growth: competing pinning and driving pressures

The Gibbs free energy $G$ of a system composed of two grains A and B separated by a grain boundary is given by:

$$G = g_A V_A + g_B V_B + \gamma S \tag{4.1}$$

where $g_A$ and $g_B$ are the volume Gibbs free energy, $V_A$ and $V_B$ are the volume of the grain A and B, $\gamma$ the grain boundary energy and $S$ the grain boundary area. The driving pressure for grain growth is derived from the energy gradient through the grain boundary that can be written as:

$$P = -\frac{dG}{dV} = (g_B - g_A) + \gamma \frac{dS}{dV} = P_V + P_C \tag{4.2}$$

(i) The driving pressure for recrystallization due to the difference in stored energy between each side of a grain boundary can be written as:

$$P_V = \alpha \mu b^2 (\rho_B - \rho_A) \tag{4.3}$$

where $\alpha$ is a constant and $\mu$ is the shear modulus.

(ii) Assuming spherical grains, the capillary driving pressure for grain growth is described as:

$$P_C = \gamma \frac{dS}{dV} = \gamma \frac{8\pi R dR}{4\pi R^2 dR} = 2\frac{\gamma}{R} \tag{4.4}$$

where $R$ is the mean radius of the grain. Typical values of grain boundary energies are 0.2 J.m$^{-2}$ for low angle grain boundary and 0.5 J.mm$^{-2}$ for high angle grain boundary [147]. Calculations of this pressure are reported in 4.1, considering three types of grains: ultra-fine grains ($R_1 = 0.2\ \mu m$), micronic grains ($R_2 = 2\ \mu m$) and coarse grains ($R_3 = 20\ \mu m$). The dragging pressure impeding the grain growth is due to heterogeneities that consist of obstacles for solvent atom diffusion. They can be solute atoms that can either segregate at grain boundaries, or form second phase particles with full, partial or no coherency with the matrix.

(iii) The solute drag effect is due to solute atoms (impurities) that reduce grain boundary migration [148]. The lowered mobility $M'$ is dependent on the solute

concentration:

$$M' = \left( \frac{1}{M_{pure}} + \alpha_{drag} X_i \right)^{-1} \tag{4.5}$$

where $\alpha_{drag}$ is temperature-dependent and therefore defined by an activation energy, $X_i$ the solute concentration. For instance, Cram *et al* [149] evaluated the influence of tin content in pure copper and highlighted that the solute effect is considerable at low temperature but much less effective at higher temperature. In the current study, the solute effect was neglected due to the considered temperature range.

(iv) If solute diffusion is high enough and miscibility low enough to form second phase particles, the latter can induce a pinning effect, whose efficiency is related to their distribution [150]. The influence of this particles dispersion on grain boundary mobility can be modeled using a tough boundary [151]. The resulting pressure exerted by a particle distribution is then:

$$P_Z = \frac{3}{2} \gamma \frac{f_p}{r_p} \tag{4.6}$$

where $f_p$ and $r_p$ are the volume fraction and mean radius of the precipitates, respectively. The maximum size that a grain can reach is defined by an equilibrium state where driving pressure and pinning pressure are equal:

$$R_c = C \frac{r_p}{f_p} \tag{4.7}$$

where C is a constant depending upon the hypothesis [152]. Considering typical microstructural features that are described in the next section (grain size, dislocation density, precipitation state), the driving and dragging pressures for grain growth were calculated using equation (4.3), (4.4), (4.6) and reported in Table 4.1. Grain boundary energies are taken 0.2 J.m$^{-2}$ for ultrafine grains (UFG) and 0.5 J.m$^{-2}$ for coarse grains because UFG were found to be surrounded by low angle grain boundaries whereas coarse grains by high angle grain boundaries.

Deforming a metal generates a drastic change of properties due to the increased number of defects in the material that make it unstable. Dislocations have significant influence on the behavior of a deformed metal during subsequent annealing or thermo-mechanical treatment. Consequently, various methods to measure the stored energy have been used for the last decades. Dislocations density can be derived by calorimetry for some metals with well-known stacking fault energy [153, 154]. Yet, annealing behavior of a deformed metal does not only depend upon the overall stored energy but more importantly on its spatial distribution, especially in heterogeneous grain structure. On a local scale, inhomogeneity of stored energy will affect the onset of recrystallization, and larger scale heterogeneity will influence the growth of the new grains. Recently, EBSD technique has emerged as a powerful tool for determining an orientation map within a grain structure [155]. This permits to highlight

| CAPILLARY EFFECT (driving pressure) | | | | | |
|---|---|---|---|---|---|
| Experimental internal variables (inputs) | Grain radius $R$ ($\mu m$) | $5.10^{-2}$ | $2.10^{-1}$ | 2 | 20 |
| | Grain boundary energy $\gamma$ (J.m$^{-2}$) | 0.2 | 0.2 | 0.5 | 0.5 |
| Calculation output | **Capillary pressure $P_C$ [MPa]** | 8 | 2 | $5.10^{-1}$ | $1.10^{-2}$ |
| STORED ENERGY EFFECT (driving pressure) | | | | | |
| Experimental internal variables (inputs) | Variation of dislocation density $\Delta\rho$ (m$^{-2}$) | $10^{16}$ | $10^{15}$ | $10^{14}$ | $10^{13}$ |
| Calculation output | **Strain-induced pressure $P_V$ [MPa]** | 23 | 2.3 | $2.3.10^{-1}$ | $2.3.10^{-2}$ |
| PINNING EFFECT (retarding pressure) | | | | | |
| Experimental internal variables (inputs) | Precipitate radius $r$ ($nm$) | 2 | 20 | 200 | |
| | Volume fraction | 0.01 | 0.01 | 0.01 | |
| Calculation output | **Pinning pressure $P_Z$ [MPa]** | 8 | 2 | $5.10^{-1}$ | |

**Table 4.1:** Driving and pinning pressures governing grain growth. Calculations of $P_C$, $P_V$ and $P_Z$ are independent and performed using typical microstructural features measured on either as-milled powder or consolidated materials (SPS and HIP).

local metallurgical heterogeneities such as specific orientation gradient, for instance at phase boundaries in dual phase steels [155] or after mechanical testing on ODS Fe-9Cr alloys [156]. In the current study, the Kernel Average Misorientation (KAM) has been calculated from EBSD orientation maps. The KAM evaluates the mean misorientation of a pixel based on the comparison of the orientation of n layers of neighboring pixels that constitute a Kernel. Misorientations above a certain value – 2 or 5° are standard thresholds – are excluded in order to avoid the influence of grain boundaries. Only the first layer of neighboring pixels has been considered in this calculation. For each pixel $i$ surrounded by $n$ pixels, the KAM value is given by:

$$\theta_i^{KAM} = \frac{1}{n} \sum_{j=1}^{n} \Delta\theta_{ij} \qquad (4.8)$$

where $\Delta\theta_{ij}$ represents the misorientation between the pixels $i$ and $j$. Contrary to the global mean misorientation of a grain, which is defined by the mean misorientation between every pixel constituting the whole grain, the KAM does not depend on the grain size. Thus, this gives pertinent information for the study of local heterogeneity. The KAM can be related to the geometrically necessary dislocations density to accommodate plastic deformation using the equation [37,39,40]:

$$\rho_{GND} = \frac{2\theta_m^{kam}}{ub} \qquad (4.9)$$

where $\theta_m^{kam} = \sum_{i=1}^{P} \theta_i^{kam}$ is the average misorientation calculated by KAM in radians, $b = 0.248$ nm the Burgers vector in ferrite and $u$ the unit length defined by $u = na$ if $n$ is the number of neighbors layer and a the EBSD step size. In opposition to the KAM, the density of GND is assumed to be independent of the acquisition parameters.

## 4.1.2 Microstructure characterization

### 4.1.2.1 The as-milled powder

As microstructural and mechanical properties of compacts strongly depend upon the original nanostructure, it is of prime importance to characterize the initial grain structure before sintering. The as-atomized powder particles are spherical with an average diameter of 70 $\mu m$. After mechanical alloying, the particles are highly deformed, describing stratified cold-welded structure with an angular shape. In order to characterize the deformed microstructure, powder particles were milled by Focused Ion Beam (Fig. 4.1(c)) and characterized by EBSD using a SEM-FEG with resolution down to 10 nm.
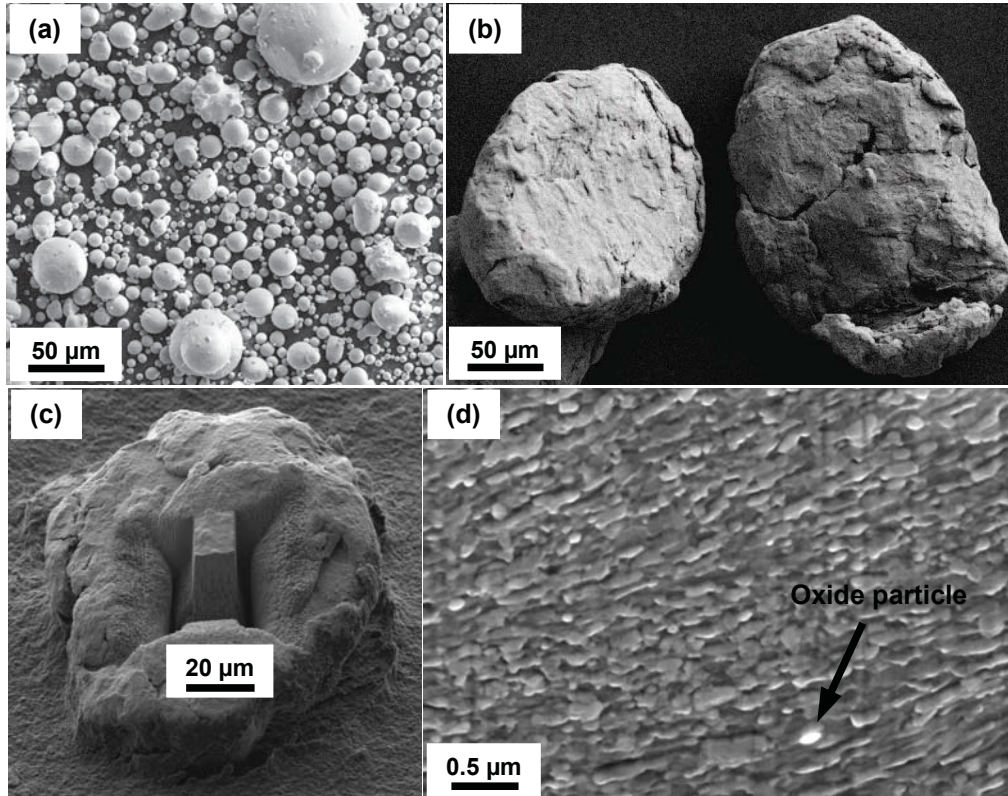


**Figure 4.1:** (a) Atomized Fe-14Cr powder, (b) Mechanically Alloyed powder, (c) powder particle milled by Focused Ion Beam (FIB) cross-sectioning, (d) corresponding SEM-FEG image of the nanosized grain structure.

74

Fig. 4.1(d) illustrates the nanostructure observed on a cross-section. A few particles enriched in yttrium and oxygen were scarcely dispersed in the powder. These phases are most likely remaining fragments of yttria particles that were introduced into the ferritic matrix during mechanical alloying but not fully dissolved into solid solution. The heterogeneous nanostructure is reported in Fig. 4.2(a), where black pixels correspond to the most cold-worked grains that could not be indexed. The grain size distribution is wide, with ultra-fine grains from 50 to 800 nm, defining a mean diameter of 250 nm.

### 4.1.2.2 Microstructure of consolidated samples

As temperature drastically influences grain growth, SPS cycles were performed at different soaking temperatures at a constant dwell time fixed at 5 min. The heating rate was 8.3 K/s (500 K/min). Fig. 4.2 illustrates the evolution of the microstructure as a function of SPS soaking temperature, then during further annealing.
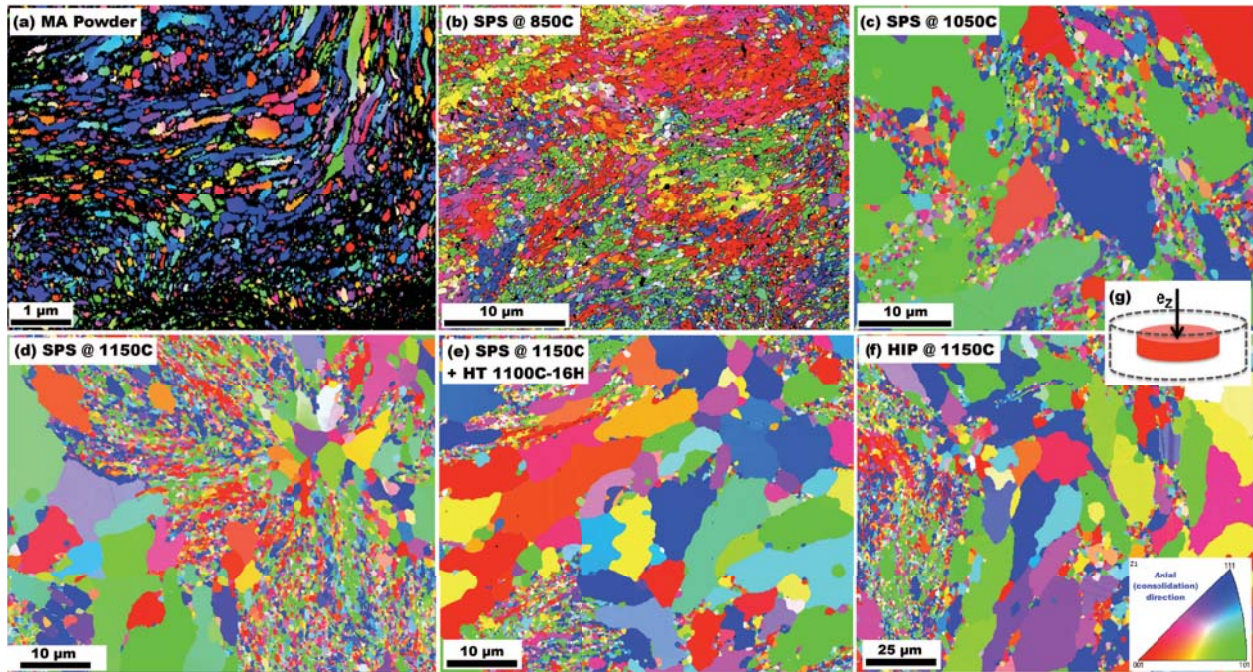


**Figure 4.2:** (a) EBSD maps of as-milled powder, (b) SPSed ODS at 850°C, (c) at 1050°C, (d) at 1150°C, (e) SPSed at 1150°C and heat-treated at 1100°C for 16 hours, (f) HIPed ODS at 1150°C – $\mathbf{e}_z$ is the axial direction during SPS/HIP consolidation.

Fig. 4.2(f) also describes the microstructure of the HIPed sample. The microstructure of the compact SPSed at 850 °C is composed of isotropic grains from 50 nm to around 1 $\mu$m for the largest ones, which is very close to what was observed on the as-milled powder. At this state, the structure is composed of ultra-fine grained zones where subgrains of same or close orientation are surrounded by low

angle grain boundaries (LAGB). Primary recrystallization may occur around this temperature.

When considering the grain structure of the sample SPSed at higher temperatures (T=1050-1150 °C), there is no evidence of large grains with equivalent orientation. Thus, the large recrystallized grains do not form from the substructured grains but more likely from new nuclei with random orientation. Moreover, ultrafine grains or substructured grains are very stable in size, although they represent a much lower volume fraction after high-temperature SPS processing. From 1050 °C, the grain size distribution drastically broadens, with the largest grains reaching an equivalent circle diameter of 20 to 25 $\mu$m (Fig. 4.3). This distribution is comparable
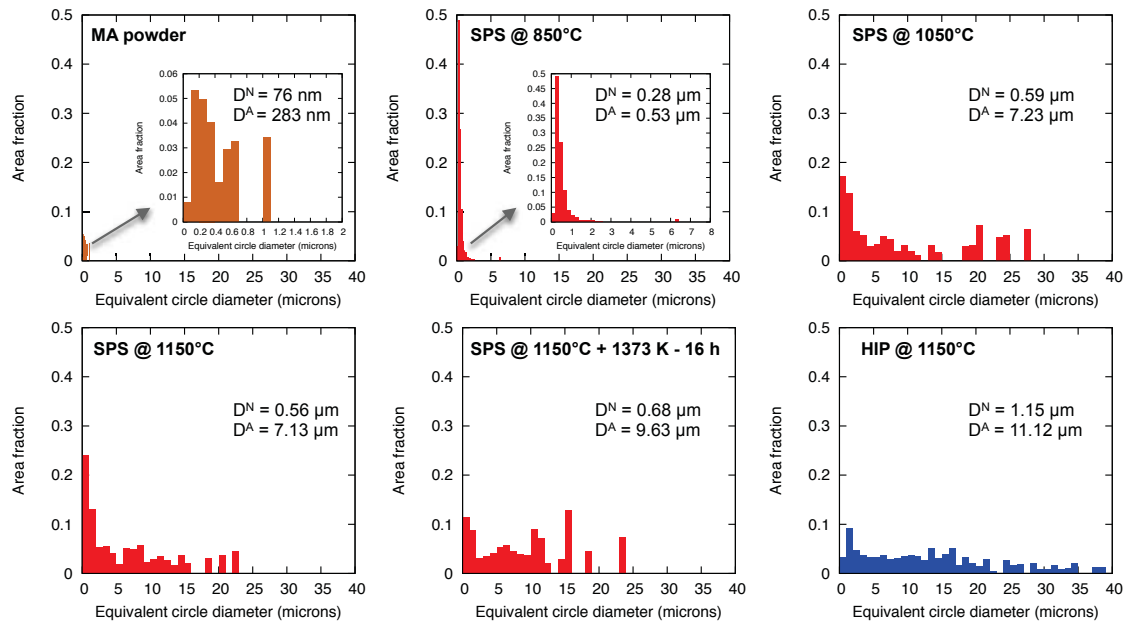


**Figure 4.3:** Grain size distribution in Area Fraction determined from the EBSD maps of (a) as-milled powder, (b) ODS steels SPSed at 850°C, (c) at 1050°C, (d) at 1150°C, (e) SPSed at 1150°C then annealed at 1100°C for 16 hours and (f) HIPed at 1100°C

to that of the SPSed compact processed at 1150 °C, showing a certain stability of the grain structure within the temperature range 1050-1150 °C, with no significant growth of the smallest grains that seem to be still stable at these temperatures. These results point out the reproducibility of such structure, which is necessary to justify when seeking good and repeatable mechanical properties. When looking at the sample SPSed at 1150 °C subsequently treated at 1100 °C (roughly equal to 0.8 times the solidus temperature for steels) for 16 hours, the grain size distribution indicates that (i) the smallest grains keep showing a strong resistance to coarsening (ii) the critical size of the largest grains does not increase whereas their volume fraction increases. These observations illustrate that pinning has an efficient effect on the whole grain structure. Finally, the HIPed material contains a higher volume fraction of coarse grains, demonstrating the benefit of short SPS treatments. As

mechanical alloying is well known to introduce huge amount of plastic work into the milled powder, one can expect a strong influence of the stored energy on the microstructural behavior during hot consolidation. This section describes how the Kernel Average Misorientation was used to characterize the spatial distribution of this stored energy and how it annihilated during hot processing. The linear relationship between KAM and dislocation density (see Eq. 4.8) allows a direct comparison between deformation levels within the same EBSD map. Thus, the evolution of the stored energy was measured on different metallurgical states depending upon the consolidation temperature, which is reported in Fig. 4.4. First of all, the MA powder contains various levels of plastic deformation. Some grains are poorly deformed whereas the major part of the nanosized grains underwent drastic cold work, which are the unindexed grains (black areas). The kinetics study clearly shows that some grains are already recovered at 850 °C whereas some others are still deformed.
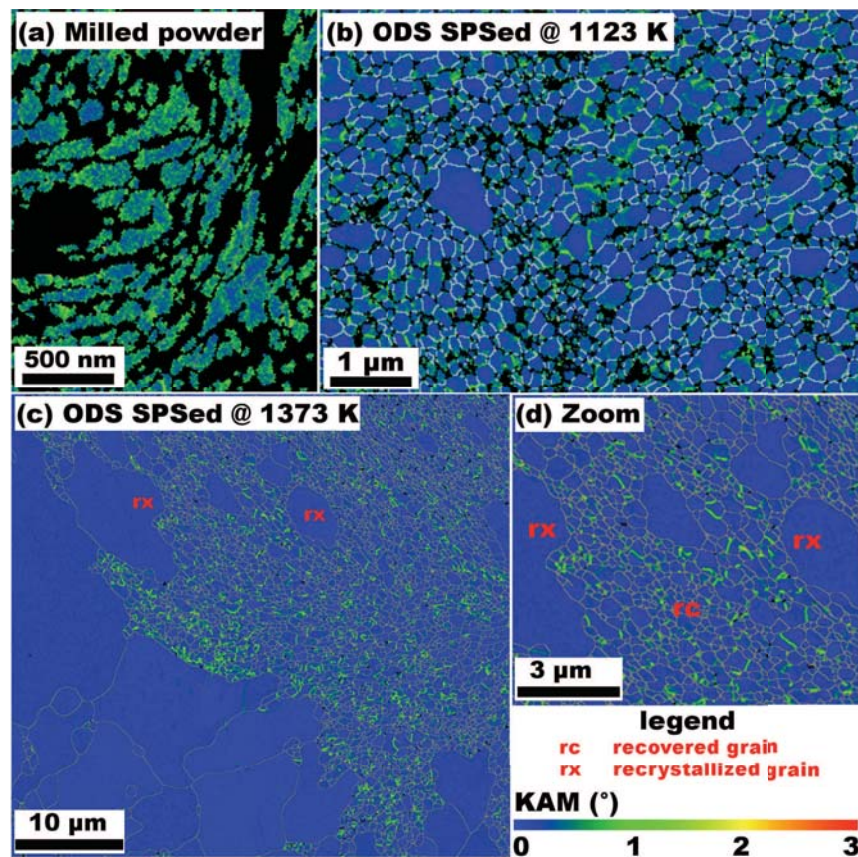


**Figure 4.4:** Evolution of local intragranular misorientation from (a) milled powder to (b) ODS processed by SPS at 850°C and (c-d) at 1100°C. Unindexed black areas and green dots highlight the local concentration of plastic deformation. Blue grains are completely recrystallized. (c-d) illustrate the evidence of entire recovery in small grains around large recrystallized grains, lowering the difference in stored energy.

Above 1100 °C, the large recrystallized grains show very limited local misorientation. The major part of the local misorientation is contained in ultrafine-grained
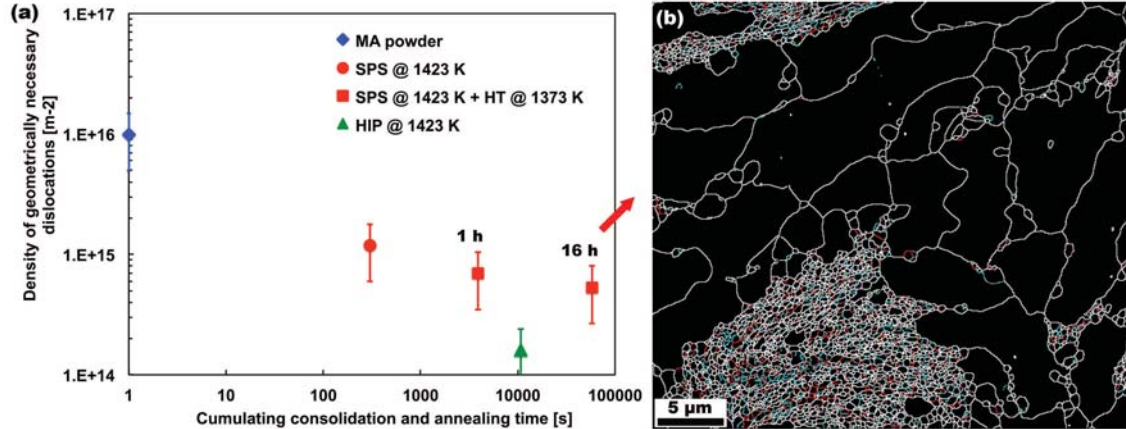
**Figure 4.5:** (a) Dislocations density according the cumulated processing time at 1150°C and annealing time at 1100°C. Error bars correspond to the deviation between measurements on two samples. (b) Map of grain boundaries measured by EBSD [blue : 2 to 6° ; red : 6 to 10° ; white : over 10°] on a sample SPSed at 1423 K then annealed at 1100°C for 16 hours.

zones with low angle grain boundaries. The geometrically necessary dislocations density (GND) was derived for each microstructure from the whole KAM distribution, as shown in Fig. 4.5(a). GND drops from $10^{16}$ m$^{-2}$ for the as-milled powder to $10^{15}$ m$^{-2}$ for the ODS SPSed at 1150°C. This decrease of only one order of magnitude is expected to be due to dislocations recovery. GND logically decreases with consolidation temperature. The comparison between SPS and HIP shows higher volume fraction of recrystallized grains, which highlights the effect of heating rate during consolidation. This kinetic effect is exacerbated in SPS consolidation because very fast heating induces partial appearance of thermally activated phenomena, such as recovery mechanisms. Thus, a plateau value of $(5 \pm 2)\ 10^{14}$ m$^{-2}$ is reached on a SPSed compact annealed at 1100°C for 16 hours, versus $1.4 \times 10^{14}$ ($\pm\ 5\times10^{13}$) m$^{-2}$ for the HIPed materials. Competing recovery and recrystallization of the grain structure play a role on this reduction. Large recrystallized grains have low dislocation density when ultra-fine grains contain non-negligible amount of stored energy [157]. These areas are defined by a network of low angle grain boundaries (LAGB). The stability of such subgrain boundaries has been assessed with a heat treatment at 1100 °C for 16 hours. The extreme stability of the grain structure is highlighted in Fig. 4.5(b).

One can notice the network of LAGB within the ultrafine grains when large grains are uniquely separated by high-angle grain boundaries (HAGB).

## 4.1.3 Precipitation

Analyses by SEM-FEG for coarse oxides and by small angle neutron scattering for nanosized precipitates were carried out. The precipitation state is composed of at least two types of particles.

(a) Ti-enriched oxides from 50 to 250 nm in diameter were observed in both the SPSed and HIPed materials at grain boundaries but mainly in the largest grains (Fig. 4.6). Electron microprobe analysis showed Ti-O enriched lines, the major part of which had no yttrium content. The typical distance between precipitates lines is 10 to 70 $\mu$m, which corresponds to the size range of MA powder particles. This emphasizes the influence of topology in powder metallurgical microstructure, especially coarse precipitation [158]. This was confirmed by Sakasegawa *et al* from TEM replicas on an ODS steel of composition Fe-14Cr-1.0Ti-0.25Y$_2$O$_3$ (in wt%) [159]. Other coarse oxides of more than 50 nm in diameter were also found by de Castro *et al*: Al-Y-O, Cr$_2$O$_3$ and Y-Cr-V-O [160]. These coarser particles may have two consequences: (i) the decrease of titanium and oxygen contents available for nanoparticles precipitation, therefore the decrease in volume fraction of nanosized oxides (ii) a potential pinning effect depending upon the size and number density of the coarse particles, which will be discussed in the next section.
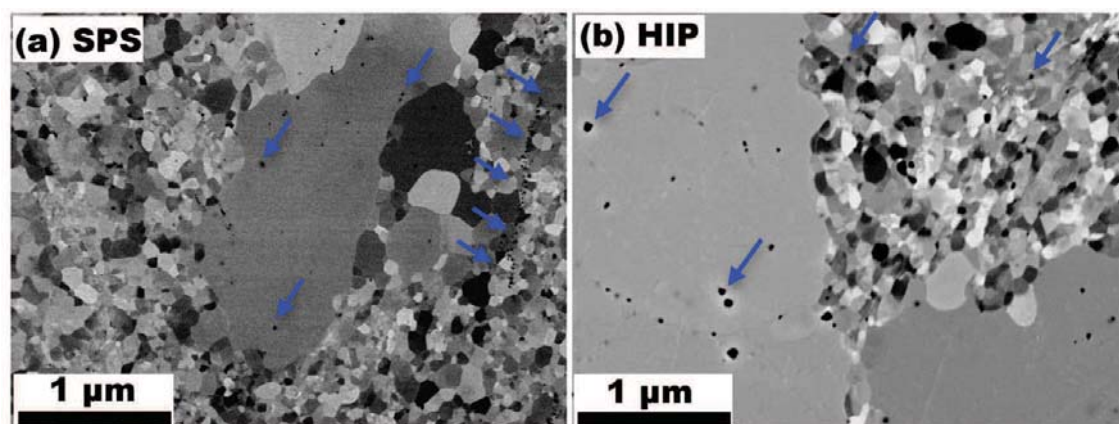


**Figure 4.6:** SEM-FEG images (BSE mode) of ODS steels (a) SPSed at 1150 °C and (b) HIPed at 1150 °C. This reveals coarse oxides (black dots) within the micronic grains.

(b) Nanoparticles, having a mean diameter of 3.2 nm, were detected by small-angle neutron scattering (Fig. 4.7(a)).

They were also measured in HIPed materials, as reported in Table 4.2. This highlights the importance of adding titanium to refine the distribution, as demonstrated by Ukai and confirmed by Ratti [39, 96]. Furthermore, although a slight decrease in number density is observed with increased processing time, the mean volume fraction of detected nanoparticles is constant and equal to 1%. The volume fraction for SPSed ODS at 1323 K and 1423 K for 5 min is overestimated, as the theoretical maximum volume fraction of Y$_2$Ti$_2$O$_7$ would be 0.9%. Local enrichment in oxygen, iron or chromium could explain higher volume fraction detected by SANS [161]. In this sense, atom-probe tomography would be necessary to quantify the composition of the nanoparticles.

The scattering A-ratio (see Eq. 5.3) measured in SPSed and HIPed ODS steels was constant and equal to 2.3. This value is fairly consistent with Y-Ti-O complex
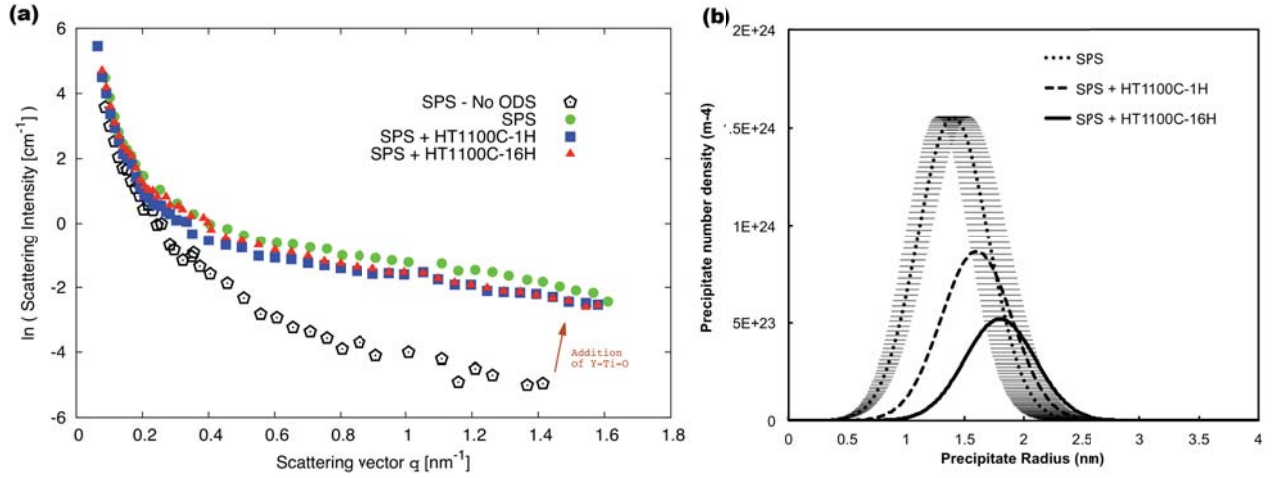
**Figure 4.7:** (a) Magnetic scattering intensity measured by Small Angle Neutron Scattering on samples SPSed at 1150°C and then annealed at 1100°C and (b) the corresponding nano-oxides distribution in number density. Horizontal errors bars in (b) take into account the uncertainty of 10% in $r_m$ due to direct fitting.

nanoparticles. For instance, in a ferritic steel hot isostatically pressed at 1423 K (1150°C), Alinger *et al* determined a ratio of 2.04 and 2.60 for $Y_2Ti_2O_7$ and $Y_2Ti0_5$, respectively [161]. The value of *A* depends on the atomic volume, thus on the crystallographic structure. The latter was assumed to be of pyrochlore type, as refered in [137]. Various studies by transmission electron microscopy [159, 160, 96, 162, 163, 58], atom-probe tomography [164] or small-angle neutron scattering [161, 165] report at least two kinds of nano-particles: - Complex Fe-Cr-Y-Ti-O non-stoichiometric nanoclusters ($d \approx 2\,nm$) that are fully coherent within the bcc matrix - Nanosized oxides ($d \approx 5-15\,nm$), mainly having a pyrocholoric structure composed of $Y_2Ti_2O_7$ even if $Y_2Ti0_5$ have been observed as well [166]. We will discuss in more details the precipitation behavior in chapter 5.

| Consolidation parameters | Annealing | $r_p$ [nm] | $\sigma$ [nm] | $f_p$ [%] | A-ratio |
|---|---|---|---|---|---|
| | / | 1.4 | 0.3 | $1.54 \pm 0.4$ | 2.3 |
| SPS 1150°C - 5 min | 1100°C - 1 h | 1.6 | 0.3 | $1.03 \pm 0.2$ | 2.3 |
| | 1100°C - 16 h | 1.8 | 0.3 | $1.03 \pm 0.2$ | 2.3 |
| | / | 1.4 | 0.2 | $1.14 \pm 0.2$ | 2.3 |
| HIP 1150°C - 3 h | 1100°C - 1 h | 1.6 | 0.3 | $1.03 \pm 0.2$ | 2.3 |
| | 1100°C - 16 h | 1.6 | 0.4 | $1.14 \pm 0.2$ | 2.3 |

**Table 4.2:** Nano-particles detected by Small Angle Neutron Scattering (SANS).

### 4.1.4    Discussion on abnormal grain growth

Grain growth and precipitation are strongly linked in complex systems such as ODS steels. Appearance of heterogeneous grain structure, as described in this current study, has been often reported. Second phase particles are known to strongly pin either grains or subgrains. Although numerous on-going studies clearly report the extreme stability of the oxides with less than 10 nm in diameter, other larger particles were found in the sintered materials. The composition of these "coarse" oxides has a high content in titanium and oxygen. Such coarse precipitation, mainly at grain boundaries, is most likely due to:

(i) initial chemical inhomogeneity within the as-milled powder particles. Even nowadays high-energy milling is known to be efficient enough to produce homogeneous ODS powder, one should keep in mind that a perfect solid solution of several kilograms in batch production is difficult to achieve. Besides, the oxygen content has been reported by C. Williams *et al* to come from contamination during consolidation, rather than from the yttria powder itself. They introduced either $FeY_2$ or $Y2O_3$ with no relevant change in oxygen content in the consolidated materials [164].

(ii) A large gap between titanium and oxygen diffusion coefficients with respect to that of other solutes, such as yttrium, and tungsten. Due to their size, these large particles most likely have a weak pinning effect (see Table 4.1). Thus, grain boundaries may surround these particles with no drastic change in their mobility. This is why they are mainly localized in large grains. Using the same criteria, one can explain the extreme stability of UFGs pinned by nanosized particles. The latter have been observed to delay the onset of recrystallization of mechanically alloyed iron-base and nickel-base alloys [167]. Bhadeshia suggested that triple junction pinning might stabilize these alloys. In addition to basic pinning due to geometrical interaction between grain boundary and particles, an effect of topology was emphasized.

The grain structure of SPSed ODS steels may be explained by the following scenario: (a) The initial nanostructure contains highly deformed ultra-fine grained zones. The stored energy due to plastic work is considerable and somehow inhomogeneous in a powder particle. Thus, the driving pressure for recrystallization is significant (above 20 MPa, see Table 2). Heterogeneous, competing recovery and recrystallization occur when heating the material. At moderate temperatures during SPS/HIP consolidation (T<850°C), substructures may be annealed to form dislocation-free subgrains. Stored energy of recovered cells, consequently the driving pressure for grain boundary mobility, are sharply decreased (Fig. 4.8). This induces exceptional stability of ultra-fine grains. Simultaneously, new grains nucleate on favorable sites such as plastically strained zones. Since there is a significant difference in stored energy between clean nuclei and their deformed and unrecovered neighbors, grain boundaries of recrystallized grains are highly mobile, which favors their growth at the expense of the deformed ones. This mechanism can be much quicker than dislocation recovery. Moreover, temperature gradient effects may enhance this discontinuous evolution. Grains located at the powder particle upper shell have a

81
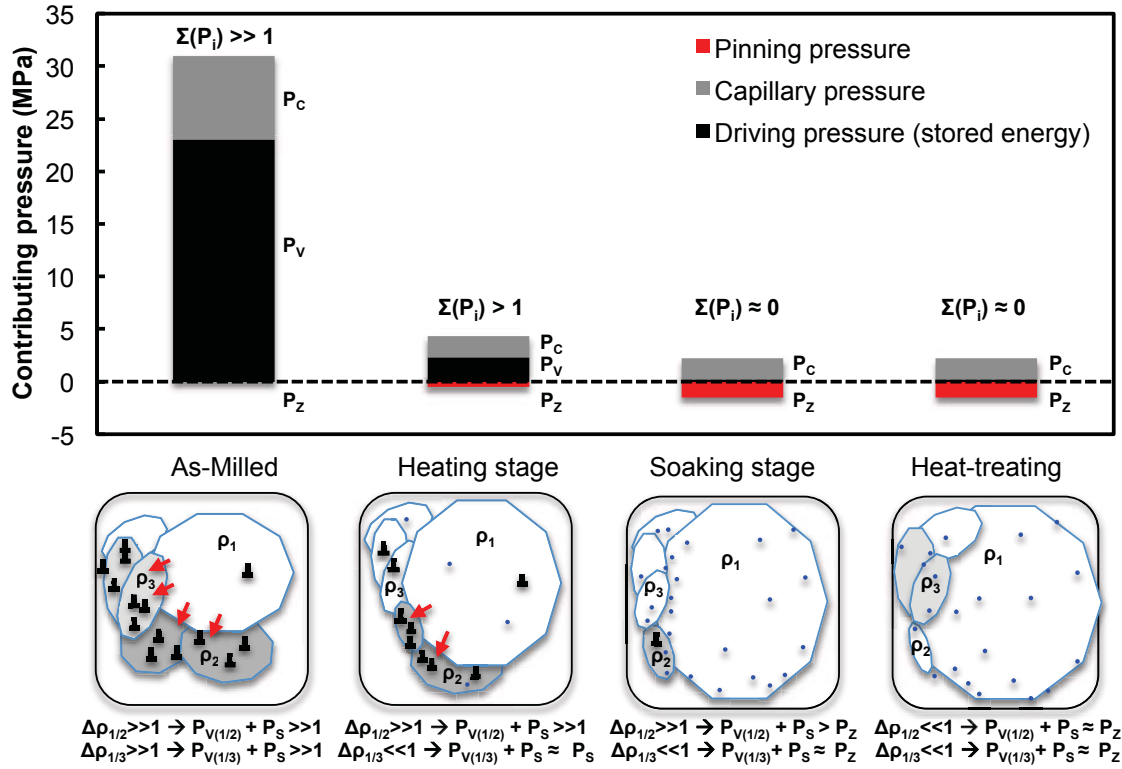
**Figure 4.8:** Evolution of the contributing mechanisms to grain growth along the processing route. Pressures are calculated according the measured microstructural features, as recalled in Table 4.1. Pinning pressure is taken negative due to its competition with the driving pressures. Interactions between grains (1/2 and 2/3) are described along the process. Nano-oxides are represented by blue dots.

higher probability to recrystallize, as local temperature gradients can be generated by reactive heating at free surfaces in the SPS furnace. Indeed, Ji et al argued that this effect could be responsible for the onset of recrystallization within a Fe-Al alloy [84]. Yet, the current study demonstrates that the hypothetic SPS heating effect must be moderate because the heterogeneous recrystallization was observed on HIPed materials as well.

(b) At higher temperature (T=850-1150°C), precipitation occurs. Grain boundaries and dislocations are favorable sites for nucleation [168, 169, 170]. De Castro *et al* [160] observed heterogeneously distributed unrecovered zones where dislocations and nano-particles were numerous. The number density of nano-oxides is high enough to induce precipitation in the bulk as well. Both UFG and large grains contain nanoparticles. Oxides pinning effect is efficient enough to annihilate the subgrain mobility in UFG. Thus, the subgrain growth mechanism inducing large grains is excluded [171]. In this study, pinning pressure was not decreased due to limited coarsening of nanoparticles (see Table 4.1), as observed by others [160]. Indeed, thermal stability of nanoparticles can be extreme in ODS steels, as they do

not coarse at temperatures up to $0.8T_s$, with $T_s$ being the solidus temperature of the alloy. The mean diameter of the nanoparticles was 3.2 nm after annealing of the SPSed materials at 1100°C for 16 hours. Such stability can be explained by a full lattice coherency between the ferritic bcc matrix and nanoparticles that decreases the interface energy and consequently boosts the oxides' stability [137, 172]. Coarse particles (d>50 nm) were also observed, but their contribution to pinning is much lower. Once precipitation has occurred, one can expect the capillary driving pressure and the pinning pressure to compete with each other. If considering the pinning effect induced by the nanoparticles with a volume fraction of 1%, the pressure is high enough (3.8 MPa, see Table 4.1) to impede grain growth (Fig. 4.8).

However, a quantitative study of grain boundary mobility in ODS steels is still lacking. Measurement of grain boundary mobility can be done by determining the velocity of boundaries in a well-known system with constant driving pressure for grain growth [147]. This kind of data is difficult to obtain in mechanically alloyed industrial steels where driving pressure is unlikely a constant.

### 4.1.4.1 Conclusions

A mechanically alloyed ferritic ODS steel was consolidated by SPS and HIP. A multi-scale characterization was performed after consolidation and subsequent heat-treating, providing substantial insight on the grain growth mechanisms.

The resulting grain structure was observed to be heterogeneous with both ultra-fine grains and much larger grains. Appearance of this structure was explained by the initial heterogeneous spatial distribution of stored energy due to high-energy attrition of the MA powder, which induced inhomogeneous recrystallization of the grains. The local driving pressure is so high that new nuclei rapidly grow at the expense of the deformed ones. Until recovery has been completed, recrystallized grains are highly mobile even if precipitation has started. Thus, plastic work due to milling is the cause of the so-called abnormal growth. Consequently, this scenario could be applied to any metallic materials that have been deformed in a heterogeneous manner, particularly by high-energy milling.

Only completed recovery and precipitation are able to impede grain growth. Once the stored energy has been lowered, the dense dispersion of nano-particles is effective to pin grain boundaries. The strong resistance to coarsening of the nano-oxides formed during consolidation justifies the extreme thermal stability of the ultra-fine grains. Calculations of critical grain size due to pinning effect from Zener and Rios give rise to a range of grain mean radii between 40 nm and 270 nm, respectively (see Table 4.1). This corresponds to the size range of remaining ultra-fine grains.

Precipitation is not the major cause of abnormal growth but is responsible for thermal stability of heterogeneous fine structure. This highlights the importance of precipitation that not only brings effective Orowan strengthening but also is a key-factor for the stability of the UFG that enhances Hall-Petch hardening. Further

work will be focusing on in-situ studies of microstructural instabilities of such milled powder to quantify the kinetics of recovery and recrystallization with respect to precipitation in order to be able to manage the grain structure during consolidation.

## 4.2 Kinetic study using *in situ* synchrotron X-Ray diffraction

*Related published article: [D].* This work was performed with N. Sallez.

### 4.2.1 On the need of an *in situ* characterization

Abnormal grains are frequently reported in ODS steels and related to Zener pinning due to nanoparticles, often extended to corner pinning on multiple junctions [173, 174, 175, 176]. Appearance of abnormal grains is a key-issue that does not only affect ODS materials but largely influences the properties of nanostructured metallic materials. Indeed, tailoring the nanosized-to-coarse-grains ratio is a way to achieve a good compromise between mechanical strength and uniform tensile elongation [108, 115, 177]. Yet, the microstructural instabilities occurring during hot processing of industrial nanostructured metallic materials such recovery, recrystallization and grain growth remain partially explored since they can be concomitant and are tough to quantify in a time-resolved manner. For powder metallurgical alloys, kinetic studies of the phenomenon leading to this abnormal microstructure while starting from the as-milled powder are essential. This requires to be able to perform in situ characterization of the physical parameters that can give insight of both the consumed energy and the microstructural changes occurring during hot processing. X-Ray Diffraction (XRD) can be very accurate to describe the dislocation structure for highly deformed material and ultrafine grains [178, 179, 180]. Well resolved phase detection can be also achieved, even with low phase fraction in the case of precipitation in steels [181, 182]. For kinetic studies, combining synchrotron X-Ray diffraction for high resolution diffraction peaks analysis with very fast acquisition brought considerable advances in microstructural transformations of metallic materials. For instance, recrystallization kinetics of cold rolled aluminum alloys was quantified by Lauridsen et al [183] and phase transformation kinetics in titanium alloys was successfully determined by Malinov et al [184].

So far, no time-resolved study of recovery, recrystallization and further grain growth upon heating of a nanostructured ODS steel has been reported. From an engineering point of view, the temperature at which abnormal grains appear is a key factor for optimizing the consolidation process. Besides, the growth behavior of abnormal grains with respect to that of the ultrafine grains is a part of physical metallurgy that needs to be better investigated. In this work, an in situ X-ray diffraction acquisition was used to determine the kinetics of microstructural mechanisms within a milled powder. One reports the general annealing behavior at low temperatures

responsible for the first growth stage of the deformed nanostructure. The occurrence of heterogeneous recrystallization is then described, resulting in two different growth behaviors depending upon the grain size. The evolution of ultra-fine grains and coarser recrystallized grains during heating is thus specifically discussed. In addition, complementary field-emission scanning electron microscopy (SEM-FEG) at mesoscopic scale was used to reveal grain size in the annealed structures.

## 4.2.2 Synchrotron X-Ray diffraction

### 4.2.2.1 Experimental set-up: 2D detection and *in situ* study

Various XRD experiments have shown the benefits of the synchrotron source to study recrystallization kinetics [183, 185]. This study, based on line profile analysis of in situ acquired high resolution XRD peaks, was performed at the DIFFABS beamline of the synchrotron SOLEIL. Incident energy of photons was selected to 19 keV, which corresponds to a wavelength of 0.653 Å. This energy allows optimizing the penetration depth, the number of available peaks and peak width, each of these values being essential for the precision of the results. At this energy, the penetration depth of the beam into the powder was around 25 $\mu$m for the (211) planes. 11 X-ray peaks can be detected in a $2\theta$ range from 15 to 67°. Samples were tilted to 15° with respect to the axis parallel to the incident beam in order to minimize the geometrical spread of the beam onto the powder. Given these parameters, the 4 most intense diffraction peaks (110), (200), (211), (220), were located in a $2\theta$ range at 18.5°, 26.3°, 32.3° and 37.5°, respectively. In-situ X-ray diffractograms of these 4 peaks were recorded independently by a last generation 2D detector XPAD S140 composed of chips containing $120 \times 80$ pixels with 130 mm $\times$ 130 mm dimensions. The resulting 1D diffractograms were obtained from a radial $2\theta$-range of 7° and an azimuthal $\psi$-range of 6°. Each peak was detected in a single detection sequence, leading to 4 different detection phases in order to center the $2\theta$-domain around each peak center position. Acquisition time was chosen at 2 s/peak, leading to a good statistics (peak intensity of more than 1 million of counted photons, giving a signal to noise ratio of more than 500 for the silicon reference sample ; for the ODS samples the maximum intensity over background ratio was 85). Taking into account the XPAD displacement time from a peak position to the next and the acquisition time of the four peaks took 15 s with 10 additional seconds for returning to the initial position. The 2D diffraction rings were then integrated over the whole $\psi$ range for a classic measurement and over specific $\psi$ range to separate ultra-fine grain and coarse grain signal when abnormal microstructure was obtained. This step was carefully performed by customized routines in order to eliminate reconstruction artifacts that can arise during evaluation [186].

Using a furnace dedicated to powder heating, anisothermal treatments from room temperature up to five different soaking temperatures (T = 600°C; 800°C; 850°C; 900°C; 1100°C) were performed under vacuum. The heating rate was chosen low
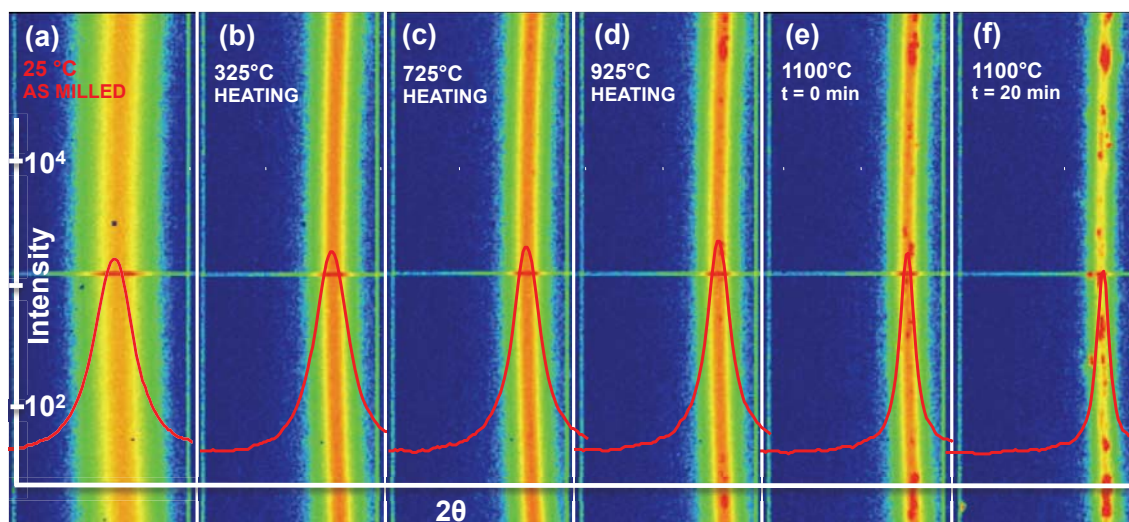
**Figure 4.9:** Evolution of 2D diffraction ring corresponding to the peak (211), from (a) as milled powder to various annealed states (b-f) upon heating up to 1423 K (1100°C). The converted plot I(2θ) is also reported upon heating.

enough (30°C/min) to ensure that the acquisition time induced temperature shift is only few degrees. The powder was put onto a boron nitride sample holder that was heated by direct contact with a resistor. This experimental set-up was mounted on a rotating board that allowed the rotation around the axis perpendicular to the incident photon flux. A transparent Kapton window ensured the transmission of incident and scattered photons. A vacuum system allowed to rapidly obtain a secondary vacuum of around $3.10^{-7}$ mbar within the furnace chamber. Thus, considering a heating rate of 0.5°C/s (30°C/min), the temperature variation during a diffractogram acquisition (4 peaks - 15 s) upon heating was less than 10°C. Consequently, the whole diffractogram was approximated as being isothermal. Since diffractograms were measured every 25 s, the effective temperature can be estimated with an error of 13°C.

### 4.2.2.2 Data analysis: from diffraction theory to metallurgical studies

XRD analyses have historically played a very important role in the study of heavily deformed materials. During the 1930s, it was thought that heavily deformed materials would produce amorphous diffraction patterns due to the high lattice distortion. Yet, the first diffraction experiments on highly plastically deformed materials revealed that the matter was still ordered: the diffraction peaks were drastically broadened but still well defined. Following this discovery, the Williamson-Hall (W-H) and Warren-Averbach (W-A) methods, both developed in the 1950s [187, 188] made possible to separate crystallite size and lattice strain, which both contribute to peak broadening. The methods have been continuously improved over the years [189, 190, 191]. More recently, a new step was achieved [178] by taking into account

86

the contrast factors of dislocations (see Table 4.3) which depend on the elastic constants of the studied material and on the relative orientations between the line and Burgers vectors of the dislocation and the diffraction vector [192]. This led to the so called modified Williamson-Hall and modified Warren-Averbach methods.

**Table 4.3:** Average calculated contrast factors for mixed (50/50) screw and edge dislocations [192]

| Reticular plan | 110 | 200 | 211 | 220 |
|---|---|---|---|---|
| Contrast factor $\bar{C}$ | 0.141 | 0.2839 | 0.141 | 0.141 |

### 4.2.2.3 Coupling the modified Williamson-Hall and Warren-Averbach methods

- modified Williamson-Hall method (mWH)

The Williamson-Hall method requires the knowledge of the physical broadening due to microstructural evolution for each peak. In order to obtain this, the instrumental contribution was measured with a reference silicon powder mounted on a zero background sample holder. It was found that instrumental broadening follows a Caglioti function that was then fitted by a parabolic function [193]. The Full Width at Half Maximum (FWHM) of the physical profile was obtained using the following equation (see [194, pp. 94-126]):

$$\beta_{raw}^2 = \beta_{ODS}\beta_{raw} + \beta_{inst}^2 \qquad (4.10)$$

where $\beta_{raw}$, $\beta_{ODS}$ and $\beta_{inst}$ are the FWHM of the raw measured profile, the physical profile of the ODS and that of the instrument, respectively. Diffraction peaks were fitted by pseudo-Voigt functions that are defined by a convolution between Gaussian and Lorentzian functions. This function fits particularly well the diffraction pattern as the Lorentzian profile describes the grain size contribution to broadening whereas the Gaussian profile describes the strain contribution.

Since the initial mWH equation developped by Ungàr & Borbély [178], numerous evolutions of this equation have been introduced [179, 195, 196, 197, 185]. In order to compare our results with similar materials we have chosen to describe the peak broadening with the following form [185]:

$$\beta_{ODS} \approx 0.9/D + (\frac{\pi M^2 b^2}{2})\rho^{1/2}(K^2\bar{C}) \pm O(K^4\bar{C}^2) \qquad (4.11)$$

where $K$ is the scattering vector defined by $K = \frac{2\pi sin(\theta)}{\lambda}$, $D$ is the crystallite size, $M$ is a dimensionless parameter linked to the dislocation density $\rho$ and the outer cut-off radius $R_e$ by $M = R_e\sqrt{\rho}$, $b$ is the Burgers vector magnitude and $\bar{C}$ the contrast factor (see Table 4.3). Compared to the original quadratic formula found in earlier literature [179] dislocation density will be maximized has there is a 1/2 exponent

difference between the two forms. $M$ is sensitive to the dislocations arrangement within the material [178]. Its evolution can be summarized as following:

- $M > 1$ indicates that dislocations are numerous and randomly distributed to form a screening strain field.

- $M \leq 1$ indicates that remaining dislocations are mostly entangled into low-angle grain boundaries (well defined (sub)grain boundaries).

  - modified Warren-Averbach method (mWA)

The mWH method relies only on the FWHM of the peaks. To obtain more accurate results, the modified Warren-Averbach (mWA) method, based on the asymptotic behaviour of the Fourier transform of the peak profile, was also applied. This permitted to obtain information on more parameters, for example the evolution of the effective outer cut-off radius $R_e$ upon heating. In this case, the instrumental contribution was corrected by dividing the Fourier coefficients of the total diffraction profile $A_n^{raw}$ by instrumental Fourier coefficients $A_n^{inst}$:

$$A_n^{ODS} = \frac{A_n^{raw}}{A_n^{instr}}$$

Instrumental coefficients were calculated by an interpolation of the neighbour silicon peak coefficients weighted by their respective $\theta$ distance to the ODS peak according to the Cagliotti formula. According to Warren [187, 198], the Fourier coeffcients are products of size and distortion coefficients:

$$A_{ODS}(L) = A^S(L) \times A^D(L) \tag{4.12}$$

Finally, the modified Warren–Averbach equation is [178, 199]:

$$\ln(A_n(L)) = \ln(A^S(L)) - \frac{\pi}{2}\rho b^2 L^2 \ln(\frac{R_e}{L})(K^2 \bar{C}) + \frac{\pi^2}{4} Q b^2 L^4 \ln(\frac{R_1}{L})\ln(\frac{R_2}{L})(K^2 \bar{C})^2 \tag{4.13}$$

where L is the Fourier length defined as $L = n \times a_3$, $a_3 = \lambda/[2(sintheta_2 - sintheta_1)]$, $n$ are positive integers, $\lambda$ is the wavelength of X-rays and $(theta_2 - theta_1)$ is the angular range of the measured peak. $Q$ is directly related to the fluctuation of the dislocation density [190, 195]. The quadratic part of this equation is important when studying monocrystals or large grained polycrystals [178]. For the present situation of an ultrafine grained material, this term was neglected [179]. A step size $L = 3$ nm was then used to fit the remaining part of the equation by an affine function to extract $\ln(A^S(L))$ and $\ln(A^D(L))$ at each L value. $R_e$ and $\rho$ were obtained by fitting the values obtained as the slope of the fitted segment. This method is only valid for small L (where atoms will only be affected by the stress field of one dislocation). For larger L, the result is affected by the contribution of other dislocations. $\ln(A^S(L))$ is used to determine the crystallite size $D$ as follows:

$$\left. \frac{dA^S(L)}{dL} \right|_{L \to 0} = -\frac{1}{D} \tag{4.14}$$

- Coupling modified Warren-Averbach and modified Williamson-Hall methods (mWA-mWH)
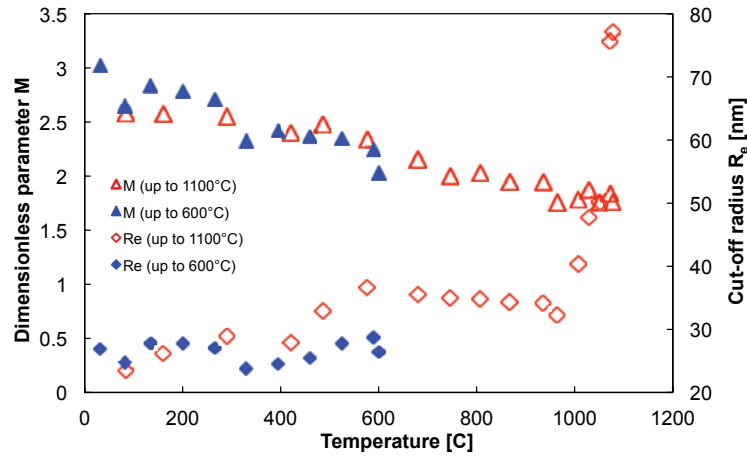


**Figure 4.10:** Outer cut-off radius $R_e(t)$ and dimensionless parameter $M = \sqrt{\rho(t)}R_e(t)$ determined by the modified Warren-Averbach method upon heating up to 600°C (blue) and 1100°C (red).

During high temperature annealing the peaks became so narrow that mWA method is no more applicable (the physical peaks are only slightly broader than the instrumental). However, in order to follow the kinetic of microstructural evolution at even higher temperatures, we have used the mWH method since the FWHM parameter could still be evaluated with enough accuracy. Despite of less accurate dislocation density data the method is still efficient and delivers meaningful qualitative results. Equation (4.11) contains, however, the unknown Wilkens parameter $M$ impeding a straightforward evaluation. From the mWA analysis performed on large enough peaks, it is clearly visible that $M$ evolves upon annealing. Indeed, as its value decreases upon heating (from 2.6 to 1.7, see Fig. 4.10), it was therefore relevant to take into consideration its evolution which accounts for the dislocation rearrangement. Nevertheless, it seems impossible to impose $M$ for estimating $\rho$ (see equation (4.11)) since by definition $M(t) = R_e(t) \times \sqrt{\rho(t)}$. It would therefore necessarily impose two different values of $\rho$ within the same equation. Therefore, we propose to take into account the physics of the dislocation rearrangement directly by the cut-off radius $R_e$ at each time step. In order to achieve this, the modified Williamson-Hall method (see Eq. (4.13)) was adjusted by coupling with the evolution of $Re(t)$ upon annealing, as follows:

$$\beta_{ODS}(t) \approx 0.9/D(t) + \frac{\pi}{2}R_e^2(t)b^2\rho^{3/2}(t)K^2\bar{C} \pm O(K^4\bar{C}^2) \tag{4.15}$$

This modification leads to the coupled mWA-mWH method which takes into account the physics of dislocations rearrangement upon heating and leads to more accurate results than the classical modified Williamson-Hall method. $R_e(t)$ is no longer a fitting parameter but is measured by the modified Warren-Averbach method. The metallurgical parameters reported in the next section are based on these calculations. Especially, the coupled mWA-mWH method was applied to in situ diffraction patterns acquired during several non-isothermal treatments from room temperature to 600°C and 1100°C. For comparison, the crystallite size and dislocation density calculated at particular points from the single modified Warren-Averbach method are also reported.

During analysis, one assumes that dislocations are responsible for the entire lattice distortion, therefore neglecting any chemical fluctuation or residual stress. When the texture is too pronounced, dislocations occupy particular slip planes and the average contrast factor cannot be used anymore [179]. Hopefully no global texture is expected on ODS ferritic steel powders and crystallites were also assumed to be isotropic [200]. In the as-milled state, dislocations are supposed to be mostly concentrated on the $\{1\bar{1}0\}\langle111\rangle$ dense slip systems. They were assumed to have balanced distribution of edge and screw types [201], which is very likely in the as-milled powder but much more questionable for annealed samples [157].

### 4.2.2.4 Growth of coarse grains : measurement method

Concomitant measurement of the kinetics of both ultrafine grains and coarse grains is difficult to achieve since this requires getting access to the spatial distribution of grains at every time during annealing. Recently, growth of 6 individual recrystallized grains has been quantified on rolled high-purity aluminum [183, 202, 203]. What is proposed here is to quantify the growth kinetics of abnormal grains detected in industrial ODS steels with non negligible amount of second-phase particles. Some selected grains detected by high-intensity spots on the diffraction patterns were studied upon heating. When abnormal growth occurs the intensity in the powder diffractogram is no longer continuously distributed over the $\psi$ range but it becomes spotty (see Fig. 4.9). The intensity of the corresponding diffraction contribution of each grain was integrated at each time step of the annealing process. To do so, the 2D diffraction ring was integrated in selected $\psi$ and $2\theta$ ranges so that only the intensity due to individual coarse grains is taken into account. Since diffraction intensity is proportional to the volume of the selected grain, this allows measuring the increase in volume as a function of annealing time. The relationship between the intensity of a nanocrystalline material and that of a single grain can be given by [198]:

$$V_{grain} = m \times \frac{I_{int}^{gr}}{I_{int}^{tot}} \times \frac{sin(2\theta)}{4sin(\theta)} \times V_{probed} \qquad (4.16)$$

where $V_{grain}$ is the volume of the corresponding single grain, $m$ the crystallographic multiplicity ($m = 8$ for bcc structure), $I_{int}^{gr}$ and $I_{int}^{tot}$ are the diffraction intensities

of the single grain and the entire sample, respectively. $V_{probed}$ is the volume of the sample probed by the X-Ray incident beam. The equivalent sphere radius can be obtained as:

$$R_{eq}(t) = \sqrt[3]{\frac{3}{4\pi} \times V_{grain}(t)} \qquad (4.17)$$

## 4.2.3 Results of *in situ* measurements

### 4.2.3.1 Low temperature treatments (T $\leq$ 800°C)
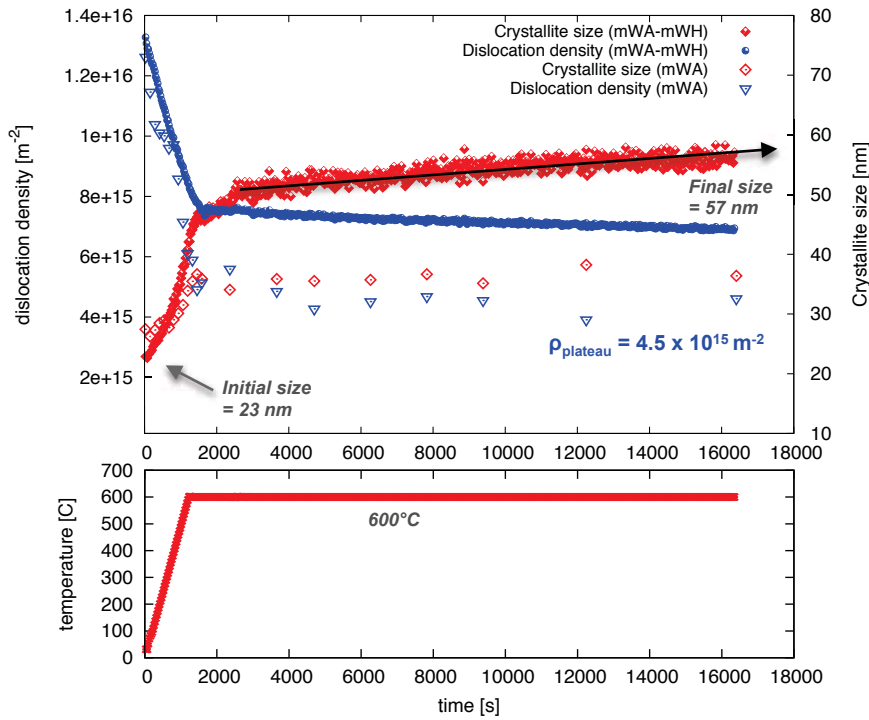


**Figure 4.11:** Microstructural features upon heating up to 600°C (873 K): dislocation density and crystallite size determined with the coupled mWH and mWA methods where $R_e(t)$ is governed by the mWA method. Given values calculated from the single mWA are also reported.

Dislocation density and crystallite size upon heating up to 600°C are reported in Fig. 4.11. Before heating, the initial nanostructure contains coherent domains with a diameter of 23 nm, demonstrating the efficiency of high-energy attrition to produce nanostructured materials [204, 205, 206]. Considerable amount of plastic work is stored during milling. Indeed, the dislocation density is $1.3 \times 10^{16}$ m$^{-2}$ which is consistent with what was observed ex situ by XRD or electron microscopy [107, 200]. A first stage of rapid grain growth occurs at low temperatures (20-600°C), as illustrated in Fig. 4.11. During these early stages of heating annealing induces a decrease in dislocation density from $1.3 \times 10^{16}$ to $8 \times 10^{15}$ m$^{-2}$ (Fig. 4.11),

and crystallite size increases from 23 to 45 nm. When the targeted temperature is reached, a first reduction of the crystallite growth rate is observed, this is probably only linked to the heating rate modification (30 °C.min$^{-1}$ to 0 °C.min$^{-1}$).

After 20 minutes of isothermal annealing, crystallite size and dislocation density reach respectively 50 nm and $7.5 \times 10^{15}$ m$^{-2}$, then a second crystallite growth phenomenon occurs. It can be interpreted as a transition from dislocations annihilation within the cells to a real increase of the crystallite size with moving crystallite boundaries. A slow increase of crystallite size is observed until the end of the soaking stage (>5 hours) at 600°C, with no slope variation, final crystallite size is then 60 nm (growth $6.6 \times 10^{-4}$ nm.s$^{-1}$). A plateau was observed for the dislocation density at $6.6 \times 10^{15}$ m$^{-2}$ (mWA-mWH) or $3.2 \times 10^{15}$ m$^{-2}$ (mWA). This microstructural evolution is characteristic of recovery.

As one can see on Fig.4.12, during the first minutes at 800°C, crystallite size sharply increases from 41 nm to 55 nm while dislocation density decreases continuously during the entire plateau from $2.9 \times 10^{15}$ m$^{-2}$ to $1.7 \times 10^{15}$ m$^{-2}$. The sigmoïdal evolution of the crystallite size can be an indication for the occurrence of the recrystallization. Furthermore, the steady and moderate decrease of the dislocation density may be an indication that no new nuclei are formed. The thermal cycle suffer trouble in the thermal control and values obtained are not exploitable to study the microstructural evolution below 400°C. Authors choose to keep the results not only to illustrate the good correlation between thermal history and microstructural response.

### 4.2.3.2 High-temperature annealing: bimodal microstructure

**850°C thermal treatment**

Upon the heating ramp, from room temperature to 650°C, dislocation density sharply decreases from $1.23 \times 10^{16}$ m$^{-2}$ to $4.2 \times 10^{15}$ m$^{-2}$, while crystallite size increase steadily from 25 nm to 37 nm (Fig.4.13). This first part exactly reproduces the recovery behaviour described in 4.2.3.1. After 750°C the dislocation density stabilizes around $3.0 \times 10^{15}$ m$^{-2}$. Meanwhile, the mWA-mWH crystallite size follows a sharp sigmoïdal increase from 40 nm to 90 nm. This can be interpreted as continuous recrystallization without formation of new germs. During the soaking stage, the crystallite growth rate increases continuously until abnormal grains appear, growth rate is 0.24 nm.s$^{-1}$. The decrease of the dislocation density during the isothermal annealing is also faster than on the 800°C cycle and reaches $1.0 \times 10^{15}$ m$^{-2}$ after 1 hour at 850°C.

**900°C thermal treatment**

During the 900°C cycle, the signal evolution allows to follow step by step almost all microstructural transformations within the material (Fig.4.14). The recovery part of the cycle is once again identical to the one observed in the low temperature
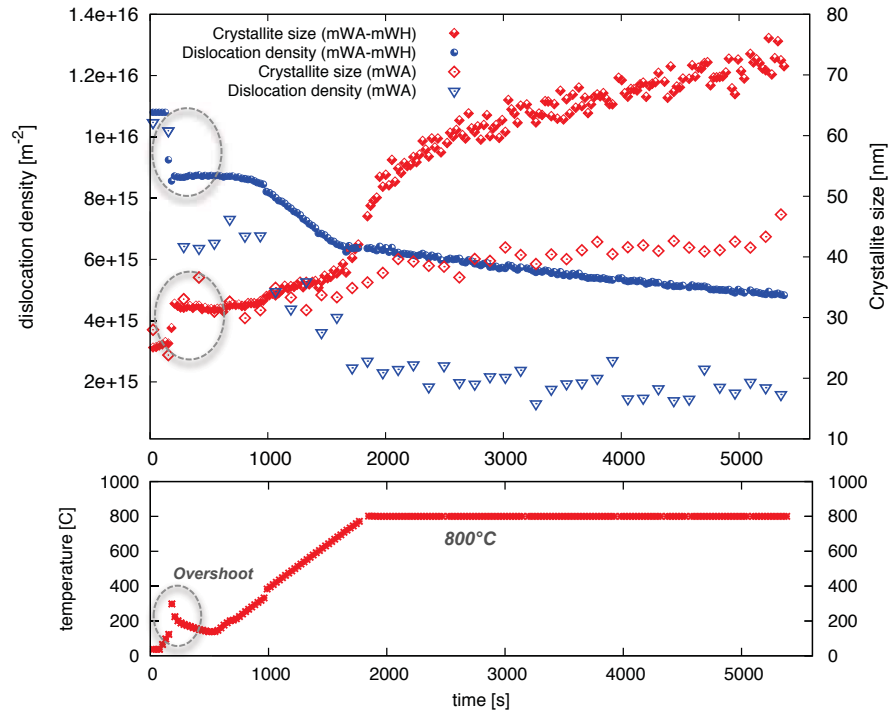
**Figure 4.12:** Microstructural features upon heating up to 800°C (1073 K): dislocation density and crystallite size determined by the mWA-mWH and the single mWA methods.
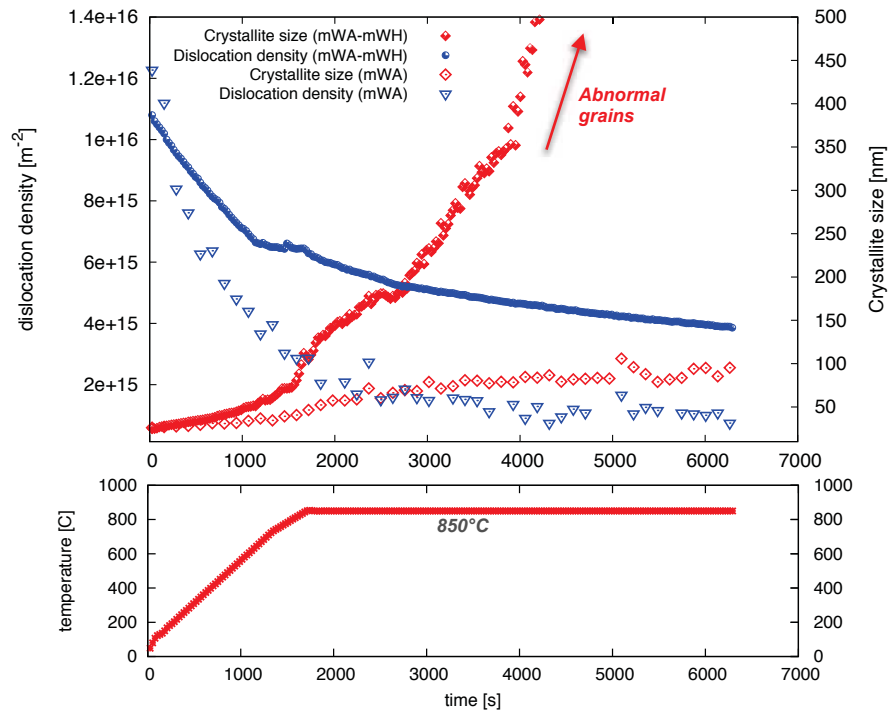


**Figure 4.13:** Microstructural features upon heating up to 850°C (1123 K): dislocation density and crystallite size determined by the mWA-mWH and the single mWA methods.

93
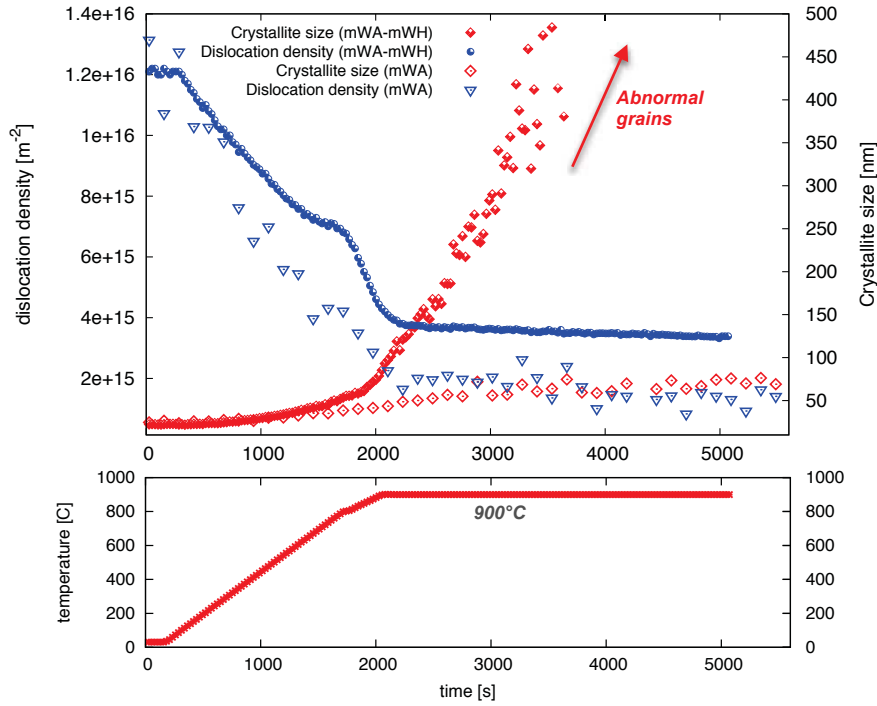
**Figure 4.14:** Microstructural features upon heating up to 900°C (1173 K): dislocation density and crystallite size determined by the mWA-mWH and the single mWA methods.

cycle. The transition step between recovery and recrystallization between 650°C and 800°C is also clearly confirmed. This is consistent with the fact that recovery is favored over recrystallization in high stalking fault energy material and the presence of solute [147]. Soon after 800°C, mWA-mWH crystallite size increases drastically and continuously until abnormal grains prevent from exploitable results, growth rate is 0.4 nm.s$^{-1}$. While crystallite size increases, dislocation density literally drops from $4.3 \times 10^{15}$ m$^{-2}$ to $1.9 \times 10^{15}$ m$^{-2}$ between 800°C and 900°C. After the soaking time, dislocation density reaches $9.0 \times 10^{14}$ m$^{-2}$. Here, there is no transition from recrystallization and abnormal grain growth, the two phenomena occur simultaneously.

**1100°C thermal cycle**

A heat treatment was performed until 1100°C, the typical consolidation temperature for ODS steels processing. As illustrated in Fig. 4.9, the diffraction ring is no longer homogeneous and becomes spotty upon heating up to 1100°C, this clearly involves the occurrence of abnormal grain growth. Abnormal grains are identified as large spots of high intensity. As emphasized in Fig. 4.15, the initial crystallite size and dislocation density are 22 nm and $1.2 \times 10^{16}$ m$^{-2}$, which are identical to those determined from the previous treated samples. A dislocation density plateau is still observed between 650°C and 800°C definitively validating the separation be-
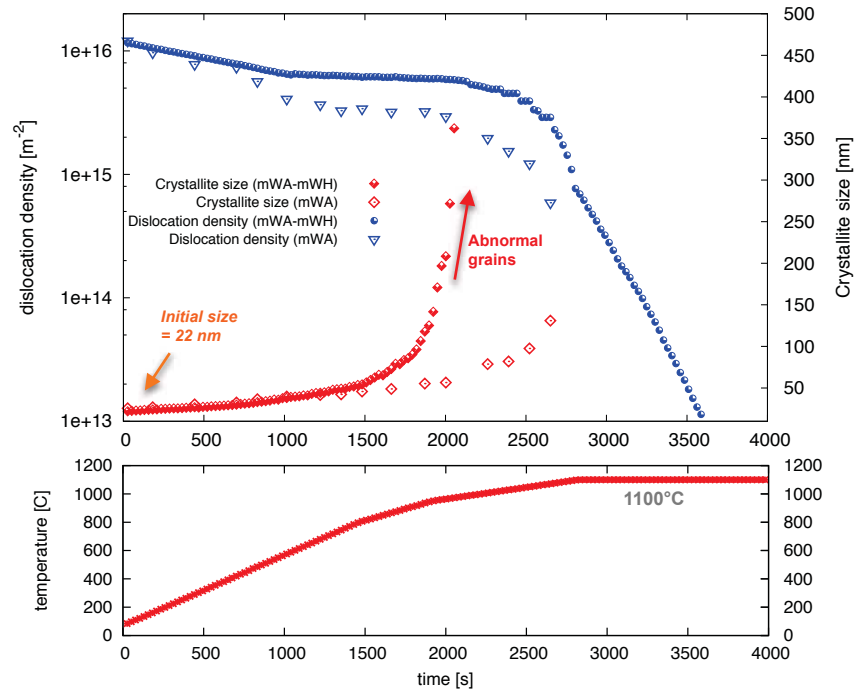
**Figure 4.15:** Microstructural features upon heating up to 1100°C (1373 K): dislocation density and crystallite size determined by the mWA-mWH and the single mWA methods.

tween recrystallization and recovery . On the contrary, annealing above 900°C leads to a much more significant drop in dislocation density within the normal growth grains, which falls around $1 \times 10^{13}$ m$^{-2}$ after 20 min at 1100°C. After 800°C, crystallites grow very rapidly due to both continuous recrystallization and abnormal grain growth. It is interesting to notice that results between the two methods are really diverging.

Above 900°C, abnormal grains start to grow very rapidly. Three abnormal grains were selected manually by choosing spots with high diffraction intensity. Two of the selected abnormal grains started to grow at 1080 and 1088°C. The growth rate is much higher than that of the ultrafine grains (Fig. 4.16).

Indeed, once they start to grow, they can reach their final equilibrium size in less than 200 s at 1100°C. Given that the diffraction intensity was measured under reflection diffraction conditions and not under transmission, the error bars are larger than the grain radius itself. Two grains having the same volume can give rise to various diffraction intensities depending upon the distance between the grain and the free surface, leading to an attenuation factor from 0 to 100%. Thus the detected intensities are valuable for tracking the appearance of the abnormal grains and to observe whether they grow rapidly or not, but their volume cannot be quantified accurately. Abnormal growth occurs so rapidly that the three selected grains reach an abnormal size even before the soaking step at maximum temperature began.
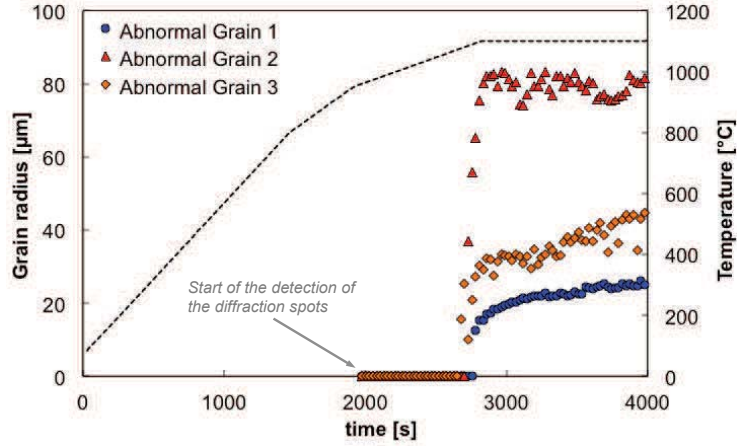
**Figure 4.16:** Growth kinetics of the abnormal grains detected by the 2D detector

## 4.2.4 Discussion on microstructure instabilities

### 4.2.4.1 Stage I: mechanisms operating at low temperature

Dislocations that formed during cold-working constitute a complex distribution of dislocations in deformed polycrystalline materials. Dislocations of same Burgers vector but of opposite signs can annihilate each other when other can rearrange by climb and form low-angle grain boundaries, such as particular tilt boundaries [147]. In this study, the nanocrystalline powder was processed by high-energy mechanical alloying, producing a huge amount of dislocations. Due to the high stalking fault energy of the ferritic steels, these dislocations are likely to form cell structures with typical size (determined as the initial crystallize size) of $22 \pm 1$ nm. At low temperature, we have identified two different recovery mechanisms. Up to 600°C the decrease of dislocation density and the increase of crystallite size was observed. It has been demonstrated that grain size does not evolve at this temperature [200]. This is characteristic of the part of the recovery mechanism where dislocations within cells rearrange and annihilate each other to form thinner cell walls. Therefore, initial growth kinetics is due to dislocation annihilation within the milled powder. Nano-sized cells are cleaned by dislocation rearrangement, which migrates into subgrain boundaries of well defined subgrains. The second part of the growth kinetics described in Fig. 4.11 can be considered as a second recovery mechanism. Indeed, it has been once again demonstrated that there is no grain size evolution [200], the crystallite growth is caused by subgrains mobility that either disappear or whose wall areas slightly decrease. Subgrains with a diameter $D$ will evolve as:

$$D^n - D_0^n = c \times t \tag{4.18}$$

where $t$ is the time at 600°C, $n$ and $c$ are constants and $D_0^n$ the diameter before subgrain growth occurred, that is 50 nm. A least square method was applied to calculate the best fit exponent $n = 4.9$ (Fig. 4.17). Scattered values of $n$ were

96
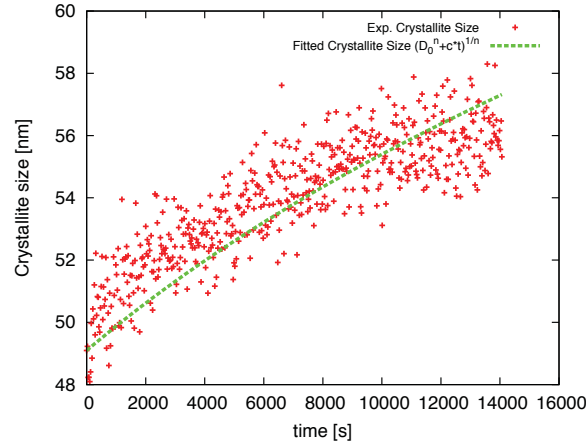
**Figure 4.17:** Change of the crystallite size with time at 600°C fitted by equation (4.18)

reported in the literature ($n = 2$ in high purity iron [207]). The value found in our study is high enough and corresponds to a very slow subgrain growth. The increase is so slow that one can expect the mobility of the moving interfaces to be very limited. This suggests that recovery of the nanostructure at low temperature involves only homogeneous recovery with no significant effect on grain growth. The influence of solute drag and eventual yttria clusters coming from mechanical alloying may be the cause of such poor kinetics. One can expect recovery to homogeneously reduce the amount of stored energy within the deformed nanostructure. However, recovery at this temperature involves a limited decrease in dislocation density, reaching $6.8 \times 10^{15}$ m$^{-2}$ after 4 hours of annealing at 600°C. As referred in several studies [107, 147], the decrease of stored energy will reduce the driving pressure for recrystallization $P_V$:

$$P_V = \alpha G b^2 \times \Delta \rho \tag{4.19}$$

where $\alpha$ is a constant, $G$ the bulk shear modulus, $b$ the Burgers vector magnitude and $\Delta \rho$ the variation in dislocation density between two neighbor grains, which can be approximated by the mean dislocation density in the material. Consequently, the driving pressure for recrystallization is still very high even after long annealing treatment at low temperature. Since the overall solute content within the matrix is far from negligible (17 at%), the solute atoms may act as obstacles and largely impede dislocation mobility [208]. At temperatures high enough to allow oxide precipitation, the precipitates have the same impeding effect. The amount of stored energy available for microstructural evolution at higher temperature is therefore very high.

### 4.2.4.2 Comparison of the microstructural evolution during soaking time

When comparing the crystallite size during soaking time, two distinct evolutions can be observed Fig. 4.18. At low annealing temperature (i.e :600 and 800°C),

crystallite size almost reaches a plateau and increases very slowly while for high temperature annealing (i.e :850 and 900 °C) crystallite size increases very rapidly. Information related to the dislocation density allows to go further. Indeed, while it remains stable at 600°C, dislocation density decreases steadily at 800°C. Occurrence of recrystallization can be observed undoubtedly by the sharp increase of crystallite size combined with the sharp decrease of dislocation density occurring at 800°C. It is also important to notice that the dislocation density remains stable during soaking time at 900°C while ultra-fine grains (UFGs) are recrystallized. This is a sign of the microstructural stability of UFGs at high temperature.
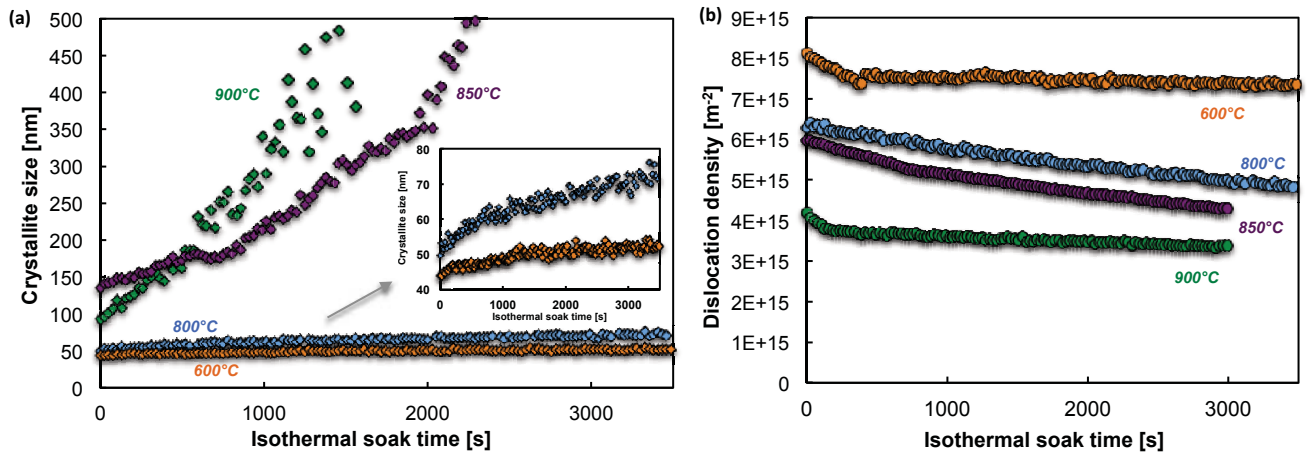


**Figure 4.18:** Comparison of the microstructural evolution during soaking time for different temperatures.

#### 4.2.4.3 Stage II: Emergence of the bimodal microstructure at higher annealing temperature

- Growth of ultra-fine grains

During annealing treatments at high temperature, ranging from 800°C to 1100°C the microstructural evolution is no longer confined to recovery. Nevertheless, a very clear transition is observed between recovery and the following mechanisms. On every annealing sequence, from 650°C to 800°C, both dislocation density and crystallite size stabilize. The crystallite growth mechanism, earlier identified as a second recovery step, ensures this transition.

Around 800°C, the ultra-fine grain size sharply increases before returning to a steady growth meanwhile dislocation density drops rapidly before returning to a steady decrease. This abrupt evolution is a clear sign that recrystallization occurs around 800°C and is then followed by grain growth. An important point is to note the constant increase of the crystallite size. If new nuclei were formed, the crystallite size growth would have been at least stopped during the first steps of the

recrystallization. Therefore, the ongoing phenomenon is very likely to be continuous recrystallization rather than primary recrystallization with germs formation. A further argument supporting this interpretation was put forward by [200], where it as been shown that grain growth involves no textural change within the UFGs regions. Nevertheless, being at such a small scale the appearance of few large nuclei can perfectly go unnoticed.

Heterogeneous grain growth was detected around 900°C as the diffraction rings begin to spottify. Occurrence of abnormal grain growth strongly limits the contribution of nanosized grains to the diffraction signal. Indeed, diffraction intensity is proportional to the volume of crystallite (Eq. (4.16)). Thus, the intensity of diffraction patterns due to UFGs is much lower than the one due to coarse grains, as illustrated in Fig. 4.9. Despite their relative small size ($0.2 - 1 \ \mu m$) UFGs are no longer quantitatively measurable and diffraction pattern analysis methods reach their limits, values obtained above 0.3 $\mu m$ are no longer reliable. Fig. 4.9 illustrates that there is still a non-negligible amount of ultra-fine grains remaining in the annealed powder, as confirmed by SEM observations (Fig. 4.19).
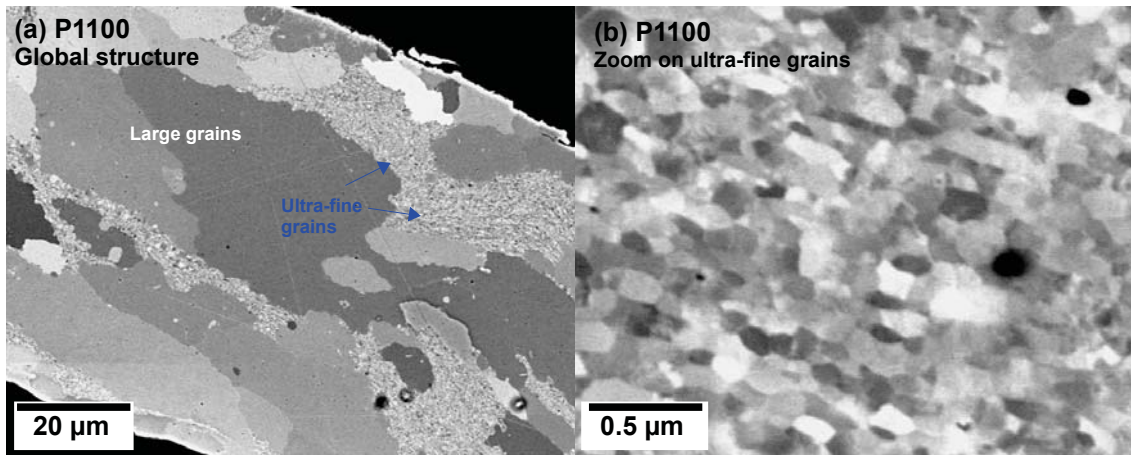


**Figure 4.19:** SEM-FEG images of the ODS steel powder after in situ annealing up to 1100°C

Remaining ultra-fine grains are stable at high temperature. The dislocation density within the powder is higher than expected in annealed steels. Retained stored energy is most likely located in the ultra-fine grained zones where abnormal growth has not occurred. When reaching the typical temperature at which recrystallization mechanism is being activated the microstructure recovery is still limited to a dislocation density drop of less than one order of magnitude: from $1.2 \times 10^{16}$ to $3 \times 10^{15}$ m$^{-2}$. As stated before, this does not significantly reduce the driving force for recrystallization.

- Abnormal grain growth

Precipitation of nanoparticles responsible for grain boundary pinning occurs between 600°C and 900°C [164]. Nevertheless, a rapid growth of grains with specific

99

advantages (such as lower initial stored energy, higher initial grain size, lower boundary pinning force, etc.) occurs. Abnormal grain growth remains difficult to control as the factors to enable the growth of particular grains at the expense of others can be multiple and not so easily separable. In ODS steels two parameters are more likely to influence this evolution : precipitation as generating a pinning force or stored energy heterogeneity. Unfortunately both involve local measurements and are out of reach for diffraction studies. The abnormal grain structure is thermally stable even at high temperatures, close to the solidus temperature. As one can see on the annealed powder during in situ measurement, the bimodal structure is still observed after heating at 1100°C (Fig. 4.19).

From a processing point of view, one major conclusion can be emphasized. Whatever the consolidation time, once the process involves a temperature higher than the abnormality occurrence temperature, the resulting grain structure will be drastically abnormal. This statement is consistent with the quantitative study of the same ODS ferritic steel consolidated by either spark plasma sintering (processing time at 1150°C $\approx$ 5 min) or hot isostatic pressing (processing time at 1150°C $\approx$ 3 hours). An equivalent heterogeneous grain size distribution was observed within the consolidated materials [107]. Indeed, the high density of nanoparticles dispersed in the ODS steels exert an efficient Zener pinning on grain boundaries, resulting in a strong thermal stability of the bimodal microstructure. Consequently, this kind of abnormal grain structure might be difficult to avoid by accelerating the consolidation process kinetics. However, long annealing treatments performed just below the abnormal growth temperature may result in a significant reduction of the available energy for secondary recrystallization and therefore limits its effects. Moreover, a complete description of the influence of precipitation reinforcement on the onset of recrystallization and grain growth will allow a better control on the appearance of the abnormal microstructure.

### 4.2.4.4  Discussion about the methods to study grain growth

- Comparison between methods

One very important point that can account for the discrepancy between mWA-mWH and mWA results is to keep in mind that XRD diffraction patterns display the reciprocal space. That is to say that short range correlation in the direct space (for example regions close to dislocations) will affect the diffraction patterns far away from the peak center, while long range correlations such as crystallites walls will have effects very close to the peak center. mWA-mWH coupled method is based on the FWHM of the peaks, which means that it will be more influenced by large-scale effects. On the contrary, the mWA method takes into account the Fourier coefficients corresponding to small $L$. The latter, based on the asymptotic theories of dislocation-induced peak broadening [209], deliver a more accurate value of the dislocation density and the outer cut off radius.

- Parameters evolution

An interesting parameter to study the microstructural evolution is the outer cut-off radius of dislocation: $R_e$. $R_e$ increases during recovery (Fig. 4.10). This illustrates the transition from a random distribution of un-screened dislocations to reorganized walls. Indeed, the stored energy is reduced by dislocation migration within the crystallites into more defined low-angle grain boundaries or subgrains. This favours the associated screening of the deformation field of the dislocations. Once recovery is achieved, $R_e$ is stable during the entire transition phase between recovery and recrystallization since dislocations entanglement is unchanged and dislocation effect on lattice distortion is confined within a constant crystallite size. Up to 900°C, $R_e$ can be related to recovery and recrystallization: it increases at low temperature, then stabilizes while dislocations rearrange and subgrain growth is completed. Finally strongly increases when the microstructure recrystallize. Above 900°C, $R_e$ starts to increase exponentially. $R_e$ drastically increases since the crystallite size increases until it reaches its highest possible value (Fig. 4.10). Indeed, since the influence of the strain created by a dislocation on the crystal is physically limited a saturated value of $R_e$ was chosen and set by the final mWA measurement step (Fig. 4.10).

## 4.2.5   Conclusion

In-situ XRD experiments have been performed to reveal the microstructural evolution process leading to the bimodal grain structure of ODS ferritic steels. A coupled modified Warren-Averbach and Williamson-Hall method has been proposed to analysis the XRD patterns. Combined with a robust routine detecting in situ microstructural instabilities the method allows taking into account the evolution of dislocations rearrangement during recovery and recrystallization. The growth kinetics of specific abnormal grains was quantified. Regarding the selected grains only, no significant incubation time was detected. This suggests that above the onset temperature, around 850°C, recrystallization occurs quasi instantaneously. Therefore, annealing around this temperature seems to be of particular interest to tailor the abnormal grain ratio. Key steps of recovery and recrystallization have been identified and the microstructural evolution can be summarized as follows:

- High-energy attrition of the powder introduced a huge amount of plastic deformation, leading to a dislocation density of $1.1 \times 10^{16}$ m$^{-2}$. Decrease of the stored energy is limited even after recrystallization.

- At low temperature (600°C), a first step of recovery involving dislocation rearrangement induces a rapid increase of crystallite size from 23 to 49 nm.

- Between 600°C to 800°C, a second step of recovery involves a slight growth of the crystallite size while the dislocation density remains almost stable.

- Around 800°C, Grains grow sigmoïdaly, while dislocation density drops significantly, indicating a continuous recrystallization.

- Above 1123 K (850°C), abnormal grains appear with no incubation time. The possible mechanism leading to this heterogeneous microstructure is the preferential growth of particular grains. It induces drastic growth and enhanced boundary mobility, either due to stored energy or pinning force heterogeneities.

A complete description of the influence of precipitation reinforcement and annealing temperature on the onset of recrystallization and grain growth will quantify the role of the nanoparticles on the appearance of the abnormal microstructure.

## 4.3 Influence of titanium and yttrium content on abnormal growth

*Related article : [E]. This work was performed with N. Sallez.*

### 4.3.1 Introduction

The influence of second-phase particles on abnormal grain growth is of great importance since it governs the resulting mechanical properties of nanostructured and ultrafine-grained metallic materials. From an engineering point of view, the temperature at which abnormal grains appear is a key factor for optimizing the consolidation process. In this work, a pre-alloyed ferritic powder Fe-14Cr was mechanically alloyed with an increasing content of yttrium and titanium (0%, 0.05%, 0.3% and 1%). In-situ X-ray diffraction acquisition was used to determine the kinetics of microstructural mechanisms within different powder. We report the annealing behavior during non-isothermal treatments up to the consolidation temperature 1100°C. The recovery, crystallite growth and the occurrence of heterogeneous (secondary) recrystallization are then described. The fraction of retained nanostructured to ultrafined grains increases with the content of yttrium and titanium. Complementary scanning (SEM) and transmission electron microscopy combined with an orientation determination device: automatic crystallographic orientation mapping (TEM-ACOM) were used to characterize the microstructure and the precipitation of fine particles. The aim of this work is to establish that Zener pinning evolves with the content of yttrium and titanium, which will induce a variation in the critical size and the fraction of ultrafine grains. Therefore one demonstrates that the ferritic ultrafined grains can be tailored by powder metallurgy.

### 4.3.2 Materials and methods

The four powders were milled in a high-energy attritor for 10 hours in the same conditions with various contents of titanium and yttrium (Table 4.4).

| Sample ID | Fe [wt%] | Cr [wt%] | Y [wt%] | Ti [wt%] |
|---|---|---|---|---|
| P0 | bal. | 14.5 | 0 | 0 |
| P005 | bal. | 14.5 | 0.05 | 0.05 |
| P03 | bal. | 14.5 | 0.3 | 0.3 |
| P1 | bal. | 14.5 | 1 | 1 |

**Table 4.4:** Content of yttrium and titanium for each powder sample

The powders were then canned and further consolidated by hot isostatic pressing (HIP) at 1100°C for 2 hours. The same powders were kept "as-milled" and studied in situ in order to understand their microstructure evolution upon heating.

X-Ray Diffraction (XRD) was used to study the microstructure evolution of the nanostructured powders during annealing. More specifically, X-ray diffractograms of the 4 major ferrite peaks were recorded separately with a last generation 2D detector XPAD S140. The obtained diffractograms are later analyzed with the coupled modified Warren-Averbach and Williamson-Hall method, which allows to calculate dislocation density and the crystallite size. The method is introduced and fully described in [138]. Crystallite size and lattice strain contributions to peak broadening are given by:

$$\beta_{ODS}(t) \approx 0.9/D(t) + \frac{\pi}{2}R_e^2(t)b^2\rho^{3/2}(t)K^2\bar{C} \pm O(K^4\bar{C}^2) \qquad (4.20)$$

The terms were previously described in equation (4.15). TEM-ACOM maps have been acquired on a 200 keV Tecnai F20 ST (FEI) using a 1 nm nano-beam and a 2.75 nm step size. Since it is based on the indexation of spot diffraction patterns, this method is operative whatever the amount of strain within the material. Strain will affect the grains through misorientation which will be measured using the diffraction indexation. TEM-ACOM provides orientation maps very similar to the ones obtained by EBSD. Using the dedicated data analysis software OIMTM (Orientation Imaging Microscopy), information like grain size, grain shape, grain boundary identification, dislocation density (more precisely the Geometrically Necessary Dislocations GND), misorientation profile and texture can be derived [200]. TEM thin foils were prepared by Focus Ion Beam (FIB) on a Strata 400S (FEI), and were directly taken from the annealed powder particle. A final thinning was performed using 5kV Ga+ ions to reach a thickness of $\approx$ 70 nm.

### 4.3.3 Microstructure evolution during *in situ* annealing

Identical non-isothermal heating cycles were performed from room temperature to 1100°C on the four milled powders. Dislocation density and crystallite size were determined all along the cycles. Figure 4.20(a) reports the evolution of the crystallite size for the four grades. The upper limit of detectable crystallite size was set at 100 nm, which corresponds to the resolution limit of the overall experiment set up. The initial size is 20 nm for the unreinforced grade whereas it seems to be quite constant for the three others, that is 15 nm. The kinetics of each powder can be decomposed into two distinct parts: first a slow increases of the crystallite size followed by a sudden acceleration of this crystallite growth rate. The first part can be interpreted as recovery while the slope breaks is the signal for the beginning of recrystallization. Recrystallization temperature rises as the content of yttrium and titanium in the powder increases. As detailed later, this leads to rapid growth of recrystallized grains, inducing much higher final crystallite size of the least reinforced powders P0 and P005 compared to P03 and P1. The annihilation rate is decreased by solute atoms and nanoscale precipitates that act as obstacles for dislocation motion.

In this context, increasing the solute content can be an efficient solution to avoid the appearance of abnormal grains during high-temperature consolidation. Specially, the grades P03 and P1 resist to recrystallization up to 1100°C. The final crystallite size of the milled powders was found to decrease with increasing amount of additional element.
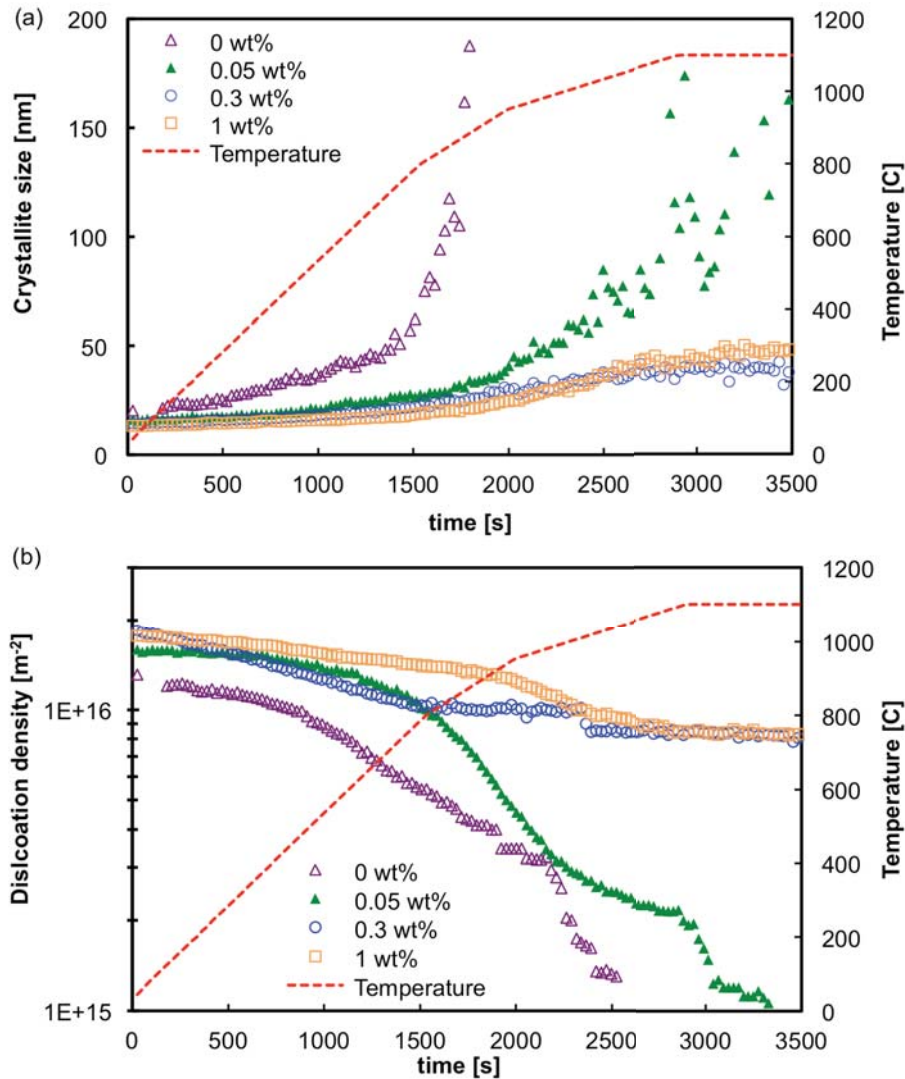


**Figure 4.20:** Evolution of crystallite size and dislocation density in P0, P005, P03 and P1 upon non-isothermal heating up to 1100°C (1373 K)

This is consistent with the evolution of dislocation density with the solute content upon annealing. First, in Figure 4.20(b) , the initial dislocation density is lower in the Y-Ti free powder ($\approx 1.2 \times 10^{16}$ m$^{-2}$) compared to those of Y-Ti containing powders ($\approx 1.5 - 1.8 \times 10^{16}$ m$^{-2}$). The dislocation density then follows different trends depending upon the solute content. The higher the solute content, the lower the decreasing rate. Therefore, there is also a clear correlation between the final

dislocation density and the content of additional elements.

### 4.3.4 Microstructure characterization after annealing
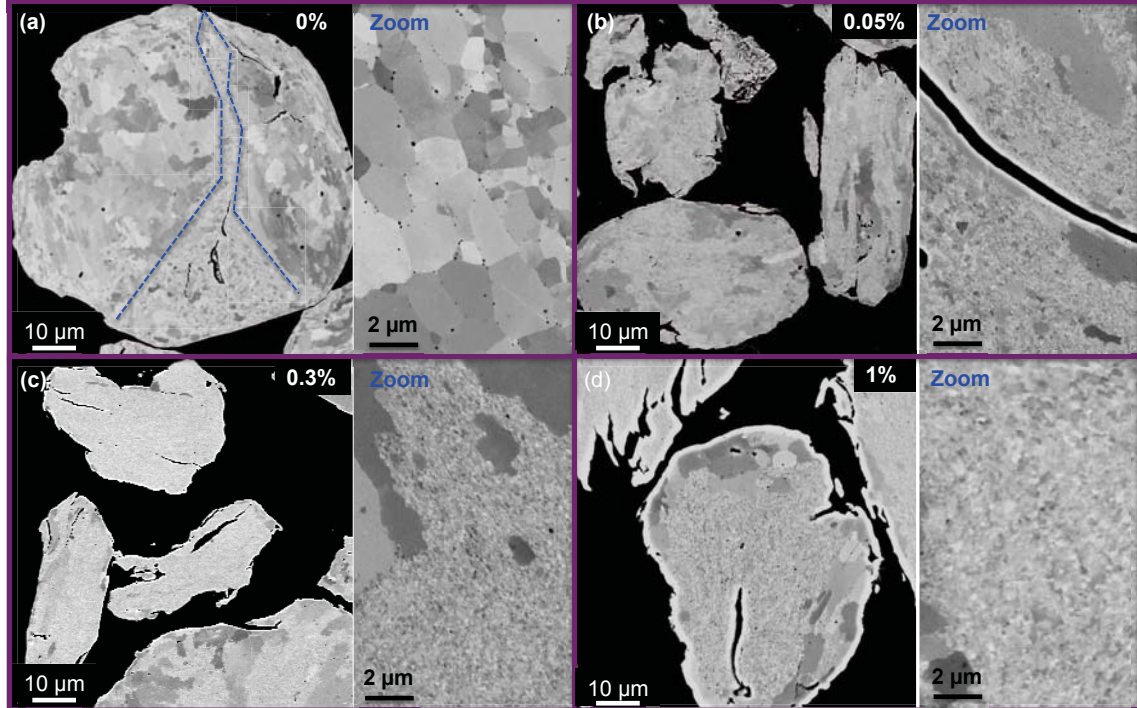


**Figure 4.21:** SEM images of the microstructures of annealed powders: (a) P0, (b) P005, (c) P03 and (d) P1

After annealing at the synchrotron, the powders were then characterized by SEM-FEG. The microstructures obtained are reported in Figure 4.21. The yttrium oxides having been identified as the main cause for abnormal grain growth [173], we expected the bimodal microstructure to disappear with the decrease content of yttrium and titanium. Surprisingly, a bimodal microstructure was observed on the four powders. However, the ultrafine to coarse grains ratio clearly increases with the solute content. The Y-Ti free powder P0 contains a majority of coarse grains with a diameter of 10 to 25 $\mu$m. Also, the finest grains are quite large, with a diameter from 0.5 to few microns. The latter are visibly pinned by particles at boundaries. These particles were found to be carbides or coarse oxides (not nanoclusters). The powder P005 has much less abnormal grains. Also, the finest grains are drastically smaller than those in the P0, with a mean diameter under 1 $\mu$m. Interestingly, the powder P03 exhibits some coarse grains even if they have mainly located close to the powder particles interfaces. Ultra-fine grains seems possess higher fraction and lower mean size than those in the two powders P0 and P03, which confirms the important role of solute content on this population. Similarly, the powder P1 shows limited number of abnormal grains, mainly located on the powder particles edges.

106

It is interesting to note that whatever the solute content the abnormal grains have always the same size. The size of UFGs is very small and requires transmission electron microscopy to be quantified. This was performed on each annealed powder by TEM-ACOM mapping, as reported in Figure 4.22.
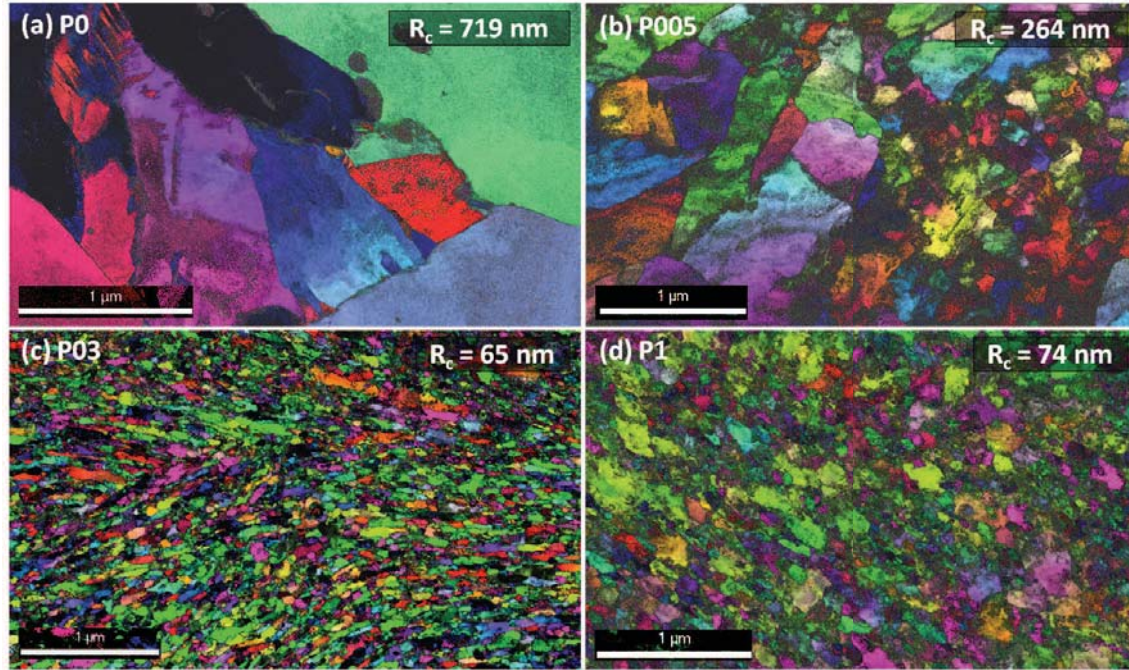


**Figure 4.22:** TEM-ACOM orientation maps of each annealed powder (a)-(d). The mean grain radius for each sample is also reported.

The radius of the ultrafine grains drastically decreases with the solute content. The unreinforced grade contains few fine grains below 1 $\mu$m in diameter. These grains are probably pinned by carbides or coarse oxides, eventually located at triple junctions. A significant decrease in UFG size between P0 and P005 is observed, demonstrating the benefit of adding oxygen, yttrium and titanium to produce fine precipitates able to efficiently pin grain boundaries. P03 and P1 have finer UFG size than P005, indicating that the critical grain size can be tailored by the amount of the precipitating solutes. There is no difference in UFG size between P03 and P1 and P1 UFG size is even slightly smaller than that of P03. However, the measured P1 grain size is probably overestimated. Indeed, TEM-EBSD mapping is made more difficult by very dense nanoprecipitation that induces lots of misfit strain in UFG. Thus, the orientation map is much worse resolved that the others (Fig. 4.22(d)).

### 4.3.5 Precipitation state in the consolidated/annealed materials

The heating cycle used in the in situ synchrotron XRD is representative of typical consolidation with hot isostatic pressing (HIP): non-isothermal treatment from

room temperature to around 1100°C with a slow cooling. The microstructure of annealed powders and HIPed ODS steels are thus expected to be equivalent both in term of grain size and precipitation state. This is showed in Figure 4.23 where the same powder HIPed at 1100°C and annealed during in situ synchrotron is described. One gets a bimodal microstructure with coarse grains and UFG with roughly the same fraction. Thus, the precipitation state was measured on the 4 different powders processed by HIP at 1150°C. The characterization was done by small-angle X-Ray scattering (SAXS) and transmission electron microscopy (TEM). A detailed presentation of SAXS and TEM characterization and data treating would fall out of the scope of the present paper, readers are reported to [210]. However, one example
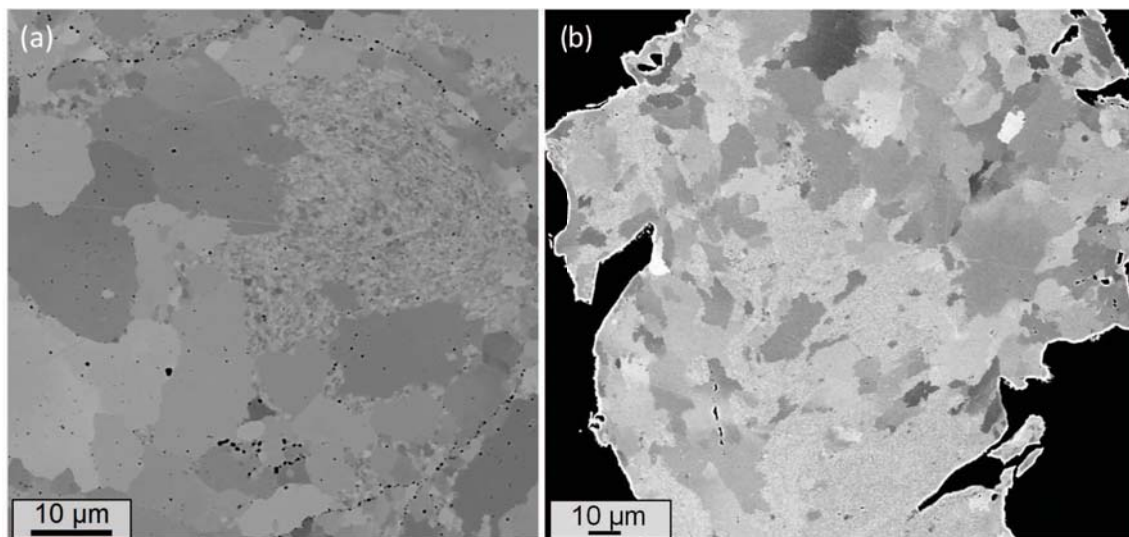


**Figure 4.23:** Figure 5: (a) SEM-FEG image (backscattered electrons) of the powder P03 processed by HIP at 1150°C for 3 hours. (b) SEM-FEG image of the powder P03 after annealing at 1100°C at the synchrotron. The bimodal microstructure is clearly observed in both cases.

of TEM observation performed on the HIPed P03 powder is presented in Fig. 4.24. The precipitates are mostly cubic ones, with a diameter of about 2 to 3 nm, by judging to their particular structure factor contrast, precipitates are coherent or semi-coherent [211]. The precipitates fraction and mean radius measured on each HIPed powder by SAXS are then summarized in Table 4.5. As expected, the volume fraction increases with the initial titanium and yttrium content, from 0.3% to 1.9% for the most highly reinforced grade . The average radius of the few particles detected in the P0 powder is 3 nm, whereas the average radius in the three other powders is approximately 1 nm. This is consistent with the presence of coarser oxides or carbide in P0 while fine Y-Ti-O are expected in the three reinforced powders (P005, P03 and P1). This is particularly interesting because the Zener pining pressure $P_z$ in the reinforced powders can be more easily tailored by the precipitation fraction at constant mean radius:

$$P_z = \frac{3}{2}\gamma\frac{f_p}{r_p} \tag{4.21}$$

where $\gamma$ is the grain boundary energy, $f_p$ and $r_p$ the fraction and mean radius of the precipitates. Values of pinning pressures exerted by particles on grain boundaries are given in Table 4.5.
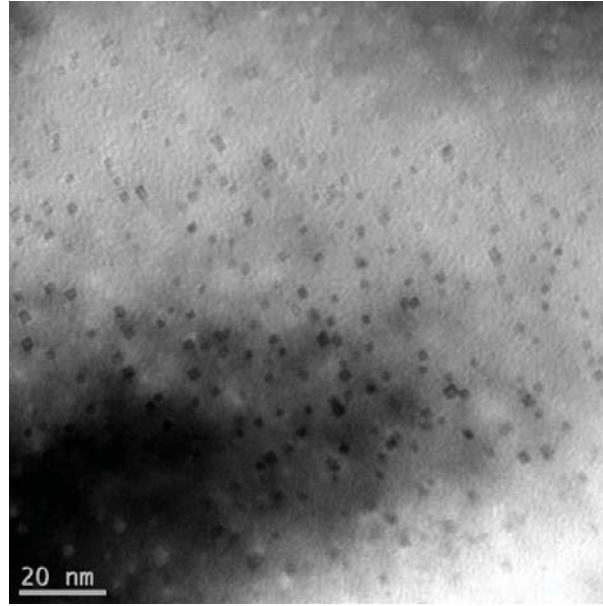


**Figure 4.24:** TEM image of nanosized particles in the HIPed P03 powder.

| Sample | Volume fraction | Mean radius [nm] | Zener pinning pressure [MPa] |
|--------|-----------------|------------------|------------------------------|
| HIP-P0 | $3.0\times10^{-3}$ | 3.0 | 0.7 |
| HIP-P005 | $3.5\times10^{-3}$ | 1.1 | 2.4 |
| HIP-P03 | $7.2\times10^{-3}$ | 1.3 | 4.2 |
| HIP-P1 | $1.9\times10^{-2}$ | 0.9 | 15.6 |

**Table 4.5:** Precipitation state from SAXS experiments [212] and resulting Zener pinning pressure for each HIPed sample using equation (4.22) with a grain boundary energy $\gamma = 0.5$ J.m$^{-2}$.

## 4.3.6   Discussion: effect of precipitation on grain growth

### 4.3.6.1   Bimodal microstructure

The first relevant result that needs to be discussed is the appearance of the bimodal microstructure whatever the titanium and yttrium content. Consequently, it seems that this phenomenon is not entirely governed by the precipitation state. Since the plastic deformation on each powder is drastic, this gives rise to a high

level of stored energy. The latter is directly related to the driving pressure of what is called strain-induced boundary migration (SIBM). This can be interpreted as an increase of grain boundary migration due to the difference in stored energy between two neighboring grains. Therefore, the grain boundary will move into the more deformed grains, resulting in the growth of the least deformed one. The evolution of this driving pressure upon heating was previously reported in [107]. It has a great importance on the appearance of the abnormal grains. The pressure may result in either primary recrystallization (nucleation of new grains) or secondary recrystallization (growth of existing grains). In any case, the more defect-free grain will grow at the expense of the others. Since this driving pressure combined with the capillary driving pressure $P_c$ will compete with the pinning pressure, the formation and further growth of the abnormal grains will be affected by the precipitation state. This is clearly emphasized by the increase of the recrystallization temperature with titanium and yttrium content.

The abnormal grains appear with a short incubation time due to high driving force. They do not fit the Zener's theory based on the competition between pinning and capillary driving pressures. However, what is interesting in ODS steels is the extreme stability of utrafine grains. Indeed, UFG may be responsible for Hall-Petch hardening and are of key interest. Specially, they are very stable under thermal treatment at high temperature. We propose here to explain the evolution of this population as a function of yttrium and titanium content and therefore as a function of its interaction with nanosized particles. The competition between the driving pressure against the retarding pressure can be translated into the following equation:

$$\sum P_i = P_c - P_z = \gamma \left( \frac{2}{R} - \frac{3f_p}{2r_p} \right) = 0 \qquad (4.22)$$

where $R$ is the grain size, $f_p$ and $r_p$ the precipitate fraction and radius, respectively. This allows us to derive the critical size that is reached by UFG when Zener pinning pressure and driving pressure are equal in a steady state [151]:

$$R_c^{Zener} = \frac{4r_p}{3f_p} \qquad (4.23)$$

It is worth noticing that Rios modified the Zener's theory, resulting in a critical grain size 8 times smaller [152]:

$$R_c^{Rios} = \frac{r_p}{6f_p} \qquad (4.24)$$

The critical size of ultrafine grains was calculated using the Small-Angle X-ray Scattering (SAXS) data on the four powders consolidated by Hot Isostatic Pressing at 1100°C. The measured radius of the ultrafine grains is well predicted by the theory of competing pressures and is included between the two values predicted by Zener and Rios for each yttrium and titanium content (Fig. 4.25). When dealing

110
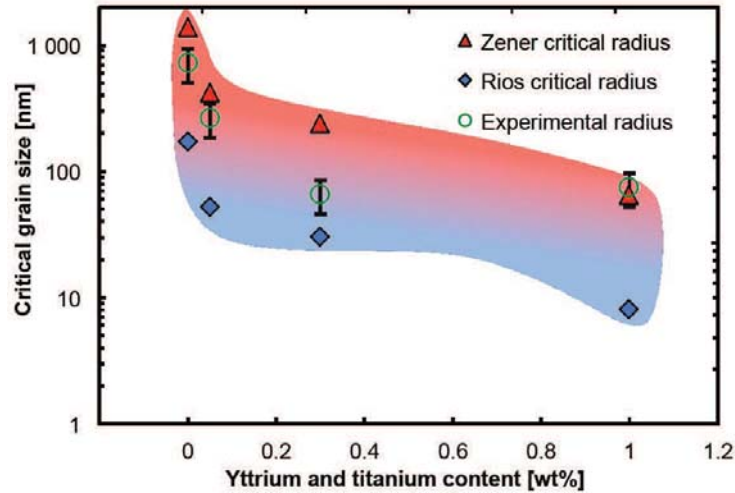
**Figure 4.25:** Critical size calculated from Zener's and Rios' theories based on the precipitation state determined on each grade. Experimental measurements of ultrafine grains (UFG) size were performed by TEM-EBSD.

with low fraction of second-phase particles, more efficient pinning by particles located at multiple grain junctions is most likely responsible for reducing the grain size [173]. However, the calculated critical size of the ulfrafine grains accurately matches the UFG size measured by TEM. As mentioned before, the measured grain size of P1 can be overestimated by TEM-EBSD since lots of misfit is observed. Given the experimental errors, one can consider that the Zener critical grain size is in good agreement with the measured grain size. One can conclude that only UFG are effectively pinned by the fine particles whereas grain boundaries of abnormal grains are capable to migrate more easily. This capability to avoid pinning may be due to predominant strain-induced boundary migration induced by heterogeneous stored energy. The micro-mechanisms leading to improved grain boundary mobility would require systematic TEM investigation of the same zone annealed at short time intervals, which would induce experimental issues.

### 4.3.7 Conclusion

In order to quantify the effect of the precipitation on the microstructure of ODS ultrafine grained ferritic steels, four powders were milled with different amounts of titanium, yttrium and oxygen. Using synchrotron X-Ray diffraction with in situ annealing, a coupled modified Warren-Averbach and Williamson-Hall method was applied to determine the crystallite size and dislocation density during heating. A focus was made on the evolution of ultrafine grains, which are known to harden the metallic materials. Specially, the powders annealed in the synchrotron were characterized by TEM-EBSD. The size of ultrafine grains was determined and compared to the critical grain size predicted by the Zener's theory. This critical grain size was

111

calculated from the precipitation state (mean radius and volume fraction) measured by Small-Angle X-Ray Scattering (SAXS).

- Concerning the as-milled powder before heating, the initial plastic deformation due to mechanical alloying is important, with a dislocation density of more than $10^{16}$ m$^{-2}$. Also, the dislocation density increases with the amount of titanium and yttrium.

- Abnormal growth during heating is observed for every powder. This demonstrates that if the milled powder is not homogeneous in terms of nanostructure and plastic stored energy, abnormal grains will form and rapidly grow at the expense of the UFG.

- Increasing the content of titanium and yttrium increases the precipitates fraction and therefore the Zener pinning pressure on grain boundaries. This induces an increase in the temperature above which abnormal growth occurs. If this temperature is higher than that necessary to consolidate the powder, abnormal growth can be avoided and a homogeneous and ultrafine microstructure can be obtained. Also, increasing the solute content gives rise to an increase in the ratio between ultrafine and coarse grains and a decrease in the size of the UFG. The critical grain size of ultrafine grained ODS steel responds to the following criterion:

$$\begin{cases} R_c^{ODS} = C^{ODS} \times \frac{r_p}{f_p} \\ C^{Zener} = {}^4/_3 \leq \boldsymbol{C^{ODS} \approx 0.71} \leq C^{Rios} = {}^1/_6 \end{cases} \tag{4.25}$$

Since the fraction and the size of the UFG in bimodally structured metallic materials can govern the mechanical properties, this comprehensive relationship between the solute content and the UFG is of great importance. This could be applied to accurately tailor the mechanical properties of ODS ferritic steels.

## 4.4 Conclusion

This aim of this thesis was to control and limit abnormal grain growth in ODS ferritic steels using short thermo-mechanical treatments. Despite of both high heating rates and short soaking time during SPS processing, abnormal grains appeared at temperatures above 850°C, which are necessary to efficiently consolidate the powders. Thanks to *in situ* thermal annealing in Synchrotron facilities, the grain growth behavior was characterized upon heating. It was demonstrated that abnormal grains are recrystallized grains that almost instantaneously grow once the critical temperature (T = 850°C) is reached. It is though complex to conclude whether these "recrystallized" grains are new nuclei or existing grains with low stored energy or

specific orientations. Considering other experimental evidences such as EBSD orientation and intragranular deformation maps, the grains must be rather undeformed (well recovered) grains that grow at the expense of the others, the latter being more deformed. This statement confirms the observations of strain-induced boundary migration (SIBM) proposed by Toualbi [47].

Whereas the kinetics of this phenomenon was determined and the major reason was understood (difference in stored energy), the atomic/microscopic mechanisms leading to the formation of abnormal grains are still unknown. This would necessitate systematic TEM investigation of grain boundaries upon heating, mainly focusing on the grain boundaries / particles interactions. Specially, if the precipitation of oxides is completed before the critical temperature of secondary recrystallization, how could the grain boundary pass through the high density of particles? Is the appearance of an abnormal grain a matter of the local particle interdistance? These are open questions that N. Sallez thesis may answer [213].

# Chapter 5

# Characterization and modeling of oxides precipitation in steels

*The precipitation kinetics of nano-particles during hot processing of ODS steels was modeled using the nucleation, growth, coarsening theory. Two different numerical models were used to study the precipitation of $Y_2O_3$ and $Y_2Ti_2O_7$. Numerical results are compared to experimental nanoscale characterization.*

*Related published article: [G].*

## Contents

# 5.1   Introduction

Oxide-dispersion strengthened (ODS) steels owe their good high-temperature mechanical properties to a fine dispersion of nano-sized oxides that act as efficient obstacles for dislocations and grain boundaries. Depending upon the chemical composition and the consolidation technique and parameters, various kinds of oxides have been reported in the literature. Among the most interesting are yttrium oxides $Y_2O_3$ and ternary oxides $Y_2Ti_2O_7$. The latter were observed to give rise to better mechanical properties due to an increased number density of the precipitated particles. They have been the subject of numerous characterization studies at the nanoscale, including transmission electron microscopy, small-angle scattering (neutron or X-rays) and more recently atom-probe tomography. What is widely recognized is that these nanoparticles exhibit an extraordinary thermal stability, even at temperatures close to the solidus of the ferritic matrix. Very recently, nanoscale to atomic scale studies were used to bring some insight into this coarsening resistance. One theory highlights the role of a large amount of oxygen vacancies ($\approx 10\%$) that stabilize the clusters [172]. Another by Ribis and de Carlan demonstrated that the morphology of the particles $Y_2Ti_2O_7$ evolve upon heating in order to minimize their energy within the system [137]. The shape transition from spherical to cubical geometry was described as a way to reduce the elastic distortion created at the interfaces. Typically, the $\gamma - \gamma\prime$ particles in Nickel-base superalloys [214] show this type of behavior: the phases change from single cuboidal precipitates into doublets of plates, then into octets of cubic phases, and so on. For instance, Khachaturyan determined the elastic energy of the $\gamma\prime$ phases as a function of their morphology [215]. Thus, it seems that the elastic energy governed by the misfit between the precipitates and the matrix can influence the precipitation of these fine particles.

Based on these observations, the benefits of having a precipitation model are quite straightforward. First, since the particles are nanosized, the characterization can be tedious, expensive and sometimes subject to controversy. Being able to predict the precipitation state (at least the mean radius and the number density of the particles) as a function of the thermo-mechanical treatments will be precious, specially to estimate the mechanical properties. Also, the modeling tools are excellent means to understand things. For precipitation, the role of yttrium diffusion, the influence of the elastic misfit during nucleation and further growth or coarsening, the role of vacancies on the particles stability are not well understood yet. Of course these metallurgical issues are complex and finding their solution would necessitate both experimental investigations at nanoscale and fine modeling tools at atomic and mesoscopic scales. Indeed, various models may be used to simulate the solid-state precipitation in metallic materials. Readers are referred to [216] for an elaborate review of solid-state precipitation theories and associated calculation algorithms. Three main categories are distinct and complementary. First of all, the predictive models like DFT (density functional theory) or Monte

Carlo tend to determine analytically the behavior of the material at the atomic scale. Then, semi-predictive models aim at simulating the precipitation behavior at longer time. Calphad-based commercial program such as ThermoCalc or Matcalc use combined thermodynamic database and diffusion database to model solid-state precipitation in multi-components systems. Finally, JMAK-type (Johnson-Mehl-Avrami-Kolmogorov) phenomenological models allow to kinetically describe the level of thermally activated phase transformation (recrystallization, precipitation) based on physical (activation energy) and no physical (arbitrary coefficients) parameters. These different kinds of model involve complementary time and space scales. JMAK models are useful for modeling phase transformation in large components and occurring for hours and longer time but encounter difficulties to reproduce non-isothermal treatments and physical mechanisms [217]. At the opposite, atomistic models are powerful tools to understand physical mechanisms but the time scale is reduced to approximately $10^{-6}$ s and involve very long time calculation for a limited number of atoms [218, 219]. For precipitation, a good compromise consists of thermokinetic model using the nucleation, growth and coarsening theories. This kind of model is described in the next section.

Classic thermodynamic modeling consists in calculating the driving force of the formation of a possible compound (phase) from a supersaturated solid solution. In ODS steels, some controversial studies lead to contradictory conclusions on whether yttrium, oxygen atoms transform into a solid solution in the iron matrix. Indeed, mechanical alloying involves far-from-equilibrium mass transport, local heating, cold welding and other mechanisms that are difficult to model. To try to understand what occurs during milling, the usual method is to follow step by step the evolution of the initial yttria powder and the iron matrix. Indirect methods that are typically used are: X-ray and neutron diffraction for phase detection and lattice parameter calculation, transmission electron microscopy, atom-probe tomography and small-angle X-ray or neutron scattering for following up the evolution of the nanofeatures within the milled powder. From recent studies by atom-probe tomography, clustering of yttrium and titanium-rich particles was observed after a certain milling time [220, 221, 164]. This is not surprising since perfect solid solution is always hard to achieve, especially for highly non soluble elements. However, the community mainly agrees with the fact that these subnanometric clusters are quite homogeneously distributed in the powders. Also, after annealing or consolidation at high temperature, the clusters tend to crystallize and form stoichiometric phases [137, 58, 172, 222]. Thus, the starting point before high-temperature consolidation still deals with the need of diffusion-governed atoms transport to form well-defined, crystalline precipitates. In this sense, one chose in this study to use a classic continuous precipitation model based on the nucleation, growth and coarsening theory.

The possible second phase particles in oxide-dispersion strengthened steels are numerous. Some are enriched in undesirable impurities such as aluminum or silicon and appear to be much coarser than targeted nanoparticles. Also, various intermetallic Y-Fe phases can form in iron, as recently reported by Kardellass [223].

Complex ionic compound Y-O-Fe can also form in the system [224]. In contrary, the finest dispersoids found so far in ODS steels appear to be either $Y_2O_3$ or more recently $Y_2Ti_2O_7$ or other equivalent phases like $YTiO_5$. A tendency of what is reported in literature is the refinement effect of titanium [96]. The very first published work on this system was that of Guisca in 1939, who prepared the mixed oxide $Y_2Ti_2O_7$ and showed that the phase had a face-centred pyrochlore-type structure [225]. They suggested that a continuous solid solution range between $Y_2Ti_2O_7$ and $Y_2O_3$ might exist. Theoretically, the fluorite structure is stable only when the cation/anion radius ratio is greater than 0.73. Ault *et al* noticed in 1966 that in the $TiO_2$-$Y_2O_3$ fluorite phase, if the cation radius is taken to be the average of the radii of the yttrium and titanium ions, the ratio is always less than 0.73 and becomes even smaller as the percentage of yttrium oxide decreases, with a consequent decrease in the stability of the structure [226]. Thus, this could be the cause of the change-over from the fluorite to the pyrochlore phase. Meanwhile, other complex oxides such as orthorhombic $Y_2TiO_5$ were entirely described by Mumme *et al* [227]. In two high-chromium steels containing aluminum (4.5 wt%) with and without titanium, Hsiung *et al* observed solely complex Ti-free $Y_4Al_2O_9$ and a few $YAlO_3$ and concluded that under the presence of aluminum, titanium did not influence the precipitation state of nanoparticles in steels. A complete list of forming oxides in steels can be found in [228]. In the mentioned work, Chinnappan found by thermodynamic assessment that the most negative formation enthalpies are those of oxides which are the most often reported in literature, that is $Y_2O_3$ and $Y_2Ti_2O_7$. By now, no relevant study allowed the community to understand clearly the thermodynamic effect of titanium on the formation and further stability on the resulting nano-oxides. Since the thermodynamic stability of compounds does not inform about the precipitation kinetics of the phases and their further thermal stability, a kinetic model based on classic nucleation, growth and coarsening theories has been applied on these systems.

A previous work on nanoclusters $Y_2O_3$ precipitation kinetic was performed by Hin *et al* [229]. Since $Y_2O_3$ is only one phase among others in ODS steels and since $Y_2Ti_2O_7$ has more importance in last generation Y-Ti-O containing ODS steels, we propose here to go further by studying the precipitation kinetics of the complex Y-Ti-O nanoparticles which are known to be more finely and densely distributed than $Y_2O_3$. In this work, a more representative and realistic precipitation state in ODS steels is considered. **Three phases than can be seen as reference compounds in ODS steels are studied: coarse $TiO_2$ and fine $Y_2O_3$ and $Y_2Ti_2O_7$.**

## 5.2 Materials and Methods

The material of this study is the reference material with the chemical composition recalled in Table 5.1. Various consolidation cycles were performed, further followed by heat treatments (Fig. 5.1).

118

**Table 5.1:** Mean Composition (in wt%) of the milled powder

| Fe | Cr | W | Y | O | Ti |
|------|------|-----|------|------|------|
| bal. | 13.9 | 1.0 | 0.16 | 0.15 | 0.32 |
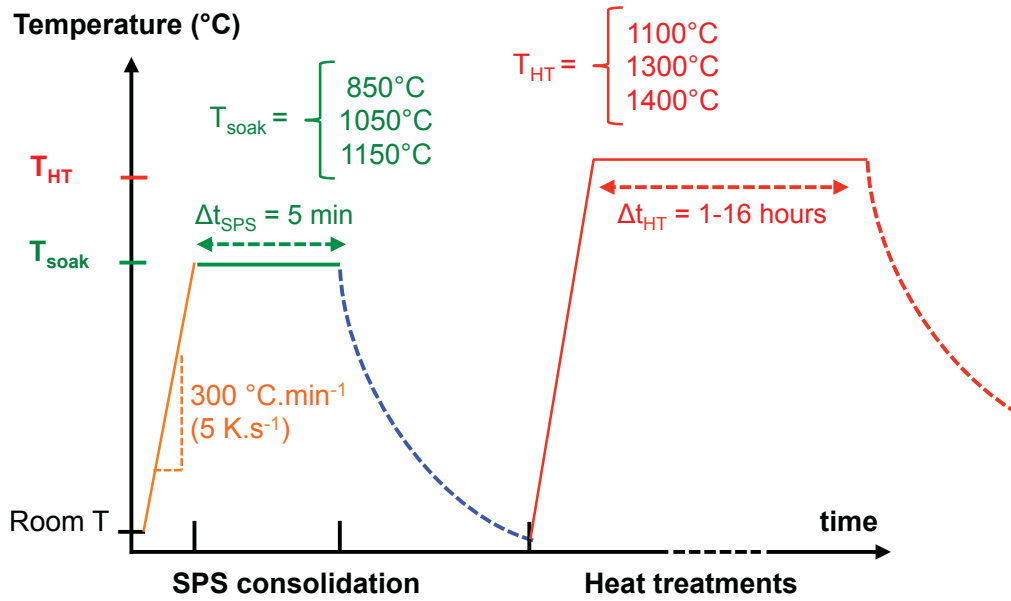


**Figure 5.1:** SPS consolidation and heat treatments performed on the samples investigated at the nanoscale.

The microstructure was characterized by a scanning electron microscope (SEM) Zeiss Supra 55 VP with field-emission gun (FEG) associated with an electron backscatter diffraction (EBSD) Oxford system for orientation and grain size measurement. Acquisition step size ranged from 10 to 60 nm with a tension of 15 kV.

Transmision Electron Microscopy (TEM) characterization was performed on an apparatus TEM JEOL 2010F equipped with an Energy Dispersive X-Ray Spectroscopy (EDX) XMAX 80 for chemical analysis.

Small-Angle Neutron Scattering (SANS) experiments were performed at the Laboratoire Léon Brillouin CEA Saclay. The experimental setup is recalled in [107]. SANS was performed to determine the volume fraction and density of particles with a mean radius ranging from 1 to 15 nm.

Atom Probe Tomography samples were prepared using a FEI Helios microscope equipped with a Focused Ion Beam, and APT analyses were made on a IMAGO LEAP 3000XHR, with laser or electric pulses. Analysis were realized at 50 K, with a pulse fraction of 20% and a pulse rate of 200 Hz.

# 5.3 Nanoscale characterization of oxides precipitation

As mentioned in the previous section, the precipitation plays a significant role on the abnormal growth and more specially on its thermal stability. Consequently, a focus was made on the particles that influence the grain growth, specially the nanosized oxides.

## 5.3.1 Small-angle neutron scattering (SANS)

Small-angle neutron scattering finds numerous applications in materials science, from fundamental studies (spinodal decomposition in unstable alloys) to microstructure evolution in complex industrial alloys. Able to detect inhomogeneities disturbing the coherent scattering within a medium, this technique is used in studies at interatomic distances up to the micronic scale. This allows the characterization of precipitates, point or linear defects and fluctuation of chemical composition as well [230]. The major interest resides in the electronic neutrality of the neutrons that do not interact with the electronic irradiated elements, which gives rise to two main advantages:

(i) The non destructive analysis in a much larger probed volume than that from X-Ray scattering (more than 50 mm$^3$ against less than 1 mm$^3$ for X-ray scattering). This brings higher guarantee of representativeness of the detected precipitation state, specially in the case of heterogeneous distribution.

(ii) The scattering contrast is better for light elements than with X-Ray scattering.

SANS experiments were performed at the Laboratoire Léon Brillouin CEA Saclay, using the PAXY small angle scattering spectrometer for high resolution in q-space, under strong magnetic field (1.7 Tesla). As mentioned in [87], a magnetic field of magnitude 1.2 T is sufficient to separate the magnetic and nuclear contributions. SANS experiments were set to determine the distribution of particles smaller than 15 nm in radius. This corresponds to a scattering vector $q$ between 0.1 and 1.6 nm$^{-1}$. This was obtained by selecting neutron wavelengths of 0.6 and 1 nm ($\pm$ 10% due to monochromator dispersion) and a distance between sample and detector of 2 and 5 m, respectively. A 2D detector with area $64 \times 64$ cm$^2$ was used to collect scattered neutrons. Recently, the technique has emerged as a powerful tool for nanoscale characterization of oxide-dispersion strengthened (ODS) steels, often associated to TEM analysis [161, 231, 87]. As detailed in [165], a direct modeling was used in the current study. The scattering function was calculated for a given distribution of nano-scatterers and compared to the experimental function. A least squares method was used to obtain the best fitting parameters. The particles were assumed spherical - even some can have cuboidal or ellipsoidal shapes [137] - and of constant chemical composition. Particle mean radius $r_m$ of the scattering population was calculated assuming a normalized number density function of radii $h(r)$. Given these assump-

tions, one can write the scattering intensity as:

$$I(q,r) = \Delta\rho^2 N_p V_p^2 F_{sph}(q,r) S(q,r) \tag{5.1}$$

where $N_p$ is the scatterers density, $V_p$ the volume of a scattering particle, $\Delta\rho$ the variation in diffusion length densities between the matrix and the scatterers. $F_{sph}(q,r)$ is the shape factor for spheres:

$$F_{sph}(q,r) = \frac{3\left[sin(qr) - qrcos(qr)\right]^2}{(qr)^3}$$

$S(q,r)$ is the structure factor resulting from the particles interaction. If the volume fraction of precipitates is observed to be less than 1% (diluted system), $S(q,r)$ tends to 1. A Gaussian distribution of spherical particles was chosen for direct modeling:

$$h(R) = \frac{1}{\sigma\sqrt{2\pi}} \frac{e^{-(r-r_m)^2}}{2\sigma^2} \tag{5.2}$$

Considering that the matrix is ferromagnetic, one can verify the global chemical composition of the nano-scattering particles by decoupling the nuclear and magnetic contrasts [161, 165]. Indeed, the scattering ratio A is given by:

$$A = 1 + \frac{\Delta\rho_M}{\Delta\rho_N}^2 \tag{5.3}$$

where $\Delta\rho_M$ and $\Delta\rho_N$ are the magnetic and nuclear contrasts, respectively. Regarding ODS steels, the ratio $A$ depends upon the composition of the steel and the nature of the oxides. In Fe-14Cr steel, typical values are 2.5 for pyrochloric structure $Y_2Ti_2O_7$ and 3.2 for cubic $Y_2O_3$, as demonstrated in [165]. The main drawback of this indirect method is that two different populations of scatterers can give rise to the same signal. Thus, complementary characterization methods such as transmission electron microscopy or atom probe tomography may be necessary to accurately describe the precipitation state. The SANS experiments were carried out during 4 different beam times of 2 to 5 days. The samples were characterized from the milled powder, to consolidated materials and eventually further heat treated. Probed samples are summarized in Table 5.2. Normalized magnetic intensities of SPS and HIP samples are reported in Fig. 5.2 and Fig. 5.3, respectively.

The initial powder contains few nanofeatures detected by SANS. It can be either fragmented yttria particles or clustered yttrium oxides. This was already observed by others in high-energy milled powders [27, 30]. They do not constitute evidences of crystalline yttrium oxides but rather express the deviation of the as-milled state from a perfect solid solution.

SANS data give rise to interesting conclusions. First, the formation of nanosized particles occurs at both low temperature and short consolidation time, since a high density of particles is detected in the sample SPSed at 850°C for 5 min. Particles
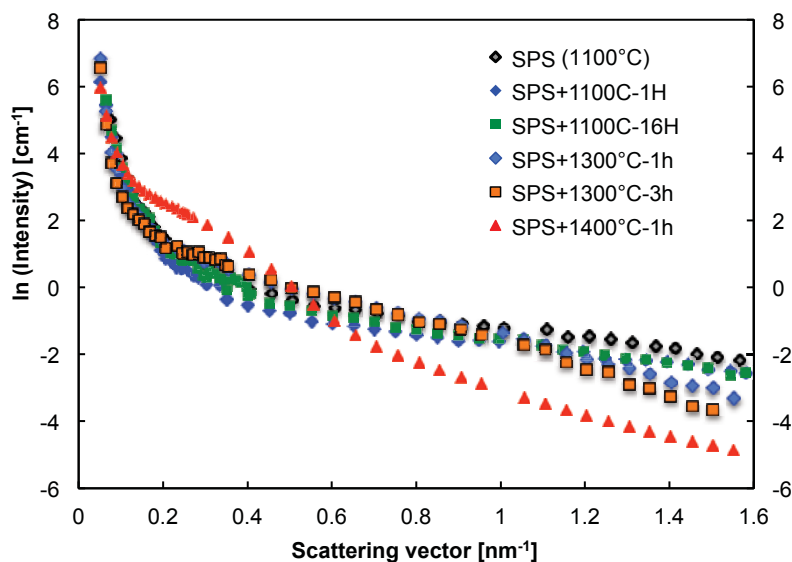
**Figure 5.2:** Measured magnetic intensity as function of scattering vector for various SPS samples.
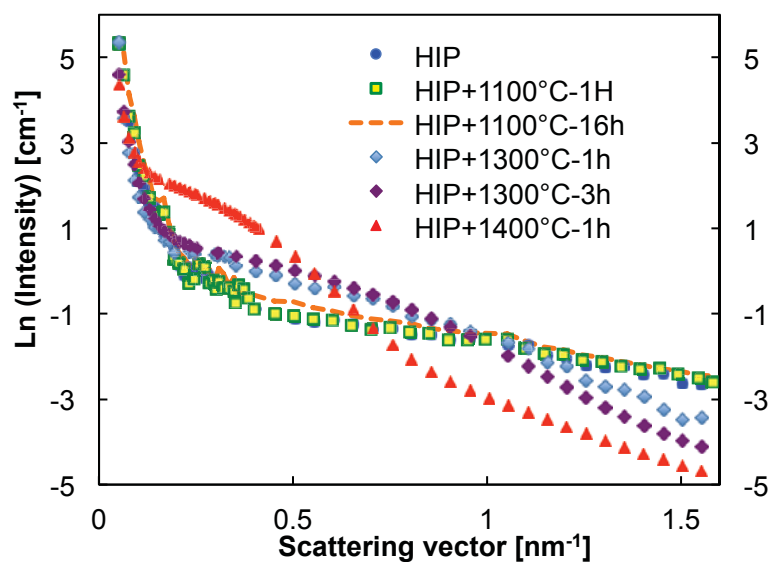


**Figure 5.3:** Measured magnetic intensity as function of scattering vector for various HIP samples.

formed during SPS or HIP have constant mean radius and number density after heat-treating at 1100°C. These particles are thus probably fully nucleated after SPS consolidation. Mean radii of particles after SPS and HIP are 1.4 and 1.6 nm, respectively. These particles seem to be smaller than those found in ODS-Fe9Cr reinforced with $Y_2O_3$ after SPS investigated by Heintze *et al* [87]. This is consistent with the refining effect of titanium [96]. At 1100°C, the detected particles begin to coarsen since number density decreases. Clear coarsening occurs at very high temperature, that is 1300 and 1400 °C. This gives rise to both a decrease of the number density and an increase of the mean radius, consistent with the growth of larger oxides that consume the smaller ones (Oswald ripening).

**Table 5.2:** SANS characterization of ODS steels processed by SPS and HIP

| Consolidation and heat treatment (ht) | Mean radius [nm] | Density [m$^{-3}$] | $A$-ratio |
|---|---|---|---|
| As-milled powder | $1.4 \pm 0.2$ | $1.3 \ 10^{23}$ | 1.4 |
| SPS 850°C ($\phi = 20$ mm) | $1.0 \pm 0.2$ | $1.6 \ 10^{24}$ | 2.1 |
| SPS 1050°C ($\phi = 20$ mm) | $1.2 \pm 0.2$ | $9.7 \ 10^{23}$ | 2.2 |
| SPS 1150°C ($\phi = 20$ mm) | $1.2 \pm 0.4$ | $9.7 \ 10^{23}$ | 2.2 |
| SPS 1150°C ($\phi = 60$ mm) [1] | $1.4 \pm 0.3$ | $1.2 \ 10^{24}$ | 2.2 |
| SPS 1150°C + ht 1100°C-1h | $1.6 \pm 0.4$ | $5.4 \ 10^{23}$ | 2.3 |
| SPS 1150°C + ht 1100°C-16h | $1.8 \pm 0.4$ | $3.9 \ 10^{23}$ | 2.2 |
| SPS 1150°C + ht 1300°C-1h | $4.0 \pm 1.1$ | $2.8 \ 10^{22}$ | 2.5 |
| SPS 1150°C + ht 1300°C-3h | $4.6 \pm 1.4$ | $2.2 \ 10^{22}$ | 2.2 |
| SPS 1150°C + ht 1400°C-1h | $5.2 \pm 1.4$ | $1.1 \ 10^{22}$ | 2.2 |
| HIP 1150°C | $1.2 \pm 0.2$ | $9.0 \ 10^{23}$ | 2.1 |
| HIP 1150°C + ht 1100°C-1h | $1.2 \pm 0.4$ | $1.7 \ 10^{23}$ | 2.1 |
| HIP 1150°C + ht 1100°C-16h | $1.4 \pm 0.4$ | $1.1 \ 10^{23}$ | 2.6 |
| HIP 1150°C + ht 1300°C-1h | $2.2 \pm 0.8$ | $2.0 \ 10^{22}$ | 2.1 |
| HIP 1150°C + ht 1300°C-3h | $2.4 \pm 0.7$ | $1.2 \ 10^{22}$ | 2.1 |
| HIP 1150°C + ht 1400°C-1h | $4.2 \pm 1.3$ | $1.5 \ 10^{22}$ | 2.2 |

SANS investigation led to the following conclusions:

- Precipitation of most likely nano-oxides occurs very rapidly (in a few minutes) during SPS processing, even at the lowest temperature (850°C).

- These particles are quite stable at 1100°C, which explains the similarities in precipitate state between SPS and HIP ODS ferritic steels. At higher temperatures, particles size increases whereas the density decreases, which tends to prove that coarsening occurs at 1300 and 1400°C.

## 5.3.2 Transmission electron microscopy (TEM)

Even if SANS data are precious to determine the precipitation kinetics of nanoparticles, this only gives global values: mean radius, number density, and $A$-ratio related to the chemical composition of the scattering particles. In order to identify the nature of these particles and how they are distributed in the consolidated samples, direct observations are necessary. Thus, complementary TEM observations were carried out by Sophie Cazottes (MATEIS) on 3 samples: (i) SPS at 850 °C, (ii) SPS at 1150 °C and (iii) SPS at 1150 °C and then annealed at 1100°C for 16 hours. This section describes the precipitation state observed by TEM and the microstructure as well, since the two influence each other.

### 5.3.2.1 After consolidation at 850°C
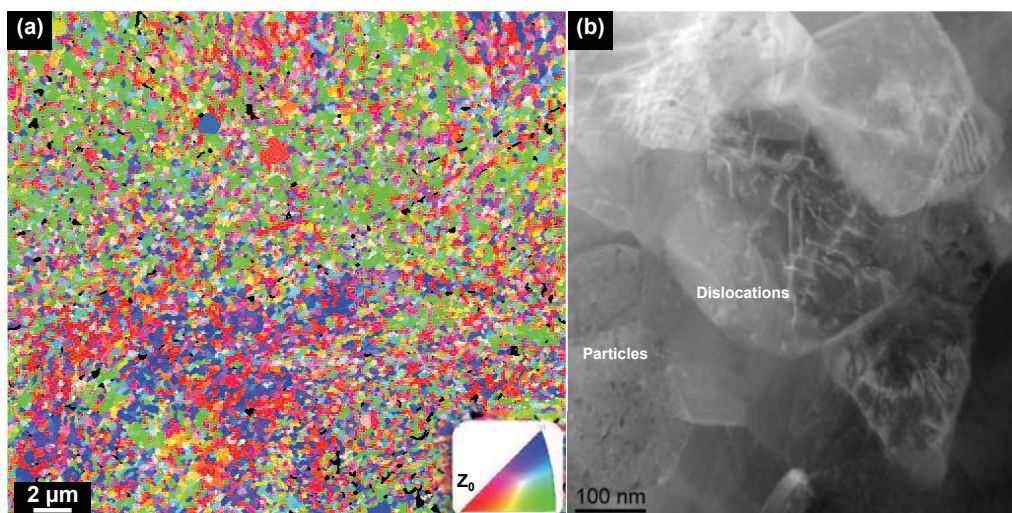


**Figure 5.4:** (a) EBSD map of the ODS SPSed at 850°C and (b) Ultra-fine grains observed by TEM-ADF (Annular Dark Field)

The microstructure of the consolidated material at 850°C is reported in Figure 5.4. The material is composed of ultrafine grained regions with grains with a diameter down to 50 nm (Fig. 5.4(b)). Since these ultrafine grains (UFGs) contain numerous dislocations, they originate from the initial nanostructure and cannot be small recrystallized grains. Dislocation density is still very high and dislocations walls are visible within the grains. Some UFGs seem to be weakly disoriented with neighbors, as highlighted in Fig. 5.4(b).

At this stage, nanosized particles are visible in some UFGs. This observation is consistent with SANS data that confirmed the presence of nanosized precipitates in the ODS SPSed at 850°C. This precipitation is intragranular in this micrograph. When scanning the sample, sparse "coarse" grains with more than 1 $\mu$m in diameter are detectable. They are isolated and surrounded by UFGs. They are at the

124

origin of the abnormal structure obtained at higher temperature and it is of interest to characterize their precipitation state. This was done on few coarse grains (Fig. 5.5(d)). Nanosized particles are also present in these coarse grains. The particles size distribution has been determined in the coarse grain by image analysis and reported in Fig. 5.6. The mean radius is 1.2 nm, which is consistent with SANS data (1.4 nm). Due to their size, the chemical composition cannot be accurately quantified by classic EDX. We will discuss their chemistry based on the atom-probe tomography experiments. An example of high-resolution TEM on a nanoparticle located in the coarse grain is given in Fig. 5.5(c). In this particular case, a slight ellipsoidal shape was found, with an elongation factor close to 1.3. This ellipsoidal shape was also found in extruded PM2000 alloy [232].
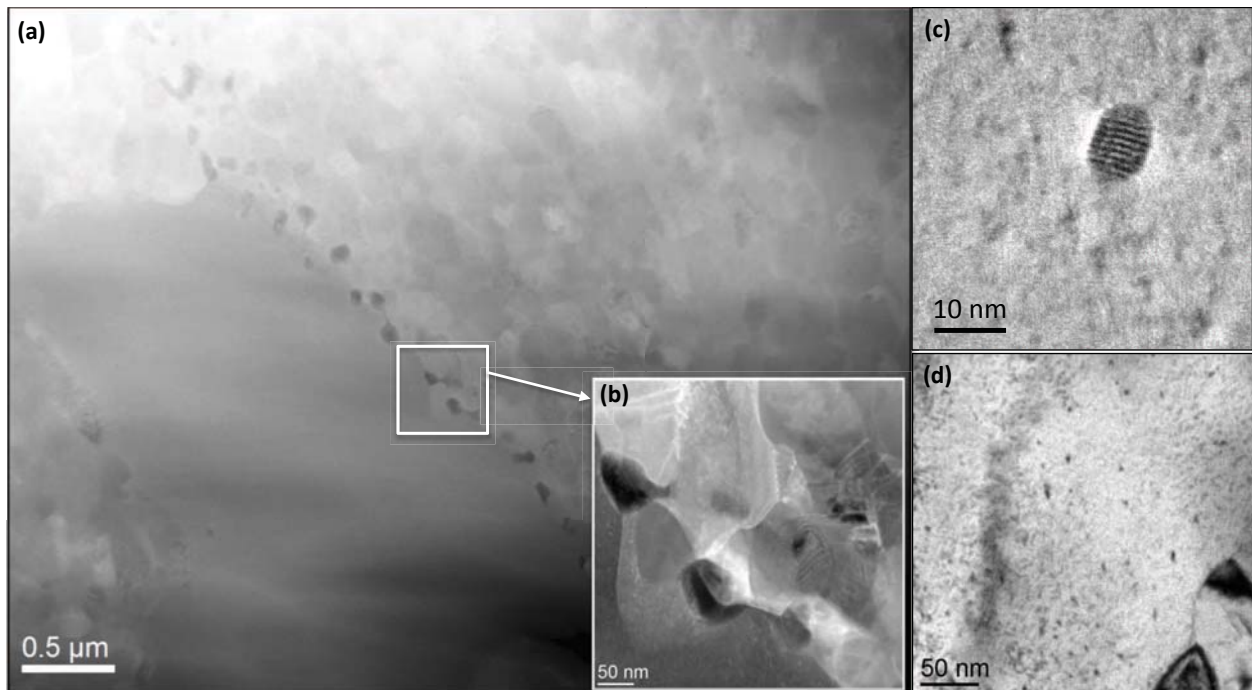


**Figure 5.5:** (a) TEM-HAADF image on an abnormal grain surrounded by ultrafined (UFG) to nanosized grains (b) Inset on particles located on the grain boundary between the coarse grain and the UFGs (c) HRTEM image of a coherent nanoparticle located in the coarse grain (d) two-beam image of nanoparticles in the coarse grain

The grain boundary at the right side of Fig. 5.5(a) is densely decorated by second-phase particles. These particle have a diameter up to $\approx$ 80 nm (Fig. 5.5(b)), which is much higher than that of conventional nanosized oxides widely reported in ODS steels. Energy dispersive X-Ray spectroscopy (EDX) indicates that the composition is mainly titanium and oxygen, most likely $TiO_x$ with $x$ varying from 1 to 2 (Fig. 5.7). It seems that there is a correlation between the morphology and the chemical composition of theses particles: elongated rods-like particles have a ratio $x_{Ti}/x_O$ above 1 whereas this ratio is less than 1 for the spherical particles (#5 and #6).
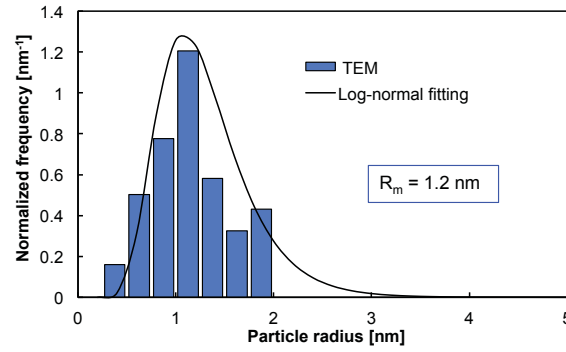
**Figure 5.6:** Experimental particles size distribution in ODS SPSed at 850°C determined by image analysis of TEM micrographs and fitted log-normal distribution.

Titanium and oxygen have a high diffusion coefficient in $\alpha$-ferrite (see equation (2.1) and Fig. 2.19). Consequently, atoms of the two species can rapidly combine to form a new phase. Besides, the formation of $TiO_x$ is not only kinetically favorable but also thermodynamically stable [233, 228]. Indeed, the enthalpy formation is very negative, as we will discuss in the modeling part. The formation of coarse oxides is also most likely favored by grain boundary diffusion at powder particles interfaces. This hypothesis is consistent with observations in Fig. 5.8. Indeed, aligned coarse precipitates lie not only on grain boundaries of few coarse grains but are also observed throughout utrafine grained zones. In the latter case, it is highly doubtful that this alignment is related to any metallurgical grain boundary but rather to former powder particles interfaces. There might be several origins of the presence of these coarse oxides at grain boundaries. The most probable reason is that a mobile grain boundary can move (during grain growth) and drag particles with it until the number of oxides is high enough to efficiently pin the grain boundary and stop its migration.

126

| EDX | #1 | #2 | #3 | #4 | #5 | #6 |
|---|---|---|---|---|---|---|
| Ti [at %] | 42.0 | 25.5 | 25.6 | 33.6 | 29.1 | 22.5 |
| O [at %] | 30.8 | 24.6 | 14.1 | 26.7 | 47.9 | 39.2 |
| Y [at %] | < 0.5 | < 0.5 | < 0.5 | < 0.5 | < 0.5 | < 0.5 |
| Al+Si [at %] | < 1 | < 1 | < 1 | < 1 | < 1 | < 1 |
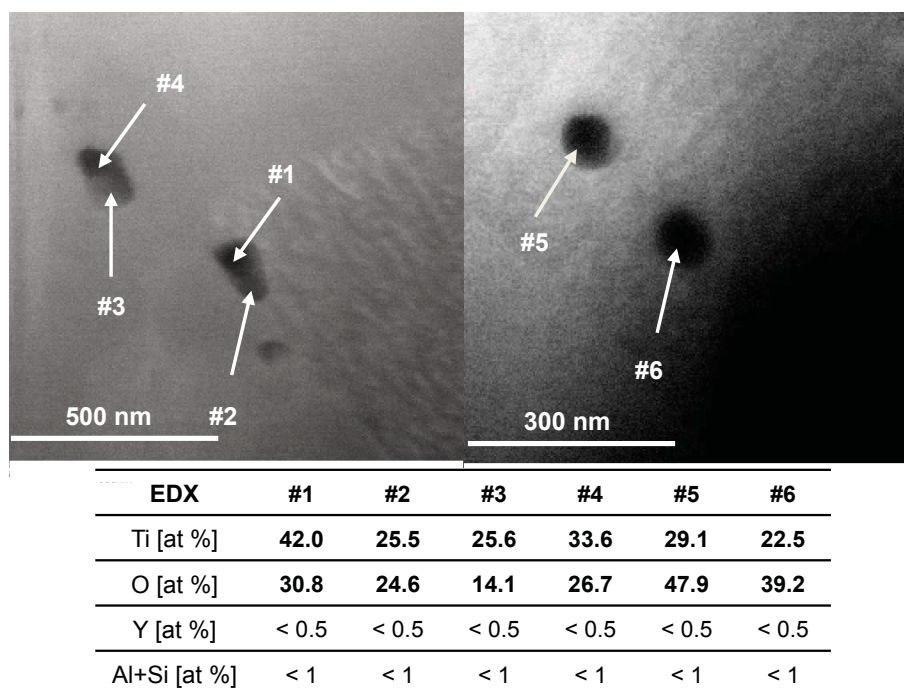
**Figure 5.7:** Chemical composition of coarse particles with various geometries in ODS SPSed at 1150°C.
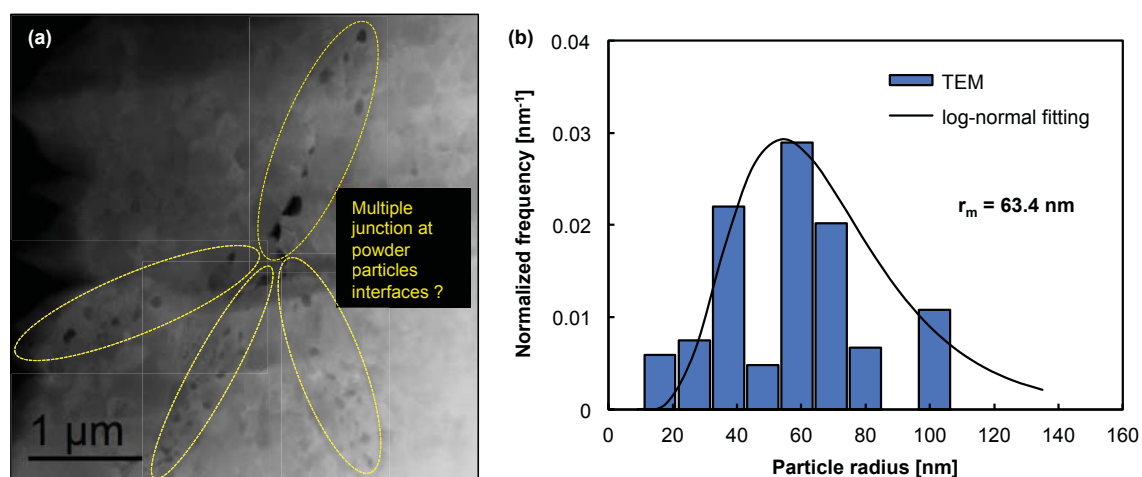


**Figure 5.8:** Alignment of coarse particles in ODS SPSed at 850°C. Few lines of precipitates converge into what is most likely a multiple junction between former powder particles.

### 5.3.2.2   After consolidation between 900°C and 1150°C

Above a processing temperature of 900°C, the consolidated material is systematically composed of ultrafine grained zones combined with coarse grains with a diameter of few microns. As an example, the microstructures of consolidated ODS steels at 1050°C and 1100°C are reported in Figure 5.9.
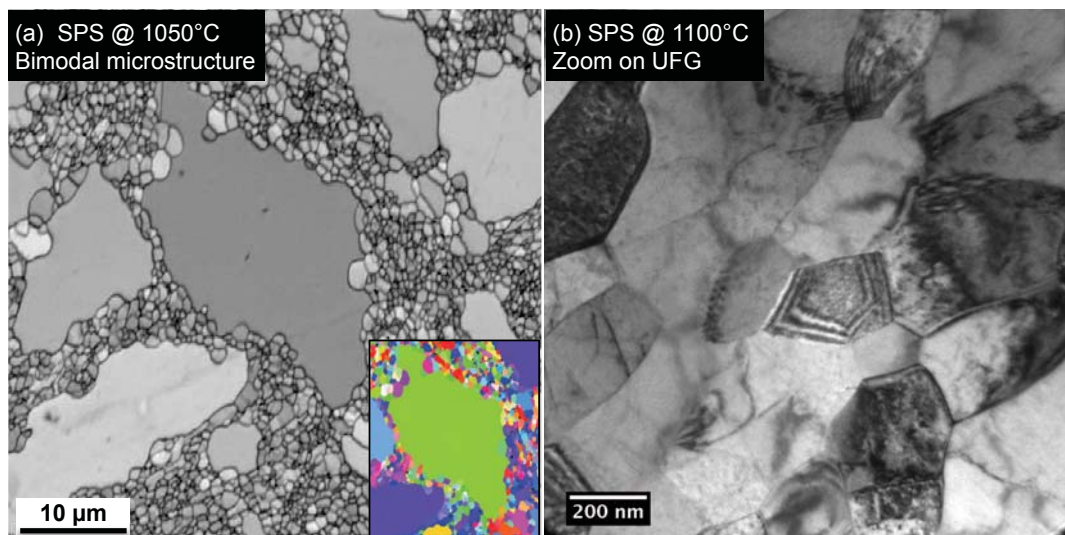


**Figure 5.9:** (a) Band contrast EBSD map of an ODS steel consolidated at 1050°C for 5 min. Inset: Orientations of the center coarse grain and neighboring ultrafine grains (b) TEM image of ultrafine grains.

Similarly to what was observed in Fig. 5.4(b), ultrafine grains are still present with a diameter down to 50 nm (Fig. 5.9(b)). This saturated grain size was previously explained by the efficient pinning effect of nanosized to 50 nm-particles partly located on grain boundaries [107]. Both nanoparticles and coarser particles are observed as well (Fig. 5.10). The coarse precipitates were identified as titanium oxides, as in the sample SPSed at 850°C.

Since it is of prime importance to verify whether the particles distribution is homogeneous within the microstructure, TEM characterization was performed in both coarse grains and ultrafined grains. As illustrated in Fig. 5.11, both types of grains contain a high density of nanoparticles.

An attempt to quantify the nanoparticles number density is reported in Fig. 5.12. Although the representativeness of these measurements are debatable, the size distributions are quite similar in ultrafine and coarse grains. Lots of dislocations were found in the grains, interacting with precipitates. Thus, heterogeneous nucleation on dislocations is highly probable. The rapid precipitation of populous nanoparticles is most likely a key factor of the limited dislocation annihilation. Somehow, the synergistic combination between high dislocation density and high density of particles enhances the stability of this metallurgical state.

128
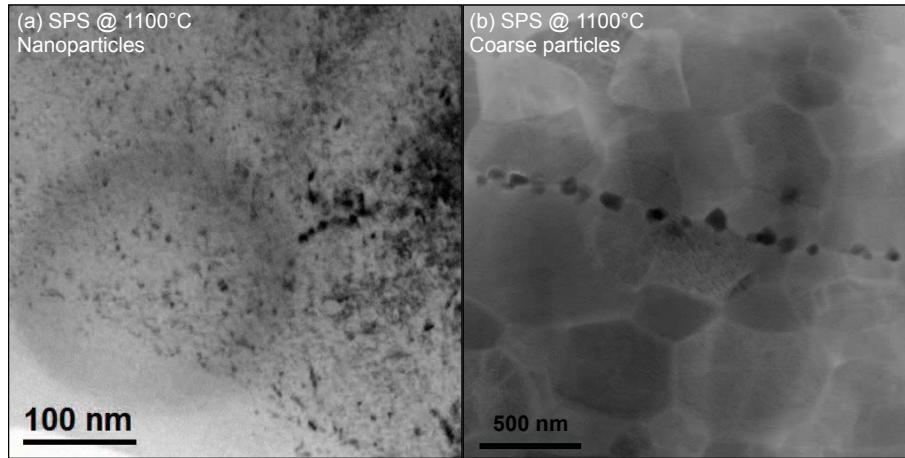
**Figure 5.10:** (a) Bright field TEM image of nanoparticles in a coarse grain (D > 1 $\mu$m) (b) TEM image of coarse particles in ultrafine grains.
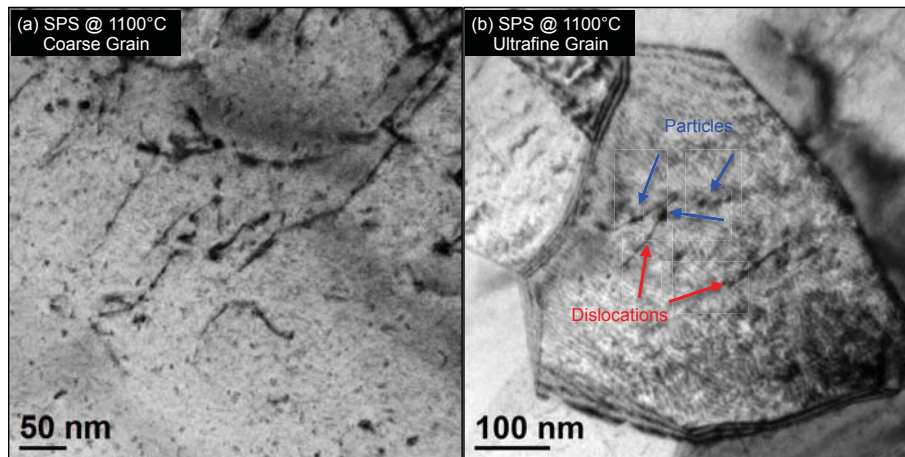


**Figure 5.11:** (a) Nanoparticles in a coarse grain and interacting with dislocations (b) TEM image on nanoparticles in ultrafine grains. Some of these are also located on dislocations.
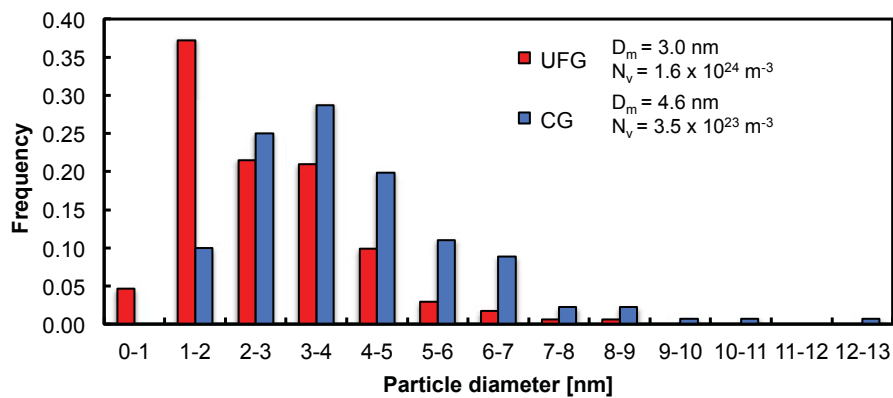


**Figure 5.12:** Precipitate size distribution measured in ultrafine grains (UFG) and coarse grains (CG) of the ODS steel SPSed at 1100°C.

129

### 5.3.2.3 Post-consolidation annealing: thermal stability at 1100°C
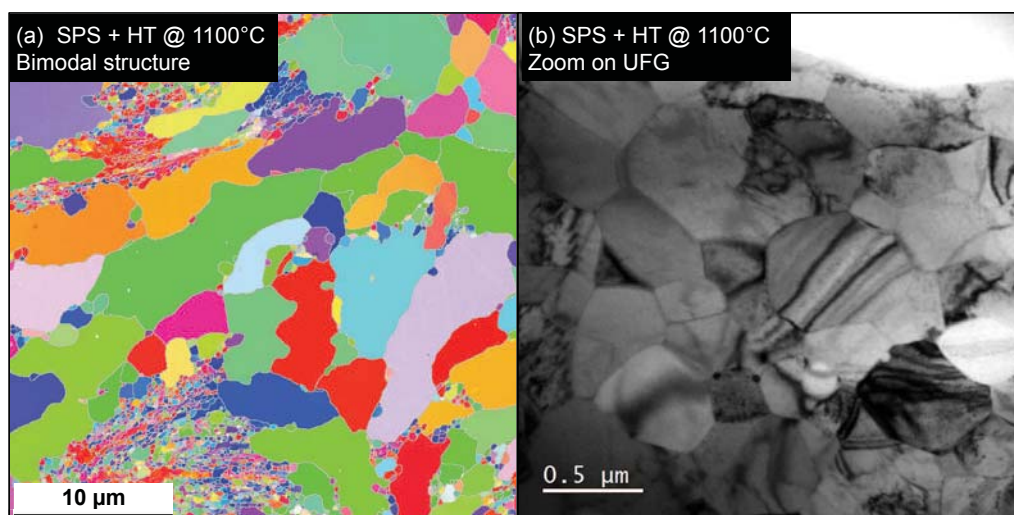


**Figure 5.13:** EBSD map orientation of ODS steel SPSed at 1150°C and annealed at 1100°C for 16 hours (b) Zoom on ultrafine grains in the same sample.

Annealing treatment was performed under vacuum at 1100°C for 16 hours. Again, the bimodal microstructure is still present and composed of numerous ultrafined grains (Fig. 5.13).

The precipitation state is similar to that before the annealing, which shows the extreme stability of the particles in both ultrafine and coarse grains. The heterogeneity of the precipitation is emphasized in this sample. Various types of coarse oxides were observed, mainly at grain boundaries (Fig. 5.14). The EDX investigation confirms that they are titanium oxides but also enriched in silicon and aluminum.



| | Ti | O | Y | Al | Si | Mn |
|------|----|----|-----|-----|-----|-----|
| 2-10 | 43 | 54 | 0.4 | 2.1 | 0.7 | / |
| 2-11 | 43 | 55 | / | 1.0 | 1.2 | / |
| 2-13 | 63 | 35 | / | 1.5 | / | / |
| 2-14 | 56 | 18 | 6.8 | 0.5 | 0.5 | / |
| 2-15 | 54 | 30 | / | / | 0.7 | 1.5 |
| 2-16 | 55 | 41 | / | 1.1 | / | 2.8 |
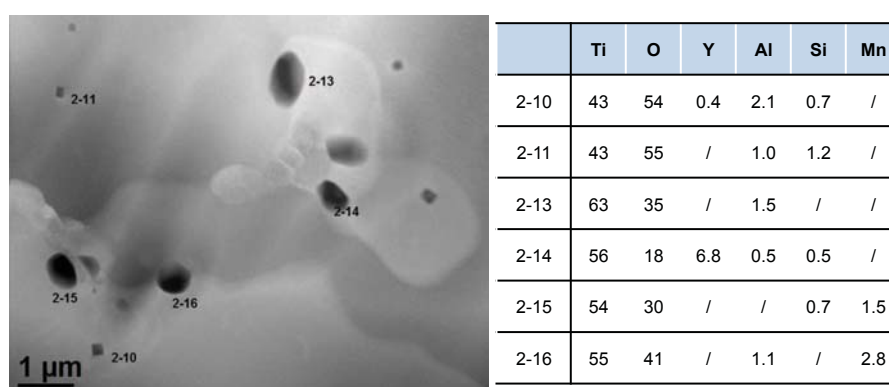
**Figure 5.14:** Bright field TEM image of coarse particles and corresponding chemical composition determined by EDX.

Regarding the nanoparticles, evidence of precipitates trapping on dislocations is given in Fig. 5.15 and Fig. 5.16. In some grains, a dense network of both precipitates
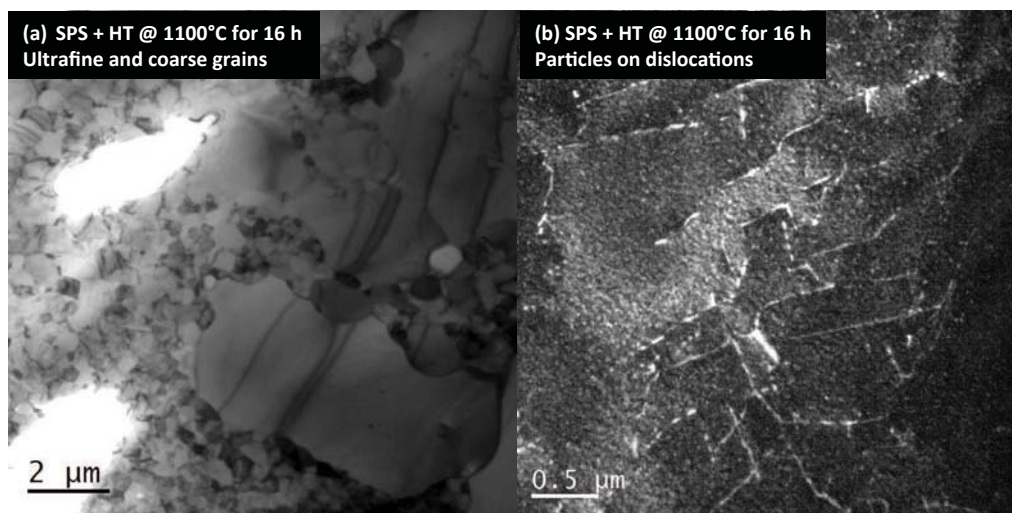
**Figure 5.15:** (a) Bright field TEM image of ultrafine grained region with some coarse grains (D>1$\mu$m) (b) TEM dark field of aligned nanoparticles on a dislocations network.
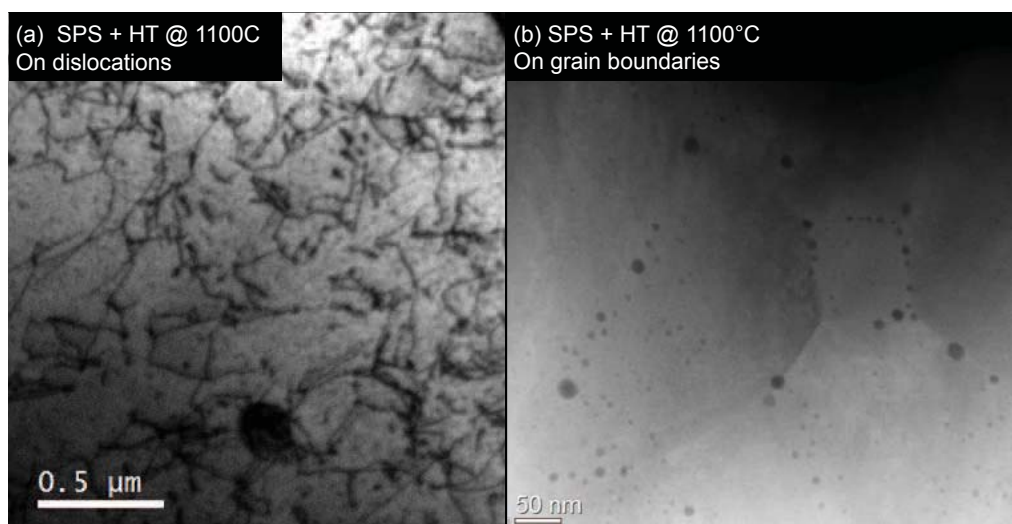


**Figure 5.16:** (a) Bright field TEM image illustrating the strong interaction between the particles and the dislocations (b) Nanoparticles aligned on grain boundaries of UFGs.

and dislocations can be observed, confirming the stability of these two interacting populations (Fig. 5.16(a)). After annealing, there is an abundant precipitation at grain boundaries, more significant that just after consolidation (Fig. 5.16(b)). This was particularly observed in ultrafine grained regions.

### 5.3.2.4 Identification of the nanosized particles

Fine particles were detected all over the grains by High-Resolution TEM (HRTEM) or in two beam conditions. Indeed, the coherent character of the particles makes it difficult to visualize these nanoscale precipitates in conventional mode. When observing in two beam mode, the misfit between precipitates and matrix generates so-called Moiré fringes [137]. The distance between the fringes can be related to the interplanar distance of the planes generating the fringes with the following relationship: :

$$D^{fr} = \frac{d_p \cdot d_m}{|d_p - d_m|} \tag{5.4}$$

where $d_p$ and $d_m$ are the inter-reticular distance of the precipitate and the matrix, respectively. The precipitates observed and the orientation relationship (OR) found are in agreement with what was previously observed by Ribis and de Carlan [137] in an ODS steel extruded at 1100°C and then annealed at 1100°C. Three types of precipitates were detected in this sample:

(i) $Y_2Ti_2O_7$-type pyrochlore oxide with a face-centered cubic structure, with a lattice parameter $a = 10.1$ Å ;

(ii) the $Y_2O_3$-type yttria oxide with a body-centered cubic structure, with a lattice parameter $a = 10.6$ Å ;

(iii) $Y_2O_3$ with a fcc structure, with a lattice parameter $a = 5.2$ Å.

Note that the $Y_2Ti_2O_7$ cell is twice larger than the fcc $Y_2O_3$ cell. Figure 5.17 presents different kind of precipitates observed in the 16h annealed sample. Both coherent $Y_2O_3$ and $Y_2Ti_2O_7$ were identified.

On Fig. 5.18(a), two cuboidal fcc precipitates were evidenced presenting the following OR1 with the matrix:

$$\{100\}_{Fe} \parallel \{100\}_{fcc} \text{ and } <100>_{Fe} \parallel <100>_{fcc}$$

fcc being $Y_2Ti_2O_7$ or $Y_2O_3$. The lattice parameters of $Y_2Ti_2O_7$ and $Y_2O_3$ bcc phase are too close to strictly distinguish between the two phases. Fig. 5.18(b) presets a fcc $Y_2O_3$ precipitate observed in $(110)_{Fe}$ two beam conditions which presents the following OR2 with the matrix:

$$\{001\}_{Fe} \parallel \{001\}_{Y_2O_3} \text{ and } <110>_{Fe} \parallel <110>_{Y_2O_3}$$

A $Y_2Ti_2O_7$ precipitate presenting a cube-on-cube OR with the matrix is presented in Fig. 5.18(c), whereas smaller precipitates of the same type were also observed, see Fig. 5.18(d). It has to be noted that the predominant type of precipitates seem to be $Y_2O_3$. However, indexation was done on the larger precipitates (d > 5 nm), that are
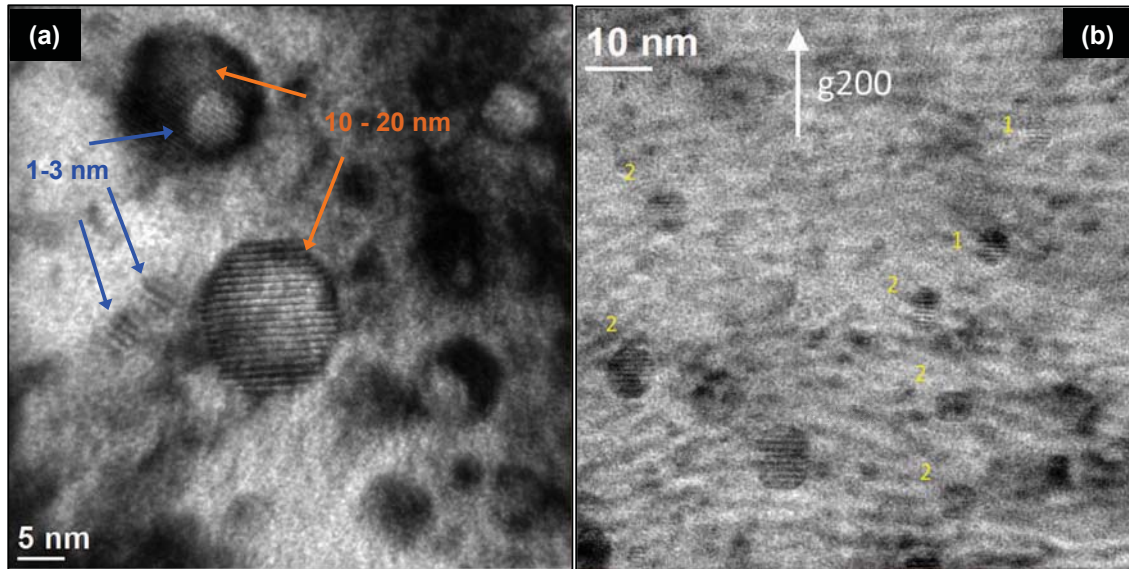
**Figure 5.17:** Nanoparticles observed in two beam conditions in the sample consolidated at 1100°C and annealed 16 h. (a) Various sizes of precipitates are found (b) Precipitates numbered 1 are fcc $Y_2O_3$ precipitates whereas precipitates numbered 2 are fcc $Y_2Ti_2O_7$ precipitates.

more easily detected, whereas the smaller particles (d < 2 nm) were more difficult to identify. When assuming that the ratio between $Y_2Ti_2O_7$ and $Y_2O_3$ is the same for small precipitates and large precipitates, $Y_2O_3$ would then be the predominant type of precipitates in this sample. It also appears preferentially with a spherical shape.

---

TEM investigation led to the following conclusions:

- TEM allowed the direct observations of the particles detected by SANS. They were observed in the three specimens SPS 850°C, SPS 1100°C and SPS 1100°C + HT 1100°C-16h.

- Nanosized particles are located in both ultrafine and coarse grains.. Indexation highlighted the presence of $\mathbf{Y_2O_3}$ and $\mathbf{Y_2Ti_2O_7}$ with orientation relationships consistent with recent literature.

- Lots of these particles are located on dislocations. This tends to prove that **heterogeneous nucleation** of oxides occurs during the consolidation.

- Coarse titanium oxides were observed in all investigated samples. They most likely nucleate at former powder particles boundaries.

---
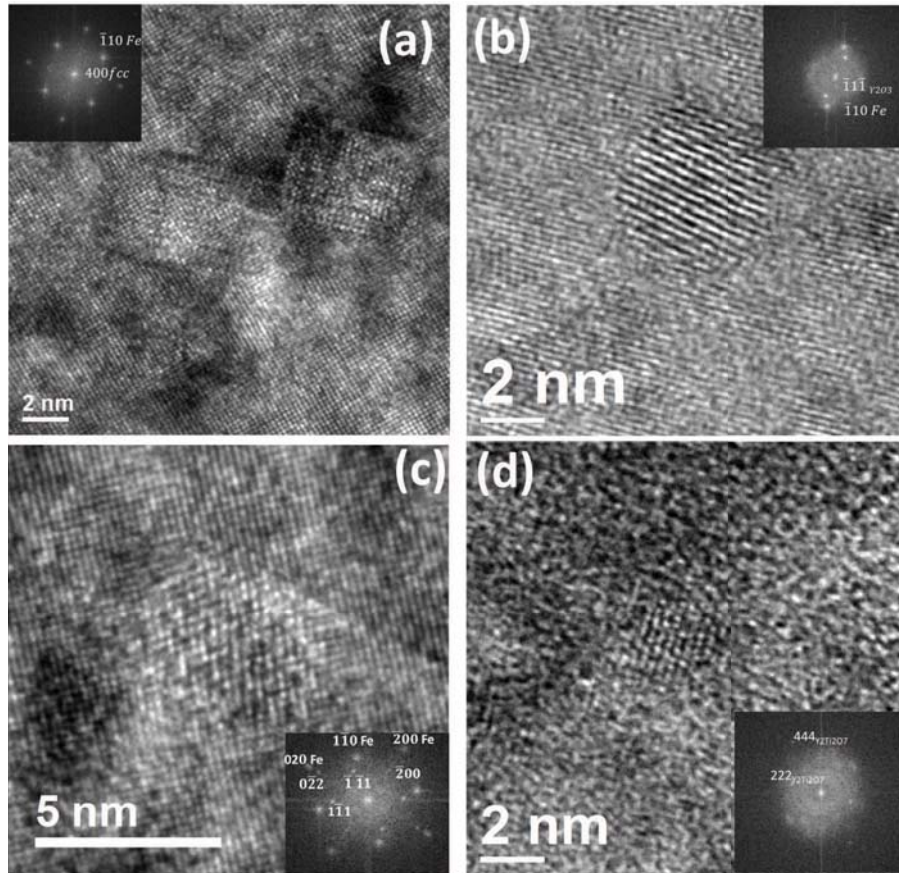
**Figure 5.18:** Nanoprecipitates observed in the 1100°C annealed sample: (a) 5-7 nm cuboidal fcc precipitates of $Y_2O_3$ or $Y_2Ti_2O_7$ type in OR1 with the matrix, (b) $Y_2O_3$ precipitate presenting OR2 relative to the matrix, (c) $Y_2Ti_2O_7$ precipitate presenting a cube-on-cube OR with the matrix, (d) 2.5 nm diameter $Y_2Ti_2O_7$ precipitate.

## 5.3.3 Atom-probe tomography (APT)

In order to determine the chemical composition of the precipitates, atom-probe tomography (APT) was performed on two metallurgical states: (i) after SPS at 850°C where the microstructure was homogeneous and ultrafine grained (see Fig. 5.19) and (ii) after SPS at 1100°C where the bimodal microstructure was clearly observed. A Lift-out method was used to mill the APT tips from the samples (Fig. 5.19).

The APT analysis was carried out using an Imago LEAP 3000 HR operating in laser pulsing mode. An APT specimen base temperature of 50 K was used with a laser energy of 0.4 nJ at a repetition rate of 200 kHz. The reconstruction volume of the tip from SPS 850°C is given in Fig. 5.20. There is no major clustering of yttrium atoms whereas titanium atoms have clearly diffused to form clusters. Also, a 'coarse' titanium oxide was detected with an equivalent diameter of 43 nm. This is not surprising given that numerous titanium oxides were detected at grain boundaries and within the bulk of ODS steels SPSed at 850°C and higher temperatures (see

134
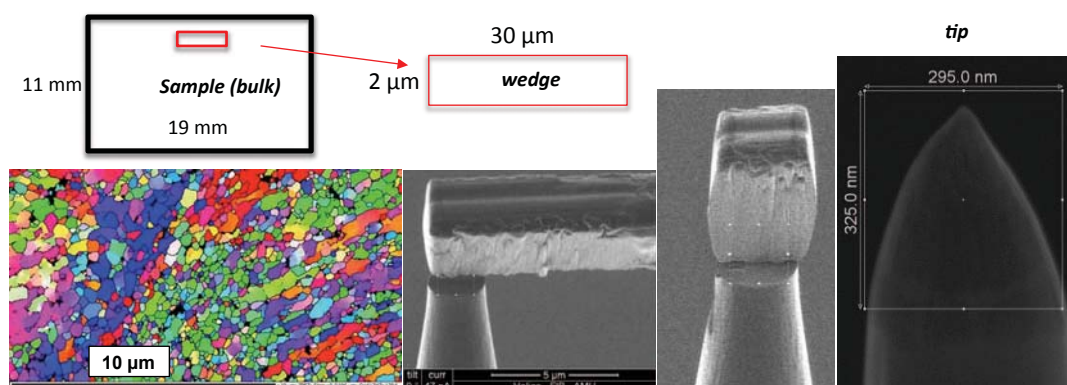
**Figure 5.19:** Lift-out method in the case of the tip from the sample SPSed at 1100°C.

TEM in Fig. 5.5 and Fig. 5.7). The composition of this oxide was measured as $Ti_{33}O_{60}Cr_{\alpha}Y_{\beta}$ with $\alpha + \beta < 10$, which tends to be the composition of $TiO_2$.
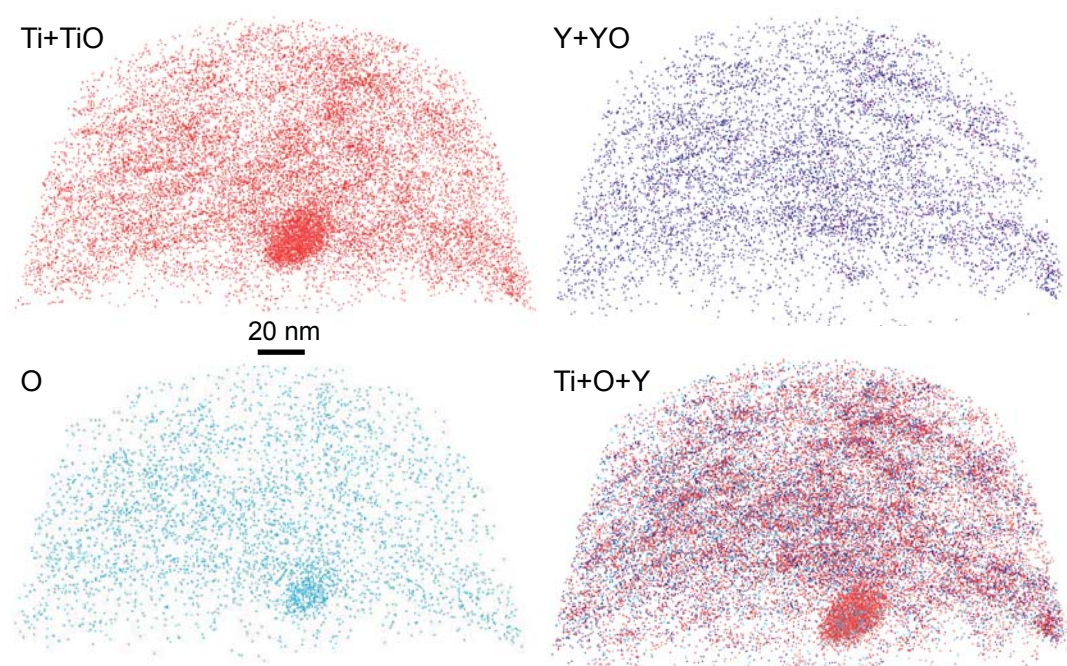


**Figure 5.20:** Reconstruction volume of the tip milled from the sample SPS 1100°C.

At the opposite, there is a much higher tendency of yttrium and oxygen atoms clustering in the ODS steel SPSed at 1100°C. In the Fig. 5.21, not only Ti and TiO ions but also Y and YO ions are seen in the nanoclusters. This demonstrates that yttrium diffusion is indeed lower than that of titanium and oxygen and most likely constitutes the diffusion limiting species for the formation of oxides.

This first analysis pointed out the presence of yttrium, titanium and oxygen in the clusters (Fig. 5.21). Then, a "nanocluster analysis" was performed on the two tips in order to study the composition and the size of the nanoparticles. This was
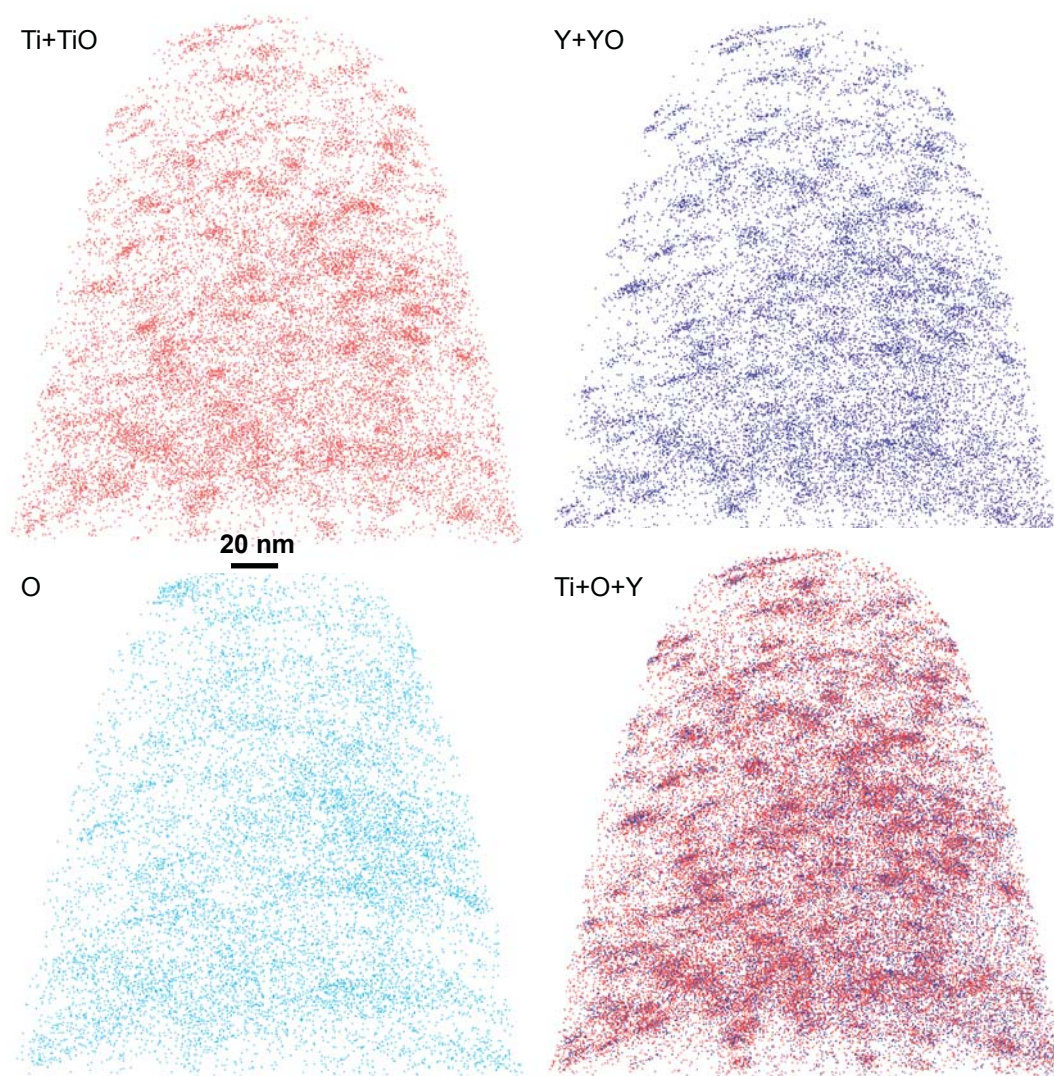
**Figure 5.21:** Reconstruction volume of the tip milled from the sample SPS 1100°C.

done using the 'maximum separation algorithm'. This consists in detecting particles or clusters within the matrix by an algorithm governed by different parameters. The analysis parameters were chosen after C. Williams [234]:

$$
\begin{cases}
D_{max} = 0.6 \text{ nm} \\
N_{min} = 8
\end{cases}
\tag{5.5}
$$

$D_{max}$ is the maximum distance between two atoms within a cluster. $N_{min}$ is the minimum number of atoms in a cluster. There is a step-by-step program to make these arbitrary parameters less arbitrary. This roughly consists in comparing the distribution of atoms in the tip to a fully random distribution. A complete description of this method can be found in [234]. The cluster analysis (CA) gives the number density of the detected clusters with the associated composition and size. The mean radius and number density from APT are 0.7 nm and 1.8 $10^{24}$ m$^{-2}$ in SPS 850°C and 0.7 nm and 3.7 $10^{24}$ m$^{-2}$ in SPS 1100°C. The mean radius is twice lower than that from TEM and SANS. The results from the CA are much more sensitive to subnanometric clusters compared to TEM, which can explain this discrepancy. Also, there is a large difference in the probed volume between APT and TEM, and at higher extent between APT and SANS. In this sense, SANS is much more representative than APT for number density and volume fraction. More relevant is the composition of the solid solution after extracting the clusters from the matrix (Table 5.3). The small content of yttrium remaining in solid solution is consistent with the onset of precipitation during consolidation. The amount of oxygen is still high and may come from either contamination during consolidation or from the APT data treating (segregation at grain boundaries or potential coarse oxides not extracted out from the measurement).

**Table 5.3:** Matrix composition [at%] in yttrium, titanium and oxygen from APT measurement. Measurements are estimated by removing the particles using the maximum separation method.

| Sample | Yttrium | Titanium | Oxygen |
|---|---|---|---|
| SPS 850°C | 0.09 | 0.21 | 0.22 |
| SPS 1100°C | 0.06 | 0.16 | 0.21 |

## 5.3.4 Conclusion of the precipitation characterization

Complementary techniques of characterization at the nanoscale were used to characterize the precipitation state in SPSed samples. The overall precipitation kinetics in term of mean radius and number density of the nanosized particles was determined by Small-angle neutron scattering. Further, TEM observations revealed that not only nanoparticles but also coarse oxides were formed during consolidation.

The precipitation of oxides after very short consolidation processes (few minutes instead of hours) like SPS had not been characterized yet. This study proved that oxides form very soon during processing since the maximum fraction of particles is obtained on SPSed samples with no further heat treatment. Also, the volume fraction and the mean radius of the nanosized particles are constant within the range of the consolidation temperatures, that is 850 to 1150°C.

To observe a difference in the precipitation state, annealing at higher temperatures is needed. Indeed, the treatments at 1100°C did not give rise to coarsening whereas the ones at 1300°C and 1400°C induced an increase in the mean radius and a decrease in the number density. This leads to the conclusion that ODS steels processed by SPS possess similar nanosized particles than conventional ODS steels and exhibit the same resistance to coarsening, at least at the consolidation temperature.

TEM observations showed than heterogeneous precipitation can occur on dislocations for nanosized particles and at grain boundaries for coarse titanium oxides. This complex precipitation is inherited from the powder metallurgy route:

(i) dislocations come from the milling process and the limited recovery due to solute drag and precipitation

(ii) grain boundary precipitation most likely occurs at former powder particles interfaces where oxygen is preferentially trapped and where titanium can rapidly diffuse during consolidation.

APT characterization confirmed the role of yttrium diffusion as a limiting factor for oxides growth and coarsening. Indeed, at low temperature, it seems that yttrium has not completely migrated into titanium-rich clusters. Consolidation or anneals at higher temperatures are needed to form complex YTiO particles. After consolidation at 1100°C, the content of yttrium remaining in solid solution is very low, highlighting the low solubility of yttrium in ferrite.

The amount of titanium in this alloy and more generally in ODS steels seems to be not fully optimized. Indeed, the titanium content is quite high, which results in the formation of coarse oxides due to both rapid diffusion and high affinity with oxygen.

# 5.4   Precipitation modeling

## 5.4.1   The Nucleation, Growth, Coarsening Theory (NGTC)

In this current study, the nucleation, growth, coarsening theory (NGCT) is used to model the precipitation behavior of both $Y_2O_3$ and $Y_2Ti_2O_7$.

The path to model the precipitation of a second phase within a host phase from a supersaturated solid solution of given solutes (here yttrium, oxygen, titanium) comprises the calculation of:

(i) the NUCLEATION RATE $dN/dt$ at which particles form ;

(ii) the GROWTH RATE $dR/dt$ of the nucleated particles ;

(iii) the COARSENING KINETICS during which the larger precipitates grow at the expense of the smaller ones that dissolve.

These key-steps are described in the next section.

### 5.4.1.1   Nucleation

The nucleation[2] theory is based on the calculation of the variation of the Gibbs free energy between a solid solution with no precipitates and the same system after the eventual nucleation of new precipitates. In other words, the driving forces representing the propensity of a given system to generate new phases must be favorable. Since a system will tend to change its microscopic state into another to loose energy, the driving force has to be negative. Classically, one admits that the creation of a daughter (forming) phase within the mother (host) phase costs energy because of the creation of an interface. One simple consequence is that the less perfect the interface, the more energy it costs. However, the system will overcome this energy cost if thereafter the whole Gibbs free energy is reduced. In the case of spherical particles, this competition between the volume energy against interface energy is illustrated by the following equation:

$$\Delta g_{tot} = \frac{4}{3}\pi R^3(\Delta g_{ch} + \Delta g_{el}) + 4\pi R^2\gamma \qquad (5.6)$$

The volume energy is thus defined by two components: the chemical driving force $\Delta g_{ch}$ and the elastic energy $\Delta g_{el}$. The later is rarely mentioned since its contribution can be negligible compared to the chemical driving force, or more likely because it is sometimes hard to quantify[3]. The influence of elastic energy in the case of oxides in steels will be discussed in section *5.6*.

---

2. From latin word *nucleus*, this can be few atoms.

3. My personal opinion is that the elastic energy classically requires Eshelby-like mechanical calculations whereas the NGCT is used by metallurgists.

Then, the nucleation critical radius that allows the Gibbs free energy to be maximized, thus above which the nucleus will be stable, is given by:

$$\frac{d\Delta G(R)}{dR}\Big|_{R=R^*} = 4\pi R^{*2}(\Delta g_{ch} + \Delta g_{el}) + 8\pi R^*\gamma = 0 \tag{5.7}$$

Which gives $R^*$:

$$R^* = \frac{-2\gamma}{(\Delta g_{ch} + \Delta g_{el})} \tag{5.8}$$

Please note that higher (in negative values) is the chemical driving force, smaller are the nuclei. At the opposite, higher the interfacial energy between the nuclei and the matrix, larger the critical nuclei. $\gamma$ and $\Delta ch$ somehow govern the area/volume ratio of the particles. Once $R^*$ is known, one can derive the thermodynamic barrier for nucleation:

$$\Delta G^* = \Delta G|_{R=R^*} = \frac{16}{3}\pi \frac{\gamma^3}{(\Delta g_{ch} + \Delta g_{el})^2} \tag{5.9}$$

Here, one notes that the interfacial energy plays a dramatic role on the energy barrier: increasing $\gamma$ of 10% will increase the energy barrier of 33%. The chemical driving force $\Delta g_{ch}$ can be calculated from the solid solution supersaturation $s$, which quantifies the excess of the solute elements compared to the amount needed to form the precipitates at the equilibrium. For a given precipitate, for instance $Y_2Ti_2O_7$, the supersaturation $s$ is given for a diluted regular solution by:

$$s = \ln\left(\frac{X_Y^2 X_{Ti}^2 X_O^7}{X_Y^{eq^2} X_{Ti}^{eq^2} X_O^{eq^7}}\right) \tag{5.10}$$

The driving force is logically proportional to this distance from equilibrium:

$$\Delta g_{ch} = \frac{-k_B T}{V_{mol}^p} \cdot s = \frac{-k_B T}{V_{mol}^p} \cdot \ln\left(\frac{X_Y^2 X_{Ti}^2 X_O^7}{X_Y^{eq^2} X_{Ti}^{eq^2} X_O^{eq^7}}\right) \tag{5.11}$$

$V_{mol}^p$ is the molar volume of the precipitate, $k_B$ the Boltzmann constant, T the temperature. $K_s = X_Y^{eq^2} X_{Ti}^{eq^2} X_O^{eq^7}$ defining the equilibrium is called the solubility product and is assumed to follow this form [4]:

$$\log_{10}(K_s) = \frac{1}{\ln(10)} \times \left(\frac{\Delta H_f - T\Delta S}{k_B T}\right) = -\frac{A}{T} + B \tag{5.12}$$

$K_s$ can be interpreted as the solubility limit of one element extrapolated at $n$ dimensions, $n$ being the number of species forming the precipitate. $A$ and $B$ are well known for nitrides [235], carbides [169, 236] and carbonitrides [237] in steels [56] or silicates in Aluminum alloys [141, 55]. At the opposite, $K_s$ is clearly unknown for

---

4. $Log_{10}$ rather than $ln$ is used in literature.

oxides in steels, as we will discuss later.

Once $\Delta G^*$ and $R^*$ are known, the nucleation rate is given by the Kampmann and Wagner's equation [170]:

$$\frac{dN}{dt} = N_0 Z \beta^* \exp\left(\frac{-\Delta G^*}{k_B T}\right) \cdot f(t,\tau) \tag{5.13}$$

$N_0$ is the number of nucleation sites available for the nuclei. If the precipitation is **homogeneous** and occurs wherever in the material, then $N_0 = 1/V_{at}^m$ where $V_{at}^m$ is the atomic volume of the matrix. In this hypothesis, one thus considers that any atom in the matrix can act as a nucleation site. However, in industrial alloys where numerous defects can constitute preferential sites for precipitates, $N_0$ is lower and is governed by the number of particular defects: dislocations [238], grain boundaries or existing second-phase particles like dispersoids [239]. In this case, the nucleation is referred as **heterogeneous**. Heterogeneous nucleation is the most realistic phenomenon that not only fits solid-state precipitation, but also most of physical phenomenon (see for instance rain in clouds [240] or bubbles in a glass of champagne or mineral water).

$\beta^*$ is the frequency at which atoms can migrate from interstitial position to another and equals to [241, 242]:

$$\beta^* = \frac{4\pi R^{*2}}{a^4}\left(\sum_i \frac{X_i^p}{D_i X_i}\right)^{-1} \tag{5.14}$$

where $a$ is the lattice parameter, $X_i^p$ the atomic fraction in the precipitate, $D_i$ the diffusion coefficient in the matrix and $X_i$ the atomic fraction in solid solution of the species $i$. The expression of $\beta^*$ is sometimes simplified and only the diffusion coefficient of the slowest element is taken into account. This simplification was used for precipitation of $Y_2O_3$ where yttrium was limitant for nucleation [122] [5]:

$$\beta^* \approx \frac{4\pi R^{*2}}{a^4}\frac{D_Y X_Y}{X_Y^p} \tag{5.15}$$

The incubation time function $f(t,\tau)$ varies in the literature. In the present model, $f(t,\tau) = 1 - \exp(-t/\tau)$ was used since it matches atomistic models for precipitation of carbonitrides in steels [235]. $\tau$ is the incubation time and is given by $\tau = 2/(\pi\beta Z^2)$ [242].

$Z$ is the Zeldovitch factor, which is given for the case of spherical particles by:

$$Z = \frac{V_{mol}^p}{2\pi R^{*2}}\sqrt{\frac{\gamma}{k_B T}} \tag{5.16}$$

---

5. $X_Y^p$ was actually omitted (neglected ?) in the original article.

where $V_{mol}$ is the molar volume of the precipitate.

To summarize, the nucleation at a given temperature $T$ is ruled by the driving force that depends on how far from equilibrium is the amount of solute elements in solid solution, which is given by the solubility product (eq. 5.11). Then, if nucleation occurs, its kinetics depends on the properties of both the matrix and the precipitates. The main factor for the matrix is the available nucleation sites, which can be for instance modified by the amount of plastic deformation (dislocations) in the case of cold-worked alloys. For the particles themselves, the influence of the interfacial energy $\gamma$ is significant since it dictates the energy barrier (eq. 5.9) and, at lower extent, the nucleation rate through the Zeldovich factor (eq. 5.16). Last but not least, the diffusion coefficients of the precipitating species, specially that of the slowest element, will determine the occurrence of nucleation (eq. 5.14). Consequently, the evolution of the diffusion coefficient of the slowest element with the temperature should be as accurate as possible for the modeling of nucleation.

### 5.4.1.2 Growth and coarsening

The growth of nucleated particles is then governed by diffusion. Like nucleation, diffusion-governed growth and coarsening are thermally activated. The temperature dependence is traduced by the diffusion coefficient that follows the Arrhenius law:

$$D_i(T) = D_i^0 \times \exp\left(\frac{-Q_i}{R_g T}\right) \tag{5.17}$$

where $D_i^0$ is the pre-exponential factor in $m.s^{-2}$, $Q_i$ the activation energy in $J.mol^{-1}$, $R_g = 8.314$ $J.K^{-1}.mol^{-1}$ the gas constant and $T$ the temperature in K.

For spherical particles of radii $R$ of composition $Y_2Ti_2O_7$:

$$\begin{cases} \frac{dR}{dt} = \frac{D_Y}{R} \frac{X_Y^m - X_Y^i(R)}{\alpha X_Y^p - X_Y^i(R)} \\ \frac{dR}{dt} = \frac{D_{Ti}}{R} \frac{X_{Ti}^m - X_{Ti}^i(R)}{\alpha X_{Ti}^p - X_{Ti}^i(R)} \\ \frac{dR}{dt} = \frac{D_O}{R} \frac{X_O^m - X_O^i(R)}{\alpha X_O^p - X_O^i(R)} \end{cases} \tag{5.18}$$

where $\alpha$ is the ratio between the atomic volume of the matrix $V_{at}^m$ and of the precipitate $V_{at}^p$. $D_Y$, $X_Y^m$, $X_Y^p$ and $X_Y^i(R)$ are the diffusion coefficient of yttrium in $\alpha$-iron, the atomic fraction of yttrium in solid solution, in the precipitate and at the interface, the latter being dependent of the radius $R$.

Indeed, the solubility product is modified by the curvature of the precipitate and thus depends on the precipitate radius. The solubility in the presence of small particles with a large ratio of surface area to volume is larger than that for larger ones [170]. This is due to the minimization of the interfacial energy that is actually

142

higher for smaller precipitates. This size-dependence is called the Gibbs-Thomson effect and is traduced for the case of $Y_2Ti_2O_7$ by equation (5.19) [243]:

$$X_Y^{i^2}(R)X_{Ti}^{i^2}(R)X_O^{i^7} = K_s \cdot exp\left(\frac{2\gamma V_{mol}^p}{R_g k_B T}\right) \quad (5.19)$$

This gives rise to coarsening, which is traduced by a general increase in the mean radius when smaller particles are diluted into the larger ones[6]. During this process also commonly referred to as Ostwald ripening, the precipitate number density can be reduced from $\approx 10^{25}$ m$^{-3}$ to less than $10^{19}$ m$^{-3}$ in typical two-phase alloys during aging [170]. Even if the coarsening process is considered to be confined to the latest stages of precipitation, it may accompany the growth process or may even start while the system is still in its nucleation period, depending on the initial supersaturation of the solid solution.

## 5.4.2 Application to ODS steels using *PreciSo*

*PreciSo* is a precipitation software primarily developed by M. Perez and co-workers [242, 241]. A complete description of the adopted approach can be found in french in [244]. This is a semi-predictive model based on the nucleation, growth and coarsening theories of solid-state precipitation described previously. Thus, its operating requires the input of thermodynamical data that have to be determined experimentally: the solubility product of the precipitates, the interfacial energy and the diffusion coefficients of the alloying elements. This is a multi-class model that easily permits to couple the precipitation state to strengthening model for the prediction of the yield strength (see [125] for its application on aluminum alloys). Also, this kind of model takes into account the particle size distribution and not only predicts the global values. For instance, Deschamps *et al* successfully used a mean radius approach to predict the precipitation kinetics of second phase particles in aluminum alloys [118] but demonstrated that this type of model was limited for complex non-isothermal treatments involving dissolution at constant mean radius [245].

In this model, it is assumed that :

- The chemical composition of the precipitates is constant: the particles are stoichiometric $Y_2O_3$ or $Y_2Ti_2O_7$.

- The precipitation is homogeneous. There is no preferential nucleation on defects such as dislocations or grain boundaries.

- The precipitates are isotropic and spherical.

- The misfit elastic energy due to the precipitates is negligible compared to the chemical driving force (see eq. 5.7).

---

6. Coarsening is different than coalescence. Coalescence induces a migration of particles that merge together to form larger particles. This phenomenon requires high precipitate phase fraction with enough mobility to encounter and merge.

- The interfacial energy does not depend neither on the temperature nor the precipitate size. Its size dependency is discussed in [246].

- The chemical composition of the alloy is somehow spatially constant, which can be questionable when dealing with inhomogeneities in consolidated materials.

- The boundary conditions at the interface are given by the local equilibrium: the solute content at the interface matrix/precipitate is given by the solubility product.

- The diffusion process that governs the precipitate growth is ruled by the diffusivity of the slowest element, that is yttrium. This is applied to the model only if the condition $\{\forall \text{ element i, } D_Y^\alpha/D_i^\alpha < 10^{-4}\}$ is verified.

- The particles size distribution is described by the evolution of $N_i$ and $r_i$, which are the precipitates number density ($\text{m}^{-3}$) and the radius of the class $i$.

Given this, the thermodynamic system can be defined by the **diffusion coefficients** of the solutes in $\alpha$-iron, the **interfacial energy** between the precipitates and the matrix, and the **solubility product** of the precipitates in $\alpha$-iron. The solubility product of oxides in steels is not well known because both oxygen and yttrium are not soluble in iron, which make yttrium oxides very stable in the studied temperature range (from room temperature to the solidus temperature of steel). In between, it is very difficult to determine the evolution of the amount of solute elements in the matrix with temperature and thus to derive the solubility product. Similarly, the diffusion coefficient of yttrium in iron has not been accurately measured. This makes oxide precipitation modeling not straightforward. Recently, the precipitation kinetics of binary Y-O oxides in ferritic alloys has been modeled by Hin *et al* using a NGCT-based model [122]. The parameters $A$, $B$, $D_Y(T)$ and $\gamma$ were all fitted with experimental data (mean radius and number density) from Alinger's Phd [121]. The latter were collected with small-angle neutron scattering (SANS) on an ODS ferritic steel with 0.13 at% yttrium and 0.18 at% oxygen [121]. The parameters were found to be:

$$\begin{cases} ln(K_s^{Y_2O_3}) = -\frac{29200}{T} + 1.33 \\ \gamma = 0.4 \ J.m^{-2} \\ D_Y(T) = 10^{-5} \times exp\left[\frac{-314 \ [kJ.mol^{-1}]}{R_gT}\right] \end{cases} \qquad (5.20)$$

**Solubility product:** In 2014, Chinnappan *et al* performed first principle calculations of the enthalpy formation of oxides in steels [228]. Considering that the formation enthalpy $\Delta G_f$ is related to the solubility product of a forming phase $K_S$ by :

$$\log(K_S) = \frac{1}{\ln(10)} \times \left(\frac{\Delta H_f - T\Delta S}{k_BT}\right) = -\frac{A}{T} + B \qquad (5.21)$$

Thus, the parameter $A$ was derived from Chinnappan's calculation whereas $B$ was fitted. All the thermodynamic and thermokinetic parameters are given in Table 5.4.

**Table 5.4:** Thermodynamic and diffusion parameters from literature and used for the precipitation model of $Y_2O_3$ and $Y_2Ti_2O_7$.

| | Parameter | Value | | Source |
|---|---|---|---|---|
| | lattice parameter | $a = 2.886 \times 10^{-10}\ m$ | | XRD [This work] |
| | atomic volume | $v_{at}^{\alpha} = 1.202 \times 10^{-29}\ \mathrm{m^3}$ | | XRD [This work] |
| | diffusion coefficient | $D^0\ \mathrm{[m^2.s^{-1}]}$ | $Q\ \mathrm{[J.mol^{-1}]}$ | |
| | yttrium | $D_Y^0 = 1 \times 10^{-5}$ | 299102 | [247] |
| $\alpha$-ferrite | titanium | $D_{Ti}^{\alpha} = 0.21$ | 293200 | [248] |
| | | $D_O^{\alpha} = 4 \times 10^{-5}$ | 166942 | [249] |
| | | $D_O^{\alpha} = 2.9 \times 10^{-7}$ | 89500 | [250] |
| | oxygen | $D_O^{\alpha} = 4 \times 10^{-5}$ | 161129 | [247] |
| | | $D_O^{\alpha} = 3 \times 10^{-5}$ | 139193 | [This work] |
| BCC $Y_2O_3$ | atomic volume | $v_{at}^{Y_2O_3} = 1.49 \times 10^{-29}\ \mathrm{m^3}$ | | [This work] |
| | solubility product | $\log(K_S) = -20000/T - 4$ | | |
| | | $\gamma^{Y_2O_3} = 0.35\ \mathrm{J.m^{-2}}$ | | TEM [137] |
| | interfacial energy | $\gamma^{Y_2O_3} = 0.4\ \mathrm{J.m^{-2}}$ | | [247] |
| | | $\gamma^{Y_2O_3} = 0.60\ \mathrm{J.m^{-2}}$ | | [This work] |
| Pyrochlore type $Y_2Ti_2O_7$ | atomic volume | $v_{at}^{Y_2Ti_2O_7} = 9.9 \times 10^{-30}\ \mathrm{m^3}$ | | [This work] |
| | solubility product | $\log(K_S) = -19000/T - 25$ | | |
| | interfacial energy | $\gamma^{Y_2Ti_2O_7} = 0.25\ \mathrm{J.m^{-2}}$ | | TEM [137] |
| | | $\gamma^{Y_2Ti_2O_7} = 0.48\ \mathrm{J.m^{-2}}$ | | [This work] |

**Interfacial energy:** The fitted interfacial energy, $0.4\ \mathrm{J.m^{-2}}$, was discussed to be consistent with semi-coherent particles. A close value was found by Ribis *et al* ($0.35\ \mathrm{J.m^{-2}}$), based on the comparison between TEM observations and further calculations using simplified solutions of Eshelby's inclusion problem [137]. Yet, the value of the interfacial energy is fully model-dependent. Specially, Ribis took into account the elastic energy (competing with the chemical driving force) whereas Hin did not, *de facto* creating a bias between the two studies. Interestingly, Barnard *et al* [251] determined the interfacial energy by *ab initio* calculations and found $3.06\ \mathrm{J.m^{-2}}$, which is far much higher than the previous values.

**Yttrium diffusion coefficient:** The yttrium coefficient not only governs the nucleation onset but also determines the growth rate. Indeed, since it is the slowest solute element in the precipitate compared to titanium and oxygen, it will regulate the diffusion from the matrix into the precipitate. The 'calculated' diffusion coefficient of yttrium in $\alpha$-iron suggested that yttrium diffused 400 times lower than iron self-diffusion at 850°C [229], which confirmed the role of yttrium as diffusion-limitant species for the precipitation process[7]. There is no reliable direct experimental mea-

---

7. Note that the value reported in eq. 5.20 is taken from [122] (3.25 eV) when the same authors reported an activation energy of 3.1 eV in [229].

surement of yttrium coefficient diffusion in either ferrite or austenite, which makes the coefficient after [229] a unique value to work with [137]. An alternative expression was determined by Murali *et al* [252] by density functional theory (DFT). The diffusion coefficient determined by Hin was fitted with experimental data in a limited temperature range, up to 1150°C. This was indeed restricted to the range of typical consolidation temperatures of ODS steels. However, all recent studies prove that the coarsening behavior of $Y_2O_3$ and more importantly $Y_2Ti_2O_7$ is observed at higher temperature, typically 1200°C, 1300°C and 1400°C. Consequently, if the diffusion coefficient accurately reproduces the precipitation kinetics of $Y_2O_3$ during consolidation, it seems to overestimates the diffusivity of yttrium at higher temperature. This induces a much too high coarsening rate compared to that calculated from the aforementioned studies at very high temperatures. As a consequence, a new expression of the diffusion coefficient is proposed:

$$D_Y = 10^{-7} \ \exp\left(\frac{-260000}{R_g T}\right) \tag{5.22}$$

The pre-exponential factor was decreased so that the diffusion of yttrium was retarded and so was the nucleation. Also, the growth rate of precipitates was proportionally decreased. In the same manner, the activation energy was decreased down to 260 kJ.mol$^{-1}$ instead of 320 kJ.mol$^{-1}$, thus the temperature dependency of the diffusion mechanism (the slope in the Arrhenius' plot) was decreased. The present value is equal to that from Hin at low temperatures but significantly deviates into lower values at high temperatures. At 1300°C, $1.2 \times 10^{-15}$ for the former value versus $2.3 \times 10^{-16}$ for the new value.
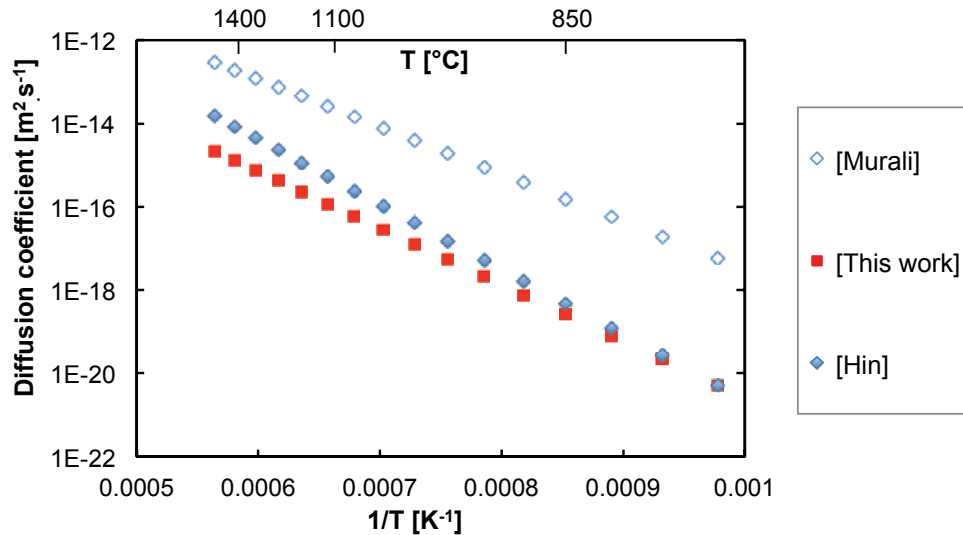


**Figure 5.22:** Diffusion coefficients of yttrium from Hin [229], from Murali [252] and modified for this work.

The assessment of this model is based on:

(i) the validation of the numerical model thanks to the case study of uniquely $Y_2O_3$. This is permitted by both the comparison with experimental data available in the literature and with a numerical model developed by Hin *et al* [122].

(ii) Then, the precipitation of complex $Y_2Ti_2O_7$ is studied in ODS steels containing yttrium, titanium and oxygen. Since no model is available in literature, the numerical results are compared to published experimental data.

(iii) Finally, this model is applied to fast non-isothermal consolidation processes, namely Spark Plasma Sintering. These results are compared to experimental data collected by SANS, TEM and APT described previously.

### 5.4.2.1  Precipitation of $Y_2O_3$

**Table 5.5:** Composition in solute elements, treatments and resulting precipitate states of Ti-free ODS steels used for comparison with the numerical results.

|        | Cr   | Y    | O    | Ti  | Treatment        | $R_m$ [nm] | $N_p$ [m$^{-3}$]    | Ref.  |
|--------|------|------|------|-----|------------------|-----------|---------------------|-------|
| (wt%)  | 18   | 0.24 | 0.06 | **0** | 850°C - 1h     | 1.5       | $9.1\times10^{23}$  | [96]  |
| (at%)  | 19.2 | 0.15 | 0.22 | **0** | 1100°C - 1h    | 6         | $9.0\times10^{21}$  |       |
| (wt%)  | 13.9 | 0.21 | 0.05 | **0** | HIP 850°C -3h  | 1.43      | $1.1\times10^{24}$  | [121] |
| (at%)  | 15   | 0.13 | 0.18 | **0** | HIP 1100°C - 3h | 5.39     | $7.9\times10^{21}$  |       |

Since $Y_2Ti_2O_7$ are known to preferentially form in titanium, yttrium containing steels, only Ti-free ODS steels were considered to model the precipitation behavior of $Y_2O_3$. The ODS steels with published experimental nanoscale characterization that were used for this study are summarized in Table 5.5. In order to compare to the precipitation state of ODS steels produced by HIPing or extrusion, non-isothermal treatments were simulated at the possible consolidation temperatures (850, 1000, 1100°C).

Figure 5.23 describes the temporal evolution of the mean radius and the number density of $Y_2O_3$ during non-isothermal treatments simulating the HIP process usually made on the milled powder with composition recalled in Table 5.5. The HIP cycle chosen here consists of a heating at 20 K.min$^{-1}$ up to the consolidation temperature and then a soaking stage of 3 hours [121]. In order to illustrate the influence of the interfacial energy on the precipitation, the figure reports the precipitation kinetics with four different interfacial energies, from 0.3 to 0.6 J.m$^{-2}$. Within the temperature range, the nucleation of $Y_2O_3$ is rapidly achieved, mainly during the heating stage of the HIP cycle. Then, the mean radius increases whereas the number density decreases, which corresponds to the coarsening stage. Based on these results, the nucleation of $Y_2O_3$ seems to be completed before that the maximum

temperature is reached. Thus, coarsening occurs early during the consolidation at the maximum temperature, from 850°C to 1150°C. The mean radius of $Y_2O_3$ after HIP is well reproduced at 850°C but slightly differs from SANS results at 1000 and 1100°C since the simulated mean radius is overestimated.
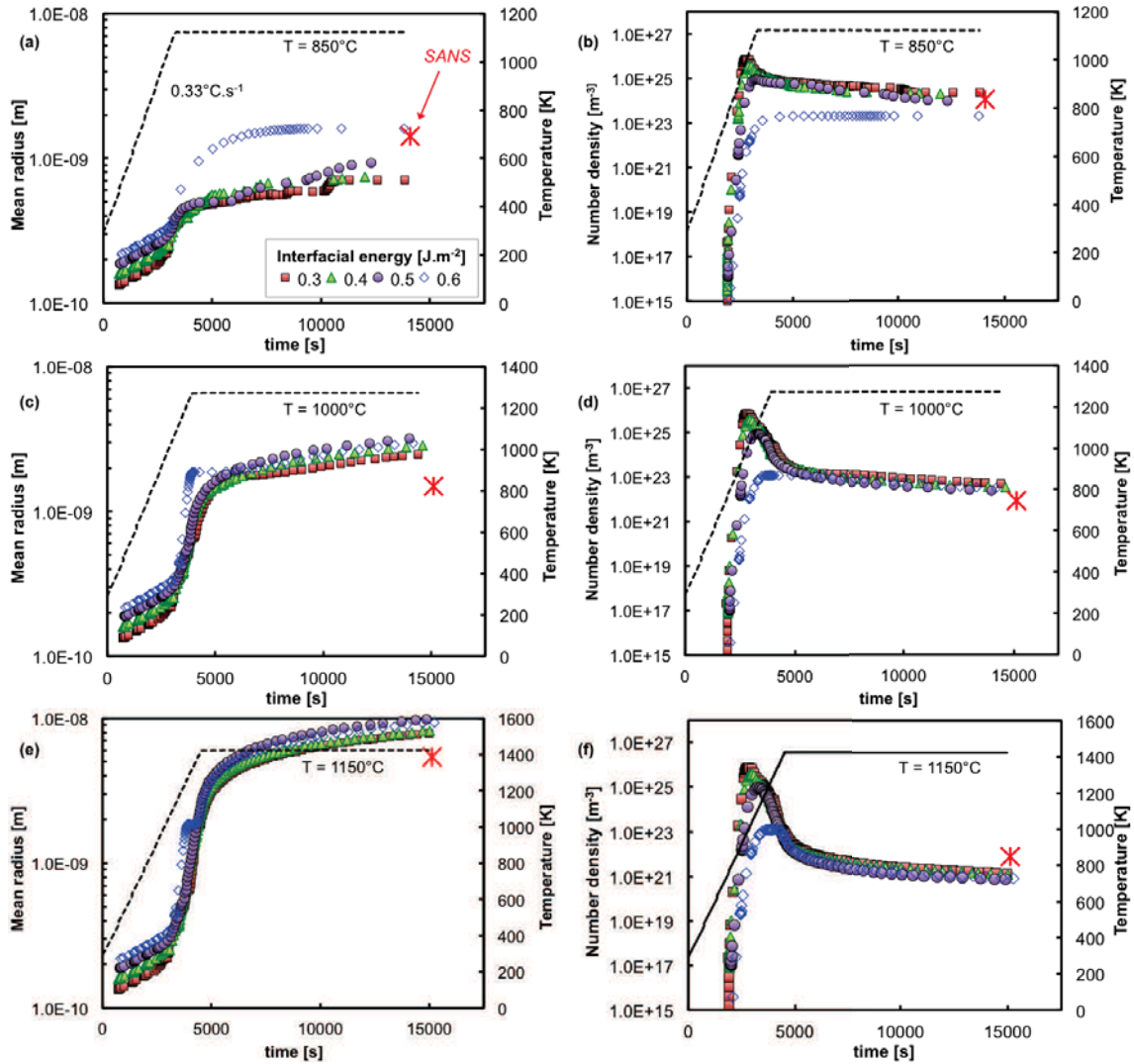


**Figure 5.23:** Time evolution (linear scale) of simulated mean radius and number density of $Y_2O_3$ particles during non-isothermal HIPing at (a-b) 850°C, (c-d) 1000°C, (e-f) 1100°C. SANS data from Alinger *et al* [121, 161] and [122].

Figure 5.24 describes the temporal evolution of the simulated mean radius and number density of $Y_2O_3$ and the comparison of published experimental data of the same composition from Ratti *et al* [27]. The simulation also reproduces consistent results at 850°C but slightly underestimates the mean radius observed by SANS at 1100°C. Since at 1000°C and 1100°C the mean radius of $Y_2O_3$ after Alinger and Hin

148

is at the contrary overestimated, one can conclude that there is no biased tendency of the model to underestimate/overestimate the coarsening behavior of $Y_2O_3$. Instead, the numerical results are in very good agreement with the experimental data from SANS. The interfacial energy giving rise to the best match between experiments and simulations is $\gamma_{Y_2O_3} = 0.6$ J.m$^{-2}$, which is higher than those from either Hin (0.4 J.m$^{-2}$) or Ribis (0.35 J.m$^{-2}$) but this is still consistent with semi-coherent particles.
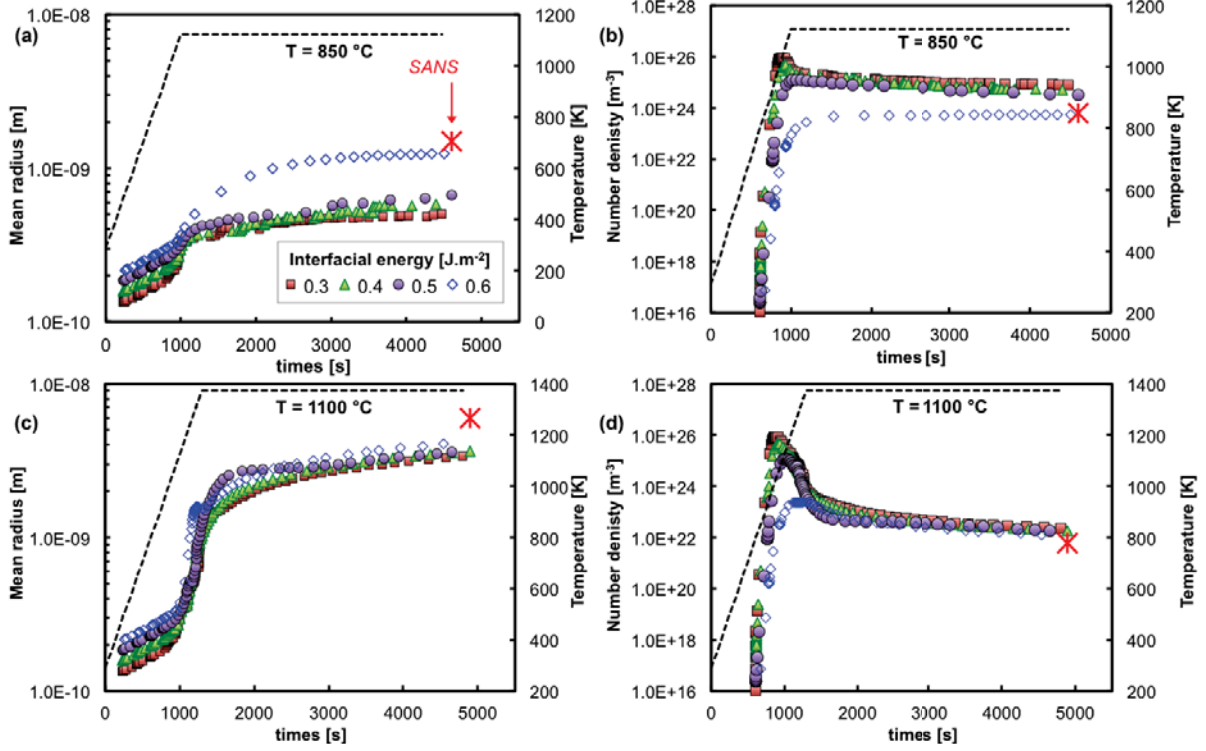


**Figure 5.24:** Time evolution (linear scale) of simulated Mean radius and number density of $Y_2O_3$ particles during non-isothermal pressure-free heat treatments at (a-b) 850°C and (c-d) 1100°C. SANS data are from Ratti *et al* [96, 27].

### 5.4.2.2 Precipitation of $Y_2Ti_2O_7$

**Table 5.6:** Composition of Y, Ti and O, heat treatments and resulting precipitate states of ODS steels used for comparison with the numerical results.

|        | Cr   | Y    | O    | Ti  | Treatment         | $R_m$ [nm] | $N_p$ [m$^{-3}$]      | Ref.  |
|--------|------|------|------|-----|-------------------|------------|----------------------|-------|
| (wt%)  | 13.9 | 0.21 | 0.05 | **0.4** | HIP 850°C -3h     | 1.25       | $2.57\times10^{24}$  |       |
| (at%)  | 15   | 0.13 | 0.18 | **0.4** | HIP 1000°C - 3h   | 1.53       | $8.5\times10^{23}$   | [121] |
|        |      |      |      |     | HIP 1100°C - 3h   | 1.71       | $3.02\times10^{23}$  |       |

The simulated precipitation behavior of $Y_2Ti_2O_7$ during HIPing is represented in Fig. 5.25. The kinetics is quite similar to that of $Y_2O_3$ since it is governed by the

149
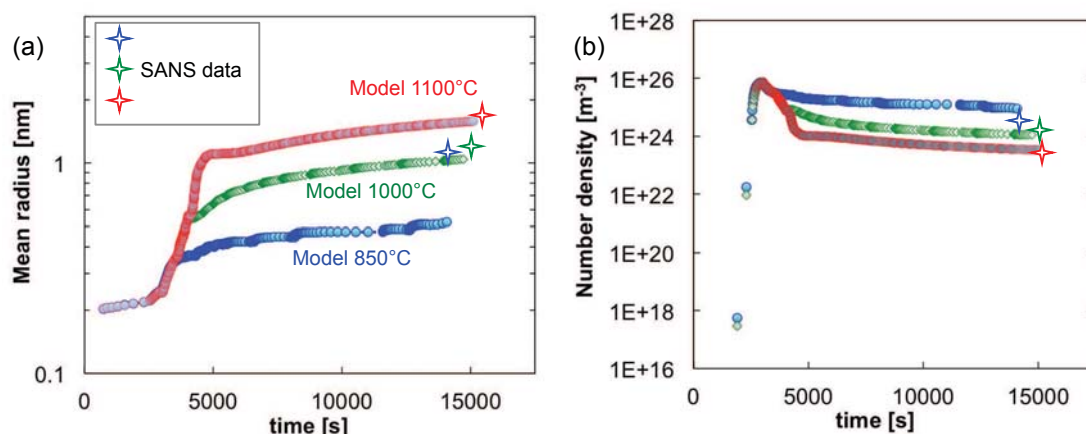
**Figure 5.25:** Time evolution (linear scale) of simulated Mean Radius and Number Density of $Y_2Ti_2O_7$ particles during non-isothermal heat treatments at (a-b) 850°C, 1000°C and 1100°C. SANS data are from Alinger *et al* [121, 161].

diffusion of yttrium (Fig. 5.23). The main difference is the higher number density for $Y_2Ti_2O_7$ compared to $Y_2O_3$, which can be explained by the larger solute content available for the precipitation of $Y_2Ti_2O_7$.
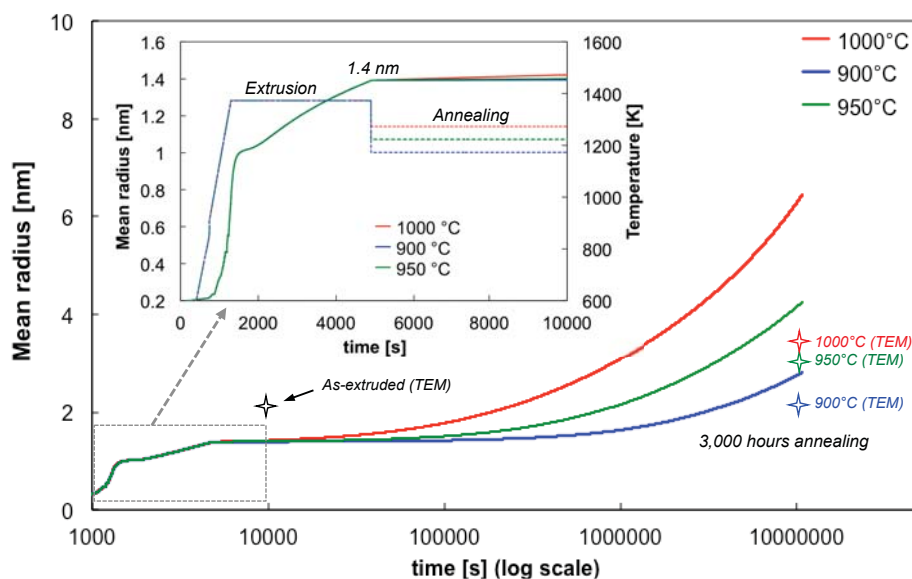


**Figure 5.26:** Time evolution of simulated Mean radius and Number Density of $Y_2Ti_2O_7$ particles. The inset focuses on the mean radius evolution during extrusion. Experimental values after [253].

Also, the thermal stability of the oxides was assessed using the model. The annealing treatments were taken from Miao *et al* [253] who performed annealing treatments for very long time (3,000 hours) on an extruded ferritic steel. The Fig. 5.26 reports the precipitation behavior during successive hot extrusion and annealing at either 900, 950 or 1000°C for 3,000 hours. At long annealing treatments, the model

slightly anticipates the coarsening stage compared to what was observed by Miao *et al.*

The present model was applied to the precipitation kinetics during SPS consolidation. Fig. 5.27 shows the comparison between experimental data collected by SANS, ATP and TEM and numerical data from the model. Given the scattered experimental data of the mean radius and the number density, the numerical results are acceptable. However, it seems to accentuate the effect of the temperature on the coarsening behavior because the difference in the number density between SPS850°C and SPS1100°C is higher than that observed experimentally. The coarsening behavior is handled by the Gibbs-Thomson effect through Eq. (5.19). This effect was applied assuming a spherical shape of the precipitates, which may not be fully accurate. Indeed, Ribis showed that a deviation from spherical into ellipsoidal or cuboidal shape was observed upon annealing at high temperature. In this context, the coarsening kinetics would be impacted, which may explain the difference in coarsening kinetics between experimental and numerical results.
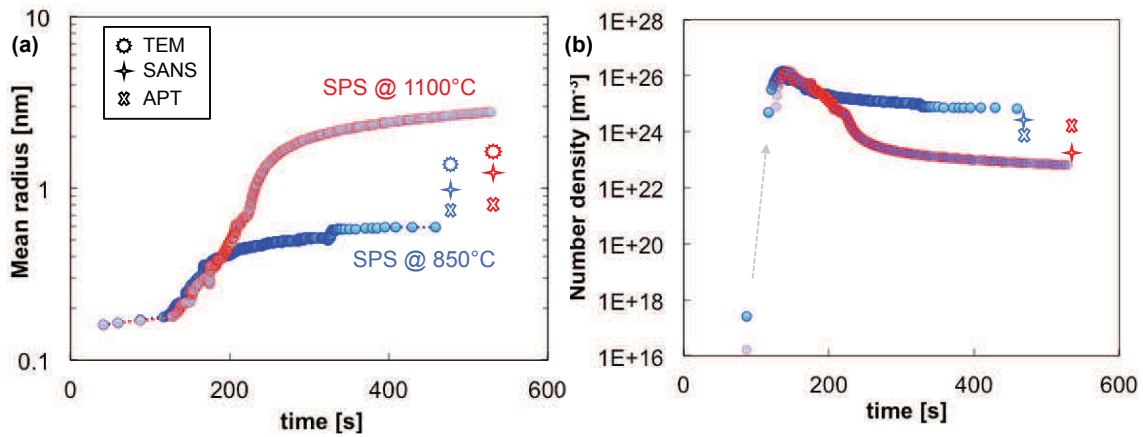


**Figure 5.27:** Time evolution of simulated Mean radius and Number Density of $Y_2Ti_2O_7$ particles compared to experimental data from TEM, SANS and APT.

### 5.4.3 Conclusion on the present model

The precipitation kinetics of $Y_2O_3$ and $Y_2Ti_2O_7$ from a supersaturated solid solution of yttrium, oxygen and titanium during non-isothermal treatments similar to industrial high-temperature consolidation was simulated. Despite of strong assumptions (homogeneous nucleation, stoichiometric phases, etc), the model gave rise to interesting results. Since the driving force is dependent on the level of saturation in the solid solution (chemical composition), the present results are not applicable to any alloy and further calculations must be made with the proper chemical composition and the suitable thermal treatment.

A new expression of the diffusion coefficient of yttrium in iron was proposed. First, the nucleation was achieved during the heating stage of the non-isothermal treatment, nearly 600°C. This early nucleation is in very good agreement with the literature and with the actual precipitation state within the ODS SPSed in a few minutes at 850°C and 1100°C. The simulations reproduce the precipitation kinetics during non-isothermal treatments in the temperature range of typical consolidation cycles (from 850°C to 1100°C).

The model also predicts the thermal stability of $Y_2O_3$ and $Y_2Ti_2O_7$ but seems to overestimates the coarsening stage compared to the published experimental data. The number density from the simulation is higher than that measured on SPSed ODS steels. This can be explained by the assumption of a unique and stoichiometric phase in the simulation whereas in the reality the particles may observe variation in the composition, not only in yttrium, titanium and oxygen but also in the enrichment in other solutes like aluminum, silicon or chromium. The latter has been located in nanosized particles [57] or under the form of a shell surrounding the particles [160]. This deviation is probably emphasized in SPSed ODS steels compared to HIPed materials because SPS gives rise to very rapid treatments during which particles may have no time to reach their equilibrium state. Hence, the assumption of stoichiometric particles instead of probable far-from-equilibrium nanoclusters is most likely not applicable. Also, the excess vacancies were neglected, in terms of both diffusion and atomic volume of the 'compound'. The latter have been reported to play a role on the nanoparticles stability [172]. Most importantly, the effect of morphological change upon heating was not taken into account in the present model. The modification of the Gibbs-Thomson effect due to morphological variations is discussed later in subsection 5.6.

152

# 5.5 Multiple precipitation kinetics with MatCalc®

## 5.5.1 Introduction

Another method to simulate the solid-state precipitation requires the assessment of both diffusion and thermodynamic data using a fitting polynomial function of the evolution of the Gibbs energy with temperature. This so-called CALPHAD (**Ca**lculation of **Pha**se **D**iagram) method is performed to determine the database in the software MatCalc®. MatCalc® was used under the license 5.44 and the thermodynamic database $Mc\_Fe2$, the latter having been developed during this thesis. More details can be found on $http://matcalc.tuwien.ac.at$.

In the previous section, the precipitation kinetics was reproduced to some point by fitting the solubility product and the interfacial energies of the precipitates. The reasoning was to minimize the fitting parameters that are usually detrimental to a proper study of a physical phenomena and particularly the interfacial energy. This parameter takes into account not only the chemical (crystallographic) effect due to the chemical broken bonds at the interface but also the elastic energy assumed for either coherent precipitates (related to the misfit of lattice parameters) or incoherent (related to misfit dislocations). This can be traduced by:

$$\gamma_t = \gamma_{ch} + \gamma_{coh}^{str} \tag{5.23}$$

The chemical component $\gamma_{ch}$ comes from the difference in composition and structure between the precipitate and the matrix. This can be determined by counting the broken bonds between the particle and the Nearest Neighbors Broken Bonds (NNBB) [246]. The interfacial energy is then linked to the enthalpy solution of the system by:

$$\gamma = \frac{n_S.z_{S,eff}}{N.z_{L,eff}}.\Delta E_{sol} \tag{5.24}$$

with $N$, $n_S$, $z_{S,eff}$ et $z_{L,eff}$ respectively the number of nearest neighboring atoms, the number of atoms by surface area, The number of broken bonds per atom at the interface and the total number of bonds per atom. One needs to determine $n_S$, $z_{S,eff}$ and $z_{L,eff}$ in the considered system.

$$n_S = n_V^{2/3} = \begin{cases} \frac{4^{2/3}}{a^2} \text{ for fcc system (4 atoms per unit cell)} \\ \frac{2^{2/3}}{a^2} \text{ for bcc system (2 atoms per unit cell)} \end{cases} \tag{5.25}$$

$n_V$ is the number of atoms per volume, $a$ is the lattice parameter. Finally, the coherent interfacial energies can be derived. Worth noticing that equation (5.24) is theoretically accurate for coherent interfaces. As soon as the particles loose coherency and misfit dislocations appear, a subsequent increase in the interfacial energy arises. A generalized model (GNBB) was developed by Kozeschnik and was

accurately applied on coherent to semi-coherent interfaces, such as copper in Fe-Cu ($\gamma = 520 - 610$ mJ.m$^{-2}$) or cobalt in Cu-Co ($\gamma = 520 - 610$ mJ.m$^{-2}$) that are paradoxically not fully coherent.

**What is the right value?**

- For coherent precipitates that have a weak misfit with the matrix, the interfacial energy can be very low ($\approx 0.02$ J.m$^{-2}$ for the Ni-Ti system).

- For semi-coherent precipitates, the misfit is high enough to induce a release of energy through the creation of dislocations misfit. In comparison to coherent particles, the interfacial energy is higher ($\approx 0.2$ J.m$^{-2}$ in the system Cu-Co).

- For incoherent precipitates, the interfacial energy becomes higher than semi-coherent precipitates. For example, carbides Fe$_3$C in ferrite have an interface energy of $0.5 - 1$ J.m$^{-2}$ [56].

It is generally accepted that the interfacial energy induced by a precipitate that loses its coherency with the matrix is then preponderant compared to the misfit elastic energy, the latter being drastically reduced by the relaxation effects thanks to the misfit dislocations. Even if this concept seems to be justified, the GNNB model contradicts the debatable assumption that semi-coherent precipitates must have an interface energy lower than an absolute value, often chosen around 0.5 J.m$^{-2}$. There is no evident reason to consider that coherent particles should have an interface energy lower than 0.5 J.m$^{-2}$, neither that incoherent particles should have an interface energy larger than 1 J.m$^{-2}$. Based on the number of broken bonds through the interface, some coherent particles may create a lots of broken bonds when semi-coherent particles may create few broken bonds.

The interfacial energy is kept as a constant along the precipitation simulation. This is because particles nucleate coherently with the matrix and only $\gamma_{ch}$ is important for nucleation. The eventual increase in the interfacial energy due to the loss of coherency is neglected. This is not detrimental to the simulation accuracy because small fluctuation of $\gamma$ does not have drastic influence on the coarsening stage, since $\gamma$ is only proportional to $r^3$.

## 5.5.2 Application to heterogeneous precipitation in ODS steels

Nanostructured and ultrafine-grained (UFG) materials have been considerably developed these last years. The development of UFG metallic components is being boosted by encouraging mechanical properties in terms of both excellent mechanical strength and very acceptable ductility. Two processing routes are so far employed to produce UFG materials. One way is severe plastic deformation, where a huge amount of cold work is applied on bulk materials thanks to processes like

equal channel angular extrusion or high pressure torsion. Along these high-energy processes, complex mechanisms lead to the formation of ultrafine grains: (i) rearrangement of a high density of dislocations that form small cells (ii) formation of subgrains (iii) and afterwards high-angle grain boundaries. Another way consists of powder metallurgy routes. The latter are used for Oxide-Dispersion Strengthened (ODS) steels, where oxide particles of few tens of nm are mechanically alloyed with prealloyed gas-atomized micronic powders. This gives rise to nanostructured and highly deformed milled powder that can be further consolidated to produce bulk materials. The possible consolidation steps are either hot isostatic pressing or spark plasma sintering for the isotropic processes, and hot extrusion for the anisotropic process. All involve non-isothermal cycles, with a heating ramp with a rate varying from few degrees per minute for HIPing to 500 degrees per minute for SPS. Then, a soaking step at maximum temperature is applied, usually at 1100°C for few minutes for SPS up to few hours for HIPing (Fig. 5.28).
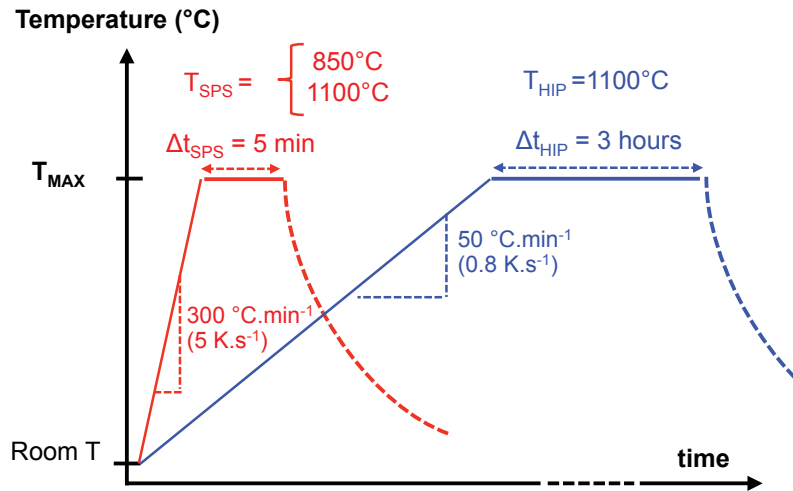


**Figure 5.28:** Non-isothermal treatments used for the precipitation simulation.

During the early stages of heating, lots of microstructural instabilities can occur. Since these materials are strongly deformed and thus high unstable, a strong mobility of dislocations and subgrain boundaries is expected, even at low temperature. This is what was observed in nanostructured ODS steels by Sallez *et al* [200] using synchrotron X-Ray diffraction during *in situ* annealing. The dislocation density rapidly decreased even at moderate temperatures but recovery was somehow limited by solute drag and precipitation. Given the initial amount of dislocations ($10^{16}$ m$^{-2}$ for the milled powder) and the moderate dislocation annihilation due to impeded recrystallization, nanostructured ferritic steels still contain numerous defects at temperature where precipitation of oxides most likely occurs. Thus, a strong heterogeneous nucleation of nanoparticles is expected. We propose here to describe the heterogeneous nucleation and precipitation kinetics of nanoparticles in ODS steels.

155

Instead of homogeneous bulk precipitation, the precipitation on dislocation and at grain boundaries was studied. Nucleation on dislocations was considered for the nanosized oxides, as observed by TEM (Fig. 5.11). For this case, both binary $Y_2O_3$ and complex Y-Ti-O populations were assumed to nucleate on dislocations. Besides, binary titanium oxides were assumed to form at grain boundaries. Indeed, the latter most likely form at the interfaces between consolidated powder particles, as illustrated by the FIB-3D characterization (Fig. 5.29). Hence, for these specific precipitates, the nucleation at grain boundaries with a grain size of 50 $\mu m$ was chosen, which corresponds to the mean diameter of the milled powder particles. In this particular configuration, grain boundary diffusion was applied. This consists in limiting the diffusion process to the 2D grain boundary, instead of classic bulk diffusion.
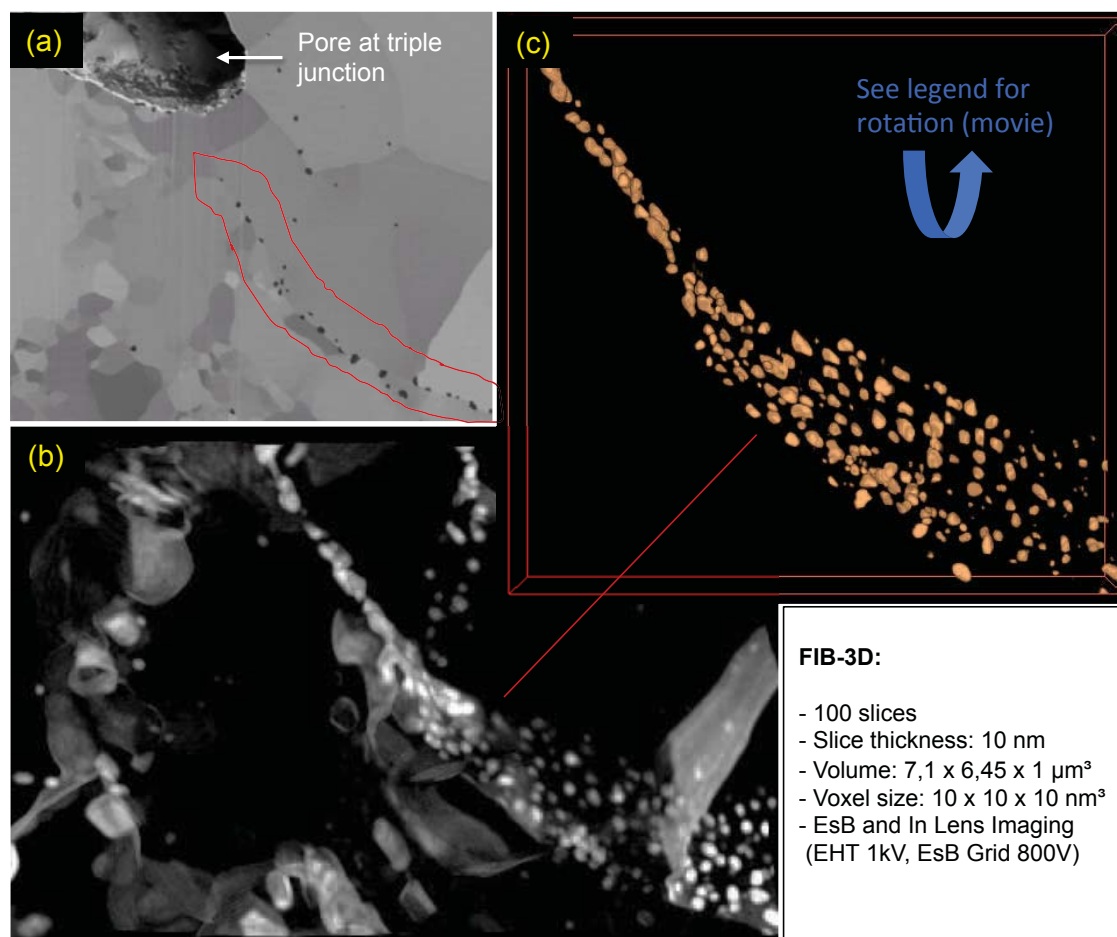


**Figure 5.29:** FIB-3D imaging based reconstruction volume of grain boundary precipitation of titanium oxides forming an envelop along the former powder particles interfaces. Click here to get into the 3D viewer (c).

The kinetics of multiple precipitation considering $Y_2Ti_2O_7$, $Y_2TiO_5$, $Y_2O_3$ on dislocations and $Ti_2O_3$ at grain boundaries was simulated during non-isothermal

consolidation process. Three thermal cycles were considered (Fig. 5.28): HIPing at 1100°C, SPS at 850 and 1100°C.

MatCalc, like PreciSo for homogeneous precipitation, predicts the nucleation of nanoparticles within the first minutes of the consolidation cycles, typically during the heating stage (Fig. 5.30 and Fig. 5.31).
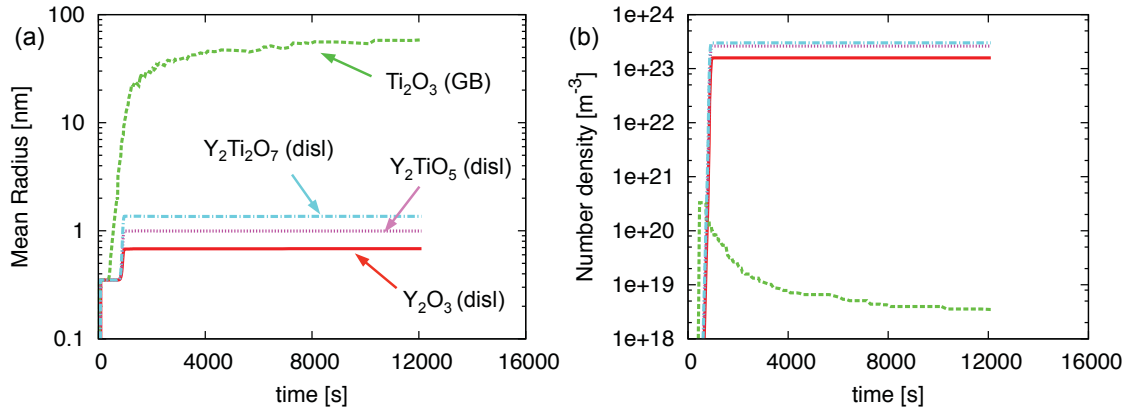


**Figure 5.30:** Time evolution of simulated mean radius and number density of $Y_2Ti_2O_7$, $Y_2TiO_5$, $Y_2O_3$ and $Ti_2O_3$ particles during HIP at 1100°C

Complex $Ti_2O_3$ and $Y_2Ti_2O_7$ possess an equivalent number density, around $2 \times 10^{23}$ $m^{-3}$, whereas binary $Y_2O_3$ has a number density two times lower. Considering that dislocations act as nucleation sites, the nucleation site density $N_{disl}$ can be calculated using the following equation [216, Chapter 2.4]:

$$N_{disl} = \frac{\rho}{a} \qquad (5.26)$$

with $\rho$ the dislocation density and $a$ the lattice parameter. For $\rho = 10^{15}$ $m^{-2}$ and $a = 0.29$ nm, $N_{disl} = 3.5 \times 10^{24}$ $m^{-3}$. The three populations of oxides $Y_2O_3$, $Y_2Ti_2O_7$ and $Y_2TiO_5$ fill a cumulated density of around $10^{24}$ $m^{-3}$, which is of the same order of magnitude that the dislocation nucleation site density.

Also, the mean radius is constant after the nucleation is completed. This stage may correspond to a regime where growth and dissolution occur simultaneously. This stage is particularly long compared to what is simulated by PreciSo. The completion of very long annealing treatment actually gives rise to coarsening (not shown here). Only binary titanium oxides undergo coarsening to finally reach a mean radius of 25 nm after SPS at 1100°C. This is a bit smaller than the 'coarse' oxides observed at grain boundaries (see for example Fig. 5.8).
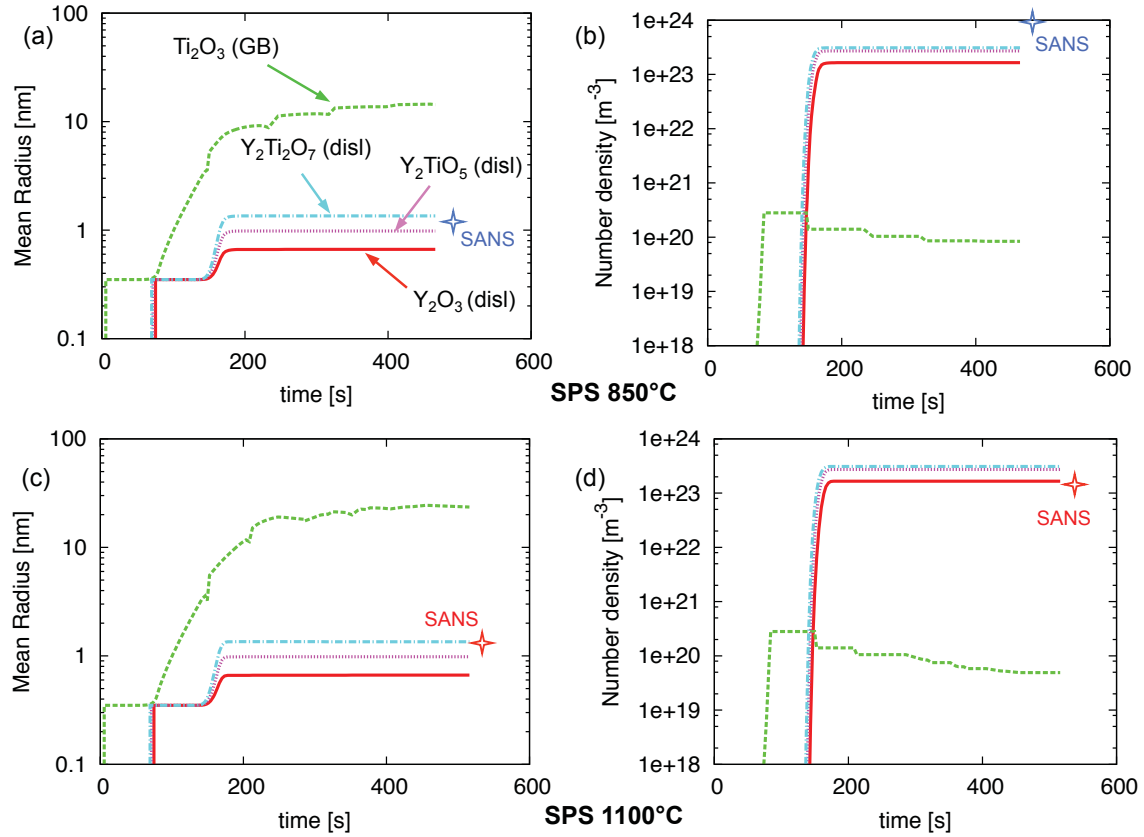
**Figure 5.31:** Time evolution of simulated mean radius and number density of $Y_2Ti_2O_7$, $Y_2TiO_5$, $Y_2O_3$ and $Ti_2O_3$ particles during SPS at 850°C and 1100°C

## 5.6  Conclusion and outlooks

The interfacial energy does not have a large influence on the coarsening kinetics, which is actually what the community is interested in. The interfacial energy drastically changes the nucleation behavior, since it completely influences the critical Gibbs free energy for nucleation:

$$\Delta G* = \frac{16\pi\gamma^3}{3(\Delta g_{ch} + \Delta g_{el})^2} \tag{5.27}$$

But considering that nucleation is highly inhomogeneous and occurs on dislocations, which are numerous in mechanically alloyed powders, all the nucleation sites are actually filled at the early stages of precipitation. If there is a significant difference in the coarsening resistance of $Y_2O_3$ and $Y_2Ti_2O_7$, it is doubtful that it is due to the interfacial energy.

However, the coarsening resistance can have other origins that were not considered in this study. For instance, the chemical composition of the particles was assumed constant while far-from-equilibrium nanoclusters are present at the early

158

stages of the precipitation. Also, the excess vacancies were neglected, in terms of both diffusion and atomic volume of the 'compound'. Another aspect that could make the difference in the precipitation of $Y_2O_3$ and $Y_2Ti_2O_7$ is the elastic energy of these two particles.

## Elastic energy and anisotropy

An attempt to numerically implement this complex morphology and associated nucleation, growth and coarsening equations consists an interesting path to quantify the effect of the elastic energy on the shape variation of oxides in steels. In the Annexe 5, the details of modified nucleation, growth and coarsening equations in the case of anisotropic particles are presented. This constitutes a basis for the implementation of a model that takes into account the elastic energy upon precipitation.

## Toward coupling recovery, grain growth and precipitation

An interesting outlook is the coupling between grain growth and precipitation. This can be implemented as soon as the precipitation kinetics can be predicted. Indeed, the precipitation state at each time step will define the pinning pressure exerted on grain boundaries, which depends on the mean radius and the volume fraction of the precipitates. Meanwhile, the driving pressure for grain growth is governed by the grain size itself, which can easily be defined with experimental data (XRD or EBSD). This may be traduced by the following system:

$$\begin{cases} \frac{\partial D(t)}{dt} = M_0 e^{-Q_m/RT} \times [P_C(t) + P_V(t) - P_Z(t)] \\ P_C(t) = 2\frac{\gamma}{R(t)} \\ P_V(t) = \frac{1}{2}\mu b\Delta\rho(t)^2 \\ P_Z(t) = \frac{3}{2}\gamma\frac{f_p(t)}{r_p(t)} \end{cases} \tag{5.28}$$

where $M = M_0 e^{-Q_m/RT}$ is the grain boundary mobility, $P_V(t)$ and $P_C(t)$ the driving pressure for recrystallization and for growth, $P_Z(t)$ the Zener pinning pressure. $\gamma$ is the grain boundary interfacial energy, $D(t)$ and $R(t)$ the diameter and radius of the grain, $\mu$ the shear modulus of the matrix, $b$ the Burgers vector magnitude, $\Delta\rho$ the variation in dislocation density between two neighboring grains, $f_p$ and $r_p$ the precipitation fraction and mean radius, respectively.

The dislocation density and the crystallite size were determined *in situ* by X-ray diffraction during heating. Hence, the recovery (dislocation density evolution) and grain growth kinetics can be implemented into the precipitation model.

# Conclusion and outlooks

## Conclusion

ODS ferritic steels microstructure evolution during high-temperature consolidation and further heat treatments involves a legion of parameters. This class of alloys combines two specific features that make the understanding of its microstructural behavior not straightforward.

(i) Firstly, these alloys are produced by powder metallurgy. Even if the influence of the milling parameters was not extensively studied in this thesis, the dramatic effect of the stored energy through cold-working of the powder was emphasized. If heterogeneous, the plastic deformation plays a tremendous role on the grain boundary mobility during consolidation because it governs the driving force for recrystallization. In my opinion, ODS ferritic steels will undergo abnormal grain growth as soon as mechanical alloying will be used[8]. Recently, several direct dispersion strengthened alloys were developed through the direct atomization of a prealloyed powder containing yttrium, titanium and oxygen. But achieving the right composition with the targeted size of powder particles is still a challenge [254]. This option is being studied at CEA on 11Cr direct atomized ODS steels [255].

(ii) Secondly, ODS ferritic steels are precipitation hardening alloys. For this type of commercial alloys, very well-known heat treatments are available to dissolve the second-phase particles (carbides, carbo-nitrides, silicates, etc) and further recrystallize the microstructure to soften the material. At the opposite, oxides in ferritic steels not only precipitate easily due to the very low solubility of oxygen and yttrium in ferrite, but also are extremely stable up to the solidus temperature of high-chromium steels. In this context, none classic anneal would permit to dissolve the precipitates and recrystallize easily the material.

Based on these statements, and knowing that point (i) cannot be changed, two major alternative methods to tailor the microstructure can be considered. For ODS fully ferritic steel, the optimization of the solid solution must be studied in order to control the recrystallization behavior. In the recent past studies, the effect of

---

8. at least at industrial scale when large batches are produced

adding titanium in the solid solution was evaluated as very positive since a denser and finer precipitate distribution was obtained. Thus, better mechanical properties were achieved since, as showed in Chapter 3, the precipitation hardening is significant in these alloys. However, two collateral consequences are, in my opinion, not so favorable for ODS steels optimization. First of all, titanium, as shown in this thesis, form coarse oxides that most likely degrade the ductility of the steels, specially when they are located at former powder particles interfaces. Besides, as emphasized by the *in situ* synchrotron studies on various powders, the effect of the solute content, including titanium, is drastic on the recrystallization behavior. Solute drag effect and Zener pinning efficiently act against the recrystallization because the grain boundaries have much lower mobility than that in unreinforced steels. In this context, Ukai *et al* demonstrated that no more than 0.25 wt% of yttrium should be added in titanium-free ODS ferritic steels to permit recrystallization [40]. In grades that contain titanium and thus complex Y-Ti-O particles, the optimized amount of yttrium must be even lower. The effect of initial chemical composition on the recrystallization behavior shall be further quantified [256].

In this context, the influence of the heating cycle during consolidation is somehow moderate. This is why, even if SPS does gain time on the overall processing route, it does not bring drastic change in the microstructural behavior. Consequently, the microstructures of SPSed and HIPed ODS steels from the same base powder are equivalent. Thus, SPS shall be considered only as an interesting process for the production of ODS ferritic steels equivalent to HIPed materials. Yet, SPS consists of a great investigation tool for comprehensive studies, as made for the strengthening model. In the next future, if the optimization of ODS ferritic steels in terms of atomization, milling, chemical composition, etc, are studied experimentally, SPS will be an excellent consolidation technique.

As both a global conclusion and an outlook, the development of transformable ferritic/martensitic steel seems to be the most promising path. A reproducible manufacturing route of the tubes is necessary. This is why Toualbi [47, 257] advised the use of 9Cr transformable ferritic/martensitic steels for process optimization, as suggested before by Ukai [40]. This option was thus considered by using SPS as well. The next section presents the main results of this additional study.

## 9Cr ferritic/martensitic ODS steels by SPS

In order to assess the advantage of producing 9Cr ODS steels instead of fully ferritic 14Cr ODS steels, a 9Cr powder was mechanically alloyed with yttrium oxide and consolidated by SPS in the same temperature range as the one used on 14Cr ODS steels. The aim of this work was to demonstrate the feasibility of SPS to obtain a homogeneous ultrafine grained ODS steel. After consolidation, the resulting microstructure and high-temperature tensile properties were characterized and com-

pared to those of 14% chromium ODS steels. Knowing that the 9Cr ODS steel can undergo $\alpha$ to $\gamma$ transformation at high temperature, SPS could allow the microstructure to be homogeneous thanks to the formation of ultrafine ferritic grains during cooling. Also, a fast cooling will produce martensitic phase in the steel, which could induce higher tensile strength than that of the 14Cr ODS steel. The classification of criteria as followed are in the decreasing order of importance: (i) low porosity (ii) homogeneous microstructure (iii) fine microstructure (iv) minimization of carbon diffusion.

In this sense, a careful microstructure characterization was performed to describe how the grain structure evolves depending upon the processing parameters. The effect of processing parameters on the microstructure and the resulting mechanical properties of this 9Cr ODS steel will be published elsewhere. To emphasize the benefit of the $\alpha$-to-$\gamma$ phase transformation occurring during the consolidation by SPS at 1050°C, Fig. 5.32 compares the microstructures of a 14Cr versus 9Cr ODS steels processed under the same parameters.
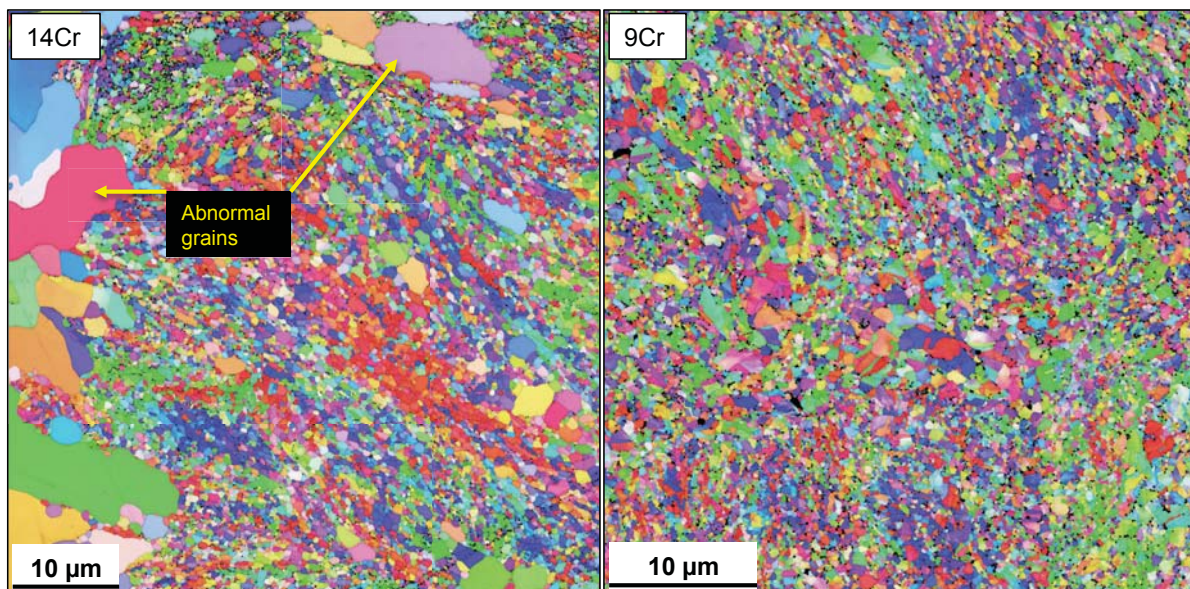


**Figure 5.32:** EBSD orientation maps of (a) abnormal microstructure in SPSed ODS 14Cr ferritic steel and (b) homogeneous ultrafine grains in SPSed ODS 9Cr ferritic/martensitic steel.

The 9Cr steel has a homogeneous and fine microstructure compared to the abnormal grain structure of the 14Cr steel. The austenitization generates a "reset" of the possible abnormal microstructure formed during heating. Then, new grains of ferrite homogeneously nucleate during further cooling down in the SPS device. Limited growth of ferrite may be due to rapid cooling, which reduces the time after nucleation during which ferrite nuclei can grow [258], but also to grain boundary pinning. A proper Continuous Cooling Transformation (CCT) diagram would be necessary to determine the amount of possible martensite that may form during

cooling. However, only few martensite blocks were detected on the SPS 9Cr ODS steel. An example of such structure is presented in Annexe.

# Outlooks

## On ODS steels

We suggest here to assess the development of base-centered cubic ferritic steels with a chromium content high enough to resist to corrosion but low enough to permit an allotropic phase transformation from ferrite to austenite during consolidation. To do so, several aspects need to be studied.

### On 11-13Cr ODS steels

The overall chemical composition shall be optimized, in term of chromium content (typically between 11 and 13 wt%) but also in other solute elements, in order to obtain a transformable ferritic/martensitic steel with a high chromium content. This can be done using various multi-components phase diagram calculation software, such as MatCalc® or ThermoCalc®. Specially, the effect of carbon contamination due to milling or during SPS consolidation on the stability of ferrite versus austenite in Fe-11/13Cr shall be investigated. Comparatively to thermodynamic calculations, X-Ray diffraction using laboratory *ex situ* or Synchrotron *in situ* acquisitions will be an efficient tool to determine the stability of the phases within the ODS alloys.

### On the precipitation

Also, the precipitation state has to be optimized. The titanium and oxygen contents shall be carefully chosen in order to avoid excessive precipitation of coarse titanium oxides, specially at grain boundaries. Indeed, the key-property of ODS steels that needs to be improved is a reproducible ductility at high temperature. The two precipitation models presented in this thesis would be helpful to study the influence of each solute content (mainly yttrium, titanium and oxygen) on the precipitation state. A systematic study of the influence of the initial composition, thus of the precipitation, on the recrystallization behavior of the ODS steels would be of interest. This has been partially explored by a recent thesis [136] and will be pursued by another [256].

Besides, since the models seem to accurately simulate the precipitation kinetics during rapid non-isothermal treatments, they may be used to study the influence of various types of welding processes on the precipitation behavior. This requires to calculate the temperature field within the weld and then to implement the precipitation model for each temperature profile, which is not straightforward. However,

this has been started in aluminum alloys [125] and may be reproduced for other systems.

## On SPS

This thesis demonstrated that similar microstructural and mechanical properties of fully ferritic or ferritic/martensitic ODS steels could be obtained by SPS compared to conventional process like HIP. The next step would be to consider SPS as an industrial tool to produce ODS steels. The first step was achieved by producing a compact (diameter $\phi = 60$ mm) that could be further extruded. So SPS could be a tool for the pre-consolidation of the powder before extrusion at industrial scale. However, the technique is not mature enough to be compared to HIP since HIP allows the production of many units at the same time whereas SPS is a unit by unit process. Thus, many technological developments are needed to consider SPS as a potential industrial tool for the production of ODS steels.

## On the characterization tools

One important aspect of this thesis was the development or the specific use of high-level characterization techniques. First, the use of *in situ* Synchrotron X-Ray diffraction was shown to constitute an efficient tool to determine the evolution of the crystallite size and the dislocation density upon heating. Specially, the modified Warren-Averbach method and the coupled modified Warren-Averbach and Williamson-Hall methods may be applied to various class of metallic materials in the field of nanostructured and ultrafine grained alloys.

Also, the visualization of grain boundary precipitates, particularly in powder metallurgy alloys with powder particles interfaces, can be achieved by the FIB-3D method. This was done on ODS alloys using classic secondary or backscattered electrons imaging in order to emphasize various types of particles in the material. This technique could be applied on other alloys. In particular, the precipitation behavior in alloys subject to ageing (duplex steels, high-chromium alloys, heat-affected zones in stainless steels or in 6xxx Aluminum alloys) may be studied.

Finally, the role of heterogeneous microstructures on the ductility is of great importance for industrial applications. Powder metallurgy, as shown in this thesis, could be used to produce various types of heterogeneous microstructures with different fraction of fine and coarse grains. Then, the plasticity mechanisms may be studied by *in situ* SEM tensile tests, including EBSD orientation maps. For the modeling part, further studies must be performed to understand the strengthening mechanisms governing the yield strength of bimodal and heterogeneous alloys, as well as the work-hardening behavior.

'*Siamo nani*', *ammise Guglielmo,* '*ma nani che stanno sulle spalle di quei giganti, e nella nostra pochezza riusciamo talora a vedere più lontano di loro sull'orizzonte.*'

Umberto Eco, Il Nome della Rosa, [259].

'*Io, [..], eterno studente, perché la materia di studio sarebbe infinita, e sopratutto perché so di non sapere niente.*'

Francesco Guccini, Addio

166

# Annexes of Chap. 3

## Tensile specimen
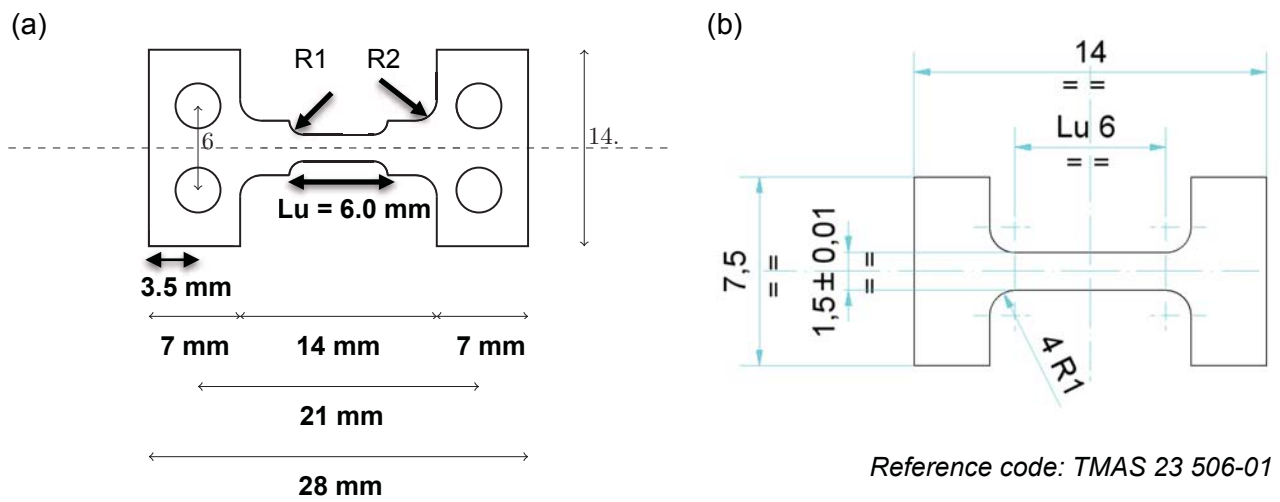


**Figure 5.33:** Tensile specimen machined for (a) *in situ* and (b) *ex situ* mechanical testing.

# Annexes of Chap. 5

## TEM sample preparation

The thin foils were prepared using the following method:

(a) Mechanical polishing: the consolidated material was sticked on a sample holder and polished in order to get a final thickness between 60 to 90 $\mu$m. Individual steps depend on the hardness and geometry of the samples but typical polishing sequence was made with SiC supports from P320, P600, P1200 to P2400.

(b) Discs with a diameter of 3 mm were then manually stamped from the metallic thin foil. They were further polished with diamond paste up to 3 $\mu m$. This finishing step suppresses cold-working due to stamping and avoids preferential etching during electrolytic polishing.

(c) Electrolytic etching was performed until a uniform hole was obtained in the center of the foil. The etching solution was composed of 70% of ethanol, 20% ethylene glycol monobutyl ether and 10% of perchloric acid and cooled to 0°C.

(d) Ionic polishing was eventually performed in order to further thin and eliminate eventual oxidation before observation. The apparatus was a PIPS (Precision Ion Polishing System) from Gatan equipped with a double ion gas gun polishing the surface with an incident angle from -10 to 10°. Gun energy was set at 4.2 keV with a magnitude of 20 A.

# Elastic energy and morphology evolution using the supersphere model

The purpose of this study is to predict the morphological change of nanosized oxides in a ferritic matrix. To do so, the effect of elastic energy and the morphological evolution on the precipitation behavior of nanosized precipitates is studied.

## Introduction of elastic energy

New phase precipitation within a metallic matrix from a supersaturated solid solution is governed by different factors, among which:

- The crystallographic structure of the phases: the daughter phase will adopt the most coherent structure with the one of the matrix in order to minimize the interface energy.

- The elastic energy: the volume variation between the two phases can cause elastic distortion that is necessary to accommodate the dilatation located at the interface.

- The eventual anisotropy of the interfaces: the growth of new nuclei will occur preferentially at the interface of highest mobility, following the geometrical conditions linked to the nucleus.

The two latter ones were not considered in the last sections. However, in some system, the elastic energy has to be taken into account for the modeling of precipitation kinetics. This has not been done yet for ODS steels. Yet, from the findings from Ribis *et al* [137], the elastic energy plays a significant role on the thermal stability of coherent particles. The elastic energy takes action as soon as one coherent precipitate generates a distortion of the matrix lattice network close to the interface. This distortion is thus quantified by the degree of misfit between the interatomic distances of the lattice plans at the interface [260]:

$$\delta = \frac{d_M - d_p}{d_p} \tag{5.29}$$

where $d_M$ and $d_p$ are the lattice parameter of the matrix and the precipitate, respectively. The elastic energy is related to the degree of misfit by [260]:

$$E_{el}^{sph} = 3\mu\delta^2 R^3 \tag{5.30}$$

with $\mu$ the shear modulus and $R$ the sphere radius. In realty, this equation dissimulates a major hypothesis: one assumes that the daughter phase has the same elastic

properties than the mother phase, which is inappropriate in most of case studies. The misfit elastic energy can be better described by [261, 262]:

$$E_{mis}^{str} = 3\varepsilon_m^2 \delta_p [1 - [1 + \frac{\delta_m}{\delta_p}(\frac{3(1-\nu_m)}{1+\nu_m} - 1)]]^{-1} \tag{5.31}$$

with

$$\delta_{m,p} = \mu_{m,p} \cdot \frac{1+\nu_{m,p}}{1-2\nu_{m,p}} \tag{5.32}$$

where $\mu_{m,p}$ and $\nu_{m,p}$ are the shear modulus and the Poisson ratio of the matrix or the precipitate, respectively. One can retrieve the equation (5.30) from equation (5.31) by taking $\delta_m = \delta_p$ and $\nu_m = \nu_p$. de Ouden et al [261] described the different volume mechanical contributions associated to the appearance of an interface between the two phases (cobalt particles in a copper matrix). In their study, the misfit energy density modifies the calculations of the total Gibbs free energy:

$$\Delta g_{tot} = \frac{4}{3}\pi R^3 (\Delta g_{ch} + \Delta g_{def}^{str} + \Delta g_{mis}^{str}) + 4\pi R^2 \gamma \tag{5.33}$$

Beside the negative chemical driving force $\Delta g_{ch} < 0$, two positive terms are added compared to the classic NGCT: the misfit energy linked to the macroscopic deformation (introduced by tensile test for instance) and the misfit energy induced by the particles themselves. The effect of an external deformation field (mechanical testing, creep testing, etc) is not considered here: $\Delta g_{def}^{str} = 0$. One will only focus on the effect of the elastic misfit energy due to the particles themselves [9]. The presence of misfit elastic energy finally increases the critical radius, which becomes:

$$r^* = \frac{-2\gamma}{\Delta g_{ch} + \Delta g_{mis}^{str}} \tag{5.34}$$

One can conclude that introducing the elastic energy around the precipitate-to-matrix interface requires changes in the NGTC equations that depend on both mechanical and geometrical assumptions [10].

## Introduction of anisotropy

The elastic energy was first taken into consideration in order to explain the morphological evolution of $\gamma\prime$ phases in nickel superalloys [215, 263]. This elastic energy was determined by Nabarro in 1940 [264] for an incoherent precipitate and by Eshelby for a coherent precipitate, of ellipsoidal shape with axes $a$ and $b$:

---

9. One notices here that the so-called concepts are different whether mechanics or metallurgy is involved. Mechanical engineers will tend to call elastic energy the tensor product of stress and strain tensors imposed by an external mechanical loading.

10. Nous appellerons ce terme énergie élastique d'accommodation. On remarque ici que le français, latin optimiste, préfère accommoder, i.e. rendre commode, tandis que l'anglo-saxon constate simplement que l'interface ne convient pas, est mal ajustée: $misfit$.

$$E_{el}^{ell} = \frac{2}{3}\mu\frac{(\Omega_p - \Omega_M)^2}{\Omega_p}f(\frac{a}{b}) \qquad (5.35)$$

with $\Omega_p$ and $\Omega_M$ the atomic volume of the precipitate and the matrix, respectively. The function $f(\frac{a}{b})$ takes into account the anisotropy, from a disk to a needle, and in between a sphere ($a = b$). The concept of anisotropic morphology necessitates to modify the classic nucleation equations to determine the geometrical features of the nuclei. If for spherical precipitates, a critical radius is enough to describe the nucleus, the critical size of a more complex and anisotropic nucleus of geometrical parameters $a$ and $b$, is described by an enthalpy maximum:

$$\begin{cases} \frac{\partial \Delta G(a,b)}{\partial a} = 0 \\ \frac{\partial \Delta G(a,b)}{\partial b} = 0 \end{cases} \qquad (5.36)$$

Ribis *et al* [137] used the superspheres model to describe the experimental observation of oxides in steels and their morphological evolution. This geometrical model allows to continuously describe, with a parameter $\eta$, the transition from cubic to spherical shape. The elastic energy of a supersphere in a given matrix was calculated by Onaka *et al* [265, 266, 267].

The elastic energy in the calculation of $\Delta G$ for an ellipsoid particle with of semi-minor and semi-major axes $a$ and $b$ was derived by Lee [262]:

$$\Delta g_{tot} = \frac{4}{3}\pi a^3 \eta(\Delta g_{ch} + \Delta g_{el}^{iso}) + \pi a^2 \gamma[2 + g(\eta)] \qquad (5.37)$$

with $\bar{\Delta g}_{el} = \frac{\Delta g_{el}}{3\mu\delta^2}$ the normalized elastic energy, $\eta = {}^b/_a$ the aspect ratio and g($\eta$) a function defined by:

$$g(\eta) = \begin{cases} \frac{2\eta^2}{\sqrt{1-\eta^2}}tanh^{-1}(\sqrt{1-\eta^2}) \text{ if } \eta < 1 \\ 2 \text{ if } \eta = 1 \text{ (spherical)} \\ \frac{2\eta^2}{\sqrt{1-\eta^2}}sin^{-1}(\sqrt{1-\eta^2}) \text{ if } \eta > 1 \end{cases} \qquad (5.38)$$

The Gibbs free energy must be derivated with respect to $a$ and $\eta$. The derivative with respect to $\eta$ in the general case can be done only numerically whereas the analytical expression in the isotropic case can be found in [268]. By minimizing $\Delta G^*$ with respect to $\eta$, $\eta^*$ can be determined:

$$\Delta G^* = \frac{\pi\gamma^3[2 + g(\eta)]}{2\eta[\Delta g_{ch} + \bar{\Delta g}_{el}]^2} \qquad (5.39)$$

Once the Gibbs free energy is calculated and the critical size and morphology of the precipitates are determined, the growth and coarsening behavior can be determined. The modified equations for the superspheres model were calculated.

The concept lies on the comparison of the Gibbs free energy of the new precipitate which has grown as a cube, a sphere or a supersphere. The most energetically favorable case is chosen step by step during the growth process. Meanwhile, the coarsening is traduced by the Gibbs-Thomson effect that was also calculated for each geometrical contribution.

# Modified nucleation, growth, coarsening equations for superspherical precipitates

## Growth system

### Case study: spheres

For the growth stage, the precipitate is assumed spherical so that the Fick's equation can be solved, at the steady state[11]:

$$\frac{D}{r^2}\frac{\partial}{\partial r}\left(r^2\frac{\partial C}{\partial r}\right) = 0 \tag{5.40}$$

And the solution is given by:

$$\frac{\partial}{\partial r}\left(r^2\frac{\partial C}{\partial r}\right) = 0 \tag{5.41}$$

And:

$$r^2\frac{\partial C}{\partial r} = A \tag{5.42}$$

And for boundary conditions: $C(r = R_i) = C_i$ and $C(r = \infty) = C_0$:

$$C(r) = -\frac{R}{r}\left(C_0 - C_i\right) + C_0 \tag{5.43}$$

The flux at the interface is given by:

$$J(r = R) = D\frac{\partial C}{\partial r}\bigg|_{r=R} = \frac{R}{r^2}\left(C_0 - C_i\right)\bigg|_{r=R} \tag{5.44}$$

So the mass balance can be expressed as:

$$4\pi R^R C_p dR = 4\pi R^R C_i dR + J(r = R).4\pi R^2 dt \tag{5.45}$$

And so:

$$\frac{dR}{dt} = \frac{D}{R}\frac{X_0 - X_i}{\alpha X_p - X_i} \tag{5.46}$$

---

11. D is the diffusion coefficient of the slowest element, here yttrium.

**Case study: cubes**

When dealing with cubic shape, one proceeds like for the supersphere:

    - One calculates before the growth the radius of the sphere with the same volume

    - One calculates $dR_{eq}$

    - One checks the shape variation

    - One derives the new parameter $a$ of the cube if there has been no shape variation

For a cube, the relationship between the equivalent volume $V_{eq_{i+1}}$ of the sphere and the parameter $a$ is:

$$V_{cub} - V_{eq} = 8a^3 - \frac{4}{3}\pi R_{eq_{i+1}}^3 = 0 \tag{5.47}$$

Thus one can derive $a_{i+1}$:

$$a_{i+1} = \left(\frac{1}{6}\pi\right)^{1/3} R_{eq_{i+1}} \tag{5.48}$$

## Coarsening: Gibbs-Thomson effect

The corrective term of the Gibbs-Thomson equation (eq. 5.19) comes from the variation in the Gibbs free energy $G(R) = G(\infty) + \gamma S$ with respect to the variation of $n$ molecules of $\beta$, $n_\beta$. In eq. (5.19), the exponential term is $\gamma \frac{\partial S}{\partial n_\beta}$. This term will be calculated for each geometry.

**Case study: spheres**

It is the classic case, see eq. (5.19).

**Case study: cubes**

The surface and the volume of the cube are:

$$\begin{cases} S = 24a^2 \\ V = V_m n_\beta = 8a^3 \end{cases} \tag{5.49}$$

From the expression of the volume one can derive:

$$a = \left(\frac{1}{8}V_m n_\beta\right)^{1/3} \tag{5.50}$$

and also:

$$n_\beta = \frac{8a^3}{V_m} \tag{5.51}$$

Now, if substituting eq. 5.50 in the expression of the surface in eq. 5.49:

$$S = 96\left(V_m n_\beta\right)^{2/3} \tag{5.52}$$

If one differentiates:

$$\frac{\partial S}{\partial n_\beta} = 64.\left(V_m n_\beta\right)^{-1/3} V_m = 64.V^{2/3}.n_\beta^{-1/3} \tag{5.53}$$

If replacing $n_\beta^{-1/3}$ by its expression in eq. 5.51:

$$\frac{\partial S}{\partial n_\beta} = 64.V_m^{2/3}.\left(\frac{8a^3}{V_m}\right)^{-1/3} \tag{5.54}$$

Which gives:

$$\frac{\partial S}{\partial n_\beta} = \frac{32V_m}{a} \tag{5.55}$$

And thus the Gibbs-Thomson becomes:

$$X_i(R)^x X_i(R)^y = K_s \exp\left(\frac{32V_m\gamma}{akT}\right) \tag{5.56}$$

## Growth/coarsening system to solve

### Case study: sphere

$$\begin{cases} \frac{dR}{dt} = \frac{D^1}{R}\frac{X_0^1 - X_i^1(R)}{\alpha.X_p^1 - X_i^1(R)} \\ \frac{dR}{dt} = \frac{D^2}{R}\frac{X_0^2 - X_i^2(R)}{\alpha.X_p^2 - X_i^2(R)} \\ X_1^x(R)X_2^y(R) = K_s.exp\left(\frac{2\gamma V_{mol}^p}{RkT}\right) \end{cases} \tag{5.57}$$

This gives $Req$ and thus the volume of the particle.

### Case study: cube

$$\begin{cases} \frac{dR_{eq}}{dt} = \frac{D^1}{R_{eq}}\frac{X_0^1 - X_i^1(R_{eq})}{\alpha.X_p^1 - X_i^1(R_{eq})} \\ \frac{dR_{eq}}{dt} = \frac{D^2}{R_{eq}}\frac{X_0^2 - X_i^2(R_{eq})}{\alpha.X_p^2 - X_i^2(R_{eq})} \\ X_i(a)^x X_i(a)^y = K_s \exp\left(\frac{32V_m\gamma}{akT}\right) \end{cases} \tag{5.58}$$

For *PreciSo*, $a$ has to be replaced by its expression with $Req$:

$$\begin{cases} \frac{dR_{eq}}{dt} = \frac{D^1}{R_{eq}}\frac{X_0^1 - X_i^1(R_{eq})}{\alpha.X_p^1 - X_i^1(R_{eq})} \\ \frac{dR_{eq}}{dt} = \frac{D^2}{R_{eq}}\frac{X_0^2 - X_i^2(R_{eq})}{\alpha.X_p^2 - X_i^2(R_{eq})} \\ X_i(R_{eq})^x X_i(R_{eq})^y = K_s \exp\left[\left(\frac{6}{\pi}\right)^{1/3}\frac{32V_m\gamma}{R_{eq}kT}\right] \end{cases} \tag{5.59}$$

This gives the new volume and one checks which $\eta$ minimizes the energy.

# Application to $Y_2Ti_2O_7$

The mechanical properties of $Y_2Ti_2O_7$ were recently determined by He *et al* [269], as summarized in table 5.7:

**Table 5.7:** Mechanical properties of ceramics that are present in ODS steels (after [269]).

| Property | $TiO_2$ | $Y_2O_3$ | $Y_2Ti_2O_7$ |
|---|---|---|---|
| $H_v$ (GPa) | 11 | 6.9-9.1 | 12.1 |
| E (GPa) | $270 \pm 12$ | 188.0 | 253 |
| G (GPa) | 109 | 72.6 | 101 |
| $\nu$ | 0.22 | 0.294 | 0.25 |
| $\sigma$ (MPa) | 426 | 219 | 206 |

Given that:
(i) the mechanical properties of the particles and the matrix are known,
(ii) the elastic energy for superspheres was determined,
(iii) the modified NGCT equations for superspheres were proposed,

it is possible to implement a model to simulate the effect of both elastic energy and morphological change on the precipitation behavior of the oxides, specially their coarsening kinetics. This shall be tested on $Y_2Ti_2O_7$ particles.

# Annexe of Conclusion
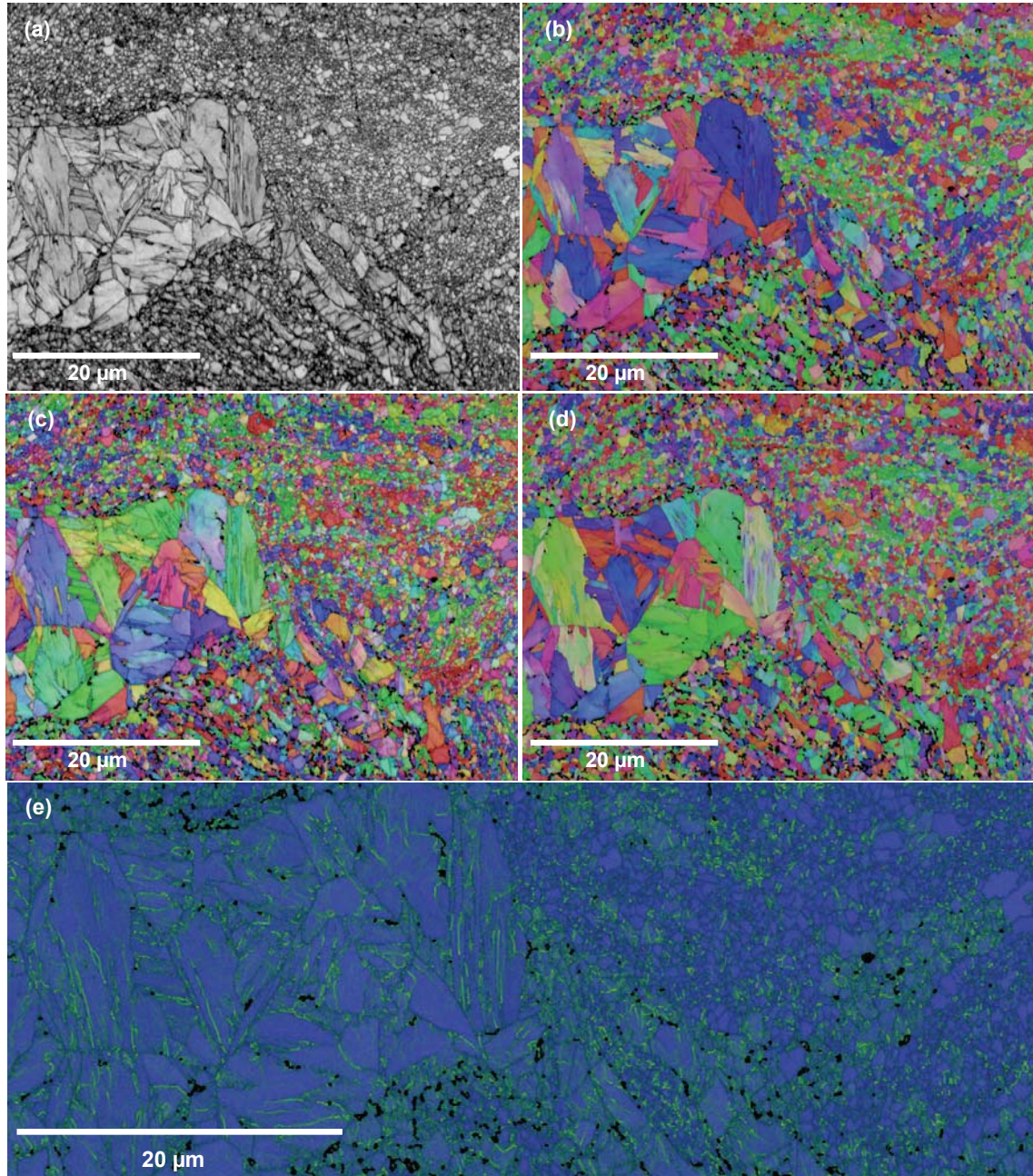
**Figure 5.34:** Microstructure of an 9Cr ODS steel SPSed at 1050°C, with a focus on a martensitic like structure surrounded by equiaxed ultrafine grained ferritic structure: (a) band contrast (b-d) EBSD orientation maps with three different inverse pole figures (IPF) and (e) Kernel Average Misorientation (KAM) highlighting the intragranular misorientation in green colour.

# Bibliography

[1] IAEA Vienna. Nuclear powder reactors in the world, REFERENCE DATA SERIES No. 2. Technical report, International Atomic Energy Agency, 2012.

[2] G. S. Was S. J. Zinkle. Materials challenges in nuclear energy. *Acta Materialia*, 61:735–758, 2013.

[3] G. S. Was. *Fundamentals of Radiation Materials Science, Metal and Alloys*, chapter Introduction. Springer, 2007.

[4] P. Dubuisson, Y. de Carlan, V. Garat, and M. Blat. ODS Ferritic/martensitic alloys for Sodium Fast Reactor fuel pin cladding. *Journal of Nuclear Materials*, 428(1–3):6 – 12, 2012.

[5] Y. de Carlan, J.-L. Bechade, P. Dubuisson, J.-L. Seran, P. Billot, A. Bougault, T. Cozzika, S. Doriot, D. Hamonand, J. Henry, M. Ratti, N. Lochet, D. Nunes, P. Olier, T. Leblond, and M.H. Mathon. CEA developments of new ferritic ODS alloys for nuclear applications. *Journal of Nuclear Materials*, 386–388:430–432, 2009.

[6] S. J. Zinkle and J. T. Busby. Structural materials for fission and fusion energy. *Materials Today*, 12(11):12 – 19, 2009.

[7] E.A. Little. Void-swelling in irons and ferritic steels: I. mechanisms of swelling suppression. *Journal of Nuclear Materials*, 87(1):11 – 24, 1979.

[8] G. R. Odette. On mechanisms controlling swelling in ferritic and martensitic alloys. *Journal of Nuclear Materials*, 155–157:921–927, 1988.

[9] G.R. Odette, M.J. Alinger, and B.D. Wirth. Recent developments in irradiation-resistant steels. *Annual Review of Materials Research*, 38:471–503, 2008.

[10] J. J. Sniegowski and W. G. Wolfer. On the physical basis for the swelling resistance of ferritic steels. In *Top. Conf. Ferritic Alloys Use Nucl. Energy Technol., pp. 579–86*. New York: Metall. Soc. Am. Inst. Min. Metall. Petroleum Eng., 1984.

179

[11] M.-L. Lescoat, I. Monnet, J. Ribis, P. Dubuisson, Y. de Carlan, J.-M. Costantini, and J. Malaplate. Amorphization of oxides in ODS materials under low and high energyion irradiations. *Journal of Nuclear Materials*, 417(1–3):266 – 269, 2011.

[12] J. Ribis, M.-L. Lescoat, Y. de Carlan, J.-M. Costantini, I. Monnet, T. Cozzika, F. Delabrouille, and J. Malaplate. Stability of nano-oxides upon heavy ion irradiation of an ODS material. *Journal of Nuclear Materials*, 417(1–3):262 – 265, 2011.

[13] R.L. Klueh, J.P. Shingledecker, R.W. Swindeman, and D.T. Hoelzer. Oxide dispersion-strengthened steels: A comparison of some commercial and experimental alloys. *Journal of Nuclear Materials*, 341(2–3):103 – 114, 2005.

[14] M-L. Lescoat, J. Ribis, A. Gentils, O. Kaïtasov, Y. de Carlan, and A. Legris. In situ TEM study of the stability of nano-oxides in ODS steels under ion-irradiation. *Journal of Nuclear Materials*, 428(1–3):176 – 182, 2012.

[15] L.K. Mansur. Theory and experimental background on dimensional changes in irradiated alloys. *Journal of Nuclear Materials*, 216(0):97 – 123, 1994.

[16] M. S. El-Genk and J.-M. Tournier. A review of refractory metal alloys and mechanically alloyed-oxide dispersion strengthened steels for space nuclear power systems. *Journal of Nuclear Materials*, 340(1):93 – 112, 2005.

[17] S. Ukai, T. Nishida, H. Okada, T. Okuda, M. Fujiwara, and K. Asabe. Development of Oxide Dispersion Strengthened Ferritic Steels for FBR Core Application, (I). *Journal of Nuclear Science and Technology*, 34(3):256–263, 1997.

[18] S. Ukai, T. Nishida, T. Okuda, and T. Yoshitake. R&D of oxide dispersion strengthened ferritic martensitic steels for FBR . *Journal of Nuclear Materials*, 258–263, Part 2:1745 – 1749, 1998.

[19] S. Ukai, S. Mizuta, T. Yoshitake, T. Okuda, M. Fujiwara, S. Hagi, and T. Kobayashi. Tube manufacturing and characterization of oxide dispersion strengthened ferritic steels. *Journal of Nuclear Materials*, 283–287, Part 1(0):702 – 706, 2000. 9th Int. Conf. on Fusion Reactor Materials.

[20] J.H. Lee, R. Kasada, A. Kimura, T. Okuda, M. Inoue, S. Ukai, S. Ohnuki, T. Fujisawa, and F. Abe. Influence of alloy composition and temperature on corrosion behavior of ODS ferritic steels. *Journal of Nuclear Materials*, 417(1–3):1225 – 1228, 2011. Proceedings of ICFRM-14.

[21] J. H. Kim, K. M. Kim, T. S. Byun, D. W. Lee, and C. H. Park. High-temperature oxidation behavior of nano-structured ferritic oxide-dispersion strengthened alloys. *Thermochimica Acta*, 579(0):1 – 8, 2014.

[22] A. Alamo, V. Lambard, X. Averty, and M.H. Mathon. Assessment of ODS-14%Cr ferritic alloy for high temperature applications. *Journal of Nuclear Materials*, 329–333, Part A(0):333 – 337, 2004.

[23] A.L. Rouffié, J. Crépin, M. Sennour, B. Tanguy, A. Pineau, D. Hamon, P. Wident, S. Vincent, V. Garat, and B. Fournier. Effect of the thermal ageing on the tensile and impact properties of a 18%Cr ODS ferritic steel. *Journal of Nuclear Materials*, 445(1–3):37 – 42, 2014.

[24] J. S. Benjamin. Dispersion strengthened superalloys by mechanical alloying. *Metallurgical Transactions*, 1:2943–2951, 1970.

[25] A. de Bremaecker. Past research and fabrication conducted at SCK-CEN on ferritic ODS alloys used as cladding for FBR's fuel pins. *Journal of Nuclear Materials*, 428(1–3):13 – 30, 2012.

[26] D. Bouvard. *Métallurgie des poudres*. Hermes Science Publications, 2001.

[27] Mathieu Ratti. *Development of new ferritic/martensitc steels for RNR-Na tube cladding materials, translated from 'Développement de nouvelles nuances d'aciers ferritiques/martensitiques pour le gainage d'éléments combustibles des Réacteurs à Neutrons Rapides au sodium'.* PhD thesis, Institut Polytechnique de Grenoble, 2010.

[28] O. Kalokhtina, B. Radiguet, Y. de Carlan, and P. Pareige. Study of Nano-cluster Formation in Fe-18Cr ODS Ferritic Steel by Atom Probe Tomography. In *Symposia Z/BB – Basic Actinide Science and Materials for NuclearApplications*, volume 1264 of *MRS Proceedings*, 2010.

[29] O. Kalokhtina. *Study of the formation of nano-particles in ODS and NDS steels by atom probe tomography*. PhD thesis, Université de Rouen, 2012.

[30] I. Hilger, M. Tegel, M.J. Gorley, P.S. Grant, T. Weißgärber, and B. Kieback. The structural changes of $Y_2O_3$ in ferritic ODS alloys during milling. *Journal of Nuclear Materials*, 447(1–3):242 – 247, 2014.

[31] H. Wen, T. D. Topping, D. Isheim, D. N. Seidman, and E. J. Lavernia. Strengthening mechanisms in a high-strength bulk nanostructured Cu–Zn–Al alloy processed via cryomilling and spark plasma sintering. *Acta Materialia*, 61(8):2769 – 2782, 2013.

[32] J. H. Kim and C. H. Park. Effect of milling temperature on nanoclusters and ultra fine grained microstructure of oxide dispersion strengthened steel. *Journal of Alloys and Compounds*, 585(0):69 – 74, 2014.

[33] J. H. Kim, T. S. Byun, J. H. Lee, J. Y. Min, S. W. Kim, C. H. Park, and B. H. Lee. Effects of processing condition on the microstructural and tensileproperties of 14Cr-based oxide dispersion strengthened alloys. *Journal of Nuclear Materials*, 449(1–3):300 – 307, 2014.

[34] J. Hoffmann. *Ferritische ODS-Stähle - Herstellung, Umformung und Strukturanalyse*. PhD thesis, Karlsruher Institut für Technologie (KIT), 2013.

[35] T. Hayashi, P.M. Sarosi, J.H. Schneibel, and M.J. Mills. Creep response and deformation processes in nanocluster-strengthened ferritic steels. *Acta Materialia*, 56(7):1407 – 1416, 2008.

[36] R. Kasada, S.G. Lee, J. Isselin, J.H. Lee, T. Omura, A. Kimura, T. Okuda, M. Inoue, S. Ukai, S. Ohnuki, T. Fujisawa, and F. Abe. Anisotropy in tensile and ductile–brittle transition behavior ofODS ferritic steels. *Journal of Nuclear Materials*, 417(1–3):180 – 184, 2011. Proceedings of ICFRM-14.

[37] M. Praud. *Plasticity mechanisms in ODS steels, translated from Plasticité d'alliages renforcés par nano-précipitation*. PhD thesis, Université de Toulouse, 2012.

[38] A. Karch. *Microstructure modeling of ferritic ODS steels during hot extrusion*. PhD thesis, CEMEF - Mines Paris Tech, 2014.

[39] S. Ukai, M. Harada, H. Okada, M. Inoue, S. Nomura, S. Shikakura, T. Nishida, M. Fujiwara, and K. Asabe. Tube manufacturing and mechanical properties of oxide dispersion strengthened ferritic steel. *Journal of Nuclear Materials*, 204(0):74 – 80, 1993.

[40] S. Ukai, S. Mizuta, M. Fujiwara, T. Okuda, and T. Kobayashi. Development of 9Cr-ODS Martensitic Steel Claddings for Fuel Pins by means of Ferrite to Austenite Phase Transformation. *Journal of Nuclear Science and Technology*, 39(7):778–788, 2002.

[41] L. Toualbi, C. Cayron, P. Olier, R. Logé, and Y. de Carlan. Relationships between mechanical behavior and microstructural evolutions in Fe 9Cr–ODS during the fabrication route of SFR cladding tubes. *Journal of Nuclear Materials*, 442(1–3):410 – 416, 2013.

[42] C. Cayron, E. Rath, I. Chu, and S. Launois. Microstructural evolution of $Y_2O_3$ and $MgAl_2O_4$ ODS EUROFERsteels during their elaboration by mechanical milling and hot isostatic pressing. *Journal of Nuclear Materials*, 335:83–102, 2004.

[43] Z. Oksiuta and N. Baluc. Effect of mechanical alloying atmosphere on the microstructure and Charpy impact properties of an ODS ferritic steel. *Journal of Nuclear Materials*, 386–388(0):426 – 429, 2009.

[44] P. Olier, Z. Oksiuta, J.-F. Melat, D. Hamon, T. Leblond, Y. de Carlan, and N. Baluc. Microstructural and cold workability assessment of a new ODS ferritic steel. In *Proc. 1st Int. Conf. on New Materials for Extreme Environments (San Sebastian, Spain, 2-4 June 2008)*, pages 313–18, 2009.

[45] J. Isselin, R. Kasada, A. Kimura, T. Okuda, M. Inoue, S. Ukai, S. Ohnuki, T. Fujisawa, and F. Abe. Evaluation of fracture behavior of recrystallized and aged high-Cr ODS ferritic steels. *Journal of Nuclear Materials*, 417(1–3):185 – 188, 2011. Proceedings of ICFRM-14.

[46] H. Réglé. *Oxide dispersion strengthened ferritic alloys, 14/20% chromium: Effects of processing on deformation textures, recrystallisation and tensile properties*. PhD thesis, Université de Paris-Sud UFR Scientifique d'Orsay, 1994.

[47] L. Toualbi. *Process optimization of ODS steels tube cladding, translated from Optimisation de la gamme de fabrication de tubes en acier renforcés par une dispersion nanométrique d'oxydes (ODS)*. PhD thesis, CEMEF - Mines Paris Tech, 2012.

[48] N. Bozzolo, A. Agnoli, N. Souai, M. Bernacki, and R. E. Logé. Strain induced abnormal grain growth in nickel base superalloys. *Materials Science Forum*, 753:321–324, 2013.

[49] T Grosdidier, E Suzon, and F Wagner. Primary recrystallization in an ODS FeAl alloy: an effective way to modify texture and microstructure. *Intermetallics*, 12(6):645 – 654, 2004.

[50] K. Mino, Y.G. Nakagawa, and A. Ohtomo. Abnormal grain growth behavior of an ods alloy. *Metallurgical Transactions A*, 18(6):777–784, 1987.

[51] M. Song, C. Sun, J. Jang, C.H. Han, T.K. Kim, K.T. Hartwig, and X. Zhang. Microstructure refinement and strengthening mechanisms of a 12Cr ODS steel processed by equal channel angular extrusion. *Journal of Alloys and Compounds*, 577(0):247 – 256, 2013.

[52] A.J. Ardell. Precipitation hardening. *Metallurgical Transactions A*, 16(12):2131–2165, 1985.

[53] E. Nembach and G. Neite. Precipitation hardening of Superalloys by ordered $\gamma$'-particles. *Progress in Materials Science*, 29:177–319, 1985.

[54] S.J. Andersen, H.W. Zandbergen, J. Jansen, C. TrÆholt, U. Tundal, and O. Reiso. The crystal structure of the $\beta''$ phase in Al–Mg–Si alloys. *Acta Materialia*, 46(9):3283 – 3298, 1998.

[55] D. Bardel, M. Perez, D. Nelias, A. Deschamps, C.R. Hutchinson, D. Maisonnette, T. Chaise, J. Garnier, and F. Bourlier. Coupled precipitation and yield strength modelling for non-isothermal treatments of a 6061 aluminium alloy. *Acta Materialia*, 62(0):129 – 140, 2014.

[56] T. Gladman. *The Physical Metallurgy of Microalloyed Steels.* Maney Publishing, 1997.

[57] M.K Miller, D.T Hoelzer, E.A Kenik, and K.F Russell. Nanometer scale precipitation in ferritic MA/ODS alloy MA957. *Journal of Nuclear Materials*, 329–333, Part A(0):338 – 341, 2004.

[58] Y. Wu, E.M. Haney, N.J. Cunningham, and G.R. Odette. Transmission electron microscopy characterization of the nanofeatures in nanostructured ferritic alloy MA957. *Acta Materialia*, 60(8):3456–3468, 2012.

[59] N. Cunningham, Y. Wu, D. Klingensmith, and G.R. Odette. On the remarkable thermal stability of nanostructured ferritic alloys. *Materials Science and Engineering: A*, 613(0):296 – 305, 2014.

[60] P. Susila, D. Sturm, M. Heilmaier, B.S. Murty, and V. Subramanya Sarma. Effect of yttria particle size on the microstructure and compression creep properties of nanostructured oxide dispersion strengthened ferritic (Fe–12Cr–2W–0.5Y$_2$O$_3$) alloy. *Materials Science and Engineering: A*, 528(13–14):4579 – 4584, 2011.

[61] A. Steckmeyer, Vargas Hideroa Rodrigo, J.M. Gentzbittel, V. Rabeau, and B. Fournier. Tensile anisotropy and creep properties of a Fe–14CrWTi ODS ferritic steel. *Journal of Nuclear Materials*, 426(1–3):182 – 188, 2012.

[62] B. Fournier, A. Steckmeyer, A.-L. Rouffie, J. Malaplate, J. Garnier, M. Ratti, P. Wident, L. Ziolek, I. Tournie, V. Rabeau, J.M. Gentzbittel, T. Kruml, and I. Kubena. Mechanical behaviour of ferritic ODS steels – Temperature dependancy and anisotropy. *Journal of Nuclear Materials*, 430(1–3):142 – 149, 2012.

[63] A. García-Junceda, M. Hernández-Mayoral, and M. Serrano. Influence of the microstructure on the tensile and impact properties of a 14Cr ODS steel bar. *Materials Science and Engineering: A*, 556(0):696 – 703, 2012.

[64] P. Unifantowicz, Z. Oksiuta, P. Olier, Y. de Carlan, and N. Baluc. Microstructure and mechanical properties of an ODS RAF steel fabricated by hot extrusion or hot isostatic pressing. *Fusion Engineering and Design*, 86(9–11):2413 – 2416, 2011.

184

[65] M. Praud, F. Mompiou, J. Malaplate, D. Caillard, J. Garnier, A. Steckmeyer, and B. Fournier. Study of the deformation mechanisms in a Fe–14% Cr ODS alloy. *Journal of Nuclear Materials*, 428(1–3):90 – 97, 2012.

[66] T. Narita, S. Ukai, S. Ohtsuka, and M. Inoue. Effect of tungsten addition on microstructure and high temperature strength of 9Cr ODS ferritic steel. *Journal of Nuclear Materials*, 417(1–3):158 – 161, 2011.

[67] T. Narita, S. Ukai, S. Ohtsuka, and M. Inoue. Microstructure and toughness of Cr-W and Cr-V ferritic steels. *Journal of Nuclear Materials*, 155-157:656–661, 1988.

[68] A. Steckmeyer, M. Praud, B. Fournier, J. Malaplate, J. Garnier, J.L. Béchade, I. Tournié, A. Tancray, A. Bougault, and P. Bonnaillie. Tensile properties and deformation mechanisms of a 14Cr ODS ferritic steel. *Journal of Nuclear Materials*, 405(2):95 – 100, 2010.

[69] J.H. Schneibel, C.T. Liu, M.K. Miller, M.J. Mills, P. Sarosi, M. Heilmaier, and D. Sturm. Ultrafine-grained nanocluster-strengthened alloys with unusually high creep strength. *Scripta Materialia*, 61(8):793 – 796, 2009.

[70] D. Fabrègue, J. Piallat, E. Maire, Y. Jorand, V. Massardier-Jourdan, and G. Bonnefont. Spark plasma sintering of pure iron nanopowders by simple route. *Powder Metallurgy*, 55:76–79, 2012.

[71] T. Grosdidier, G. Ji, and S. Launois. Processing dense hetero-nanostructured metallic materials by spark plasma sintering. *Scripta Materialia*, 57(6):525 – 528, 2007.

[72] W. M. Guo, Z. G. Yang, and G. J. Zhang. Comparison of $ZrB_2$-SiC ceramics with $Yb_2O_3$ additive prepared by hot pressing and spark plasma sintering. *International Journal of Refractory Metals And Hard Materials*, 29:452–455, 2011.

[73] H. Zhang, M. J. Gorley, K. B. Chong, M. E. Fitzpatrick, S. G. Roberts, and P. S. Grant. An in situ powder neutron diffraction study of nano-precipitate formation during processing of oxide-dispersion strengthened ferritic steels. *Journal of Alloys and Compounds*, 582(0):769 – 773, 2014.

[74] D. M. Hulbert, A. Anders, D. V. Dudina, J. Andersson, D. Jiang, C. Unuvar, U. Anselmi-Tamburini, E. J. Lavernia, and A. K. Mukherjee. The absence of plasma in "spark plasma sintering". *Journal of Applied Physics*, 104(3):–, 2008.

[75] D. M. Hulbert, A. Anders, J. Andersson, E. J. Lavernia, and A. K. Mukherjee. A discussion on the absence of plasma in spark plasma sintering. *Scripta Materialia*, 60(10):835 – 838, 2009.

[76] C.-L. Chen, C.-L., G. J. Tatlock, and A.R. Jones. Effect of annealing temperatures on the secondary re-crystallization of extruded PM2000 steel bar. *Journal of Microscopy*, 233(3):474–481, 2009.

[77] U. Anselmi-Tamburini, S. Gennari, J.E. Garay, and Z.A. Munir. Fundamental investigations on the spark plasma sintering/synthesis process: II. Modeling of current and temperature distributions. *Materials Science and Engineering: A*, 394(1–2):139 – 148, 2005.

[78] Z.A. Munir, U. Anselmi-Tamburini, and M. Ohyanagi. The effect of electric field and pressure on the synthesis and consolidation of materials: A review of the spark plasma sintering method. *Journal of Materials Science*, 41(3):763–777, 2006.

[79] D. Fabrègue, B. Mouawad, and C. Hutchinson. Enhanced recovery and recrystallization of metals due to an applied current. *Scripta Materialia*, 92:3–6, 2014.

[80] E. Olevsky and L. Froyen. Constitutive modeling of spark-plasma sintering of conductive materials. *Scripta Materialia*, 55(12):1175 – 1178, 2006.

[81] G. Molenat, L. Durand, J. Galy, and A. Couret. Temperature Control in Spark Plasma Sintering: An FEM Approach. *Journal of Metallurgy*, 2010.

[82] J. M. Torralba, L. Fuentes-Pacheco, N. García-Rodríguez, and M. Campos. Development of high performance powder metallurgy steels by high-energy milling. *Advanced Powder Technology*, 24(5):813 – 817, 2013.

[83] T.T. Sasaki, T. Mukai, and K. Hono. A high-strength bulk nanocrystalline Al–Fe alloy processed by mechanical alloying and spark plasma sintering. *Scripta Materialia*, 57(3):189 – 192, 2007.

[84] G. Ji, T. Grosdidier, N. Bozzolo, and S. Launois. The mechanisms of microstructure formation in a nanostructured oxide-dispersion strengthened FeAl alloy obtained by spark plasma sintering. *Intermetallics*, 15(2):108 – 118, 2007.

[85] G. Ji, F. Bernard, S. Launois, and T. Grosdidier. Processing conditions, microstructure and mechanical properties of hetero-nanostructured ODS FeAl alloys produced by spark plasma sintering. *Materials Science and Engineering: A*, 559(0):566 – 573, 2013.

[86] C. Heintze, F. Bergner, A. Ulbricht, M. Hernández-Mayoral, U. Keiderling, R. Lindau, and T. Weissgärber. Microstructure of oxide dispersion strengthened eurofer and iron–chromium alloys investigated by means of small-angle neutron scattering and transmission electron microscopy. *Journal of Nuclear Materials*, 416(1–2):35 – 39, 2011.

[87] C. Heintze, M. Hernández-Mayoral, A. Ulbricht, F. Bergner, A. Shariq, T. Weissgärber, and H. Frielinghaus. Nanoscale characterization of ODS Fe–9%Cr model alloys compacted by spark plasma sintering. *Journal of Nuclear Materials*, 428(1–3):139 – 146, 2012.

[88] M.A. Auger, V. de Castro, T. Leguey, A. Muñoz, and R. Pareja. Microstructure and mechanical behavior of ODS and non-ODS Fe–14Cr model alloys produced by spark plasma sintering. *Journal of Nuclear Materials*, 436:68–75, 2013.

[89] K. Rajan, V. S. Sarma, T.R.G. Kutty, and B.S. Murty. Hot hardness behaviour of ultrafine grained ferritic oxide dispersion strengthened alloys prepared by mechanical alloying and spark plasma sintering. *Materials Science and Engineering: A*, 558(0):492 – 496, 2012.

[90] Q.X. Sun, T. Zhang, X.P. Wang, Q.F. Fang, T. Hao, and C.S. Liu. Microstructure and mechanical properties of oxide dispersion strengthened ferritic steel prepared by a novel route. *Journal of Nuclear Materials*, 424(1–3):279 – 284, 2012.

[91] Y.P. Xia, X.P. Wang, Z. Zhuang, Q.X. Sun, T. Zhang, Q.F. Fang, T. Hao, and C.S. Liu. Microstructure and oxidation properties of 16Cr–5Al–ODS steel preparedby sol–gel and spark plasma sintering methods. *Journal of Nuclear Materials*, 432(1–3):198 – 204, 2013.

[92] K. N. Allahar, J. Burns, B. Jaques, Y.Q. Wuand I. Charit, J. Cole, and D. P. Butt. Ferritic Oxide Dispersion Strengthened Alloys by Spark Plasma Sintering. *Journal of Nuclear Materials*, 443:256–265, 2013.

[93] K. Rajan, T. Shanmugasundaram, V. Subramanya Sarma, and B.S. Murty. Effect of $Y_2O_3$ on Spark Plasma Sintering Kinetics of Nanocrystalline 9Cr-1Mo Ferritic Oxide Dispersion-Strengthened Steels. *Metallurgical and Materials Transactions A*, 44(9):4037–4041, 2013.

[94] S. Pasebani and I. Charit. Effect of alloying elements on the microstructure and mechanical properties of nanostructured ferritic steels produced by spark plasma sintering. *Journal of Alloys and Compounds*, 599(0):206 – 211, 2014.

[95] M.F. Riley. Method for producing powder by gas atomization, January 29 1991. US Patent 4,988,464.

[96] M. Ratti, D. Leuvrey, M.H. Mathon, and Y. de Carlan. Influence of titanium on nano-cluster (Y, Ti, O) stability in ODS ferritic materials. *Journal of Nuclear Materials*, 386–388(0):540 – 543, 2009.

[97] E. Olevsky, A. Maximenko, S.Van Dyck, L. Froyen, L. Delaey, and L. Buekenhout. Container influence on shrinkage under hot isostatic pressing - I. Shrinkage anisotropy of a cylindrical specimen. *International Journal of Solids and Structures*, 35(18):2283 – 2303, 1998.

[98] E. Olevsky and A. Maximenko. Container influence on shrinkage under hot isostatic pressing - II. Shape distortion of cylindrical specimens. *International Journal of Solids and Structures*, 35(18):2305 – 2314, 1998.

[99] ASTM C373 - 88(2006) Standard Test Method for Water Absorption, Bulk Density, Apparent Porosity, and Apparent Specific Gravity of Fired Whiteware Products.

[100] H. Sakasegawa, F. Legendre, L. Boulanger, M. Brocq, L. Chaffron, T. Cozzika, J. Malaplate, J. Henry, and Y. de Carlan. Stability of non-stoichiometric clusters in the MA957 ODS ferritic alloy. *Journal of Nuclear Materials*, 417(1–3):229 – 232, 2011. Proceedings of ICFRM-14.

[101] G. Bernard-Granger, N. Monchalin, and C. Guizard. Comparisons of grain size-density trajectory during spark plasma sintering and hot-pressing of zirconia. *Materials Letters*, 62:4555–4558, 2008.

[102] S.A. Cho, I. B. de Arenas, and F. J. Arenas. Porosity microhardness correlation of sintered $(\mathrm{Al}_{(1-y)}\mathrm{Cr}_y)_2\mathrm{O}_3$ solid solutions. *Journal of Alloys and Compounds*, 288:211–216, 1999.

[103] J.R. Cahoon, W.H. Broughton, and A.R. Kutzak. The determination of yield strength from hardness measurements. *Metallurgical Transactions*, 2(7):1979–1983, 1971.

[104] X. Boulnat, D. Fabrègue, M. Perez, M.-H. Mathon, and Y. de Carlan. High-temperature tensile properties of nano-oxide dispersion strengthened ferritic steels produced by mechanical alloying and spark plasma sintering. *Metallurgical and Materials Transactions A*, 44(6):2461–2465, 2013.

[105] B. Mouawad, X. Boulnat, M. Perez, D. Fabrègue, and Y. de Carlan. Tailoring the microstructure and the mechanical properties of ultrafine grained high strength ferritic steels by powder metallurgy. *Journal Of Nuclear Materials*, In press, 2015.

[106] Z. Oksiuta, P. Mueller, P. Spätig, and N. Baluc. Effect of thermo-mechanical treatments on the microstructure and mechanical properties of an ODS ferritic steel. *Journal of Nuclear Materials*, 412:221–226, 2011.

188

[107] X. Boulnat, M. Perez, D. Fabrègue, T. Douillard, M.-H. Mathon, and Y. de Carlan. Microstructure evolution in nano-reinforced ferritic steel processed by mechanical alloying and spark plasma sintering. *Metallurgical and Materials Transactions A*, 45A:1485–1497, 2014.

[108] Y. Wang, M. Chen, F. Zhou, and E. Ma. High tensile ductility in a nanostructured metal. *Nature*, 419:912–915, 2002.

[109] A. Takahashi, Z. Chen, N. Ghoniem, and N. Kioussis. Atomistic-continuum modeling of dislocation interaction with $Y_2O_3$ particles in iron. *Journal of Nuclear Materials*, 417(1–3):1098 – 1101, 2011.

[110] Y.H. Zhao, Y.Z. Guo, Q. Wei, T.D. Topping, A.M. Dangelewicz, Y.T. Zhu, T.G. Langdon, and E.J. Lavernia. Influence of specimen dimensions and strain measurement methods on tensile stress–strain curves. *Materials Science and Engineering: A*, 525(1–2):68 – 77, 2009.

[111] K.A. Darling, B.G. Butler, H.E. Maupin, and L.J. Kecskes. Stabilized nanocrystalline Cu-10 at.%Nb alloy and consolidation by equal channel angular extrusion. In *Proceedings of the 2012 International Conference on Powder Metallurgy and Particulate Materials*, 2012.

[112] D. Fabrègue and T. Pardoen. A constitutive model for elastoplastic solids containing primary and secondary voids. *Journal of the Mechanics and Physics of Solids*, 56(3):719 – 741, 2008.

[113] D. Fabrègue and T. Pardoen. Corrigendum to "A constitutive model for elastoplastic solids containing primary and secondary voids" [J. Mech. Phys. Solids 56 (2008) 719–741]. *Journal of the Mechanics and Physics of Solids*, 57(5):869 – 870, 2009.

[114] Y. Zhao, T. Topping, J. F. Bingert, A. M. Thornton, J. J. andDangelewicz, Y. Li, Y. Liu, W. andZhu, and E. J. Zhou, Y.and Lavernia. High tensile ductility and strength in bulk nanostructured nickel. *Advanced Materials*, 20(16):3028–3033, 2008.

[115] C.C Koch. Optimization of strength and ductility in nanocrystalline and ultrafine grained metals. *Scripta Materialia*, 49(7):657 – 662, 2003. Viewpoint Set No. 31. Mechanical Properties of Fully Dense Nanocrystalline Metals.

[116] A. K Mukherjee. An examination of the constitutive equation for elevated temperatureplasticity. *Materials Science and Engineering: A*, 322(1–2):1 – 22, 2002.

[117] D. S. Sarma, A. V. Karasev, and P. G. Jönsson. On the role of non-metallic inclusions in the nucleation of acicular ferrite in steels. *ISIJ International*, 49(7):1063–1074, 2009.

[118] A. Deschamps and Y. Brechet. Influence of predeformation and ageing of an Al–Zn–Mg alloy - II. Modeling of precipitation kinetics and yield stress. *Acta Materialia*, 47(1):293 – 305, 1998.

[119] A. de Vaucorbeil, W.J. Poole, and C.W. Sinclair. The superposition of strengthening contributions in engineering alloys. *Materials Science and Engineering: A*, 582(0):147 – 154, 2013.

[120] G. Lu. The Peierls-Nabarro Model of Dislocations: A Venerable Theory and its Current Development. In *Handbook of Materials Modeling*. Springer Netherlands, 2005.

[121] M. J. Alinger. *On the formation and stability of nanometer scale precipitates in ferritic alloys during processing and high temperature service*. PhD thesis, University of California Santa Barbara, 2004.

[122] C. Hin and B.D. Wirth. Formation of $Y_2O_3$ nanoclusters in nano-structured ferritic alloys: Modeling of precipitation kinetics and yield strength. *Journal of Nuclear Materials*, 402(1):30 – 37, 2010.

[123] J. Friedel. *Dislocations*. Pergamon Press, 1964.

[124] U.F. Kocks and H. Mecking. Physics and phenomenology of strain hardening: the FCC case. *Progress in materials science*, 48:171–273, 2003.

[125] D. Bardel. *Influence of microstructure on cyclic mechanical behavior of age hardening aluminum alloy after non-isothermal treatments, translated from 'Rôle de la microstructure d'un alliage à durcissement structural sur son comportement et sa tenue mécanique sous sollicitations cycliques après un transitoire thermique'*. PhD thesis, INSA de Lyon, 2014.

[126] C.E. Lacy and M. Gensamer. The tensile properties of alloyed ferrites. *Transactions of the American Society of Metals*, 32:88, 1944.

[127] P. Susila, D. Sturm, M. Heilmaier, B.S. Murty, and V. Subramanya Sarma. Microstructural studies on nanocrystalline oxide dispersion strengthened austenitic (Fe–18Cr–8Ni–2W–0.25$Y_2O_3$) alloy synthesized by high energy ball milling and vacuum hot pressing. *Journal of Materials Science*, 45(17):4858–4865, 2010.

[128] Q. Li. Modeling the microstructure–mechanical property relationship for a 12Cr–2W–V–Mo–Ni power plant steel. *Materials Science and Engineering: A*, 361(1–2):385 – 391, 2003.

[129] C. H. Young and H. K. D. H. Bhadeshia. Strength of mixtures of bainite and martensite. *Materials Science and Technology*, 10(3):209–214, 1994.

190

[130] C. H. Young and H.K.D.H. Bhadeshia. Computer modelling for the yield strength of the mixed micro-structures of bainite and martensite. *J. Phys. IV France*, 05:C8–267–C8–272, 1995.

[131] H. Qiu, R. Ito, and K. Hiraoka. Role of grain size on the strength and ductile–brittle transition temperature in the dual-sized ferrite region of the heat-affected zone of ultra-fine grained steel. *Materials Science and Engineering: A*, 435–436(0):648 – 652, 2006.

[132] S. Takaki, K. Kawasaki, and Y. Kimura. Mechanical properties of ultra fine grained steels. *Journal of Materials Processing Technology*, 117(3):359 – 363, 2001.

[133] M. Perrier. *Etude de la relation entre la microstructure et les propriétés mécaniques d'un acier durci par précipitation intermétallique intense: le Fer-Silicium-Titane.* PhD thesis, Université de Grenoble, 2011.

[134] M. F. Ashby. Work hardening of dispersion-hardened crystals. *Philosophical Magazine*, 14(132):1157–1178, 1966.

[135] M. Couvrat. *Fabrication of ODS steels: process-microstructure-properties relationships, translated from 'Fabrication d'aciers ODS à haute performance : relation procédé microstructure propriétés mécaniques'.* PhD thesis, Université de Rennes 1, 2013.

[136] S.-Y. Zhong. *Study of high-temperature microstructure evolution of ODS ferritic steels with various contents of yttrium, titanium and oxygen, translated from 'Étude des évolutions microstructurales à haute température en fonction des teneurs initiales en Y, Ti et O et, de leur incidence sur les hétérogénéités de déformation dans les aciers ODS Fe-14Cr1W'.* PhD thesis, Université Paris-Sud 11, 2012.

[137] J. Ribis and Y. de Carlan. Interfacial strained structure and orientation relationships of the nanosized oxide particles deduced from elasticity-driven morphology in oxide dispersion strengthened materials. *Acta Materialia*, 60(1):238 – 252, 2012.

[138] N. Sallez, X. Boulnat, A. Borbély, J-L. Béchade, D. Fabrègue, M. Perez, Y. de Carlan, L. Hennet, C. Mocuta, D. Thiaudière, and Y. Bréchet. In situ microstructure instabilities of ODS ferritic steel powder during annealing. *Acta Materialia*, Under Review, 2014.

[139] X. Boulnat, N. Sallez, M. Dadé, P. Donnadieu, A. Borbély, J.-L. Béchade, A. Deschamps, F. de Geuser, J. Malaplate, M. Perez, D. Fabrègue, Y. de Carlan, and Y. Bréchet. Influence of precipitation on the microstructure of ultra-fine grained ferritic steels. *Acta Materialia*, Being Submitted, 2014.

[140] Y. Estrin. *Unified Constitutive Laws of Plastic Deformation*, chapter Dislocation-Density-Related Constitutive Modeling, pages 69–106. Academic Press, 1996.

[141] G. Fribourg, Y. Bréchet, A. Deschamps, and A. Simar. Microstructure-based modelling of isotropic and kinematic strain hardening in a precipitation-hardened aluminium alloy. *Acta Materialia*, 59:3621–3635, 2011.

[142] A. Karmakar, S. Sivaprasad, S. Kundu, and D. Chakrabarti. Tensile behavior of ferrite-carbide and ferrite-martensite steels with different ferrite grain structures. *Metallurgical and Materials Transactions A*, 45(4):1659–1664, 2014.

[143] R. Song, D. Ponge, and D. Raabe. Improvement of the work hardening rate of ultrafine grained steels through second phase particles. *Scripta Materialia*, 52(11):1075 – 1080, 2005.

[144] S. Ukai and S. Ohtsuka. Low cycle fatigue properties of ODS ferritic–martensitic steels at high temperature. *Journal of Nuclear Materials*, 367–370, Part A(0):234 – 238, 2007. Proceedings of the Twelfth International Conference on Fusion Reactor Materials (ICFRM-12).

[145] I. Kubena, B. Fournier, and T. Kruml. Effect of microstructure on low cycle fatigue properties of ODS steels. *Journal of Nuclear Materials*, 424(1–3):101 – 108, 2012.

[146] Y. Sugino, S. Ukai, B. Leng, N. Oono, S. Hayashi, T. Kaito, and S. Ohtsuka. Grain boundary sliding at high temperature deformation in cold-rolled ODS ferritic steels. *Journal of Nuclear Materials*, (0):–, 2014.

[147] F.J. Humphreys and M. Hatherly. *Recrystallization and Related Annealing Phenomena*. 2nd edition, Elsevier, Amsterdam, 2004.

[148] A. Michels, C.E. Krill, H. Ehrhardt, R. Birringer, and D.T. Wu. Modelling the influence of grain-size-dependent solute drag on thekinetics of grain growth in nanocrystalline materials. *Acta Materialia*, 47(7):2143 – 2152, 1999.

[149] D.G. Cram, X.Y. Fang, H.S. Zurob, Y.J.M. Bréchet, and C.R. Hutchinson. The effect of solute on discontinuous dynamic recrystallization. *Acta Materialia*, 60(18):6390 – 6404, 2012.

[150] T. Gladman. *Proc. R. Soc. Lond. A*, 294A:298, 1966.

[151] C. Zener. *quoted by C.S. Smith, Trans. Met. Soc. AIME*, 175:15–51, 1948.

[152] P.R. Rios. Overview no. 62: A theory for grain boundary pinning by particles. *Acta Metallurgica*, 35(12):2805 – 2814, 1987.

[153] F. Haessner and J. Schmidt. Recovery and recrystallization of different grades of high purity aluminium determined with a low temperature calorimeter. *Scripta Metallurgica*, 22(12):1917 – 1922, 1988.

[154] B. Schmidt, P. Nagpal, and I. Baker. Assessment of ods-14%cr ferritic alloy for high temperature applications.

[155] M. Calcagnotto, D. Ponge, E. Demir, and D. Raabe. Orientation gradients and geometrically necessary dislocations in ultrafine grained dual-phase steels studied by 2D and 3D EBSD. *Materials Science and Engineering: A*, 527(10–11):2738 – 2746, 2010.

[156] X. Wu, S. Ukai, R. Miyata, N. Oono, S. Hayashi, B. Leng, S. Ohtsuka, and T. Kaito. Effect of hot-rolling and cooling rate on microstructure and high-temperature strength in 9Cr ODS steel. *Journal of Nuclear Materials*, 440(1–3):553 – 556, 2013.

[157] A. Molinari, S. Libardi, M. Leoni, and P. Scardi. Role of lattice strain on thermal stability of a nanocrystalline FeMo alloy. *Acta Materialia*, 58:963–966, 2010.

[158] M. Cabibbo, C. Paternoster, R. Cecchini, A. Fabrizi andA. Molinari, S. Libardi, and M. Zadra. A microstructure study of nanostructured Fe–Mo + 1.5 wt.%SiO$_2$ and +1.5 wt.%TiO$_2$ powders compacted by spark plasma sintering. *Materials Science and Engineering: A*, 496(1–2):121–132, 2008.

[159] H. Sakasegawa, L. Chaffron, F. Legendre, L. Boulanger, T. Cozzika, M. Brocq, and Y. de Carlan. Correlation between chemical composition and size of very small oxide particles in the MA957 ODS ferritic alloy. *Journal of Nuclear Materials*, 384(2):115 – 118, 2009.

[160] V. de Castro, E.A. Marquis, S. Lozano-Perez, R. Pareja, and M.L.Jenkins. Stability of nanoscale secondary phases in an oxide dispersion strengthened Fe–12Cr alloy. *Acta Materialia*, 59(10):3927 – 3936, 2011.

[161] M.J. Alinger, G.R. Odette, and D.T. Hoelzer. On the role of alloy composition and processing parameters in nanocluster formation and dispersion strengthening in nanostuctured ferritic alloys. *Acta Materialia*, 57(2):392 – 406, 2009.

[162] C. Cayron, A. Montani, D. Venet, and Y. de Carlan. Identification of new phases in annealed Fe–18CrWTi ODS powders. *Journal of Nuclear Materials*, 399(2–3):219 – 224, 2010.

[163] M. Klimiankou, R. Lindau, and A. Möslang. TEM characterization of structure and composition of nanosized ODS particles in reduced activation ferritic–martensitic steels. *Journal of Nuclear Materials*, 329–333, Part A(0):347 – 351, 2004.

[164] C. A. Williams, P. Unifantowicz, N. Baluc, G. D.W. Smith, and E. A. Marquis. The formation and evolution of oxide particles in oxide-dispersion-strengthened ferritic steels during processing. *Acta Materialia*, 61(6):2219–2235, 2013.

[165] M.H. Mathon, M. Perrut, S.Y. Zhong, and Y. de Carlan. Small angle neutron scattering study of martensitic/ferritic ODS alloys. *Journal of Nuclear Materials*, 428(1–3):147 – 153, 2012.

[166] H. Kishimoto, R. Kasada, O. Hashitomi, and A. Kimura. Stability of Y–Ti complex oxides in Fe–16Cr–0.1Ti ODS ferritic steel before and after heavy-ion irradiation. *Journal of Nuclear Materials*, 386–388(0):533 – 536, 2009.

[167] H.K.D.H. Bhadeshia. Recrystallisation of practical mechanically alloyed iron-base and nickel-base superalloys. *Materials Science and Engineering: A*, 223(1–2):64 – 77, 1997.

[168] M. Perez and A. Deschamps. Microscopic modelling of simultaneous two-phase precipitation: application to carbide precipitation in low-carbon steels. *Materials Science and Engineering: A*, 360(1–2):214 – 219, 2003.

[169] F. Perrard, A. Deschamps, and P. Maugis. Modelling the precipitation of nbc on dislocations in *alpha*-fe. *Acta Materialia*, 55(4):1255 – 1266, 2007.

[170] R. Wagner, R. Kampmann, and P. W. Voorhees. *Homogeneous Second-Phase Precipitation*. Wiley-VCH Verlag GmbH & Co. KGaA, 2006.

[171] Y. Huang, F.J. Humphreys, and M. Ferry. The annealing behaviour of deformed cube-oriented aluminium single crystals. *Acta Materialia*, 48(10):2543 – 2556, 2000.

[172] A. Hirata, T. Fujita, Y. R. Wen, J. H. Schneibel, C. T. Liu, and M. W. Chen. Atomic structure of nanoclusters in oxide-dispersion strengthened steels. *Nature Materials*, 10:922–926, 2011.

[173] Y. Bréchet and M. Militzer. A note on grain size dependent pinning. *Scripta Materialia*, 52(12):1299–1303, 2005.

[174] Z. Dapeng, L. Yong, L. Feng, W. Yuren, and Z. Liujieand D. Yuhai. ODS ferritic steel engineered with bimodal grain size for high strength and ductility. *Materials Letters*, 65(11):1672 – 1674, 2011.

[175] Y. Wen, Y. Liu, A. Hirata, F. Liu, T. Fujita, Y. Dou, D. Liu, B. Liu, Z. Liu, and C.T. Liu. Innovative processing of high-strength and low-cost ferritic steels strengthened by Y–Ti–O nanoclusters. *Materials Science and Engineering: A*, 544(0):59 – 69, 2012.

[176] V. Y. Novikov. Grain growth and disperse particles: Impact of triple junctions. *Materials Letters*, 84(0):136 – 138, 2012.

[177] T.T. Sasaki, T. Ohkubo, and K. Hono. Microstructure and mechanical properties of bulk nanocrystalline Al–Fe alloy processed by mechanical alloying and spark plasma sintering. *Acta Materialia*, 57(12):3529 – 3538, 2009.

[178] T. Ungár and A. Borbely. The effect of dislocation contrast on X-Ray line broadening: A new approach to line profile analysis. *Applied Physics Letters*, 69:3173–3175, 1996.

[179] T. Ungár, I. Dragomir, Á. Révész, and A. Borbély. The contrast factors of dislocations in cubic crystals: the dislocation model of strain anisotropy in practice. *Journal of Applied Crystallography*, 32(5):992–1002, Oct 1999.

[180] T. Shintani and Y. Murata. Evaluation of the dislocation density and dislocation character in cold rolled Type 304 steel determined by profile analysis of X-ray diffraction. *Acta Materialia*, 59(11):4314 – 4322, 2011.

[181] M. D. Mulholland and D. N. Seidman. Nanoscale co-precipitation and mechanical properties of a high-strength low-carbon steel. *Acta Materialia*, 59(5):1881 – 1897, 2011.

[182] E. Jimenez-Melero, R. Blondé, M.Y. Sherif, V. Honkimäki, and N.H. van Dijk. Time-dependent synchrotron X-ray diffraction on the austenite decompositionkinetics in SAE 52100 bearing steel at elevated temperatures under tensile stress. *Acta Materialia*, 61(4):1154 – 1166, 2013.

[183] E.M Lauridsen, D.Juul Jensen, H.F Poulsen, and U Lienert. Kinetics of individual grains during recrystallization. *Scripta Materialia*, 43(6):561 – 566, 2000.

[184] S Malinov, W Sha, Z Guo, C.C Tang, and A.E Long. Synchrotron X-ray diffraction study of the phase transformations in titanium alloys. *Materials Characterization*, 48(4):279 – 295, 2002.

[185] R.A. Renzetti, H.R.Z. Sandim, R.E. Bolmaro, P.A. Suzuki, and A. Moeslang. X-Ray evaluation of dislocation density in ODS-Eurofer steel. *Materials Science and Engineering: A*, 534:142–146, 2012.

[186] C. Le Bourlot, P. Landois, S. Djaziri, P.-O. Renault, E. Le Bourhis, P. Goudeau, M. Pinault, M. Mayne-L'Hermite, B. Bacroix, D. Faurie, O. Castelnau, P. Launois, and S. Rouzière. Synchrotron X-ray diffraction experiments with a prototype hybrid pixel detector. *Journal of applied crystallography*, 45:1–10, 2012.

[187] B. E. Warren and B. L. Averbach. The effect of cold-work distortion on x-ray patterns. *Journal of Applied Physics*, 21:595–599, 1950.

[188] G. K. Williamson and W. H. Hall. X-ray line broadening from filed aluminium and wolfram. *Acta Metallurgica*, 1:24–31, 1953.

[189] M. A. Krivoglaz. *Theory of X-Ray and Thermal Neutron Scattering by Real Crystals.* New York: Plenum, 1969.

[190] M Wilkens. The determination of density and distribution of dislocations in deformed single crystals from broadened X-ray diffraction profiles. *Physica Status Solidi A: Applications and Materials Science*, 2:359–370, 1970.

[191] H. Mughrabi. Dislocation wall and cell structures and long-range internal stresses in deformed metal crystals. *Acta Metallurgica*, 31:1367–1379, 1983.

[192] A. Borbély, J. Dragomir-Cernatescu, G. Ribarik, and T. Ungàr. Computer program *ANIZC* for the calculation of diffraction contrast factors of dislocations in elastically anisotropic cubic, hexagonal and trigonal crystals. *Journal of Applied Crystallography*, 36(1):160–162, 2003.

[193] G. Caglioti, A. Paoletti, and F.P. Ricci. Choice of collimators for a crystal spectrometer for neutron diffraction. *Nuclear Instruments*, 3(4):223–228, 1958.

[194] D. Balzar. *Voigt-function model in diffraction line-broadening analysis, in Defect and Microstructure Analysis by Diffraction.* IUCr/Oxford University Press., 1999.

[195] T. Ungàr, J. Gubicza, G. Ribàrik, and A. Borbély. Crystallite size distribution and dislocation structure determined by diffraction profile analysis: principles and practical application to cubic and hexagonal crystals. *Journal of Applied Crystallography*, 34(3):298–310, Jun 2001.

[196] T. Ungár. Dislocation densities, arrangements and character from X-ray diffraction experiments. *Materials Science & Engineering, A: Structural Materials: Properties, Microstructure and Processing*, 309-310:14–22, 2001.

[197] T. Ungàr, J. Gubicza, P. Hanàk, and I. Alexandrov. Densities and character of dislocations and size-distribution of subgrains in deformed metals by X-ray diffraction profile analysis. *Materials Science and Engineering: A*, 319-321:274–278, 2001.

[198] B. E. Warren. X-ray studies of deformed metals. *Progress in Metal Physics*, 8(0):147–202, 1959.

[199] A. Révész, T. Ungàr, A. Borbély, and J. Lendvai. Dislocations and grain size in ball-milled iron powder. *Nanostructured Materials*, 7(7):779–788, 1996.

196

[200] N. Sallez, P. Donnadieu, E. Courtois-Manara, C. Kübel, R. Prang, M. Blat-Yrieix, Y. de Carlan, and Y. Bréchet. On morphological anisotropy and local texture in a ferritic ODS steel : from as-milled powder to consolidated states. *Materials characterization*, Under Review, 2014.

[201] A. Pandey, H. Palneedi, K. Jayasankar, P. Parida, M. Debata, B.K. Mishra, and S. Saroja. Microstructural characterization of oxide dispersion strengthened ferritic steel powder. *Journal of Nuclear Materials*, 437:29–36, 2013.

[202] E.M Lauridsen, H.F Poulsen, S.F Nielsen, and D Juul Jensen. Recrystallization kinetics of individual bulk grains in 90% cold-rolled aluminium. *Acta Materialia*, 51(15):4423 – 4435, 2003.

[203] S.O. Poulsen, E.M. Lauridsen, A. Lyckegaard, J. Oddershede, C. Gundlach, C. Curfs, and D. Juul Jensen. In situ measurements of growth rates and grain-averaged activation energies of individual grains during recrystallization of 50% cold-rolled aluminium. *Scripta Materialia*, 64(11):1003–1006, 2011.

[204] C.C. Koch. The synthesis and structure of nanocrystalline materials produced by mechanical attrition: A review. *Nanostructured Materials*, 2(2):109 – 129, 1993.

[205] H.-J. Fecht. Nanostructure formation by mechanical attrition. *Nanostructured Materials*, 6(1–4):33 – 42, 1995.

[206] C.C. Koch. Synthesis of nanostructured materials by mechanical milling: problems and opportunities. *Nanostructured Materials*, 9(1–8):13 – 22, 1997.

[207] C. Smith and I. Dillamore. Subgrain growth in high-purity iron. *Metal Science Journal*, 4:161–167, 1970.

[208] A. Hayoune and D. Hamana. A dilatometric and high-temperature X-ray diffraction study of cold deformation effect on the interaction between precipitation, recovery and recrystallization reactions in Al-12wt.% Mg alloy. *Materials Science and Engineering: A*, 527(27–28):7261–7264, 2010.

[209] I. Groma, T. Ungár, and M. Wilkens. Asymmetric X-ray line broadening of plastically deformed crystals. I. Theory. *Journal of Applied Crystallography*, 21(1):47–54, Feb 1988.

[210] F. De Geuser and A. Deschamps. Precipitate characterisation in metallic systems by small-angle X-ray or neutron scattering. *Comptes Rendus Physique*, 13(3):246 – 256, 2012. Use of large scale facilities for research in metallurgy / Utilisation des grands instruments pour la recherche en métallurgie.

[211] M. F. Ashby and L. M. Brown. Diffraction contrast from spherically symmetrical coherency strains. *Philosophical Magazine*, 8:1083–103, 1963.

[212] M. Dadé. *Plasticity mechanisms in ODS ferritic steels.* PhD thesis, INPG, 2015.

[213] N. Sallez. *On recrystallization and abnormal growth in ODS ferritic steels.* PhD thesis, INP Grenoble, 2015.

[214] F. Louchet and A. Hazotte. A model for low stress cross-diffusional creep and directional coarsening of superalloys. *Scripta Materialia*, 37(5):589 – 597, 1997.

[215] A. G. Khachaturyan, S. V. Semenovskaya, and J. W. Morris Jr. Theoretical analysis of strain-induced shape changes in cubic precipitatesduring coarsening. *Acta Metallurgica*, 36:1563–1572, 1988.

[216] E. Kozeschnik. *Modeling Solid-state Precipitation.* Momentum Press, LLC, New York, 2013.

[217] S. Esmaeili, D.J. Lloyd, and W.J. Poole. A yield strength model for the Al-Mg-Si-Cu alloy AA6111. *Acta Materialia*, 51:2243–2257, 2003.

[218] E. Clouet, M. Nastar, and C. Sigli. Nucleation of $Al_3Zr$ and $Al_3Sc$ in aluminium alloys: from kinetic Monte Carlo simulations to classical theory. *Physical review B*, 69:1–14, 2004.

[219] E. Clouet, A. Barbu, L. Laé, and G. Martin. Precipitation kinetics of $Al_3Zr$ and $Al_3Sc$ in aluminium alloys modeled with cluster dynamics. *Acta Materialia*, 53:2313–2325, 2005.

[220] M. Brocq, B. Radiguet, J.-M. Le Breton, F. Cuvilly, P. Pareige, and F. Legendre. Nanoscale characterisation and clustering mechanism in an $Fe–Y_2O_3$ model ODS alloy processed by reactive ball milling and annealing. *Acta Materialia*, 58(5):1806 – 1814, 2010.

[221] M. Laurent-Brocq, F. Legendre, M.-H. Mathon, A. Mascaro, S. Poissonnet, B. Radiguet, P. Pareige, M. Loyer, and O. Leseigneur. Influence of ball-milling and annealing conditions on nanocluster characteristics in oxide dispersion strengthened steels. *Acta Materialia*, 60(20):7150 – 7159, 2012.

[222] A. Hirata, T. Fujita, C.T. Liu, and M.W. Chen. Characterization of oxide nanoprecipitates in an oxide dispersion strengthened 14YWT steel using aberration-corrected STEM. *Acta Materialia*, 60(16):5686 – 5696, 2012.

[223] S. Kardellass, C. Servant, N. Selhaoui, A. Iddaoudi, M. Ait Amar, and L. Bouirden. A thermodynamic assessment of the iron–yttrium system. *Journal of Alloys and Compounds*, 583(0):598 – 606, 2014.

[224] K.T. Jacob and G. Rajitha. Nonstoichiometry, defects and thermodynamic properties of $YFeO_3$, $YFe_2O_4$ and $Y_3Fe_5O_{12}$. *Solid State Ionics*, 224(0):32 – 40, 2012.

[225] D. Giusca and I. Popescu. *Bull. Soc. Roum. Phys*, 40:18, 1939.

[226] J. D. Ault and A. J. E. Welch. The yttrium oxide - titanium dioxide system. *Acta Crystallographica*, 20:410, 1966.

[227] W. G. Mumme and A. D. Wadsley. The Structure of Orthorhombic $Y_2TiO_5$, an Example of Mixed Seven- and Five fold Coordination. *Acta Crystallographica*, B24:1327–1333, 1968.

[228] R. Chinnappan. Thermodynamic stability of oxide phases of Fe–Cr based ODS steels via quantum mechanical calculations. *Calphad*, (0), 2014.

[229] C. Hin, B. D. Wirth, and J. B. Neaton. Formation of $Y_2O_3$ nanoclusters in nanostructured ferritic alloys during isothermal and anisothermal heat treatment: A kinetic Monte Carlo study. *Phys. Rev. B*, 80:134118, 2009.

[230] M. H. Mathon and C. H. De Novion. De l'intensité à la structure des matériaux. *Journal De Physique IV*, 9(1):127–146, 1999.

[231] S.Y. Zhong, J. Ribis, V. Klosek, Y. de Carlan, N. Lochet, V. Ji, and M.H. Mathon. Study of the thermal stability of nanoparticle distributions in an oxide dispersion strengthened (ODS) ferritic alloys. *Journal of Nuclear Materials*, 428(1–3):154 – 159, 2012.

[232] C. Capdevila, Y. L. Chen, A. R. Jones, and H. K. D. H. Bhadeshia. Grain boundary mobility in Fe-base oxide dispersion strengthened PM2000 alloy. *Iron and Steel Institute of Japan International*, 43:777–783, 2003.

[233] M. Tamura, H. Sakasegawa, K. Shiba, H. Tanigawa, K. Shinozuka, and H. Esaka. Decomposition of $Y_2Ti_2O_7$ particles in 8 Pct Cr oxide-dispersion strengthened martensitic steel during tempering. *Metallurgical and Materials Transactions A*, 42(8):2176–2188, 2011.

[234] Ceri A. Williams. *Atomic scale characterisation of oxide dispersion strengthened steels for fusion applications.* PhD thesis, University of Oxford, 2011.

[235] P. Maugis and M. Gouné. Kinetics of vanadium carbonitride precipitation in steel: A computer model. *Acta Materialia*, 53(12):3359 – 3367, 2005.

[236] Erik J. Pavlina, John G. Speer, and Chester J. Van Tyne. Equilibrium solubility products of molybdenum carbide and tungsten carbide in iron. *Scripta Materialia*, 66(5):243 – 246, 2012.

[237] M. Perez, E. Courtois, D. Acevedo, T. Epicier, and P. Maugis. Precipitation of niobium carbonitrides in ferrite: chemical compositionmeasurements and thermodynamic modelling. *Philosophical Magazine Letters*, 87(9):645–656, 2007.

[238] F. Perrard, A. Deschamps, F. Bley, P. Donnadieu, and P. Maugis. A small-angle neutron scattering study of fine-scale NbC precipitation kinetics in the $\alpha$-Fe-Nb-C system. *Journal of Applied Crystallography*, 39(4):473–482, 2006.

[239] C. Gallais, A. Denquin, Y. Bréchet, and G. Lapasset. Precipitation microstructures in an {AA6056} aluminium alloy after friction stir welding: Characterisation and modelling. *Materials Science and Engineering: A*, 496(1–2):77 – 89, 2008.

[240] H.R. Pruppacher and J.D. Klett. *Microphysics of Clouds and Precipitation*, chapter Chapter 9: Heterogeneous nucleation. Springer.

[241] M. Perez, M. Dumont, and D. Acevedo-Reyes. Implementation of classical nucleation and growth theories for precipitation. *Acta Materialia*, 56(9):2119 – 2132, 2008.

[242] M. Perez, M. Dumont, and D. Acevedo-Reyes. Corrigendum to "implementation of classical nucleation and growth theories for precipitation" [acta materialia 56 (2008) 2119–2132]. *Acta Materialia*, 57(4):1318 –, 2009.

[243] Michel Perez. Gibbs–thomson effects in phase transformations. *Scripta Materialia*, 52(8):709 – 712, 2005.

[244] M. Perez. *Approche multi-échelle de la précipitation*. Habilitation à diriger des recherches, 2007.

[245] M. Nicolas and A. Deschamps. Characterisation and modelling of precipitate evolution in an Al–Zn–Mg alloy during non-isothermal heat treatments. *Acta Materialia*, 51(20):6077 – 6094, 2003.

[246] B. Sonderegger and E. Kozeschnik. Size dependence of the interfacial energy in the generalized nearest-neighbor broken-bond approach. *Scripta Materialia*, 60(8):635 – 638, 2009.

[247] C. Hin and B.D. Wirth. Formation of oxide nanoclusters in nanostructured ferritic alloys during anisothermal heat treatment: A kinetic monte carlo study. *Materials Science and Engineering: A*, 528(4–5):2056 – 2061, 2011.

[248] P. Klugkist and C. Herzig. Tracer diffusion of titanium in $\alpha$-iron. *Physica status solidi*, 148:413–421, 1995.

[249] R. Barlow and P. J. Grundy. The determination of the diffusion constants of oxygen in nickel and $\alpha$-iron by an internal oxidation method. *Journal of Materials Science*, 4:797–801, 1969.

[250] J. Takada and M. Adachi. Determination of diffusion coefficient of oxygen in $\alpha$-iron from internal oxidation measurements in Fe-Si alloys. *Journal of Materials Science*, 21:2133–2137, 1986.

[251] L. Barnard, G.R. Odette, I. Szlufarska, and D. Morgan. An ab initio study of Ti–Y–O nanocluster energetics in nanostructured ferritic alloys. *Acta Materialia*, 60(3):935 – 947, 2012.

[252] D. Murali, B.K. Panigrahi, M.C. Valsakumar, and C.S. Sundar. Diffusion of Y and Ti/Zr in bcc iron: A first principles study. *Journal of Nuclear Materials*, 419(1–3):208 – 212, 2011.

[253] P. Miao, G.R. Odette, T. Yamamoto, M. Alinger, and D. Klingensmith. Thermal stability of nano-structured ferritic alloy. *Journal of Nuclear Materials*, 377:59–64, 2008.

[254] K.K. Wang, L.J. Gustavson, and J.H. Dumbleton. Dispersion strengthened cobalt-chromium-molybdenum alloy produced by gas atomization, May 26 1987. US Patent 4,668,290.

[255] N. Hervé. *Development of new NDS/ODS alloys*. PhD thesis, On going.

[256] B. Harry. *Effect of chemical composition on the recrystallization behavior of ODS steels*. PhD thesis, On going.

[257] L. Toualbi, C. Cayron, P. Olier, J. Malaplate, M. Praud, M.-H. Mathon, D. Bossu, E. Rouesne, A. Montani, R. Logé, and Y. de Carlan. Assessment of a new fabrication route for Fe–9Cr–1W ODS cladding tubes. *Journal of Nuclear Materials*, 428(1–3):47 – 53, 2012.

[258] M. Militzer, E.B. Hawbolt, and T.R. Meadowcroft. Microstructural model for hot strip rolling of high-strength low-alloy steels. *Metallurgical and Materials Transactions A*, 31(4):1247–1259, 2000.

[259] Umberto Eco. *Il nome della rosa*. Bompiani, 1989, from an original thought of Bernard de Chartres.

[260] J. Philibert, A. Vignes, Y. Bréchet, and P. Combrade. *Métallurgie: du minerai au matériau*. Elsevier-Masson, 1998.

[261] D. den Ouden, F.J. Vermolen, L. Zhao, C. Vuik, and J. Sietsma. Modelling of particle nucleation and growth in binary alloys under elastic deformation: An application to a Cu–0.95 wt%Co alloy. *Computational Materials Science*, 50(8):2397 – 2410, 2011.

[262] J. K. Lee, D.M. Barnett, and H.I. Aaronson. The elastic strain energy of coherent ellipsoidal precipitates inanisotropic crystalline solids. *Metallurgical Transactions A*, 8(6):963–970, 1977.

[263] J. K. Lee. Splitting of coherent precipitates caused by elastic non-equilibrium. *Theoretical and Applied Fracture Mechanics*, 33(3):207 – 217, 2000.

[264] F. R. N. Nabarro. The strains produced by precipitation in alloys. *Proceedings of the Royal Society of London A*, 175:519–538, 1940.

[265] S. Onaka, T. Fujii, and M. Kato. The elastic strain energy of a coherent inclusion with deviatoric misfit strains. *Mechanics of Materials*, 20(4):329 – 336, 1995.

[266] S. Onaka, T. Fujii, and M. Kato. Effects of octahedral to spherical precipitate-shape transition on elastic strain energy due to misfit precipitates in materials with cubic structures. *Mechanics of Materials*, 37(1):179 – 187, 2005.

[267] S. Onaka, T. Fujii, and M. Kato. Elastic strain energy due to misfit strains in a polyhedral precipitate composed of low-index planes. *Acta Materialia*, 55(2):669 – 673, 2007.

[268] D.M. Barnett, J.K. Lee, H.I. Aaronson, and K.C. Russell. The strain energy of a coherent ellipsoidal precipitate. *Scripta Metallurgica*, 8(12):1447 – 1450, 1974.

[269] L.F. He, J. Shirahata, T. Nakayama, T. Suzuki, H. Suematsuand I. Ihara, Y.W. Bao, T. Komatsu, and K. Niihara. Mechanical properties of $Y_2Ti_2O_7$. *Scripta Materialia*, 64(6):548 – 551, 2011.

# FOLIO ADMINISTRATIF

## THÈSE SOUTENUE DEVANT L'INSTITUT NATIONAL DES SCIENCES APPLIQUÉES DE LYON

NOM: BOULNAT                                                DATE de SOUTENANCE: 18 décembre 2014

Prénoms: Xavier

TITRE: FAST high-temperature consolidation of Oxide-Dispersion Strengthened (ODS) steels: process, microstructure, precipitation, properties.

NATURE: Doctorat                                            Numéro d'ordre: 2014-ISAL-0139

École doctorale: Matériaux de Lyon

Spécialité: Matériaux

RÉSUMÉ:

Ce travail vise à améliorer la compréhension de la microstructure d'aciers ferritiques à durcissement structural, fabriqués par métallurgie des poudres, appelés **aciers ODS** (Oxide-Dispersion Strengthened). Une technique rapide de consolidation assistée par courant électrique, le Spark Plasma Sintering (SPS), a été testée afin d'optimiser la microstructure. Pour la première fois, on montre que d'excellentes **propriétés mécaniques** peuvent être obtenues par SPS. En outre, ce procédé peut engendrer une large gamme de microstructures et donc de résistance mécanique et de ductilité.

Cependant, la consolidation par SPS échoue quand il s'agit d'éviter l'apparition d'une **microstructure ferritique hétérogène**, composée de grains dits ultrafins (D<500 nm) entourée de grains grossiers (D>10 $\mu$m), malgré la cinétique rapide de consolidation. Une caractérisation microstructurale au fil du procédé a permis de comprendre l'évolution de la microstructure durant consolidation. Le calcul des pressions gouvernant la mobilité des interfaces souligne l'importance de la déformation plastique hétérogène issue du cobroyage des poudres. Par ailleurs, il est montré que la précipitation des particules d'oxydes ancre les joints de grains et stabilise la microstructure hétérogène, même à très haute température. On montre aussi qu'augmenter la teneur en yttrium, titane et oxygène n'empêche pas la **croissance anormale** mais permet cependant de contrôler la fraction et la taille de grains ultrafins, et donc les propriétés mécaniques des aciers ODS.

Parce que les particules à travers l'**ancrage des joints de grains** jouent un rôle primordial dans la croissance des grains, une caractérisation fine de l'état de **précipitation** a été réalisée sur les matériaux consolidés par SPS. Par un **modèle thermodynamique** de type germination/croissance/coalescence, les cinétiques de précipitation des phases $Y_2O_3$ et $Y_2Ti_2O_7$ ont également été simulées durant les étapes de consolidation non isothermes.

MOTS-CLÉS: Aciers ODS, Métallurgie des Poudres, Spark Plasma Sintering, Croissance de Grains, Ferrite, Recristallisation, Transformation de Phase, Précipitation, Modélisation, Caractérisation Microstructurale, Microscopie, Synchrotron, Propriétés Mécaniques

Laboratoire(s) de recherche: Laboratoire MATEIS (Matériaux: Ingénierie et Science)
UMR CNRS 5510 - INSA de Lyon
25 avenue J. Capelle
69621 Villeurbanne Cedex FRANCE

Directeurs de thèse: Michel Perez et Damien Fabrègue

Président du jury: ROLAND LOGÉ, Professeur, EPF Lausanne
Composition du jury: ALEXIS DESCHAMPS, Professeur, SIMaP, Rapporteur
ERNST KOZESCHNIK, Professeur, TU Wien, Rapporteur
ROLAND LOGÉ, Professeur, EPF Lausanne, Examinateur
MARTA SERRANO, Ingénieur de Recherche, CIEMAT Madrid, Examinateur
MARTINE BLAT, Ingénieur de Recherche, EDF R&D, Examinateur
YANN DE CARLAN, Ingénieur de Recherche, CEA Saclay, Encadrant industriel